# Nanostructuring of electrodes, from the synthesis of materials to their use in industrialisable fabrication processes for electrochemical sensors

Michael Spann

# THÈSE

Pour obtenir le grade de

## DOCTEUR DE L'UNIVERSITÉ GRENOBLE ALPES

Spécialité : 2MGE : Matériaux, Mécanique, Génie civil, Electrochimie

Arrêté ministériel : 25 mai 2016

Présentée par

## Michael SPANN

Thèse dirigée par **Pascal MAILLEY**, CEA

et co-encadrée par **Maxime GOUGIS**, CEA

préparée au sein du **Laboratoire CEA Grenoble - LETI**
dans **l'École Doctorale I-MEP2 - Ingénierie - Matériaux, Mécanique, Environnement, Energétique, Procédés, Production**

# Nanostructuration d'électrodes, depuis la synthèse des matériaux jusqu'à leur utilisation avec des procédés industrialisables de fabrication de capteurs électrochimiques

# Nanostructuration of electrodes, from the synthesis of materials to their use in industrialisable fabrication processes for electrochemical sensors

Thèse soutenue publiquement le **11 février 2022**,
devant le jury composé de :

**Monsieur Pascal MAILLEY**
INGENIEUR HDR, CEA centre de Grenoble, Directeur de thèse
**Monsieur Guy DENUAULT**
PROFESSEUR ASSOCIE, University of Southampton, Rapporteur
**Monsieur Mathieu ETIENNE**
DIRECTEUR DE RECHERCHE, CNRS délégation Centre Est, Rapporteur
**Madame Elisabeth DJURADO**
PROFESSEUR DES UNIVERSITES, Grenoble INP, Présidente
**Madame Sophie TINGRY**
DIRECTRICE DE RECHERCHE, CNRS délégation Occitanie Est, Examinatrice
**Madame Chantal GONDRAN**
MAITRE DE CONFERENCES, UGA, Membre invitée
**Monsieur Maxime GOUGIS**
DOCTEUR INGENIEUR, CEA, Membre invité

# Acknowledgements

This thesis represents, from a scientific standpoint, three years of studies in the field of materials science and electrochemistry. At the same time, it is the written result of three years of exchange with mentors and colleagues, fellow students, family and friends. The realization of the project would have been impossible without the contribution and the company of all these people to whom I would like to express my sincere gratitude.

The project laid in the guiding hands of Dr. Pascal Mailley as thesis director and of Dr. Maxime Gougis in the position of my direct supervisor. Dr. Mailley continuously shared his immense scientific passion and knowledge on electrochemistry throughout the project, resulting in numerous educational and clarifying discussions, which were always marked by his good humour. Dr. Gougis provided invaluable scientific advice, personal support, as well as experimental insight. His quick and critical way of thinking resulted in many inspiring questions and was of principal importance for proposing efficient solutions to given problems. I am deeply grateful for their both personal enthusiasm, for the corrections and could not have imagined having a pair of better and more kind mentors.

I would like to express my full gratitude towards professor Elisabeth Djurado, Dr. Sophie Tingry, Dr. Mathieu Etienne and professor Guy Denuault for having accepted the examination of this project. Their participation as jury members, together with Dr. Chantal Gondran, has been an honour and I would like to sincerely thank them for the time invested in reading and evaluating the work.

The financement of the project was granted by Dr. Séverine Vignoud in her function as head of the laboratory, for which I am earnestly thankful. In addition, the highly supportive and very positive research environment in her laboratory was of upmost importance during these years, as was the excellent conviviality which I will keep in good memory.

I would like to express my high appreciation to Dr. Guillaume Nonglaton and Caroline Fontelaye, who shared their expertise and troubleshooting skills in connection with the supercritical fluid equipment all throughout the project. Their help was essential for maintaining the tight schedule of sample preparation.
Dr. Florence Ricoul deserves a special mention of gratitude for having carried out the nitrogen adsorption experiments and in particular for her lasting personal involvement in resolving technical problems related to the realization of krypton adsorption experiments.
The contribution of Dr. Lukasz Borowik, who performed and evaluated the XPS measurements discussed in chapter IV, is highly acknowledged.
I would like to appreciate the personal motivation of Dr. Arnaud de Geyer for carrying out a set of of Small-Angle X-Ray Scattering experiments. Despite of their particular interest in the general context of the project, they are not included in the manuscript.
Further, I am very grateful for the participation of Dr. Willy Porcher and Dr. Chantal Gondran during the annual thesis follow-up meetings. Maintaining these regular external evaluations, their scientific insight and important general remarks helped shaping the project.

Being part of the electrochemistry team was an absolute pleasure and I immensely enjoyed learning from and discussing with Dr. Mélanie Alias, Dr. Ayman Chmayssem, Dr. Gareth Keeley, Dr. Karen Monsalve Grijalba, Frederic Revol-Cavalier, Dr. Charles Chatard and Dr. Yohann Thomas. I am particularly thankful for their invaluable combined set of expertise in electrochemistry, for offering help whenever needed and for their advice regarding the thesis and beyond.

I wish to further thank all lab-members, fellow PhD students, post-docs and interns for this enjoyable experience. The discussion of philosophical, political and other, more relaxed topics around lunch, coffee or tea, the climbing sessions and the gatherings after work were some of my personal highlights during these years. Out of the long list of memorable people, I would like to specifically thank Simon, Antoine, Bilal, Murielle, Thibaut, Juliette, Natalie, Marie, Maxime and Pierre for the shared moments.

This section would not be complete without expressing my heartfelt gratitude towards my family. Without their unconditional love, encouragement and support I would not have had the same opportunities in completing all these years of studies, pursuing my personal goals far from home. Thank you for always having been there when I needed you.

Finally, I would like to especially appreciate the privilege of having been able to share the everyday highs and lows of the thesis with Andrea. Her patient and supportive company, her ideas and trust were key elements during the completion of the manuscript. Without you, life would only be half as colourful.

# Contents

# List of Figures

# List of Tables

# Abstract

Electrochemical sensors are powerful and versatile analytical tools in different fields, for example in medical analysis and healthcare applications. Today's requirements on them correlate with the advances made in electrode design and performance: the demand of portable point-of-care devices, of implantable sensors for monitoring application, as well as the analysis of small sample volumes, requires the design of small-scale sensors or arrays and thus, the fabrication of miniaturized electrodes.

Electrode miniaturization, however, imposes a physical limitation linked to the reduction of the specific and of the electrochemically active electrode area. For amperometric sensors (e.g. biosensors), this implies a loss in faradaic current, resulting in a lower signal, a worse signal-to-noise ratio and potentially reduced detection limit and stability.
In literature, the impact of electrode structure has been profoundly studied and interesting structuration approaches have been published. However, the majority involves complex, multi-step processes of time-consuming nature, which appear unsuited for the production of sensors on a large scale. Printing techniques however, well-established in the industrial production of low-cost solid-state sensors, are not designed to generate structured electrochemical interfaces and porous networks.

In this work, commercial carbon ink was deposited on polymer substrates and subjected to a process-oriented supercritical $CO_2$-treatment. In one step, electrode structuration and solvent extraction were achieved to increase the specific and electrochemically active surface. The process parameters temperature, exposure time and ink dilution were studied upon their influence on the structural generation. Physical and electrochemical techniques comprised optical and digital microscopy, nitrogen adsorption studies, scanning electron microscopy, cyclic voltammetry, electrochemical impedance spectroscopy and chronoamperometry. The results confirmed the modulation of surface structure and bulk porosity of electrodes, resulting in an increased and characteristic electrochemical behaviour.

The practical utility of the technique was confirmed by preparing a variety of sensors for the purpose of hydrogen peroxide detection. The structuration protocol was transfered to commercial, mediated carbon inks which allowed to create porous electrodes, but suggested a partial loss of mediator. Alternatively, the deposition of the enzyme horseradish peroxidase on structured carbon electrodes lead to increased sensor sensitivity, highlighting the interest for further in-depth studies and the application of the structuration technique specifically for the preparation of enzymatic biosensors.

*Keywords: Nanostructuration of electrodes, biosensor, supercritical $CO_2$, one-step fabrication, electroactive surface*

# Résumé

Les capteurs électrochimiques sont des outils analytiques polyvalents utilisés dans différents domaines, comme dans le diagnostic médical ou les applications liées à la santé. Les dispositifs médicaux point-of-care, portables et implantables, ainsi que l'analyse d'échantillons de faible volume, nécessitent la conception de capteurs ou de réseaux de capteurs à petite échelle et, par conséquent, la fabrication d'électrodes miniaturisées.

La miniaturisation des électrodes impose cependant une limitation physique liée à la réduction de la surface spécifique et électroactive. Pour les capteurs ampérométriques (par exemple les biocapteurs), cela implique une perte de courant faradique, ce qui entraîne un signal plus faible, un rapport signal/bruit inférieur et potentiellement une limite de détection élevée ainsi qu'une stabilité réduite.
L'influence de la structure des électrodes a été étudiée en détail dans la littérature et des approches de structuration intéressantes ont été publiées. Cependant la majorité de ces méthodes sont basées sur des processus complexes multi-étapes et très chronophages. De ce fait, ceux-ci semblent inadaptés à la production de capteurs à grande échelle. D'autre part, les techniques d'impression ou de sérigraphie sont très utilisées dans la production industrielle de capteurs à faible coût mais ne sont pas conçues pour générer des interfaces électrochimiques structurées et des réseaux poreux.

Dans ce travail, une encre carbone commerciale a été déposée sur des substrats polymères et soumise à un traitement industrialisable utilisant le $CO_2$ supercritique. En une seule étape, la structuration des électrodes et l'extraction de solvants ont été réalisées afin d'augmenter la surface spécifique et ainsi la surface électroactive. L'influence des paramètres, température, temps d'exposition et dilution d'encre, sur la structuration de la surface à été étudiée. Des techniques de caractérisation physiques et électrochimiques comprenant la microscopie optique, les études d'adsorption d'azote, la microscopie électronique à balayage, la voltampérométrie cyclique, la spectroscopie d'impédance électrochimique et la chronoampérométrie ont été mises en oeuvre. Les résultats ont confirmé que la structure de surface et la porosité apparente des électrodes peuvent être modifiées et optimisées, ce qui a entraîné une nette amélioration des performances électrochimiques.

Afin de confirmer l'influence de la structuration des électrodes sur les performances électrochimiques, différents capteurs ont été préparés dans le but de détecter le peroxyde d'hydrogène. Dans un premier temps, le protocole de structuration a été étendu à des encres carbone commerciales intégrant des médiateurs rédox. Les résultats obtenus confirment la création de porosité, mais suggèrent une perte partielle de médiateur pendant la structuration. L'adsorption d'enzyme peroxydase de raifort a entraînée une augmentation de la sensibilité pour les électrodes de carbone structurées. Ceci met en évidence l'intérêt de la méthode de structuration par $CO_2$ supercritique notamment pour la fabrication de biocapteurs enzymatiques.

*Mots clés: Nanostructuration d'électrodes, biocapteur, $CO_2$ supercritique, procédé de structuration en une étape, surface électroactive*

# Glossary

**BET theory**: The Brunauer-Emmett-Teller (BET) theory illustrates the multilayer adsorption of gas molecules on a surface, which is useful for measurements to determine the specific surface area of materials. Despite its intended use for non-porous surfaces, it is commonly applied on porous materials.

**BJH theory**: The Barrett-Joyner-Halenda (BJH) theory makes use of the Kelvin equation to estimate the distribution of pore size of a mesoporous solid.

**CA**: Chronoamperometry (CA) is a technique in electrochemistry, that relies on changing the potential applied on the working electrode step-wise. The current response is recorded over time.

**CE**: In a three-electrode electrochemical cell, the counter electrode (CE) closes the circuit and allows current flow, balancing the redox reaction occurring at the working electrode.

**CED**: Cohesive energy density (CED) is a measure of the increase in internal energy, required to break all intermolecular forces of one mole of a substance.

**CV**: In electrochemistry, cyclic voltammetry (CV) is a dynamic measurement, which relies on measuring the current as a function of the potential. The latter is varied linearly within a fixed potential window, with alternating direction.

**EIS**: Electrochemical impedance spectroscopy (EIS) allows studying the time response of charge displacements and charge transfer occurring in a system when applying an alternating current of low amplitude over an adjustable range of frequencies.

**H**: The thermodynamic variable and state function enthalpy (H) describes the energetic configuration or energetic capacity of a given system. It can be calculated by adding the internal energy, required to create the system, and the product of its volume with the pressure acting on it.

**HSP**: The Hansen solubility parameters (HSP) describe the separation of the cohesive energy of a substance in contributions arising from dispersion forces (van der Waals), polar forces (dipole moments) and hydrogen bonding.

**G**: The thermodynamic quantity and state function of Gibbs free energy (G) describes the capacity of a system to perform work, while temperature and pressure of remain constant. It is thus a measure of describing, whether a process can spontaneously take place.

**OCP**: The measurement of open circuit potential (OCP) of an electrochemical cell refers to the potential difference between two electrodes, e.g. working electrode and reference

electrode in a two-electrode-cell, when no external load is applied.

**RE**: A reference electrode (RE) is used in electrochemical measurements due to its well-defined half-cell potential, allowing to measure or impose a potential difference relative to a second electrode. The RE is chosen in such way, that it is as insensitive as possible to changes in the surrounding electrolyte, thereby guaranteeing relative measurement stability.

**S**: In thermodynamics, the state function or variable of entropy (S) contributes to the internal energy of a system and is associated with the degree of the system's disorder. It is commonly assumed, the smaller the entropy, the higher the degree of order in the system and the larger its internal energy.

**SEM**: A scanning electron microscope (SEM) produces high-resolution images of the surface of a sample by means of a focused, high-energy electron beam, that is directed in lines over the sample surface. Due to the interaction of the beam electrons with near-surface electrons of the sample, different types of electrons are emitted and can be collected. The information transported by secondary electrons is commonly used for the reconstruction of the sample's surface.

**SSA**: The specific surface area (SSA) of a material intends to give an information on its total surface area per unit of mass. It is of special interest, when a sample presents a microscopically structured or porous surface, implying a difference to the macroscopic, apparent geometric surface.

**$T_g$**: The glass transition temperature ($T_g$) defines, for amorphous and semi-crystalline polymers, the temperature at which the amorphous parts of the material turn from a rigid, rather brittle state to a viscous, rubbery state.

**WE**: In an electrochemical cell, the working electrode (WE) represents the electrode under study. The transfer of charges, involved in the reduction and oxidation reactions of interest, takes place at the interface between WE and electrolyte.

**XPS**: X-Ray photoelectron spectroscopy (XPS) is a surface-characterization technique, relying on the interaction of a primary X-ray photon beam with electrons in near-surface regions of a sample. The emission of photoelectrons and Auger-electrons of characteristic binding energies or energy ranges, allows e.g. deducing the elemental composition of the sample and to further specify the chemical state of said elements.

# General Introduction

In current electrode research, "nano" is a term upon which one can frequently stumble, mainly in the context of nanomaterials or nanostructure. The definitions of these terminologies are rather clear; nanomaterials referring to objects, nanostructures referring to agglomerations of molecules or atoms measuring between 1 and 100 nm in at least one dimension [21]. Nanostructuration can therefore be understood as the process of creating a surface comprising features with dimensions at said scale. The incorporation or deposition of actual nanomaterials on a surface is one way to achieve this goal, but not strictly required, as a large variety of materials can be synthesized and tailored to meet the desired specifications.

It is widely acknowledged that nanomaterials present interesting intrinsic properties which often significantly differ from the bulk materials' characteristics. One example is their generally large specific surface area or large surface to volume ratio, respectively. This aspect is of particular interest in an electrochemical context, when focusing on the surface area of a material or an electrode involved in a reaction. As its interface with the surrounding electrolyte represents the center of charge transfer, the available and electrochemically active surface area of the electrode become essential parameters for evaluating its electrochemical performance.
In electrochemical sensing, performance translates to the parameters stability, sensitivity, signal-to-noise ratio and the limit of detection. By nanostructuration of the electrode, higher currents and greater charges can be exchanged, resulting in an increase in electrochemical performance. Numerous works have confirmed the interest of applying nanostructured electrodes in e.g. analytical chemistry for medical, environmental and industrial use, or in energy storage applications. Figure 1 emphasizes recent scientific interest by plotting the number of studies linked to keywords in the context of nanostructured electrodes per year.

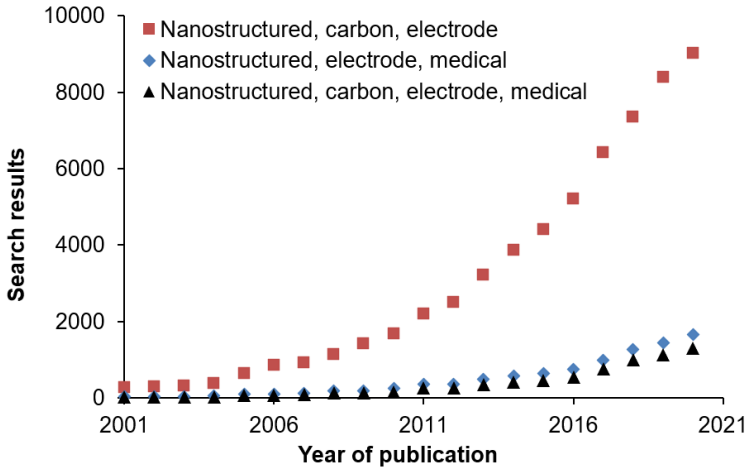


Figure 1: Number of results on the website ScienceDirect for selected key words.

One controversial aspect of the approaches commonly used for electrode structuration is their complexity. While many research groups report having obtained electrodes with highly interesting properties, the preparation itself often appears rather elaborate. Besides the elevated number of process steps, implying a time-consuming protocols, the choice of exotic, i.e. difficult to produce or expensive materials, is frequently specified. In consequence, the main question and objective of this thesis project was to identify an alternative nanostructuration method of relatively low cost, low complexity of fabrication and of short production time in comparison to the reported approaches. By fulfilling these criteria, the approach would then be of potential interest for an integration into industrial-scale fabrication.

Focusing on established technologies for electrode preparation, e.g. the deposition of conductive inks, a supercritical $CO_2$-based method was identified, which is considered compatible with an additive production process. Based on the well-studied mechanisms of phase separation of multi-component systems and polymer foaming assisted by supercritical fluids, a combined treatment was applied to structure conductive inks. The treatment was optimized by separately studying the influence of different structuration parameters. In a further step, the practical application of obtained electrodes was studied with the intention of a potential application in the medical field.
The outline of the manuscript is visualized in the scheme below (Figure 2).

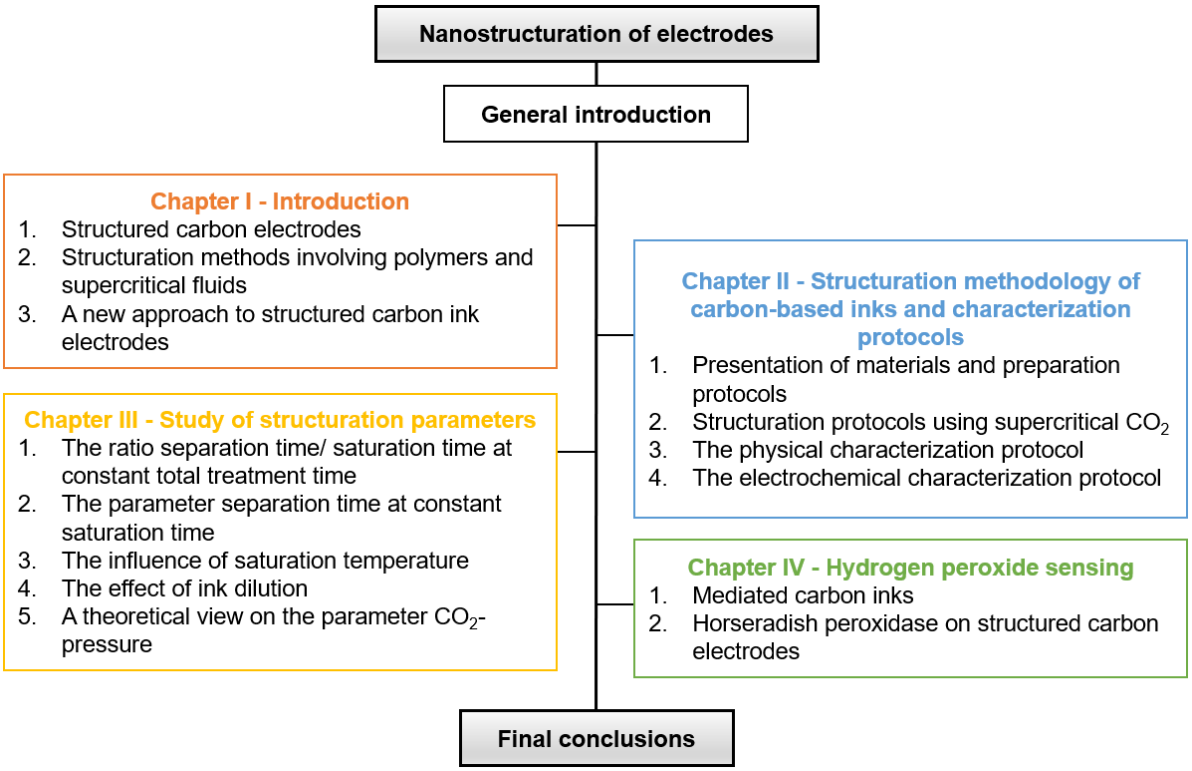


Figure 2: The thematic outline of the thesis work.

**Chapter I** serves as theoretical chapter and additionally provides a literature review on structured carbon-based electrodes in analytical chemistry and in particular for the application in the field of medical sensing and clinical analysis, where current trends involve sensor miniaturizing and monitoring. The motivation for continuous research on an alternative structure-generating technique is specified.
Subsequently, structuration mechanisms involving polymers, polymeric solutions and supercritical fluids will be presented. In particular, the phase separation of multi-component systems and polymer foaming are explained in detail, forming the theoretical base for the structuration.

The following **chapter II** focuses on materials and equipments used in the context of ink structuration, on the experimental approaches, as well as the physical and electrochemical characterization protocols. The chapter is to be understood as presentation of experimental methods with a special focus on the difficulties encountered in the context of structuration, characterization and data evaluation.

In **chapter III**, the results of studying several structuration-related parameters are presented and discussed. Based on the forementioned general characterization protocol, the effect of process parameters on the structural generation is interpreted and compared, in order to determine an optimal structuration protocol.

An application of the optimized supercritical $CO_2$-based structuration method is presented in **chapter IV** on the example of hydrogen peroxide sensors. Different approaches were explored, starting with the structuration of commercial mediated carbon ink and the functionalization of structured carbon electrodes via enzyme adsorption. The determined sensor characteristics are compared with literature in the field.

The results of the thesis are summarized and put into context in a **final conclusion**. Based on the initial scope, the major advances are evaluated, allowing to estimate the utility of a potential future application of the technique and the perspectives of this work.

# Chapter I

# Introduction to structured electrodes

Chapter I gives an introduction to the topic of structured solid-state carbon electrodes and their use in electrochemical sensing application, thus presenting a synthesis of theoretical concepts and a state-of-the-art.

Section one provides a review on the techniques commonly employed for the structuration of carbon electrodes. The electrochemical behaviour of structured surfaces or interfaces, respectively is illuminated before covering a range of structuration approaches found in literature, each with their own summary of important works in the field.
The structuration of carbon-based electrodes using sacrificial scaffolds is presented, followed by scaffoldless structuration approaches. These include in particular the subgroups of ex-situ and in-situ pore generation, i.e. pore generation before or during the electrode preparation step, which will be visualized on examples.
Based on the presented works and their compatibility with ink deposition, a traditional technique in electrode preparation is evaluated, explaining the motivation as to why an alternative structuration method is required.

Section two directs the view on the theoretical concepts behind the structure-generating processes phase separation and polymer foaming, which are classically carried out by using organic solvents and non-solvents. In this case, the interest of using supercritical carbon dioxide, a non-toxic and cheap reagent, is pointed out.
It its commonly employed in the extraction of primary solvents from prestructured samples, e.g. in critical point drying for the fabrication of aerogels. It has equally been successfully used to replace traditional non-solvents in the phase separation mechanism for the preparation of porous polymer membranes. Further, it is a common porogeneous agent in the preparation of polymer foams.
Despite the clear potential interest of unifying phase separation and polymer foaming, using supercritical carbon dioxide in both cases, it is mentioned in few reports only. More importantly, to the author's knowledge, no research group has described the exposure of conductive inks to a unified protocol consisting of phase separation, polymer foaming and critical point drying in order to structure electrodes.

Section three, in consequence, introduces an alternative structure-generating method for conductive inks, based on the mechanisms presented before. The general process schematics are laid out, allowing to determine the principal process parameters and forming the base for the experiments carried out in the experimental chapter III.

Chapter I ends with a small conclusion to summarize the key information. The outline is as presented in Figure I.1.

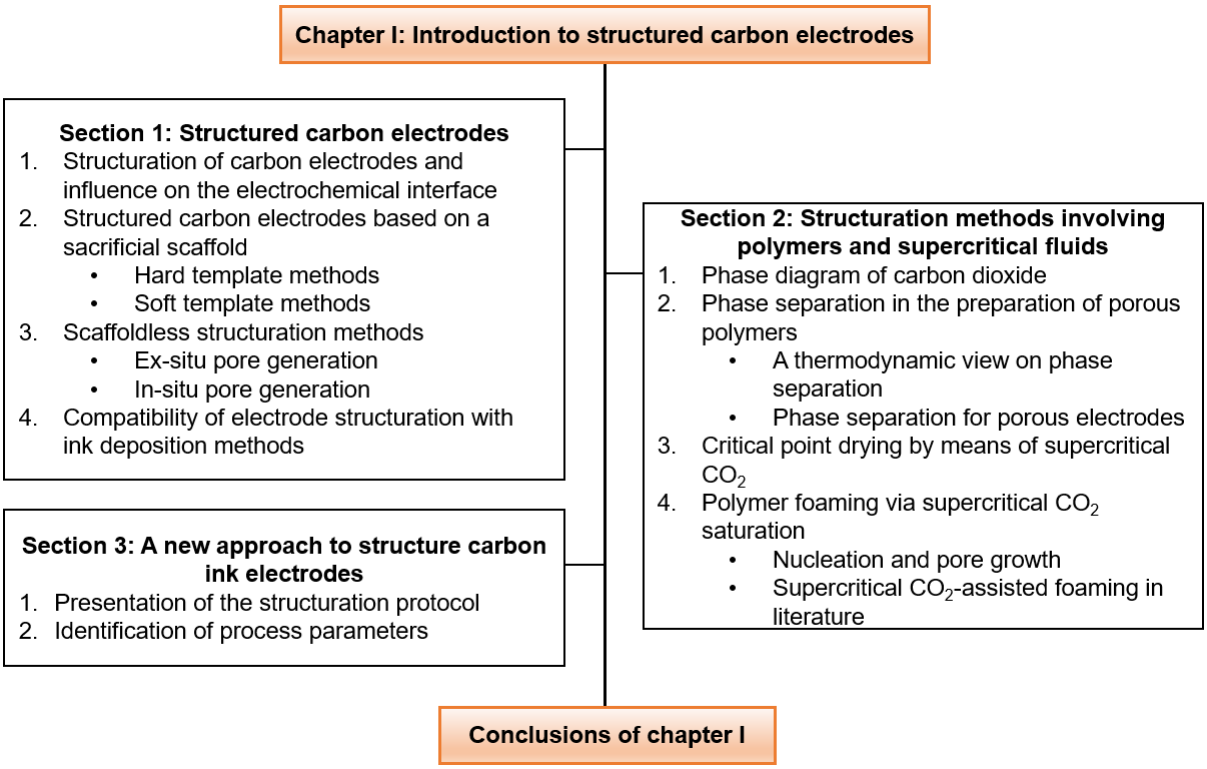


Figure I.1: The schematic structure of chapter I.

## 1.1 Structured carbon electrodes

Carbon presents itself in form of different allotropes, i.e. structural variations, comprising diamond, graphite, glassy carbon and nanocarbons to name a few. Of the conductive allotropes, some can be naturally found and represent traditional, low cost electrode materials in electrochemical application. Graphite anodes, for example, have for longtime been used in electrical arc furnaces to melt metals [22]. Glassy-carbon, a non-graphitizing allotrope of carbon, has been serving as substrate material for many decades in electrochemical analysis. Other allotropes, amongst which are graphene or carbon nanotubes, have been introduced to the domain of electrochemical research only in recent decades as tailored, chemically stable and highly functional materials, but have since then attracted the interest of many scientists in various subdomains.

All allotropes differentiate themselves by their physical properties, which arise from the characteristic structure on the atomic level and the hybridization of electron orbitals.
Graphite is a crystalline form of carbon in which layers of hexagonally arranged atoms, graphene sheets, are stacked on top of each other and held together by Van der Waals forces, as demonstrated in Figure I.2 a). As a result of the atomic structure within the layers, with each carbon atom having three direct neighbours and the electron orbitals being $sp^2$-hybridized, one valence electron remains free and is delocalized in the formed Π-orbital. In consequence, excellent electrical conductivity within the so-called basal planes is observed, whereas the electron orbitals of atoms in the edge-planes are $sp^3$-hybridized and promote the formation of covalent bonds with functional groups. Yuan et al. studied the electrochemical properties of graphene and observed faster electron transfer rates and higher electrocatalytic activity on edge-planes than the basal planes [23].
These interaction capabilities are generally adaptable to structurally similar carbon allotropes , e.g. graphite and carbon nanotubes [24] and can equally apply to subforms of the respective allotropes, such as small carbon particles of graphitic nature.
It further suggests, on the small scale and in simplified manner, that different arrangements and orientations of the conductive particles in a pratical application influence the electrochemical characteristics.

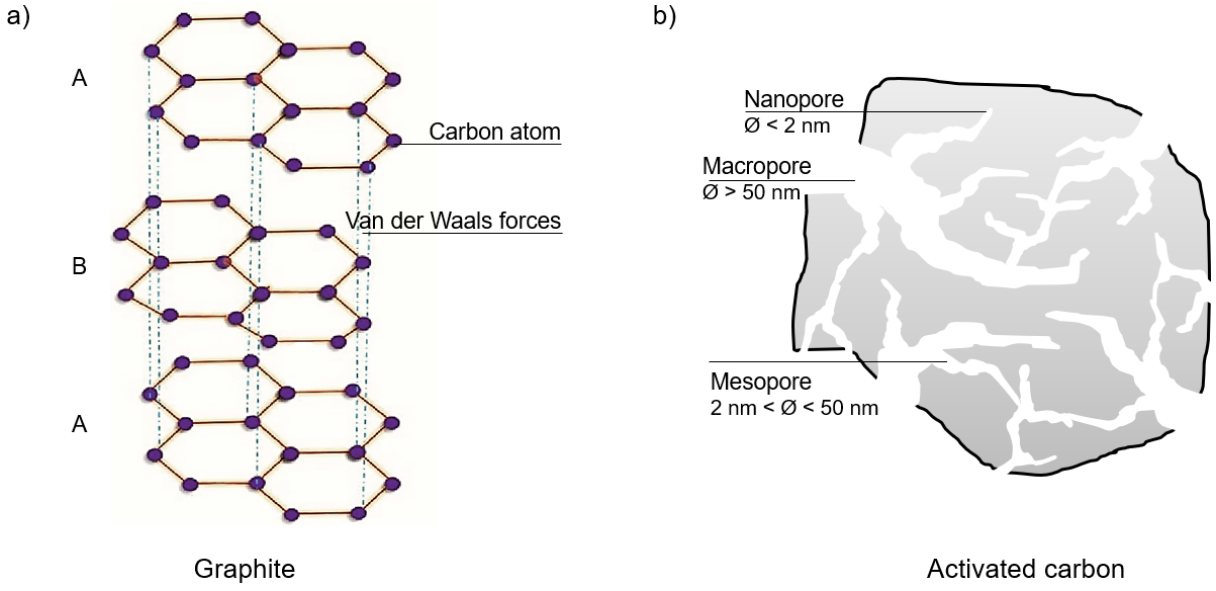


Figure I.2: The schematic atomic structure of a) AB-stacked graphite [1] and b) activated carbon in a common representation with hierarchical porosity.

An important additional aspect associated with the structural difference of the carbon allotropes is their specific surface area (SSA), which generelly varies over several orders. By means of nitrogen adsorption-desorption experiments, Shornikova et al. estimated 0.6 $m^2/g$ for natural graphite, considered nonporous [25]. Carbon blacks, equally regarded as non-porous, range between 10-60 $m^2/g$ (nitrogen adsorption-desorption isotherms) [26]. For porous, activated carbons on the other hand, up to 3164 $m^2/g$ have been measured via nitrogen adsorption-desorption isotherms [1] [28]. The schematic representation of an activated carbon particle is depicted in Figure I.2 b), suggesting the contribution of the hierarchical porosity to the large SSA.

### 1.1.1 Structuration of electrodes and electrochemical interface

The discussion of SSA is considered of high interest, as the charge transfers studied in electrochemical measurements depend fundamentally on the electrode/electrolyte interface. In particular, the expression of capacitive behaviour, i.e. the charge storage by means of reversible adsorption of ions on the electrode surface, is described by the double-layer capacitance ($C_{dl}$). As indicated by equation I.1, it is linked to the developped SSA (here only named $A$), the electrolyte's dielectric constant $\varepsilon$ and the distance $d$ between the electrode and the ion's center. It is a major element of study in electrochemical double layer capacitors.

$$C_{dl} = \varepsilon A/d \tag{I.1}$$

Faradaic charge transfer, describing the exchange of electrons between electrode and electrolyte, depends on the electrochemically active surface area, which is commonly smaller than the electrode's SSA. Still, in a simplified view, it can be assumed that an electrode of large SSA potentially features more electroactive sites, than an electrode of smaller SSA. Equally, an overall reduction of the electrode/electrolyte interface reduces the total double layer capacitance, as well as the electroactive surface.

In the context of the current trend of miniaturizing electrochemical sensors in e.g. medical analysis and healthcare, the reduction of electrodes' size leads to a smaller electrode/electrolyte interface. In turn, losses in signal stability and Faradaic current are expected for amperometric sensors, e.g. enzymatic biosensors, while the charge storage capacity is thought to decrease in cases of potentiometric sensors. In both cases, lower signal output and a potentially worse signal-to-noise ratio are expected, which translates to a less performant sensor. The structuration of electrodes, therefore, is a means to increase both SSA and electroactive surface and can be realized by increasing surface roughness. Alternatively, the entire electrode bulk material can be structured to generate a porous, three-dimensional structure.

In addition to their large SSA, carbon-based porous materials exhibit good chemical stability and electrical conductivity at relatively low production cost [29]. Their use ranges from electrode and catalyst materials [30] for sensing and energy storage to the application in electromagnetic shielding [31], thermal insulation [32] and separation material [33].
In the following, a selection of electrode structuration methods are presented which are considered promising for the preparation of porous carbon materials.

[1] Despite the result obtained by means of physical characterzation, it is pointed out by Simon et al. that the electrochemically accessible SSA of carbon materials appears to be limited to only 1000-2000 $m^2/g$ as a function of the solvated or de-solvated ion size [27].

## 1.1.2 Structured carbon electrodes based on a sacrificial scaffold

### 1.1.2.1 Hard-template methods

The fabrication of electrodes based on rigid, sacrificial templates which are generally composed of inorganic materials (silica, metal organic frameworks (MOFs) and colloidal particles), is a concept refered to as hard-template [34] [35]. The scaffold is generally intended to form a negative of the final electrode and therefore located where the porous fraction is supposed to be created. The negative is then filled with electrode material and ultimately removed by means of thermal or chemical decomposition, as depicted in Figure I.3.

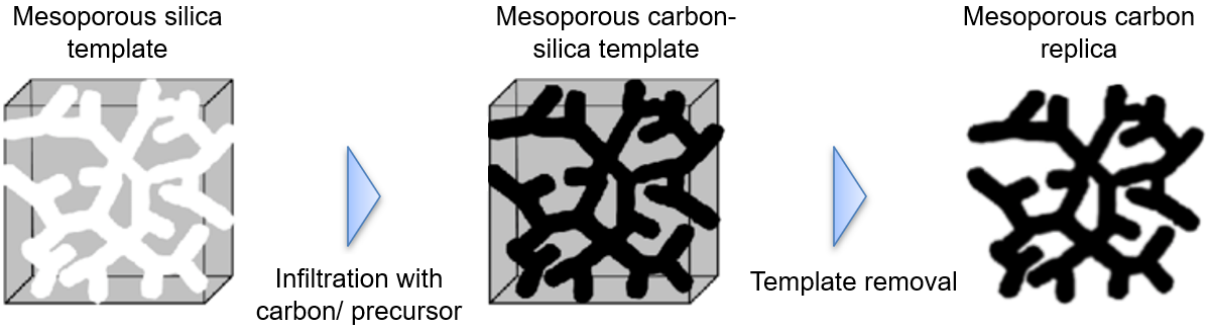


Figure I.3: A graphical representation of the hard template method, adapted from [2].

An example is the work of Lee et al., who presented an approach to fabricate hierarchical porous carbon fibers, based on a multi-step process involving a sacrificial template [36]. $SiO_2$ nanoparticles were dispersed in a polymeric solution and electrospun to obtain a primary scaffold. After a carbonization step, the $SiO_2$ particles were dissolved in hydrofluoric acid and a final activation in potassium hydroxide carried out.
The carbon fibers disposed a hierarchical structure with micro-, mesopores and larger pore diameters up to 1 µm. As a result, the specific surface area attained high values of 1796 $m^2/g$ and by using the carbon fibers as electric double-layer capacitors, a specific capacitance up to 197 F/g (5 mV/s, 1 M $H_2SO_4$) was measured.

Recently, Zheng et al. presented a hard template synthesis of porous carbon electrodes for hydroquinone and catechol detection [37], two widely encountered toxic substances. Zinc-based MOFs were prepared and subjected to pyrolysis in a nitrogen-atmosphere to achieve doping of the structure in parallel to activation. The obtained materials were characterized as prepared and attained SSA up to 1242 $m^2/g$ with a bimodal pore size of mainly mesopores and some low degree of microporosity. The sensing performance was estimated highly satisfying regarding stability, reproducibility and sensitivity to electrochemical interferents.
In the publication, the material preparation is relatively fast in comparison, but still comprises several separate synthesis steps and requires high temperatures (950 °C) until all organic electrode material has been converted to activated carbon.
The work demonstrates well, that on one hand, hard-templating methods can precisely generate micro- and nanostructured materials due to the high degree of control during the template creation. On the other hand, sample preparation is complex, time-consuming and energy demanding. Furthermore, the difficulties linked to dissolving the scaffolds with aggressive chemicals are highlighted, representing a safety hazard during and after the sample preparation upon recovery and recycling of the chemicals. The latter step usually adds another substantial expense to the overall production cost.

While not discussing the synthesis of a carbon-structure, a recent interesting study by Wang et al. has explored the fabrication of a derivate of the MOF Prussian blue via a hard-templating approach [38]. The work investigated the optical properties of the obtained mesoporous material. However, Prussian blue is well-known in electrochemistry as a mediator in the electrocatalytic reduction of $H_2O_2$. The team suggested the potential for using the hard-templating technique for creating porous, sponge-like materials and there is a potential interest, to use a likewise electrode material for sensing application. However, the process is equally time-consuming, complicated and involves handling aggressive chemicals. In conclusion, the introduction of an alternative structuration approach again appears necessary.

#### 1.1.2.2 Soft-template methods

Soft-template techniques for the preparation of porous networks are based on the inter- and intramolecular interaction of constituents in a given system. The terminology "soft" refers to the principally non-rigid nature of the template. Figure I.4 depicts one possible soft-template approach which is based on the assembly of micelles via electrostatic forces, chemical bonds, Van der Waals forces or hydrogen bonds. Carbon or precursors are introduced to the system, respectively deposited around the template. In the demonstrated case, they are polymerized before undergoing activation. The template can usually be removed under rather mild conditions and in some cases requires no special protocol at all, e.g. in case of thermally instable materials [3], which is advantageous.
A second soft-template method relies on the introduction of surfactants to a liquid solution containing a carbon precursor. Due to the aggregation of surfactants around the precursors, phase separation is initiated and after suited chemical or physical stabilization steps, e.g. polymerization, the system is comparable to the second step in Figure I.4 [35].

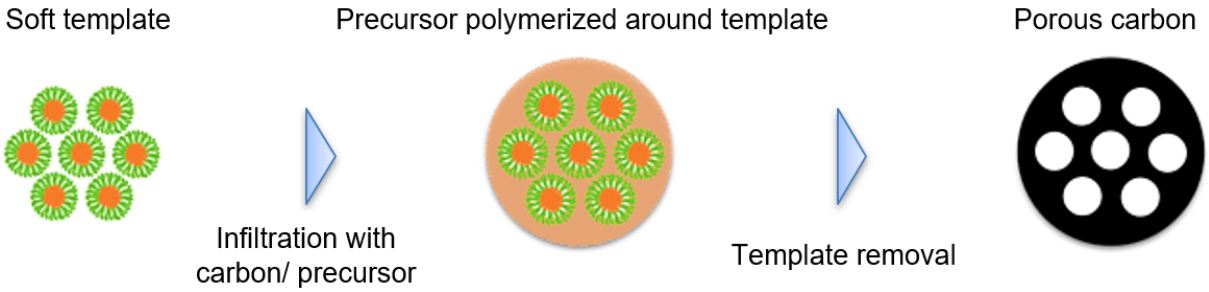


Figure I.4: A graphical representation of an exemplary form of soft template methods, adapted from [3].

The preparation of a mesoporous carbon material, obtained via a soft-template-approach, was published by Hu et al. for the potential use as supercapacitor electrode [39]. The precursors fructose and dicyanamide were mixed with the triblock copolymer Pluronic® F127. Subsequently, the soft template was generated by autoclaving, inducing self-assembly of the copolymer, followed by washing, drying and template removal. The obtained powders were found to have a developed SSA up to 730 $m^2/g$, coinciding with a specific capacitance of 212 F/g (1 mV/s).
The self-assembly of complementary sections in copolymers is a very controllable method for creating nanostructures. However, a significant drawback lies in the required time. In this particular case, the precursor solution was autoclaved during three days at 130 ℃, which is of rather low practical interest.

Lu et al. published a study on porous carbon electrodes for the reduction of $H_2O_2$. [40], in which a precursor solution was prepared and sonicated to achieve a homogeneous solution. After drying and grinding the obtained powder, a two-step pyrolisis aimed for the removal of the porogeneous agent melamine and an activation of the carbon material. The resulting nanosheets had a SSA of 431 $m^2/g$ (measured via nitrogen adsorption-desorption isotherms), containing a mix of micropores and mesopores. According to the group, good sensor characteristics were achieved with a wide linear range (0.5 µM-14 mM) and a low detection limit (0.18 µM, S/N=3). While the material's preparation is considered fast in comparison with the previous study, the total synthesis time is still estimated to exceed 10 h.

### 1.1.3 Scaffoldless structuration methods in electrode preparation

In the search for a potentially less hazardous, more sustainable and cheaper process, the generation of structured electrodes has equally been achieved by means of templateless methods. These allow to circumvent using a negative representation of the volume, which later corresponds to the pore fraction. The preparation can include the use of structured precursors, however this is not to be confounded with a the hard-template method detailed earlier on. Generally one can divide into two subcategories, which may overlap depending on the process details:

- Ex-situ pore generation: Prestructured particles, e.g. biomass-derived materials, can be added to the mix of precursors, followed by processing steps. A final pyrolysis and possibly an activation step are required to graphitize the organic fraction of the matrix.
- In-situ pore generation: The pore volume is created during fabrication, such as in sol-gel reactions which allow to retrieve a hydrogel. The extraction of the liquid phase turns the hydrogel into a generally self-supporting aerogel/xerogel, which can bepyrolized. Further, freeze-drying of aqueous solutions is reported to create porous structures. Another in-situ method are phase separation processes, e.g. thermally induced phase separation (TIPS). In addition, the introduction of porogeneous agents to the mix of precursors or during the process can lead to an in-situ pore-generation, achievable via e.g. thermal decomposition of the agent.

#### 1.1.3.1 Ex-situ pore generation

Numerous works in the preparation of electrodes for energy storage, e.g. batteries and supercapacitors, have focused on using biomass-derived carbon-based precursors for the preparation of activated carbon materials. An advantage of the organic precursors is their natural texture or structure, which can considerably contribute to the material's achievable final porosity. Activated carbons can be synthesized from organic matter such as charcoal, wood, or biomass-waste such as coconut shell [41], grape seeds [42] and tamarind fruit shell [43].
Typically, the two-step process starts with a carbonization step during which the precursors are pyrolyzed in a reducing atmosphere, followed by an activation step which aims to oxidize the surface, e.g. in an atmosphere rich in oxygen or carbon dioxide, or upon exposure to steam at high temperature [44].

Su et al. presented a process to create a hollow, activated carbon mesh [45], consisting in the calcination of biowaste at high temperature, followed by an activation step in the presence of potassium hydroxide. After a treatment with hydrochloric acid (HCl) and a washing step, a final activation step in nitrogen atmosphere at high temperature was

carried out. The SSA was determined to 1893 $m^2/g$ ($N_2$ adsorption-desorption) with an average pore size in the small mesopore range (4-5 nm). Based on the specific capacitance of 314.6 F/g, the group proposed to use the material for supercapacitor electrodes. The total preparation time, however is estimated to 7 h, in addition to the high energy demand.

#### 1.1.3.2 In-situ pore generation

Baumann et al. synthesized a monolithic carbon aerogel prepared via sol-gel polymerization of the precursors, followed by curing, washing and drying using supercritical $CO_2$ [4]. After undergoing a thermal activation at 950 ℃ in $CO_2$ atmosphere, the carbonized monoliths attained a SSA exceeding 3000 $m^2/g$ ($N_2$ adsorption-desorption). The isotherms' shapes suggest a mixed presence of mesopores and micropores. Scanning electron microscopy (SEM) images indicated a secondary pore population in the sub-µm-range. The material was proposed suitable as catalyst support and electrode material, in particular for capacitive charge storage. Figure I.5 displays SEM images of the surface of carbon aerogels before a) and after b) activation. For a later discussion in chapter II, $N_2$ adsorption-desorption isotherms are depicted in c), with the focus on the general shapes of the curves and the development of the hysteresis loop.
Despite the interesting results, the overall process is considered rather complex and includes long time-spans for curing (72 h), carbonization (3 h) and activation (2-6 h).

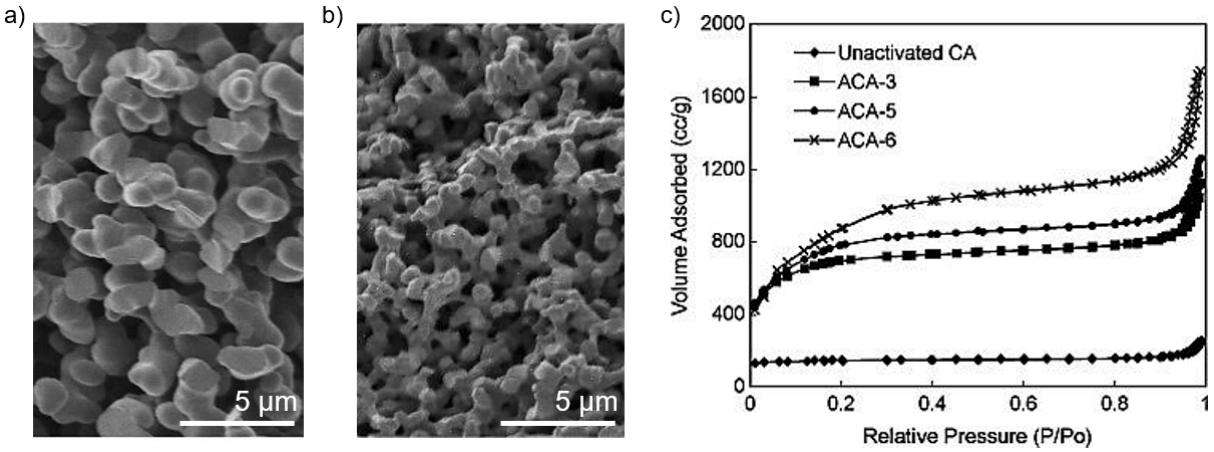


Figure I.5: SEM images of carbon aerogel a) before and b) after activation. $N_2$ adsorption-desorption isotherms in c) for different, activated carbon aerogels (ACA). Adapted from [4].

A sol-gel-based approach was presented for the formation of mesoporous $NiCo_2O_4$-MWCNT (multiwall carbon nanotubes) composite aerogels and N-doped carbon aerogels by Jayaseelan et al. [46]. After preparation of the wet gels, a supercritical $CO_2$-drying process (14 ℃, 6.89 MPa, 8 h) was employed to recover aerogels, which disposed of high aereal capacitance (471.8 $mF/cm^2$) or specific capacitance (1010 F/g), respectively. In consequence, the use as supercapacitor electrode material was proposed. While SEM images suggest the generation of a nanostructure, the overall process is rather complex and requires a total preparation time in the range of 9-10 h.

An interconnected, macroporous carbon material for supercapacitor electrodes was prepared by Li et al [47]. A precursor solution of sodium alginate was mixed with calcium chloride to collect water-saturated, linked beads which were leached and washed. Freeze-drying (24 h, -196 ℃) generated a structure governed by the formation of ice crystals

and was preserved by carbonization of the beads (1 h, 600 °C). A chemical activation with KOH followed. An exceptionally large SSA exceeding 3000 $m^2/g$ was determined ($N_2$ adsorption-desorption) with a dominating pore diameter below 5 nm. The specific capacitance reached 270 F/g.

Wu et al. published results on the preparation of a macroporous carbon monolith using thermally induced phase separation (TIPS) [48]. The schematic process is depicted in Figure I.6. Polymer solutions (polyacrylonitrile in dimethyl sulfone) were subjected to a rapid reduction of the process temperature from 160 to 30 °C to initiate the phase separation, prior to a multi-step solvent exchange and drying step. The obtained porous material was then carbonized. The SSA was estimated to around 0.26 $m^2/g$ ($N_2$ adsorption-desorption), presenting pores with a diameter between 5 and 66 µm depending on the polymer concentration in the initial solution. The material was considered suitable for various application including a use in form of electrodes in sensing, as catalyst support and for filtration. While the technique itself appears interesting, the extraction of residual solvents is considered rather time-consuming.

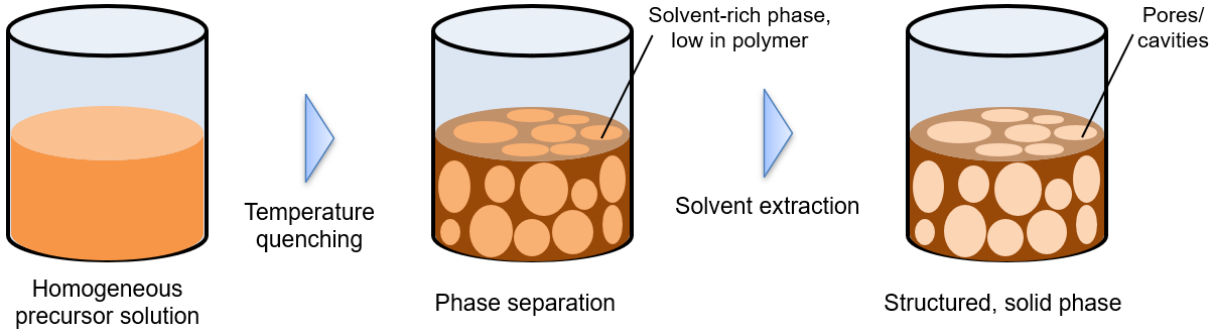


Figure I.6: Simplified scheme of thermally induced phase separation (TIPS), during which a homogeneous polymeric solution separates into a fraction rich in polymer but low in solvent (darker colour) and a fraction rich in solvent but low in polymer (light color).

A simplified approach, suppressing the need for any pyrolization, was presented by Vipin et al. to structure a polymer-solvent precursor solution (CNT in polyacrylonitrile) via TIPS [49]. The recovered porous composite networks were more conductive (2.7 S/cm) than the pure polymer, but values are low in comparison with approaches relying on carbonization of the polymer matrix [50]. Pore sizes between 0.6 and 1 µm were observed in SEM images, while a pore diameter of 5-6 nm was estimated from $N_2$ adsorption-desorption, together with a SSA of 210 $m^2/g$.

Using a different approach, Gong et al. [34] presented the carbonization of a porous polymer monolith generated via supercritical $CO_2$-foaming, a method described earlier by Wang et al. [51]. A homogeneous polyacrylonitrile solution was prepared, cast and dried (12 h, 60 °C). This first polymeric material was cut into small pieces and hot pressed in a casting mold (160 °C, 10 MPa). Cylindrical samples were punched out and saturated with supercritical $CO_2$ (100-150 °C, 10.3-31.1 MPa, 1.5 h), allowing to introduce a secondary degree of porosity via polymer foaming upon rapid depressurization. In a final multi-stage heating process, the samples were pre-oxidized (280 °C, 5 h) and carbonized (800 °C, 2 h). Electrodes were found to exhibit a closed porosity with cells smaller than 15 µm in diameter. A high electrical conductivity of 92-132 S/m was measured (12 S/m for commercial, activated carbon [52]). While a potential use as electrode material was mentioned, the overall process time, which exceeded 20 h, is considered unfavourable.

### 1.1.4 Compatibility of structuration methods with ink deposition techniques

The deposition of conductive carbon pastes or inks, respectively, represents a classical method for the large-scale preparation of electrodes in battery/capacitor fabrication, where the carbon-based electrode material is commonly screen-printed (e.g. on a metallic foil, serving as collector) and the solvent extracted in a heating step. In sensing application, a large range of printed electrodes and sensors is commercially available (e.g. from Metrohm, PalmSens, Nanoshel). These include basic carbon electrodes for direct use or as support for a modification/functionalization, as well as ready-to-use sensors for the detection of hydrogen peroxide ($H_2O_2$), heavy metals, and the electrocatalytic oxidation of small organic molecules, to name a few. Ink deposition generally yields electrodes with an apparent surface, that is relatively flat and non-porous. However, the simplicity of the roll to roll fabrication, as well as the short production times allow a relatively cheap prince which has since defined the industrial interest.
In the following, the previously mentioned structuration mechanisms are evaluated regarding their potential compatibility with the traditional process of ink deposition. In particularly, the composition of conductive inks is complex, including not only the polymeric binder and its solvent, but also conductive particles and eventual additives. Therefore, the previously presented structuration mechanisms may apply to a higher or lesser degree and may even evoke undesirable interactions[2].

- Hard-template techniques can be considered partially compatible. As the approach is of subtractive nature, any mold in which the ink is cast/filled and any template particle incorporated in the ink requires removal during later stages of the process. Low temperatures and non-agressive chemicals are considered essential in oder to preserve the physical and chemical state of the structured ink.
  Xu et al. mixed calcium carbonate microspheres into a carbon paste consisting of graphite powder and pyrrole to prepare electrodes for the detection of tannic acid [53]. After filling the paste into cavities and polymerizing the pyrrole monomers, the microspheres were washed out in 0.1 M HCl. The thus generated pores were in the range of 2-5 µm and the material was estimated to present a SSA of 59.3 $m^2/g$ ($N_2$ adsorption-desorption). Depending on the ratio of dispersed microspheres, the pores resembled either closed cells or connected networks.
  Other template particles in the preparation of carbon paste electrodes have comprised titanium dioxide hollow spheres [54]. The pore size is potentially adjustable by varying the size of template particles, which is beneficial. Drawbacks include, besides complexity, the risk of residues after washing depending on the complexity of the porous structure.
- Freeze-drying is considered an interesting method of structure generation and is potentially compatible with an additive ink deposition. However, it is limited to aqueous precursor solutions or inks, which deviates from traditional ink formulations which rely on organic solvents. Some of the carbon powders are intrinsically hydrophobic (e.g. CNT [55]) and require the use of surfactants for a proper dispersion in water.
  A second drawback is seen in the long lyophilization times required to extract the

[2]Further, the combination of ink constituents is to be chosen with care to guarantee biocompatibility whenever a potential medical use is planned. In case of commercial inks, electrodes are considered safe to use in contact with biologic tissue after guaranteeing the evaporation of solvents. In consequence, the choice of non-toxic and easy to extract liquid phases is an important element for preparing porous electrodes based on conductive inks.

liquid phase, e.g. 12 h in [47].

- Phase separation techniques present an opportunity to be integrated into a flow-process of ink deposition.
  Danesh et al. presented a non-solvent-induced phase inversion of a system composed by a polymer, its solvent, a second liquid phase (acting as non-solvent of the polymer) and carbon particles [56]. A homogeneous solution was cast and left to evaporate, before washing out solvent residues. Thus obtained porous films displayed an average pore diameter of 216-330 µm and a SSA up to 17.3-30 $m^2/g$ as a function of the solvent content.
  The approach appears highly interesting for an adaptation to commercial inks, however the removal of residual polymer solvents requires a separate step.
- The interest to generate pores by using templateless porogeneous agents or treatments is equally considered promising. The saturation of polymers with a gas or fluid, leading to the formation of pores, has to the author's knowledge only been applied to polymers and polymeric solutions. As mentioned earlier, a carbonization step is needed additionally to yield a porous structure of graphitic nature, which assures utility as electrode material [34].
  While Colton et al. had proposed the idea to incorporate nucleation agents such as carbon black in the polymer precursor[3], they found no effect on the number of pores and did not consider it in the preparation of conductive foams [57]. In the context of a conductive ink, where the ratios of carbon particles to polymer is different, the effect potentially deserves another study.

Table I.1 summarizes the estimated complexity and required time for the preparation of structured carbon electrodes. Furthermore, the compatibility with ink deposition is indicated, underlining the interest in finding an alternative structure-generating approach which may include elements of scaffoldless structuration techniques.

Table I.1: Evaluation of mechanisms (−, 0, +) for preparing structured electrodes regarding selected criteria of complexity, time and compatibility with ink deposition.

| **Category** | **Technique** | **Complexity** | **Time** | **Compatibility** |
|---|---|---|---|---|
| Scaffold | Hard-template | − | − | 0 |
| | Soft-template | − | − | − |
| Scaffoldless | Ex-situ | 0 | − | + |
| | In-situ | 0 | − | + |

[3]In this case, the particles assisted so-called heterogeneous nucleation and were not acting as templates

## 1.2 Structuration mechanisms involving polymers and supercritical $CO_2$

A supercritical fluid is the phase of a substance once it is exposed to temperature and pressure higher than the critical values ($T_c$ and $P_c$)[4]. In this state, the phase boundary between the liquid and gas state no longer exists which leads to the supercritical fluid presenting mixed, ambivalent properties associated with both liquid and gaseous state [58]. Density, diffusivity and solvating power are generally similar to liquids, while mass transfer, compressibility and viscosity are reportedly similar to gases. By adjusting the system's pressure and temperature, the properties can be modified within a certain range [59]. Supercritical fluids have been used to replace common organic solvents in a range of applications, such as chromatography, extractions, pharmaceuticals and polymer processing [60].

### 1.2.1 Phase diagram of $CO_2$

Supercritical $CO_2$, referred to as $scCO_2$ in the following, stands out in particular due to its advantageous properties. The gas as such is non-toxic, widely abundant, chemically neutral, non-flammable and non-corrosive. As it presents a low safety hazard and a rather small environmental impact, compared to other common solvents, it is a widely-used candidate for industrial "green chemistry" processes. A beneficial side-effect are low recycling costs.
Part of its popularity arises from the relative ease to reach its critical state, which is depicted in the schematized phase diagram in Figure I.7, where $T_c$ = 31.1 °C and $P_c$ = 73.8 bar. The moderate conditions at which the supercritical phase is reached are pointed out (for water $T_c$ = 374.2 °C and $P_c$ = 221 bar).

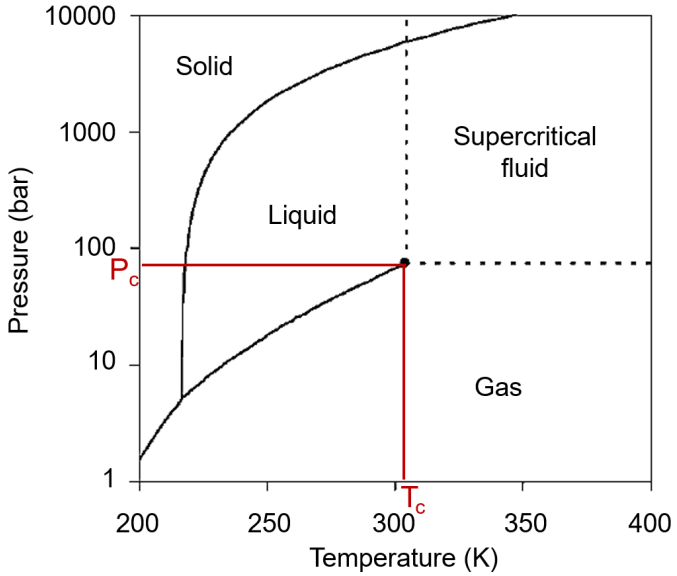


Figure I.7: Phase diagram of $CO_2$, where the critical point is defined by critical temperature ($T_c$ = 31.1 °C) and critical pressure ($P_c$ = 73.8 bar), representing the end of the gas-liquid equilibrium region. Figure reproduced from [5].

[4]The definition is potentially unprecise for some materials. It can further loose validity for very elevated pressures, when the freezing curve reaches the supercritical region.

The application of $scCO_2$ covers the extraction of organic compounds (caffeine [61] and essential oils [62]) to polymer processing on the experimental and industrial scale [59]. Regarding the creation of polymer foams, the use of $scCO_2$ is an alternative to chemical foaming agents (CFA) and to casting/leaching methods relying on hard templates [63]. As mentioned in the previous chapter, $scCO_2$ has further been used for the purpose of solvent extraction and for polymer structuration via phase separation. In this section, the theoretical principles of the three mechanisms will be discussed separately, allowing to highlight their potential interest in the preparation of porous carbon electrodes.

## 1.2.2 Phase separation in the preparation of porous polymers

### 1.2.2.1 A thermodynamic view on phase separation

The mechanism of phase separation or phase inversion has been studied and used extensively for the preparation of porous polymer membranes during the past 60 years, with pioneering work done by Loeb et al. on membranes for water desalination [64]. Until nowadays, thus-obtained membranes are used for filtration [65] [66] and for separation purpose in fuel cells [67] and for gases [68].
In the following, the thermodynamic principles of mixing processes are briefly introduced based on a book by Moulder [69], before discussing demixing on the example of multicomponent systems and phase diagrams (binary for two, ternary for three components).

The equilibrium state of any physico-chemical system at constant temperature and pressure can be described according to I.2, depending on the state functions of internal energy (U), enthalpy (H), entropy (S) and free enthalpy/ Gibbs free energy (G). Any process, e.g. mixing of several components (in the following denoted by the subscript $_m$, implies a change of the free enthalpy according to I.3. In consequence $\Delta H_m$ and $\Delta S_m$ determine, whether the process is spontaneous or not. As the criterion $\Delta G_m < 0$ applies for a spontaneous process and $\Delta S_m$ is generally small for a polymer/solvent system, $\Delta H_m$ principally influences solubility, requiring small values.

$$G = H - TS \tag{I.2}$$

$$\Delta G_m = \Delta H_m - T\Delta S_m \tag{I.3}$$

Hildebrand et al. [70] proposed an expression for the solubility parameter $\delta_i$ of a given substance i, describing its tendency to mix via the enthalpy of vaporization $\Delta H_{vap,i}$, the thermal energy available for a given temperature $RT$ and the molar volume $V_i$ (equation I.4). The parameter $\delta_i$ is also known as the square of the cohesive energy density (CED), sometimes referred to as molecular stickiness.

$$\delta_i = \sqrt{CED} = \sqrt{\frac{\Delta H_{vap,i}}{V_i}} \tag{I.4}$$

They further described the enthalpy of mixing $\Delta H_m$ for two components[5] by linking $\sigma_{i,j}$ with the volume fractions of each component $v_{1,2}$ and the combined molar volume $V_m$ (equation I.5):

$$\Delta H_m = V_m(\sigma_1 - \sigma_2)^2 v_1 v_2 \tag{I.5}$$

Interestingly, this expression allows to associate miscibility with substances of similar $\delta_{i,j}$ ($\Delta H_m = 0$), a concept that was further refined by Hansen [20]. The Hansen solubility

[5]The concept was derived for small, non-polar solvents.

parameters (HSP) separate $\delta$ into contributions originating from dispersion forces (temporary dipoles), polar forces and hydrogen bonds and are consequently named $\delta_d$, $\delta_p$ and $\delta_h$. The concept is frequently represented by vectors in a three-dimensional space, where each force points into one direction and thus composes the solubility parameter vector. The common criterion of good solubility/miscibility is fulfilled, when the vectors of two mixed substances point into a similar direction and have a similar length. The theoretical concept of ideal miscibility is implied for solubility parameter vectors of identical direction and length[6]. Practically, however, this not observed for different substances.
The Hansen solubility parameters of compounds relevant in this project, available in the work by Hansen [20], are listed in Table I.2 and compared to water as reference. Some exemplary polymers commonly used as polymeric binder in the formulation of conductive inks are included (referenced works below the table). The overall similar HSP of EGDA and $CO_2$ are highlighted and indicate good miscibility, yet particularly the solubility parameter associated with hydrogen bonding is different and suggests different interaction with polymers. This is of further interest for the choice of polymer solvent and non-solvent.

Table I.2: Hansen solubility parameters for dispersion forces $\delta_d$, polar forces $\delta_p$ and hydrogen bonding $\delta_h$ [20].

| **Substance** | $\delta_d$ **(MPa$^{0.5}$)** | $\delta_p$ **(MPa$^{0.5}$)** | $\delta_h$ **(MPa$^{0.5}$)** |
|---|---|---|---|
| Water | 15.5 | 16.0 | 42.3 |
| EGDA | 16.2 | 4.7 | 9.8 |
| $CO_2$ | 15.3 | 4.1 | 5.7 |
| Polyvinylidene fluoride$^{\dagger}$ | 17.0 | 12.1 | 10.2 |
| Ethyl cellulose$^{*}$ | 17.9-20.1 | 4.3-6.9 | 5.9-9.9 |
| Polyurethane$^{\diamondsuit}$ | 18.1 | 9.3 | 4.5 |

EGDA = Ethylene glycol diacetate, $^{*}$ referenced in [71],$^{\dagger}$ referenced in [72], $^{\diamondsuit}$ referenced in [73]

Returning to equation I.3, the theoretical derivation of Gibbs free energy curves as a function of composition of two substances can be found in literature [6] [74]. An essential representation is the following equation I.6, where $\Omega$ is a coefficient linked to the free energy change and coordination number change upon mixing components $i$ and $j$, $x_{i,j}$ representing the molar fractions [6].

$$\Delta G_m = \Omega x_1 x_2 \; + \; RT\,(x_1 ln x_1 \; + x_2 ln x_2) \tag{I.6}$$

Two particular cases can be distinguished, which are further visualized in Figure I.8, displaying the Gibbs free energy curves for an exemplary binary system composed by a polymer and a solvent, where $T_2 < T_1$.

- For exothermic solutions, $\Delta H_m \leq 0$ for all temperatures and compositions. As the entropy of mixing is always of positive value, $\Delta G_m < 0$ is granted and the two substances are completely miscible. A different description is to say, that any composition is thermodynamically stable.

- As $\Delta H_m > 0$ for endothermic solutions and $\Delta S_m$ can adopt small values for polymeric solutions, miscibility is guaranteed only for sufficiently high system temperatures when $\Delta G_m < 0$ over the entire composition range, see Figure I.8 a). For temperatures below the threshold temperature $T_{threshold}$, the term $\Delta H_m$ is larger

[6]The commonly used phrasing is "Like dissolves like".

than $T\Delta S$, see Figure I.8 b). The system therefore demixes in two phases with compositions $x_I$ and $x_{II}$, to achieve overall reduction of free Gibbs energy.

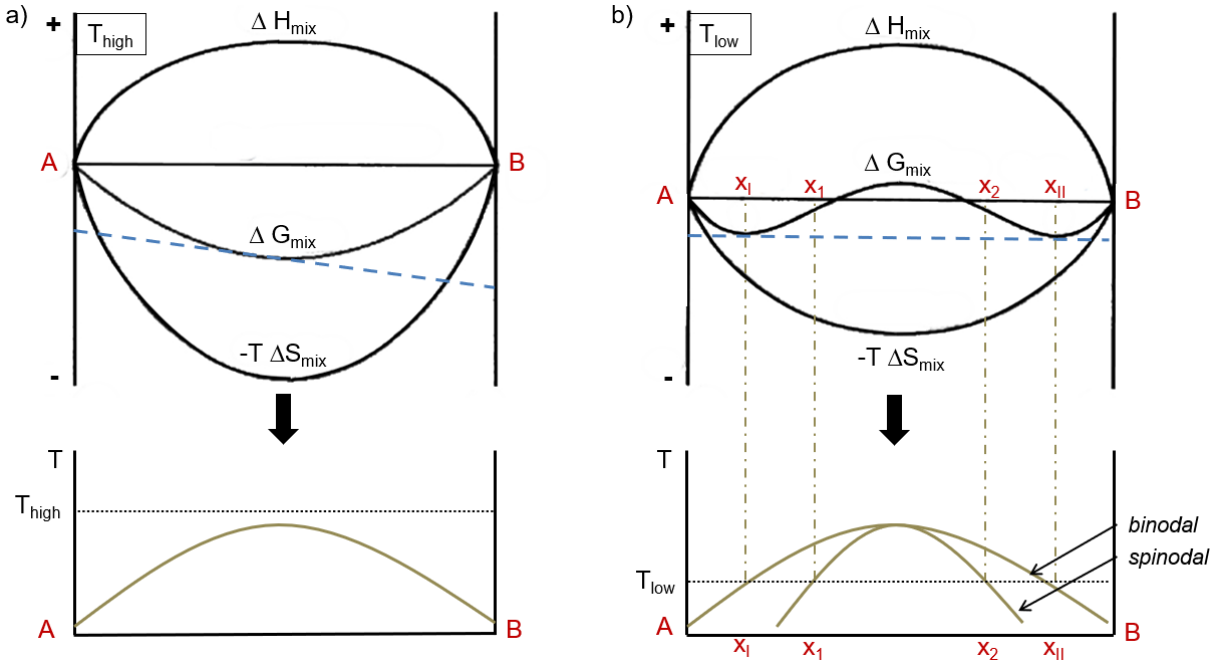


Figure I.8: Gibbs free energy of mixing as a function of composition for the binary system AB. Miscibility at a) high temperatures is given for all compositions, while b) a miscibility gap forms for temperatures smaller than $T_{thresh}$; upper part of the Figure adapted from [6]. The lower part visualizes the preparation of phase diagrams with the definition of binodal and spinodal by the minima ($x_{I,II}$) and inflection points ($x_{1,2}$) of $\Delta G_{mix}$.

Binary phase diagrams are prepared by extracting the information on miscibility or non-miscibility out of Gibbs free energy curves. To do so, tangents are placed under the $\Delta G_{mix}$ curves of each temperature. In Figure I.8 a), a tangent (in blue) can be drawn for any composition, while in b), only one tangent can be realized and defines the compositional range of the miscibility gap. The complete phase diagram is obtained for repeating the process over a large temperature range.
The location of the miscibility gap is defined by the minima of $\Delta G_{mix}$[7]. The location of inflection points[8] allows distinguishing between so-called binodal and spinodal, which are two subtypes of demixing processes (visualized in Figure I.10 below):

- The composition range enclosed by the inflection points ($x_1 < x < x_2$) is thermodynamically unstable and can undergo spontaneous or spinodal demixing, initiated by small local concentration fluctuations. With time, the concentration in the areas increases towards the final concentration, whereas no physical growth of the areas is observed. The resulting structure is defined by small, interconnected areas of stable composition $x_I$ and $x_{II}$.

- Compositions between the binodal and spinodal are considered metastable, implying demixing only upon delivery of energy required for formation of stable nuclei. The latter are of final composition $x_I$ and $x_{II}$, however growth is observed over time due to diffusion mechanisms.

[7] For $\delta\Delta G/\delta x = 0$ and $\Delta G_{mix} < 0$.
[8] For $\delta^2\Delta G/\delta x^2 = 0$.

Figure I.9 shows the binary phase diagram of a semi-crystalline polymer and a solvent, which presents an area of demixing (miscibility gap) for $T_{thresh} > T > T_e$ (subscript e for eutectic temperature) and one area of crystallization. Pochivalov et al. demonstrated the phase changes along three different paths (I-III) starting from different compositions in the homogeneous solution [7].

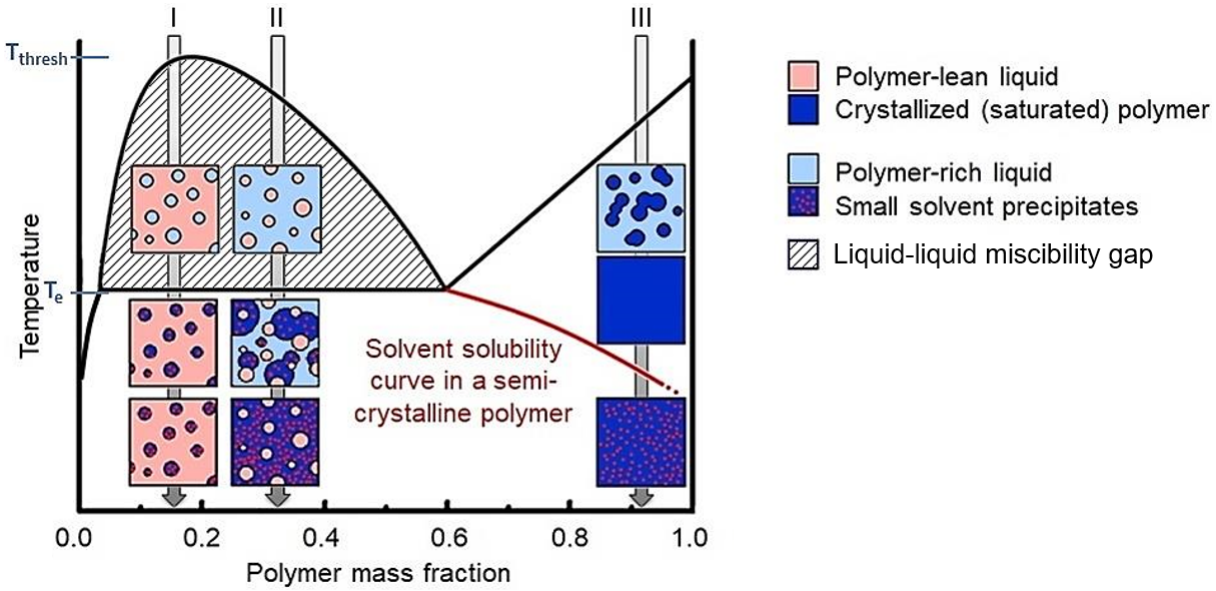


Figure I.9: Binary phase diagram for a semi-crystalline polymer with liquid-liquid miscibility gap adapted from [7]. The paths I and II represent thermally-induced demixing. Path III indicates crystallization upon temperature reduction.

At composition I and II, a reduction in temperature below $T_{thresh}$ induces phase separation of the homogeneous solution into one phase rich in polymer and low in solvent, whereas the second phase is rich in solvent but low in polymer. The process is also referred to as liquid-liquid demixing. As can be seen, the phase separation results in a primary structure which is locked in place for composition II by the crystallization of polymer below $T_e$. Crystallization equally occurs for composition I, but the overall polymer content is low, leading to the formation of separate polymer particles. It is pointed out, that liquid-liquid phase separation occurs only in the compositional range corresponding to the miscibility gap.
For composition III, the homogeneous solution undergoes crystallization of the polymer, but no phase separation occurs.
In addition, for all compositions the polymer fraction is saturated with solvent, which precipitates continuously when crossing the solvent solubility curve at lower temperatures. The paths through the binary phase diagram of a system undergoing thermally induced phase separation (TIPS) form the base for the introduction of ternary phase diagrams and non-solvent-induced phase separation. The fundamental mechanisms are comparable or identical.

Figure I.10 a) depicts an exemplary ternary system undergoing non-solvent-induced phase separation. The system is composed by a polymer, its solvent and a non-solvent of the polymer. Two paths (a) and (b) are indicated and apply for polymer solutions of different concentrations, to which the non-solvent is added. In both cases, a thermodynamically stable and homogeneous solution is formed, until crossing the binodal for (a) and the spinodal for (b), respectively. In the later stage of (b) it is suspected, that

the phases/areas undergo a certain diffusion-induced growth. The compositional change further suggests the gradual removal of solvent (and non-solvent) from the areas. Both displayed processes end before the removal of solvent and non-solvent is initiated.
In Figure I.10 b), typical structures obtained via binodal and spinodal decomposition are depicted, together with the visualization of the earlier explained mechanisms of diffusional binodal growth versus spontaneous spinal decomposition. The possibility to influence structural formation depending on the initial composition of the system is therefore given. However, each system and different types of polymers in particular behave differently and the presented mechanisms are generalized.

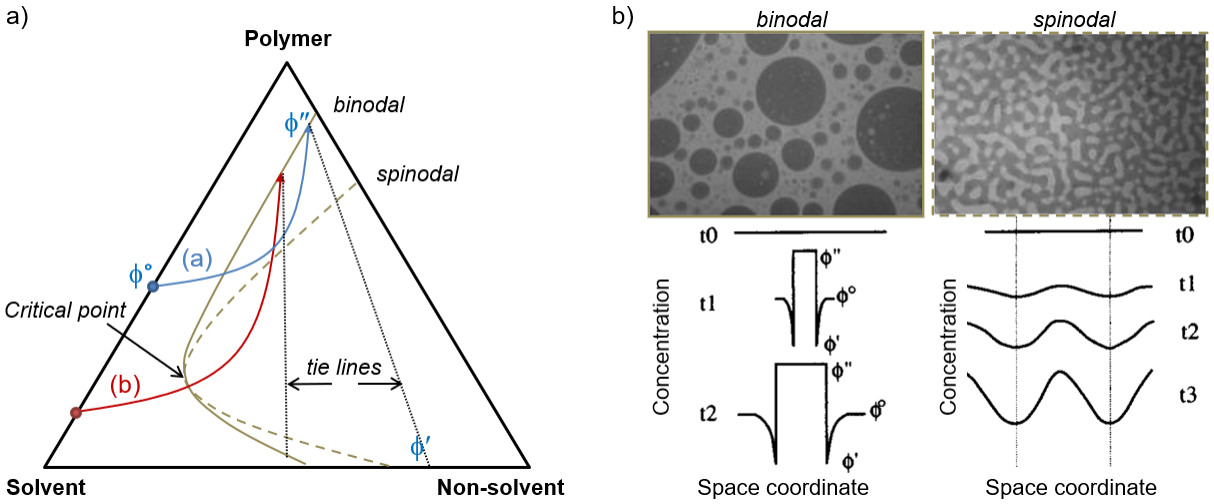


Figure I.10: a) Composition paths in a ternary phase diagram for solutions of different polymer concentration; starting compositions indicated by dots. Tie lines show the chemical equilibrium of the separated phases rich and low in polymer after crossing the binodal/spinodal. b) Depiction of the possible structure formation, with underlying demixing mechanisms in function of time t. For polymer concentrations $\phi$, $\phi'' > \phi^\circ > \phi'$ applies. Figure composed from [8] [9] [10] [11].

A list of reported factors influencing the location and extent of the miscibility gap in ternary systems undergoing phase separation is given below. The factors affect structural changes in the polymer foam or membrane [75] [74] [11] [48]:

- The choice of polymer limits the range of solvents which can be used, which is essential for the subsequent choice of the non-solvent.
- Good miscibility or generally a high affinity of solvent and non-solvent is required for the preparation of a porous sample. Else, so-called asymmetric samples with a dense top layer are likely to form.
- The polymer concentration defines the path through the phase diagram and therefore influences the obtainable structure. A lower polymer concentration at the initial interface with the non-solvent provides a higher potential for generating pores.
- The type and driving force for demixing are further influenced by the overall composition of the ternary system.
- Additives may alter the thermodynamic and kinetic interaction of the three main components (polymer, solvent, non-solvent) of the system.
- The temperature is thought to play a role, as solvent and non-solvent strength are affected. A lowered non-solvent strength is considered beneficial.

- Crystallization/ vitrification or aggregation behaviour of polymers (solid-liquid demixing) has to be taken into consideration, as the (partial) solidification limits a further growth of nuclei/pores. Generally this is the case, when the temperature drops below the polymer's glass transition temperature $T_g$. Alternatively, this is observed when the polymer concentration in the ternary phase reaches very high values. Generally, solid-liquid demixing is associated with strong interaction, i.e. low affinity, between polymer and non-solvent. Liquid-liquid demixing, on the other hand, has been associated with weak interaction (high affinity) of the two.

#### 1.2.2.2 Phase separation in the preparation of porous electrodes

In a given ternary sytem, non-solvent-induced phase separation, or wet phase inversion, has been studied for the preparation of porous electrodes. Selected contributions are presented in the following.

In a publication by Lim et al., a carbon slurry[9] was cast and immersed in water, to induce wet phase inversion [76].
A porous electrode was obtained with increased specifc surface and capacitive response up to 4.8 F/cm$^2$ (based on CV in 0.1 M $Na_2SO_4$ at 1 mV/s). The diameter of the small macropores were found to increase with the solvent content (64 to 82 nm), corresponding to theory. An application for desalination of brackish water was proposed.
While yielding very interesting results, the technique is time-consuming due to the immersion and later washing steps (more than 25 h here).

Secor et al. prepared inks composed by graphene, ethyl cellulose and nitrocellulose which were dispersed in glycerol and ethyl lactate [77]. The ink contained both solvent and non-solvent in an attempt to reduce electrode fabrication time. After ink deposition, phase separation occured during the drying step of printed electrodes.
The as-obtained porous electrodes were primarily characterized regarding their electrochemical performance. Compared to unstructured, graphene-based, printed supercapacitor electrodes the capacitive response was enhanced (0.8 mF/cm$^2$).
While the general concept of the work to use a self-initiated phase inversion after ink deposition is very interesting, thermal decomposition of polymer residues was required. Further, prolonged drying times (10 h) were required for glycerol removal, which reinforces the need for an alternative method for the removal of the wet phase.

A very recent work of Yang et al. explored the application of wet phase inversion in the preparation of an electrochemical sensor for bisphenol A detection [78]. The preparation comprised casting a poly(acrylonitrile-co-acrylic acid)-dimethyl sulfoxide (DMSO) solution on a separately prepared electrode, which presented $TiO_2$ nanotubes. Phase separation was initiated by immersion in water.
No particular characterization of the structure was carried out, however the sensor performance was considered very sensitive and selective, presumably as a consequence of the membrane porosity. It is pointed out, that the work represents a special adaptation of phase separation for the creation of a structured electrode, since a primary electrode structure already existed. It is possible, though, that similar approaches could be worth exploring to create electrodes of hierarchical porosity. Equally, adhesion of the ink to the base electrode could benefit.

[9] The paper specifies a composition based on activated carbon powder, PVDF as binder and N-methyl-2-pyrrolidone (NMP) as solvent.

#### 1.2.2.3 Supercritical fluid-assisted phase separation for the formation of porous polymers

In the following, works on the use of phase separation mechanisms relying on $scCO_2$ as the non-solvent are presented, which primarily intended to create porous polymers and membranes starting with polymer solutions. Only few works have proposed the fabrication of porous carbon electrodes by means of this technique. In particular, a carbonization step after creation of the porous structure is required to graphitize the matrix [4].

Matsuyama et al. studied the formation of polystyrene membranes [79] based on polymer solutions, which were exposed to pre-pressurized $scCO_2$ (13 MPa, 15 min, 35 ℃). The cell was then flushed with $scCO_2$ (1 h, 13 MPa) and slowly depressurized (2 h).
The increase in process temperature (25 to 70 ℃) resulted in larger average pore sizes (10 to 35 µm). Higher $scCO_2$ pressure (8 to 16 MPa) was linked to larger pores (7 to 11 µm). The reduction of polymer concentration (30 to 15 % w/w) equally yielded larger pores (11 to 13.5 µm), explained by the easier pore growth in a solution of low viscosity.
Compared to previously presented phase separation mechanisms, the preparation time was shortened, principally as both fluids were extracted during the final depressurization, suppressing the need of further washing steps. An observation window fitted in the cell allowed to notice turbidity of the system, which immediately followed the introduction of $scCO_2$, indicating a fast onset of phase separation. The group concluded, that phase separation was the structure-generating mechanism and polymer foaming did not occur[10].

The same group investigated the effect of different organic solvents on the phase separation in a ternary system with cellulose acetate and $scCO_2$ [80]. Fixed process parameters (13 MPa, 35 ℃, 15 % (w/w) polymer) guaranteed evaluation of the pore development as a function of the interaction of solvent and non-solvent.
Pore sizes were measured in central locations of the samples and an increase from less than 1 to around 2 µm was observed for larger differences of the square of the solubility parameters, i.e. for lower mutual affinity between the solvent and $scCO_2$. Overall porosity followed a similar trend, varying between 43 and 55 %.
The supplementary work is highly interesting, as it confirms the possibility to create structures on the sub-micron scale by means of $scCO_2$-assisted phase separation.

The precipitation of semi-crystalline Nylon 6 membranes in a $scCO_2$-mediated phase separation process was reported by Kho et al. [8]. Polymer solutions[11] were cast and exposed to $scCO_2$ (35 ℃, 30 min preconditioning between 2.86 and 5.62 MPa, final pressure up to 17.3 MPa).
Porous films with a modifiable pore diameter between several µm and less than one µm were obtained, as well as different structures, originating from a competition between a liquid–liquid demixing, leading to smooth and cellular pores, and solid–liquid demixing, leading to spiny structures.
The work highlights the potential to control the structure by modifying the process parameters, allowing for different degrees of interconnectivity ranging from cellular and isolated pores to networks. This applies in particular for semi-crystalline polymers. It was confirmed, that the porous structure can be dried in the later stage of the process. In addition, the possibility to add a polymer foaming step was proposed, but not carrried out.

Reverchon et al. obtained porous membranes by casting polymer-acetone solutions, followed by exposure to $scCO_2$ at different process parameters (10-20 MPa, 5-40 % w/w,

[10] In the opinion of the author, the rather slow depressurization rate was potentially unlikely to initiate nucleation and pore growth.

[11] A 15% w/w Nylon 6 polymer solution in 2,2,2-trifluoroethanol (TFE) was prepared.

45-65 ℃) [15]. The experimental protocol consisted in 1 h of $scCO_2$ exposure under static conditions, 2 h under flow conditions, followed by a slow depressurization during 2 h.
The results suggested liquid-liquid demixing for increased pressure, leading to a rapid phase separation, resulting in an open, highly connected porosity. Increasing the polymer concentration yielded smaller pore dimensions (50 to 2 µm) matching other works. With increased polymer content, the membrane's appearance changed from beads-like elements to a cellular structure. Temperature was considered to be a less important factor, but an increase could be linked to a smaller pore size, explained by a reduced non-solvent strength of $scCO_2$.
The publication serves as a useful guideline for this project regarding the influence of process parameters under the hypothesis that the effects are transposable to conductive inks. However, overall process times are still relatively long (5 h of $scCO_2$ exposure alone) and the pressures rather high, which besides for the technical limitations presents a potential safety risk.

### 1.2.3 Critical point drying by means of supercritical $CO_2$

The removal of a solvent or non-solvent phase, while technically easy to realize, generally presents problems regarding the preservation of porous structures. In particular, aqueous polymer solutions undergoing lyophilization or gelation as structure-generating mechanism are considered unsuited for a combination with a subsequent solvent evaporation. The capillary effects arising from the surface tension of some solvents, e.g. water, can lead to the collapse of networks with pores on the sub-micron scale, as depicted in Figure I.11 a).

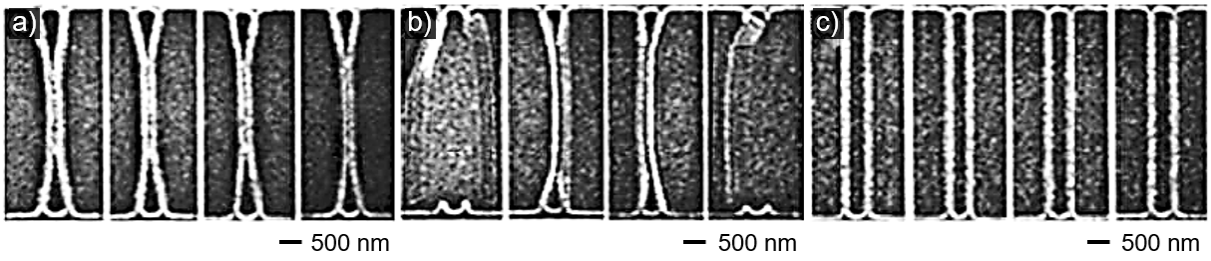


Figure I.11: The effect of solvent choice on structural presentation of pores measuring around 400 nm in diameter during evaporation of a) water, b) hexane, c) $scCO_2$. Adapted from [12].

A traditional method circumventing this problem is the step-wise replacement of water by immersing the wet, porous sample/ gel in water-ethanol solutions of successively higher alcohol content, until all water is replaced. The solvent can then be removed via evaporation.
While the surface tension of selected solvents may be lower than for water, they are unlike zero and can still damage very fragile structures, as seen on the example of hexane in Figure I.11 b). Furthermore, the process is labour-intensive and time-consuming, thus particularly limiting the interest to work with aqueous polymer solutions.

Alternatively, (super)critical point drying can serve as a structure-preserving method, allowing to avoid the passage of any boundary between liquid and gas phase and, in consequence, the occurrence of surface tension. Specifically the use of $scCO_2$ is reported and the preservation of filigree structures is confirmed. Figure I.12 presents the evolution

of surface tension of $CO_2$ as a function of pressure, indicating values at zero once the fluid is in supercritical state. Figure I.11 c) demonstrates the advantage of critical point drying using scCO2 to recover a pristine, porous sample.

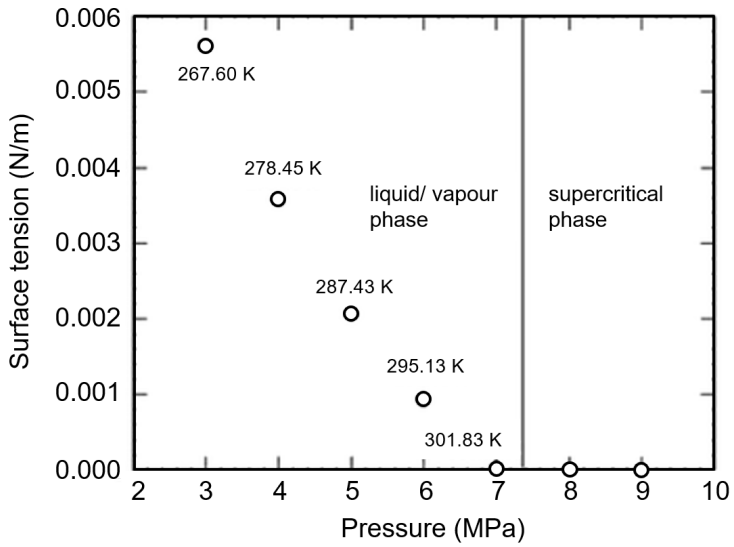


Figure I.12: The development of surface tension of $scCO_2$ as a function of pressure and temperature. Figure reproduced from [13].

In some works, critical point drying was directly applied to the aqueous gel [81]. While this is principally possible, reaching the supercritical point of water requires relatively harsh conditions (374 ℃, 22.1 MPa) [82], which are potentially incompatible with certain other materials, such as particular polymers.

The creation of a supercapacitor electrode was recently proposed by Sarno et al. based on dispersed graphene/ graphene oxide in an aqueous PVDF-derivate solution, which was lyophilized [83]. The transition of the obtained gel into an aerogel was $scCO_2$-mediated (35 °C, 20 MPa, 3 h at continuous flow of 1.5 kg/h), followed by a slow depressurization (30 min).
The electrodes displayed increased capacitive character, however the characterization conditions are not directly comparable to this study[12].
The work primarily points out the use of $scCO_2$ only for the purpose of solvent extraction and not for any additional structural modification, as it would be realizable by the cell's rapid cell depressurization. The overall process as structure-generating method again appears rather complex, requiring high $CO_2$ pressures and long overall process duration.
Meanwhile, an interesting observation was the function of the graphene nanoparticles as heterogeneous nucleation agent during the lyophilization step, favouring the formation of nanopores. An increased nanopore count with higher particle loading (10-90 % w/w) was noted.

Very recently, Sarno et al. published works on a similar critical point drying process in which the drying time was reduced to 20 min in the fabrication of a multi-layer supercapacitor device [84].
While the general approach did not promote the use of $scCO_2$ for modifying the structure, the work indicates the potential to reduce solvent extraction times. Again, this is of interest for the choice of process parameters in this work.

[12]The gravimetric capacitance was determined to 83 F/g via CV at 50 mV/s in the ionic liquid 1-Ethyl-3-methylimidazolium tetrafluoroborate.

## 1.2.4 Polymer foaming via supercritical $CO_2$ saturation

### 1.2.4.1 Nucleation and pore growth

As highlighted in previous sections, the protocols in which polymers were exposed to $scCO_2$ all ended with a slow depressurization to extract adsorbed fluid from the polymer bulk. As polymers are porous on the microscopic scale, they can undergo swelling in presence of $scCO_2$, like in presence of organic solvents, to different degrees depending on their chemical nature and their degree of cross-linking. The process is particularly pronounced due to the high diffusivity of supercritical fluids and the small size of the molecules [85]. Diffusivity is further tunable by adjusting temperature and pressure, i.e. its density, respectively [86].

In the industry, this circumstance has been used to induce pore nucleation and pore growth by a rapid depressurization of the $scCO_2$-saturated polymers. When the solubility of $scCO_2$ is rapidly decreased, the polymer becomes supersaturated and pore formation principally follows the previously explained phase separation mechanisms for a binary system. The plasticized polymer is considered as one phase and $scCO_2$ as the second phase. Depending on whether the depressurization leads the system into a thermodynamically metastable or unstable state, either nucleation and pore growth or spinodal decomposition occur [63]. In parallel, due to the Joule Thomson effect[13], the polymer's temperature decreases and vitrification occurs in case $T_g$ is passed, which stops further pore growth [87].

A side-effect of saturating the polymer with $scCO_2$ is the reduction of its glass transition temperature $T_g$[14], which favours plasticity [86]. Alessi et al. explained this observation with the increased interchain distance in the saturated polymer and a resulting enhanced mobility of the chain segments [85]. This idea validates the reduced viscosities of saturated polymers reported earlier [89].

Interestingly, pore growth only takes place in a polymer of sufficient plasticity [63], meaning that in an industrial process, samples need to be heated to temperatures above $T_g$. The reduction of $T_g$ is thus of importance, as less energy is required to transfer the polymer to the rubbery state . Specifically for amorphous and semi-crystalline polymers, reductions by several tens of degress can be achieved [90] [91].

### 1.2.4.2 Supercritical $CO_2$-assisted polymer foaming in literature

Literature suggests, that the creation of pores is a function of polymer choice, process parameters (pressure, temperature, time) and the rate of depressurization. Various pore sizes are obtainable in the preparation of polymer foams, including large mesopores (30 to 50 nm in diameter) and macropores (up to several hundred µm in diameter).

Nikitine et al. presented a screw extrusion process for the preparation of porous polymer foams [92]. A thermoplastic polymer was saturated with $scCO_2$ (110-150 ℃ process temperature), acting as plasticizer and later as foaming agent upon relaxation.
Expansion of the sample was found to increase with process temperature and pressure, generating average pore diameters between ca. 47 to several 100 µm.
Although the experimental approach was unlike the pressurization of a closed cell (in particular, no $scCO_2$ pressure was specified in the paper), it provided an interesting theoretical and experimental base.

[13]The Joule Thomson effect describes the temperature reduction of a fluid undergoing adiabatic pressure change from high to low pressure.

[14]The glass transition temperature is defined by the change of a polymer's glassy to its rubbery state, i.e. the temperature above which plastic deformation is enabled without fracture [88]

Chuaponpat et al. studied the foaming conditions of polyvinyl chloride using a more classical $scCO_2$-assisted process at various process conditions [93].
It was found that a temperature increase (40-80 ℃) yielded larger pores (around 2 to more than 100 µm diameter). Higher pressures (12-17 MPa) resulted in larger pores (around 2 to 20 µm).

Gong et al. worked on the preparation of porous polymer monoliths by means of $scCO_2$ foaming, which were transformed to carbon electrodes via carbonization [34], as cited earlier. For lower process temperatures (100 to 150 ℃), smaller cell sizes and smaller total pore volumes were observed. The influence of higher pressure (10.34 to 31.03 MPa) was found to be beneficial for the creation of smaller pores, which generally ranged in the low micron scale.
The overall process is considered rather complex and the elevated pressures and temperatures limit the practical interest.

A classical supercritical fluid-assisted polymer foaming approach was published by Otsuka et al., who exposed polystyrene poly(methyl methacrylate) blends to $scCO_2$ (8.6 MPa, 20 to 40 ℃), prior to depressurization [94].
Different polymer blends yielded varying pore diameters from 100 to 500 nm. Faster depressurization rates (0.1 to 0.5 MPa/min) were associated with even smaller pores of 50 nm in diameter and cell density increased.
The work underlines the potential to use a polymer foaming approach for the nanostructuration of materials, specifically as the process parameters are moderate, compared to the previous example.

Similarly, foaming of polystyrene by means of $scCO_2$ was studied by Arora et al., exploring different process conditions [95].
Higher temperatures during foaming (40-120 ℃) yielded fewer and larger cells (1-27 µm), while elevated saturation pressures (13.8-34.5 MPa) resulted in smaller pores (70-5 µm). Further, different cell morphologies were observed. Faster depressurization rates resulted in smaller cells, the smallest measuring less than 1 µm.
The study complements the previous work and provides important details on the influence of each process parameter.

Colton et al. developed a model for the nucleation behaviour of thermoplastic polymer foams in presence of additives [57]. They concluded, that heterogeneous nucleation was favoured for additive concentrations above the solubility limit of the additive. In that case, since heterogeneous nucleation requires lower activation energy than homogeneous nucleation, higher pore densities, as well as potentially smaller pore sizes are to be expected. For low additive loading, on the other hand, homogeneous nucleation is the dominating mechanism.
The experimental verification suggested the creation of more homogeneous polystyrene foams with small pore sizes, when adding soluble additives. Meanwhile, no increase in pore count was observed after adding up to 1 % w/w carbon black (saturation pressure between 1.3 and 9.5 MPa).
The question arising from the study is, which effect is to be expected from systems of different composition. In particular, conductive inks contain rather low polymer concentrations and high additive loadings.

## 1.3 A new approach to structure carbon ink electrodes by means of $scCO_2$

The studies presented in the last sections confirm the possibility of a controlled pore generation in multi-component systems containing polymers and conductive particles by means of phase separation, solvent evaporation and polymer foaming methods. The successful application in the preparation of electrode materials has equally been demonstrated, as well as the introduction of $scCO_2$ as non-solvent for the polymers and as solvent for initial organic solvents. While the combination of the single mechanisms seems highly promising, only few works have discussed this idea. In the context of polymeric solutions, mainly two publications are found:

- Kho et al. attempted to foam $scCO_2$-saturated (10.4 MPa, 0.5-15 h) Nylon 6 membranes, following phase separation, as mentioned earlier [8]. The depressurization took place over 10 min and samples did not exhibit any evidence of foaming. The depressurization rate of 1 MPa/min, however may have been insufficient to induce oversaturation.

- Salerno et al. prepared polycaprolactone foams with the aim to create interconnected foams of large-size pores based on 50 % w/w polymer solutions [96]. After pressurization with $scCO_2$ (50 °C, 20 MPa, 1-17 h), phase separation and polymer saturation occured, followed by a depressurization (1.2 MPa/min).
  Longer saturation time favoured solvent removal[15] and lead to higher overall porosity and higher pore uniformity. While the rate of depressurization was not studied, it was considered beneficial to introduce a two-step depressurization with an intermediate plateau at 8 MPa to prevent damage to the porous structure during a complete depressurization from very high pressures.
  It is pointed out, that the observed pore sizes (400-1200 µm) appear rather large for the adaptation of the process to the fabrication of high-surface area electrodes. Further, the depressurization rate may provide room for improvement.

**To the author's knowledge, no research group has communicated a combined protocol unifying phase separation, solvent extraction and polymer foaming in a one-step process for the application on conductive inks or pastes and with the aim to increase specific and electroactive surface of as-prepared electrodes.** The principal advantage of a such approach is considered to be its simplicity of depositing conductive inks, followed by a treatment that is compatible with an assembly line production, requiring moderate process conditions and allowing to recover ready-to-use electrodes. A general scheme of this approach is provided in Figure I.13,

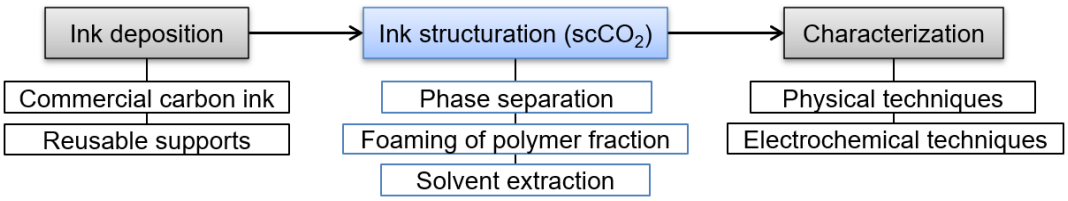


Figure I.13: A schematic representation of the structuration of carbon ink electrodes in this project, with the $scCO_2$ treatment highlighted.

[15] The residual organic solvent content in the foams was estimated to around 1 %.

### 1.3.1 Presentation of the structuration protocol

In the following, the protocol and the parameters of interest are briefly discussed based on the previously cited works. The three main structuration steps (phase separation, solvent extraction, polymer foaming), displayed in Figure I.14, are considered temporally separated to simplify the simpler presentation. In reality, a more complex overlap is expected, e.g. some degree of polymer saturation could occur since the beginning. In order to focus on the general introduction of the technique, exact parameters of the protocol are provided in the next chapter.
One main difference between the references on polymer structuration and the proposed approach is the presence of large concentrations of carbon particles in the conductive inks. Therefore, as a principal hypothesis, it is thought that the carbon particles do not hinder phase separation and polymer foaming to occur.

A commercial carbon ink was diluted, as specified in the next chapter, to prevent rapid drying of the solvent during the transfer into the cell of the supercritical fluid equipment, see step (1). It was then exposed to $CO_2$ and rapidly compressed to exceed the critical pressure and enter its subcritical phase. It was reasoned, that the more liquid-like character of compressed $CO_2$ could enhance its solubility in the solvent/diluent of the ink. The conditions were maintained, step (2), during the separation time $t_{sep}$, during which the ternary system underwent phase separation, thus creating a primary electrode structure.
Afterwards, the temperature of the cell was raised in order to access the supercritical state of $CO_2$, therefore allowing for polymer saturation to take place during the saturation time $t_{sat}$, see step (3).
Finally, during the depressurization, both solvent and non-solvent are extracted from the polymer and the ink deposit, creating thermodynamic instability. This in turn initiates nucleation and pore growth, resulting in a secondary structure. The porous ink deposit was recovered at step (4).

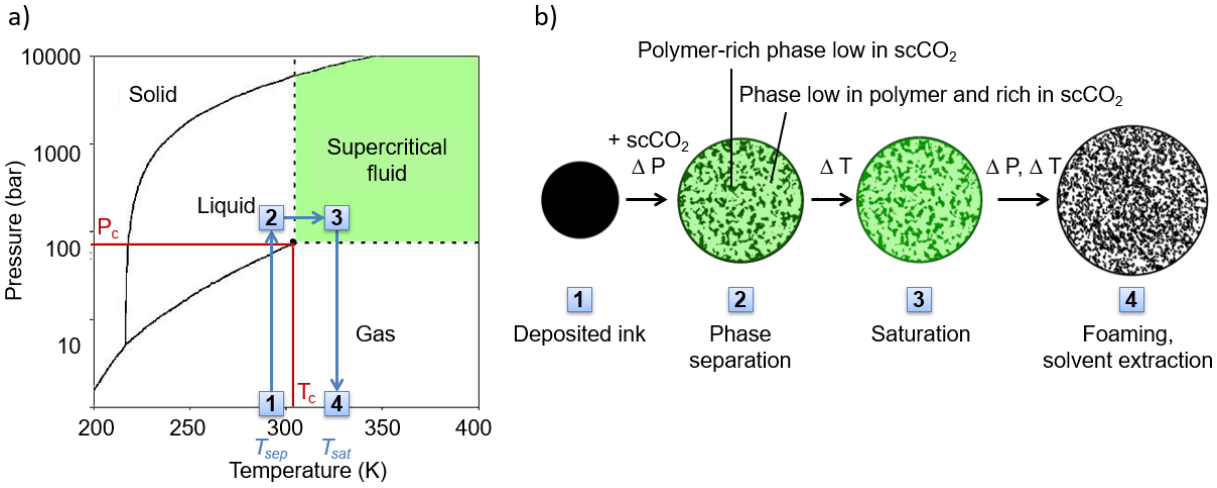


Figure I.14: The process scheme a) in the phase diagram of $CO_2$ and b) a visual representation of the structural changes during the steps.

### 1.3.2 Identification of process parameters

Parameters of interest were considered to be the same as for the separate mechanisms. During phase separation, besides for the fundamental choice of polymer, solvent and non-solvent, this included process temperature, pressure and polymer concentration. The

choice of the latter three was guided by the tendencies observed in literature with the aim to decrease pore size, considered advantageous for increasing specific and electrochemically active surface.
The strategy for a general choice of parameters is described below, with Table I.3 serving as supportive guide[16]. A general aim was the creation of small pores. It was assumed, that the pores should not exceed several µm in diameter in order to guarantee a high ratio of surface to volume.

- During phase separation, a relatively low $CO_2$-pressure and temperature were chosen [79][17]. The phase separation time $t_{sep}$ was considered of high interest for being studied, although it is rarely discussed in literature. However, due to the combination of mechanisms in this project it was considered to play a potentially important role.
- During polymer foaming, the low process pressure was maintained, although some literature suggests that working at increased pressure could increase pore densities. It was reasoned, that the high concentration of carbon particles, acting as nucleation agents, could have a comparable effect. The saturation time $t_{sat}$ was considered to be of interest in order to have a means of controlling the degree of saturation. The temperature during foaming was increased to access the supercritical state of $CO_2$, but kept low in comparison to literature to limit pore growth.
  In a separate study, the effect of slightly higher saturation temperatures was investigated, as a potential benefit was associated when exceeding $T_g$.

A commercial carbon ink was chosen, following the idea of an easily industrializable structuration technique. However, due to the lack of a precise ink composition, the estimation of the polymer concentration was less evident. In consequence, different ratios of ink dilution were prepared and studied in a separate section upon the effect on pore generation.

Table I.3: The effect of process parameters (temperature $T$, pressure $P$, saturation time $t_{sat}$, depressurization rate $\Delta P_{depress.}$, polymer concentration $C_p$) during phase separation (PS) and polymer foaming (PF) on the evolution of pore diameter $d_{pore}$ or porosity. Literature focused on $scCO_2$-assisted mechanisms.

| **Mechanism** | **Parameter change** | **Effect** | **Reference** |
|---|---|---|---|
| PS° | $C_p \uparrow$ | $d_{pore} \downarrow$ | Li et al. [76] |
| PS | $C_p \uparrow$, $P \downarrow$, $T \downarrow$ | $d_{pore} \downarrow$ | Matsuyama et al. [79] |
| PS | affinity solvent/non-solvent $\uparrow$ | $d_{pore} \downarrow$ | Matsuyama et al. [80] |
| PS | $C_p \uparrow$, $T \uparrow$ | $d_{pore} \downarrow$ | Reverchon et al. [15] |
| PF | $T \downarrow$, $P \downarrow$ | $d_{pore} \downarrow$ | Nikitine et al. [92] |
| PF | $T \downarrow$, $P \downarrow$ | $d_{pore} \downarrow$ | Chuaponpat et al. [93] |
| PF | $T \downarrow$, $P \uparrow$ | $d_{pore} \downarrow$ | Gong et al. [34] |
| PF | $T \downarrow$, $\Delta P_{depress.} \uparrow$ | $d_{pore} \downarrow$ | Otsuka et al. [94] |
| PF | $T \downarrow$, $P \uparrow$, $\Delta P_{depress.} \uparrow$ | $d_{pore} \downarrow$ | Arora et al. [95] |
| PS+PF* | $t_{sat} \uparrow$ | overall porosity $\uparrow$ | Salerno et al. [96] |

° The work focused on a classical wet phase inversion and serves as comparison to references using $scCO_2$. * The combined action of phase separation and polymer foaming is not explicitly mentioned in the paper, but possible.

[16]Some observations of different groups are contradictory.

[17]Despite Reverchon et al. [15] concluding that elevated process temperatures could reduce pore sizes, a low process temperature was chosen in this project due to a simpler technical realization.

## 1.4 Conclusion of chapter I

The first chapter has provided an introduction to the structuration of carbon electrodes for electrochemical application. The disadvantages linked to the traditional fabrication methods, using hard and soft templates, have been highlighted. While porous carbon electrodes can be prepared in very controlled manner, the complex and time-consuming nature of the approaches adds to the use of hazardous chemicals and limits the compatibility with the identified criteria of utility.
Scaffoldless methods generally involve the use of less harsh chemicals, however, the multi-step protocols, which are generally used, are linked to long process times. After structuration, a carbonization step is commonly required to obtain a conductive material of graphitic nature, which increases complexity and cost of fabrication.
In consequence, it is considered that an alternative structuration method is needed which could reduce both time and potentially the cost associated with the production of structured electrodes. Furthermore, a particular interest is seen in using the industrially well-established process of ink deposition.

The structure-generating mechanism of phase separation has been introduced, providing literature related to the preparation of porous electrodes. While the substitution of the traditional organic non-solvent phase by $scCO_2$ has been presented for preparing porous polymer materials, no study is available on the use of a $scCO_2$-assisted phase separation for the direct fabrication of porous electrodes.
Further, the $scCO_2$-mediated mechanisms of critical point drying and polymer foaming have been presented. Critical point drying has been used in the context of electrode preparation to extract a solvent phase from a structured wet material. Polymer foaming was used in the past for the creation of porous polymer precursors, but required a graphitization step for the use as electrode.

All three mechanisms appear to present high potential for a combination into one single treatment, an idea, which has not been published so far. Particularly, no research group has worked on a comparable structure-generating treatment in the context of conductive inks.
In consequence, an alternative process for the generation of porous carbon electrodes has been proposed. A principal hypothesis consisted in the assumption, that the mechanisms, which are described for the exposure of a pure polymer solution to supercritical fluids (and $scCO_2$ in particular), can be transposed to the exposure of an ink. Thus, the suggested protocol consists in the deposition of a conductive carbon ink, followed by an exposure to $scCO_2$ to induce phase separation, followed by saturation of the polymeric binder. In a final depressurization step, pore growth is induced in parallel to the extraction of the solvent phase during depressurization.
The parameters which require to be studied in this project have been specified.

# Chapter II

# Structuration of a carbon-based ink and characterization protocols

This chapter introduces the experimental methods and is intended to list reagents, experimental setups and protcols used to prepare and characterize the structured electrodes in this work. Opposed to a classical presentation of methods, particular problems which required improvements regarding the selection of materials and experimental setups are emphasized. A certain amount of results is therefore presented, to clarify why particular parameters or approaches were chosen. Figure II.1 depicts the thematic structure of this chapter.
The characterization of structured and functionalized electrodes is entirely part of the next chapter.

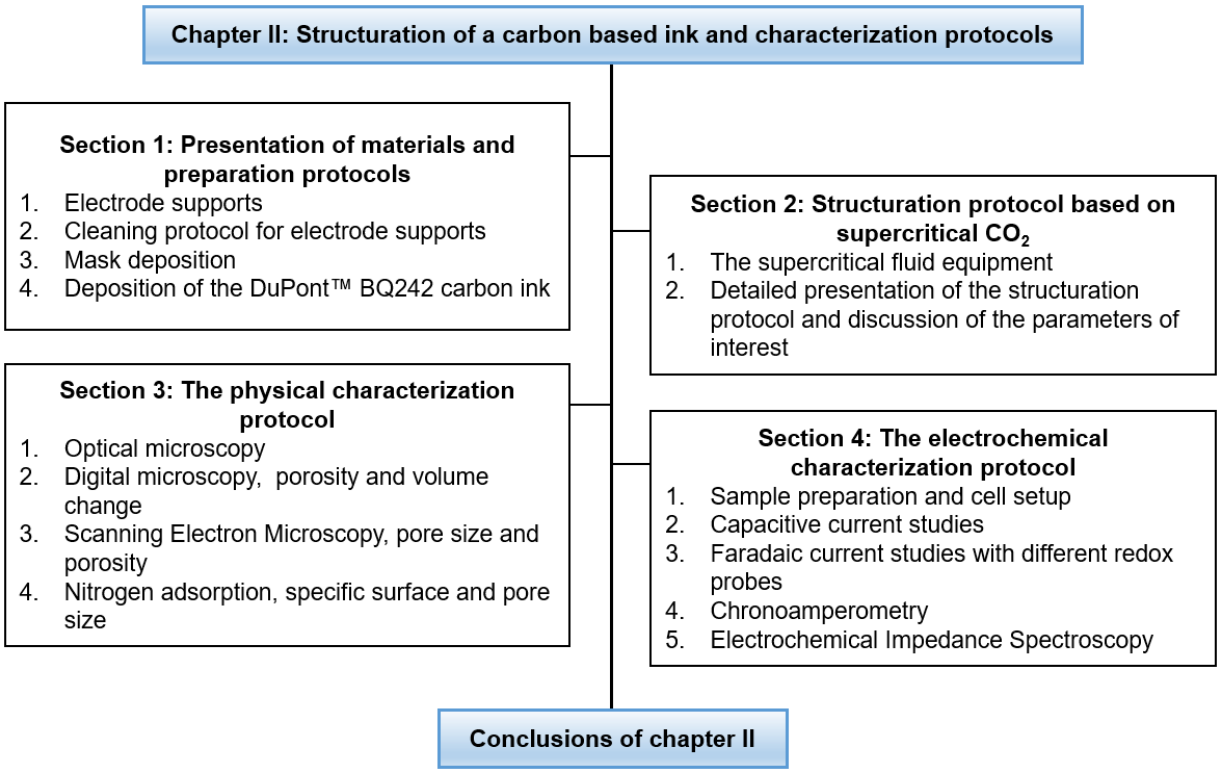


Figure II.1: The schematic structure of chapter II.

The first section gives details on the structured electrode supports, and cleaning protocols, specifying selection criteria. In a last subsection, specifications and properties of

the commercial carbon ink are given.

Section two mentions technical details concerning the supercritical fluid equipment, before revising the structuration protocol introduced earlier. The more practical standpoint taken allows to define important structuration parameters which form the base of chapter III.

The physical characterization protocol forms the core of the third section. The intention of applying different methods to access equal information was to underline intrinsic differences in the measurement approaches, possibly indicating a best suited method to study the structuration.
Based on optical and digital microscopy, an estimative, surface-related determination of porosity and volume change was done. Scanning electron microscopy was carried out to confirm the observations and to further investigate the structuration on a smaller scale. Graphic results were treated to extract data on pore size and porosity.
For a better access of the electrode volume, pore size and specific surface area were estimated by means of nitrogen adsorption experiments.

Section four is the second key component of the characterization techniques, with the focus on electrochemical results. As in the previous section, different techniques were used to compare equivalent properties of the structured electrodes. Capacitive current studies, carried out to assess the development of specific surface area, preceeded the employment of redox probes to investigate the charge transfer at the interface.
Chronoamperometry was carried out in order to link ion diffusion to the formation of electrode structure. A final experimental characterization was realized by performing electrochemical impedance spectroscopy studies.

The chapter closes with a revision of the sample preparation and characterization protocol.

# 2.1 Presentation of materials and preparation protocols

## 2.1.1 Electrode supports

### 2.1.1.1 Criteria for selection

In order to use well-characterized equipment, the initial intention was to choose commercial rod-type electrodes with an insulating Teflon housing. Advantages are an easy regeneration of the collector surface by cleaning, polishing and a cycling protocol in acidic solution, as it is commonly done for gold or platinum electrodes. The main advantage of a renewable surface consists in the constant/reproducible chemical and electrochemical quality of the collector. Furthermore, different types of collector materials are available, ranging from noble metals such as gold and platinum to different forms of carbon, e.g. glassy carbon and highly ordered pyrolithic graphite in basal or edge plane orientation.

However, compatibility with the structuration treatment was the principal practical requirement and size-related limitations prevented the use of rod-type electrodes. The supercritical fluid equipment (SFD-200, Separex, France) is a commercially available system designed for the treatment of silicon wafers and therefore presents a circular reaction chamber of approximately 25 cm in diameter, but only of 2 cm in height. The choice of electrode supports was thus limited to flat devices such as printed circuit boards (PCB) to maintain a level, horizontal orientation after deposition of the ink. Further conditions related to the supercritical fluid applied, as certain types of polymers undergo swelling or foaming upon exposure to supercritical $CO_2$ as explained in chapter I. Hence, electrode supports needed to maintain their structural integrity. The following list summarizes the requirements for electrode supports:

- Flat design
- Compatibility with supercritical $CO_2$
- Reusability of the platform and rigid/solid design
- Chemical inertness/recyclability of collectors

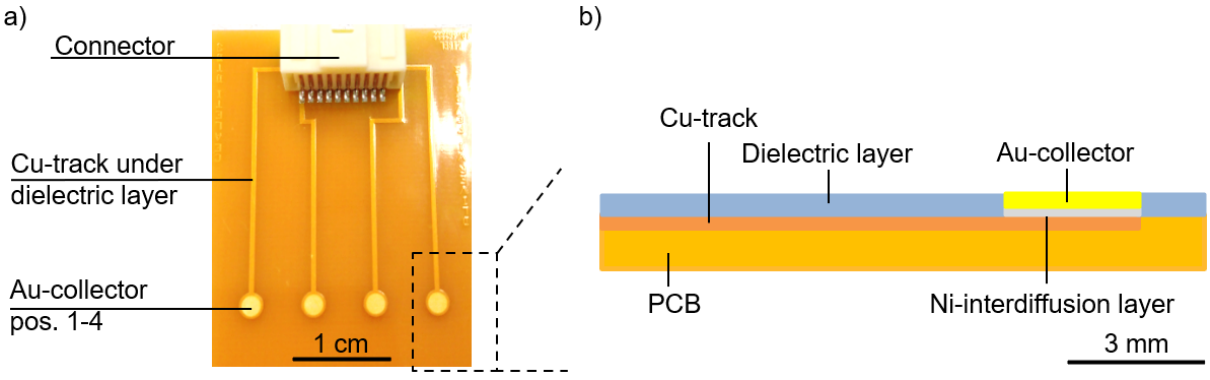


Figure II.2: Schematic representation of the reusable 4-electrode PCB-style supports in a) top view and b) a magnified side view.

Meeting the criterion of flat design, PCB-style platforms from the European project D-Liver [97], in which the laboratory was involved, were available. A visual representation of the platform (Cibel, France) is given in Figure II.2. The material was a flame retardant,

fibreglass-reinforced epoxy resin (FR-4) measuring 40 x 30 x 1.6 $mm^3$. Separate copper (Cu) tracks linked four electrode contacts/ collectors of 2.5 mm in diameter to a plug-in connector (Pico-Clasp 501189-2010, Molex). All tracks were electrically isolated by a varnish of around 400 µm thickness. The PCB presented the possibility to prepare four equivalent electrodes in one step, which was advantageous in order to increase statistical importance of the experimental data.
The collectors are in the following referenced as collector/electrode/position 1-4. Furthermore, PCB is used synonymously with "platform".
Figure II.2 b) provides a schematic cross-section of a PCB, detailing the layer-by-layer construction. Underlying Cu tracks were covered by a nickel-gold (NiAu) bonding, which was capped with a 3 µm thick flash-deposited Au layer. A Ni-inter diffusion layer was located between Au and Cu to prolong lifetime of the interface [98].

Initial tests confirmed the absence of swelling or other structural changes for PCB exposed to $scCO_2$. An explanation for this interesting behaviour may be a high degree of cross-linking for FR-4 and its stability to elevated temperatures before any deformation occurs, which is though to be beneficial for stability towards $scCO_2$[1].

Regarding the criterion of chemical recyclability, Au-collectors can be considered as ideal material for ink deposition due to chemically inertness and their excellent conductivity. Further, the possibility to electrochemically renew the collector/electrolyte interface is given when following a suited cleaning protocol, thus assuring repeatable experimental conditions. The discussion of a cleaning protocol is part of the next section.

#### 2.1.1.2 Difficulties encountered with electrode supports

Under certain circumstances, visual degradation of the PCB dielectric layer was observed, which presumably originated from repeated imposition to mechanical and chemical stress during cleaning, exposure to harsh organic solvents or even to superitical $CO_2$. Eventually, this caused some of the observed artefacts during the electrochemical characterization. Special care was therefore required to verify the functionality of electrodes and PCB, specifically with continuous use. Short, initial open circuit potential (OCP) measurements were found to be helpful and only in case of small potential drifts, i.e. relative potential stability, it was proceeded with the characterization.

### 2.1.2 Cleaning protocol for electrode supports

#### 2.1.2.1 Presentation of the initial cleaning protocol

To guarantee reproducible experimental conditions, a pretreatment the PCB underwent an initial cleaning step using acetone (Carlo Erba, France) and ethanol (96 °, Carlo Erba, France), prior to ink deposition. Care was taken not to scratch the collectors.

The addition of an electrochemical cleaning step was evaluated in the beginning of the project. Voltammetric cycling is a traditional method for electrode cleaning/activation and different protocols for Au-coated electrodes were studied in detail by Fischer et al. [99]. One particular treatment suggested electrode cycling in 0.05 M sulfuric acid in the voltage range from -400 to 1400 mV vs. Ag/AgCl at 100 mV/s until saturation of the reduction peak around 0.92 V occured. Similar approaches were proposed by Spegel et al. [100].

[1]With a reference back to the theory on polymer foaming, one of the requirements was a low $T_g$. However, as electronic components are typically designed to withstand up to 130 ℃, an elevated $T_g$ can be suspected.

In consequence, CVs in this project were acquired in 0.5 M sulfuric acid to reduce the number of cleaning cycles, potentially shortening the cleaning time. The potential range was maintained as in the references and the scan rate limited to 50 mV/s, in order to avoid surface restructuration [14]. The electrolyte was regularly deaerated by means of argon. The CVs of a selected collector are presented in Figure II.3 a). All potentials reported in the following are referenced against an Ag/AgCl reference electrode (3 M KCl).
The sets of CV are similar to what is typically reported for Au cycled in sulfuric acid [101] [102] [14]. In Figure II.3 a), the oxidation peak with an onset of around 1.25 V is well distinguishable. El Wakkad et al.[2] [103] associated it with the formation of $Au_2O_3$. The corresponding reduction peak occurs around 0.92 V with a weakly expressed shoulder that may indicate (111) indexation of the Au surface, as indicated by the results of Hamelin in Figure II.3 b).

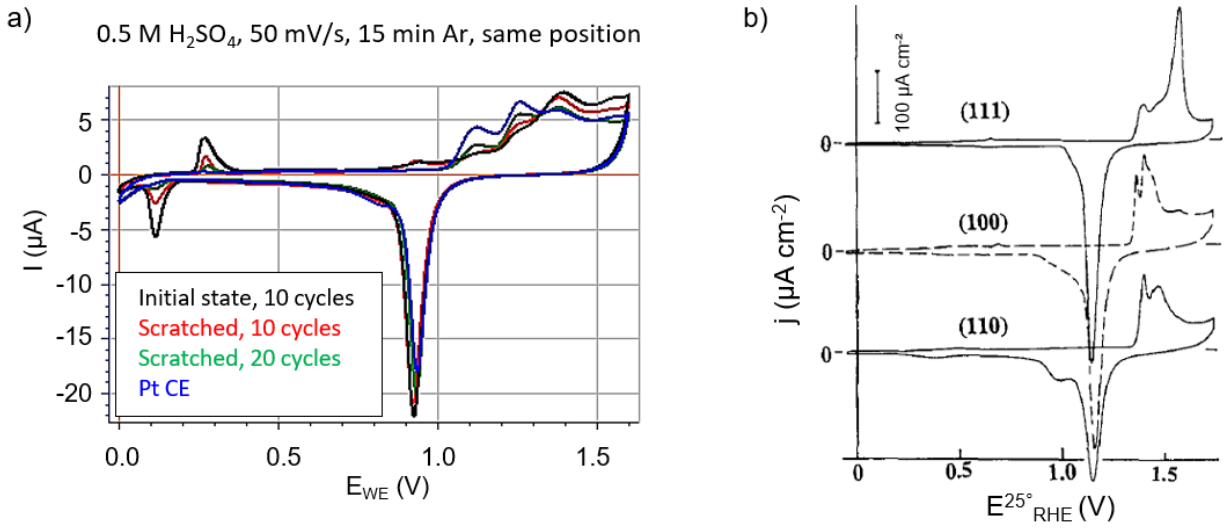


Figure II.3: Cyclic voltammograms of Au collectors in 0.5 M $H_2SO_4$ at 50 mV/s vs. Ag/AgCl, 23 ℃ with a carbon CE. a) The effects of extended cycling, a scratched surface and a platinum CE. b) CVs of differently indexed Au surfaces in 0.01 M $H_2SO_4$ at 50 mV/s and 25 ℃(vs. RHE) [14].

Pristine gold electrodes are typically of capacitive behaviour during the first 0.6 V of the anodic polarization [14] and double layer charging occurs. In this work, an exception is present in form of the redox system around 0.2 V equilibrium potential. Three possible hypotheses are discussed in the following:

1. The standard reduction potential of $Cu^{2+}$ to Cu is reportedly 0.34 V, translating to around 0.14 V vs. Ag/AgCl and therefore corresponding well to the recorded CV. However, after 10 cycles in Figure II.3 c) the collector was in anticipation of a Cu-related effect scratched and underlaying Cu/Ni was exposed. As the peaks lost prominence, contrary to the expectations, the influence on the CV can be excluded.

2. Upon cycling repeatedly it is observed that the peaks initially increase in height. However, as seen in Figure II.3 a), extended cycling almost resulted in their complete disappearance, potentially indicating some form of superficial contamination which was removed over time.

[2]The work studied the anodic oxidation of Au electrodes in 0.1 M sulfuric acid at low current densities

3. The liberation of oxygen during the cathodic decomposition of Au-$Au_2O_3$ was suggested by El Wakkad et al. [103], followed by the formation of different Au-oxide systems at lower anodic potentials, in particular Au-$Au_2O$ with an oxidation onset around 0.27 V vs. SCE [3]. Interestingly, this may account for the unusual tendency of CV in II.3 a), where the $Au_2O_3$ oxidation and reduction peaks are stabilizing, against initial expectations, towards lower peak currents, matching a decreasing quantity of the oxide. On the other hand, during the first 10 cycles, the low-potential redox system in question displays increasing peak heights towards a plateau, representing $Au_2O$ formation. Upon prolonged cycling of the collector in II.3 c), it may be possible to link the disappearing Au-$Au_2O$ system with the steady formation of oxides with higher equilibrium potential, such as AuO with an oxidation onset of 0.96 V and ultimately $Au_2O_3$ with an oxidation onset of 1.26 V [103].

#### 2.1.2.2 Simplification of the cleaning protocol

As the cycling in sulfuric acid was time-consuming, it was questioned whether the surface state of the Au-collectors had an effect on the electrochemical behaviour after ink deposition at all. Two collectors of a PCB were cleaned by acetone and ethanol and masked, while the exposed other two collectors were cycled in sulfuric acid as presented before. Then, commercially available carbon ink (specifications detailed later) was deposited by means of a manual screen-printing process and cured in a box oven (80 °C, 3 h).
Cyclic voltammetry (CV) was carried out in 0.5 M $H_2SO_4$ at a scan rate of 50 mV/s. Impedance spectra were recorded in the same solution with a frequency sweep from 100 kHz to 100 mHz (OCP, 10 mV potential amplitude).

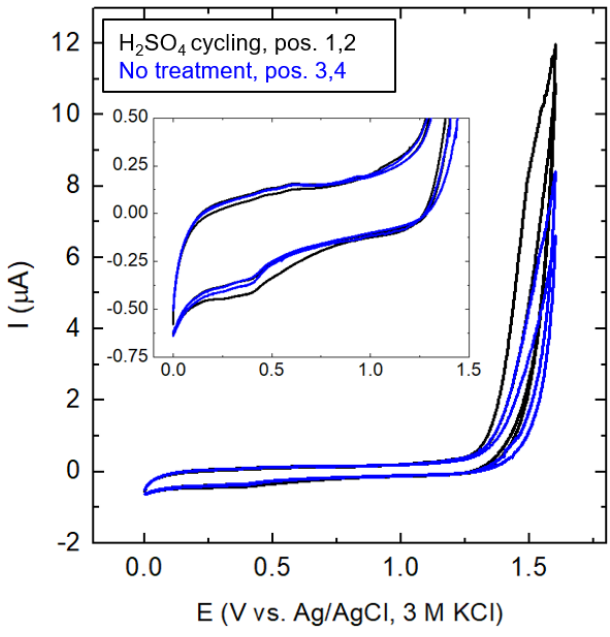


Figure II.4: Influence of cycling the Au collectors in sulfuric acid on the electrochemical behaviour for the purpose of cleaning: CV in 0.5 M $H_2SO_4$, $10^{th}$ cycles, 50 mV/s. Origin at 0 V.

[3] The voltage offset of a SCE is of around 200 mV vs. SHE and comparable to the Ag/AgCl RE with 3 M KCl filling used in this work. Furthermore, the sulfuric acid used by El Wakkad et al. was of 0.1 M (0.05 M) concentration, implying a small positive shift on the potential scale relative to the results in this work. Thus, potential values may be comparable.

The results are displayed in Figure II.4. Without going much into detail, the CV appear to be of mainly capacitive and pseudo-capacitive nature, as indicated by the deformed rectangular area enclosed by the curve[4].
The absence of any earlier identified Au-specific signatures confirms good surface coverage by the ink. Besides for a small difference regarding the onset of the oxygen evolution reaction, no difference is discernible for the collectors cycled in sulfuric acid prior to ink deposition. The CV of carbon ink electrodes are interpreted in detail in a later section.

An impedance study was performed in the same electrolyte, see Figure II.5 a), to confirm the interpretation.
The Nyquist plots (Figure II.5 a)) indicate low electrode impedance at high frequencies and a small series resistance. No charge transfer reaction was observed, which is mainly due to the absence of redox probes[5]. The electrode responses are of capacitive character with a steep slope that relates to the formation of the electrochemical double layer. While the equilibrium differential capacitance at low frequencies varies to some extent, no systematic difference is visible for the electrodes, which underwent cycling in sulfuric acid.

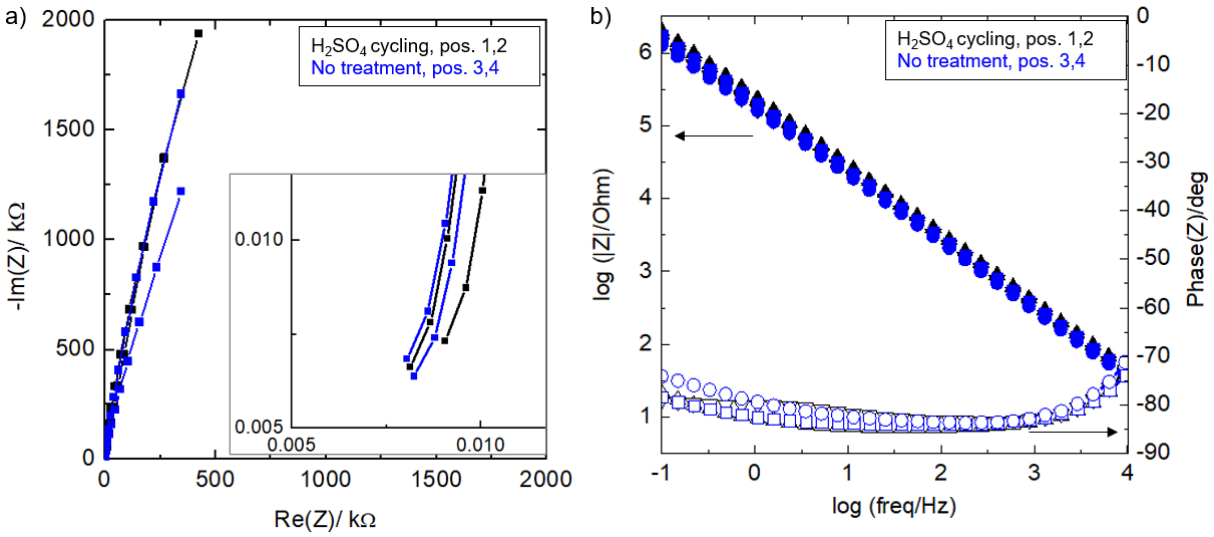


Figure II.5: Influence of cycling in 0.5 M $H_2SO_4$ for cleaning purpose on the electrochemical behaviour of Au collectors: a) Nyquist and b) Bode plots based on EIS carried out directly after the CV (100 kHz-100 mHz, 10 mV potential amplitude).

To better visualize the frequency dispersion of the electrode responses, the data is depicted in Bode plots in Figure II.5 b). The electrodes exhibit a relatively small impedance at high-frequencies, that is quickly increasing at lower frequencies. This can again be the result of the absence of any redox probe. The phase angle follows accordingly, displaying a near ideally capacitive character with a phase angle close to -90 ° over the observed frequency range. Again, no difference for collectors cycled in sulfuric acid is visible.
It was reasoned, that due to the good coverage of the collectors by carbon ink, the more basic and overall quicker cleaning step without cycling in sulfuric acid was sufficient.

[4]The pronounced current increase for potentials larger than 1.23 V is associated with the oxygen evolution reaction, i.e. the oxidation of the aqueous electrolyte.

[5]However, any charge transfer on an Au electrode would occur very rapidly and be potentially difficult to observe

### 2.1.3 Mask deposition

As presented in Figure II.6 a), deposits realized directly on the collectors spread out during the $scCO_2$ structuration, overpassing the collector area. For good electrochemical performance, however, the deposits should align with the underlying collectors. Therefore, further electrode preparation included mask deposition in order to contain the ink. The selection of the mask material was of empirical nature, i.e. several commercial electrically isolating tapes were tested upon foaming and delamination during exposure to supercritical $CO_2$[6].
3M™ polyimide film electrical tape[7] (n° 92, 3M, USA) was found to be the only product within the tested range suited for the application. Rectangular pieces of tape were cut and holes of 3 mm in diameter punched out, aligning with the collectors on the PCB. The as-obtained masks were applied on the PCB, exposing the collectors as seen in Figure II.6 b). Structured ink deposits realized with a mask were well-located and contained, see Figure II.9 c).

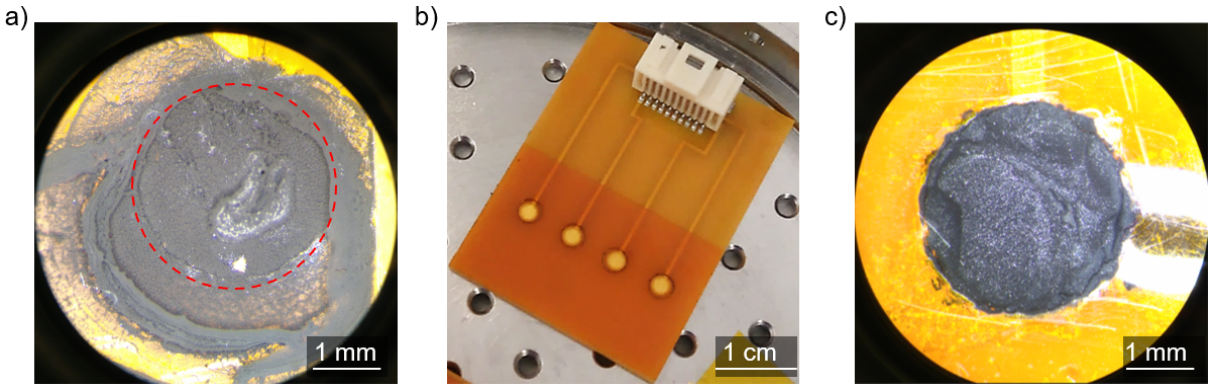


Figure II.6: a) Microscopy image of a structured ink deposit without mask. The diluted ink spread considerably beyond the collector area, indicated by the dashed red circle; b) A four collector platform with mask; c) an ink deposit contained by a mask.

### 2.1.4 Deposition of the DuPont BQ242 carbon ink

#### 2.1.4.1 Specifications of the carbon ink

A commercial, solvent-based, screen printable carbon ink (DuPont BQ242, Bristol, UK) was selected for the project. It is sold for the purpose of preparing working electrodes for amperometric sensors in biomedical devices. The supplier attributes excellent wetting and electrochemical activity to the ink and it has been used in the laboratory for different projects.
The ink is composed of 38-40 wt-% solids (150 °C), which is of further interest for determining the parameters of the structuration treatment in chapter III. Furthermore, the quantification of ink constituents is important for a potential continuation of the work, e.g. for an own ink formulation which is specifically adapted for the $scCO_2$-based structuration.

[6]These effects occur, as the polymer material and the layer of glue can equally be subject to interaction with the supercritical fluid (phase separation, swelling, foaming).
[7]The thickness of the tape was composed by 50 µm of polymer and 25 µm of adhesive.

#### 2.1.4.2 Deposition protocol

For the preparation of unstructured electrodes, serving as reference against which the structured ink electrodes were compared, a manual doctor-blade technique was used. Following the application of masks, small quantities of ink were deposited next to the collectors and spread by means of a doctor's blade, exerting light pressure. An inspection under the microscope was confirmed complete coverage of the collectors. Eventual excess ink was carefully removed, before transferring the PCB into a preheated oven.
While the ink is intended to be dried during 5-15 min in a box oven at 130 ℃, a different protocol was adopted to avoid crack formation. A temperature of 80 ℃was maintained during 3 h.

Based on the geometric values of mask and unmasked surface, the deposited ink volume per collector was calculated. As a certain pressure was applied during ink deposition, slight deformation of the masks was taken into consideration. The initial deposit thickness is estimated between at maximum 75 µm and at minimum 50 µm, when assuming that the adhesive layer is more compressible than the polymer and deforms first. In consequence, the initial volume per deposit fell into the range of 0.35 to 0.53 µL. This value is of further interest in the discussion of results.

For the preparation of structured electrodes, the conductive ink was found to be excessively viscous and a dilution was proposed. As a side effect, the diluted ink deposits could be manipulated for longer times until they started to dry, which allowed for an easier transfer to the supercritical fluid equipment. As diluent, ethylene glycol diacetate (EGDA, 99 %, Aldrich USA)[8] was added in ratios specified later.

[8]The chemical is indicated as cleaning solvent in the ink's technical data sheet.

## 2.2 Structuration protocol based on supercritical $CO_2$

### 2.2.1 The supercritical fluid equipment

The exposure of ink deposits to supercritical $CO_2$ took place in a commercial, supercritical fluid equipment (Separex R& D, FeyeCon Group, Champigneulles, France), which is separated into two main units. Unit one represents the pressurizable system, consisting in a connection point for $CO_2$ bottles, a pump and an initial heat exchanger, which is of importance for the later discussion of uncertainties. The second unit represents the operational interface, including the heatable pressure cell, accessible by means of a screw-on lid and a control unit. A simplified technical scheme is depicted in II.7 a), with a more detailed view on the pressure cell in b).
After ink deposition, the PCB were placed in the cell. The procedure of closing the cell generally lasted 5 min, before starting the protocol.

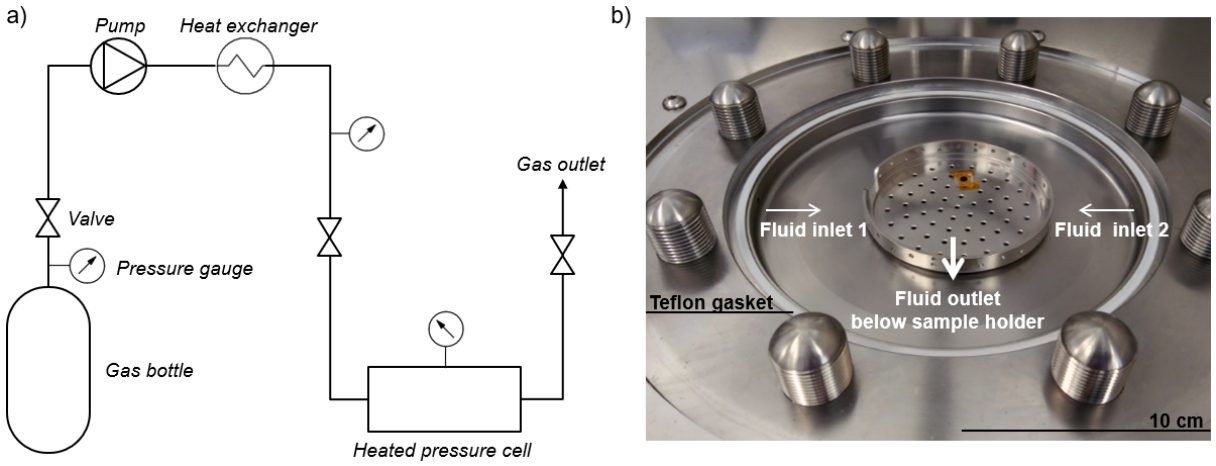


Figure II.7: The supercritical fluid equipment; a) a schematic technical drawing; b) a detailed view on the heatable pressure cell. Arrows indicate the location of inlets and the outlet of the $scCO_2$, the latter being hidden underneath the sample holder.

### 2.2.2 Detailed presentation of the structuration protocol and discussion of the parameters of interest

Based on the phase diagram of $CO_2$ and the thermodynamic principles presented in chapter I, a schematic process protocol can be drawn to emphasize the effect of changes in process parameters. Figure II.8 a) presents once more the path of the process through the phase diagram of $CO_2$, while in b), a more practical scheme shows the variation of parameters over time.

Starting at ambient conditions (1), the pressure is increased to 8 MPa (2) to enter the subcritical state of $CO_2$, where its liquid-like properties dominate. In particular the solvation capacity[9] is thought to remain high [104]. This may be of interest for the initial phase separation mechanism taking place, which is typically, but not exclusively of short duration. Particularly the deposit thickness may influence the duration until the ink deposit has entirely undergone phase separation. The duration of this step is consequently referred to as $t_{sep}$. A possible second mechanism could take place in parallel over a longer

[9]Supercritical carbon dioxide is an excellent non-polar solvent, however polar molecules can be dissolved to a low extent due to its quadrupole moment.

period of time, corresponding to a solvation/ replacement of non-polar ink constituents[10]. Subsequentially, by means of increasing the temperature to 40 ℃, the transition of compressed to supercritical $CO_2$ is initiated (3). It hs a more polyvalent character, with liquid-like properties being less prominent. Still, aforementioned processes may continue to take place. Additionally, gas-like properties of the $CO_2$ gain in importance. For supercritical fluids, a high level of diffusivity is reported, which may contribute accessing the bulk of the deposits. Following this thought, solvent extraction from the bulk of the ink deposit may be promoted. In parallel, saturation of the polymeric binder present in the ink may take place, comparable to a supercritical fluid-assisted polymer foaming, where a polymer is exposed to supercritical $CO_2$. During the saturation time, $t_{sat}$, conditions were maintained constant.
Finally, the cell is rapidly depressurized, leading to polymer foaming, i.e. pore generation and growth. Parallel to the release of $CO_2$ from the cell, any solvated components are equally evacuated following a solvent extraction process. The end of the process is reached upon returning to initial conditions (4).

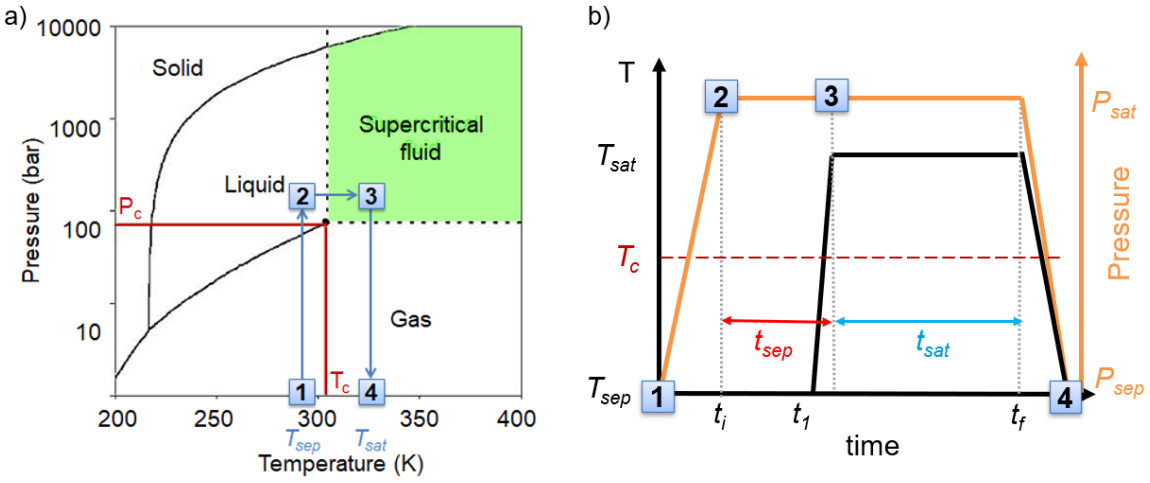


Figure II.8: a) The location of process temperature and pressure in the phase diagram of carbon dioxide and b) a schematic diagram of process temperature and pressure over time.

The parameters thought to be of relevance are listed in Table II.1, categorized into 'prior to' (asterisk) and 'during' structuration (no asterisk). It is pointed out, that only a fraction of the listed parameters was modified (see notion 'cst.'), either because the supercritical fluid equipment did not allow for a large range of modification or in order to limit the range of influencing factors.

Constant parameters include the transfer time between ink deposition to the moment, when exposure to supercritical $CO_2$ occured, i.e. the start of the treatment. Throughout the project, this time was kept short. Heating and cooling rates were imposed by the supercritical fluid equipment. Furthermore, pressurization and depressurization rates, as well as the initial temperature $T_{sep}$ and the maximum $CO_2$ pressure during the treatment. While pressure was in the past confirmed to influence the structure generation, technical limitations were imposed by the supercitical fluid equipment (12 MPa max.). Previously published works on polymer foaming suggest, however, that 20 to 25 MPa are required

[10]The mechanism is possibly less pronounced at lower process temperature, a hypothesis that requires verification.

for a structural modification of several commonly used polymers. A short theoretical discussion of the parameter process pressure follows later.

Due to the initial uncertainty as to when the mechanism had its onset and its ending point, the increase of temperature from (2) to (3) played an important role. The ratio of times at which different processes were thought to take place was manipulated with the intention to study the effect and to find a conclusion on what mechanism dominated at which point. In particular, studied parameters were the ratio between $t_{sep}$ and $t_{sat}$ at constant overall treatment time and the parameter $t_{sep}$ at constant $t_{sat}$. Furthermore, the influence of saturation temperature and the degree of ink dilution were investigated.

Table II.1: Process parameters during the structuration process with respective values. Non-modified parameters are followed by the notion 'cst.'.

| **Parameter** | **Description** | **Experimental range** |
|---|---|---|
| BQ:EGDA | *Ink dilution | 1:0-1:10 (w/w) |
| $t_{transfer}$ | *Time between ink deposition and process start | 5 ± 2 min (cst.) |
| $P_{sep}$ | Pressure during the physical phase separation | 8 ± 0.5 MPa (cst.) |
| $\Delta P_{sep}$ | Pressurization rate | 2 MPa/min (cst.) |
| $t_{sep}$ | Duration of the phase separation | 0-30 min |
| $T_{sep}$ | Temperature during the phase separation | 23 ± 3 ℃ (cst.) |
| $P_{sat}$ | Pressure during the polymer saturation step | 8 ± 0.5 MPa (cst.) |
| $t_{sat}$ | Duration of the saturation step | 0-30 min |
| $T_{sat}$ | Temperature during the saturation step | 40/60 ℃ |
| $\Delta t_{sat}$ | Heating rate | 4 ℃/min (cst.) |
| $\Delta P_{depres.}$ | Depressurization rate | 2 MPa/min (cst.) |

* Asterisks indicate parameters not accessed via the supercritical fluid equipment.

## 2.3 The physical characterization protocol

### 2.3.1 Optical microscopy

For initial attempts, the effect of the structuration protocol was loosely evaluated by means of optical microscopy, until a satisfactory process protocol had been identified, which allowed to advance to more detailed characterization techniques. A dried, unstructured electrode is compared to a structured electrode in Figure II.9. The successful surface-related structuration is indicated by the different reflection of light. The matte appearance in Figure II.9 c) indicates the presence of small pore-like features. The generation of volume by means of the treatment was even visible by direct visual comparison of the electrodes side-by-side.
Figure II.9 b) serves as example for early structuration attempts which confirmed the interest in improving the protocol. Based on a visual impression, a certain degree of structure is developed, however the deposits were frequently of inhomogeneous appearance and prone to delaminate. The following problems and solutions were encountered:

- The uncontrolled spreading of ink, surpassing the boundaries of the mask, was solved by reducing the volume deposited per collector/ cavity.
- The partial delamination, respectively flaking, of the structured electrodes could be encountered by lowering the ratio of ink to EGDA.
- The initially poor adhesion of structured ink deposits to the collectors was improved by spreading a minuscule quantity of undiluted BQ242 ink on the collectors, immediately followed by deposition of the diluted ink.

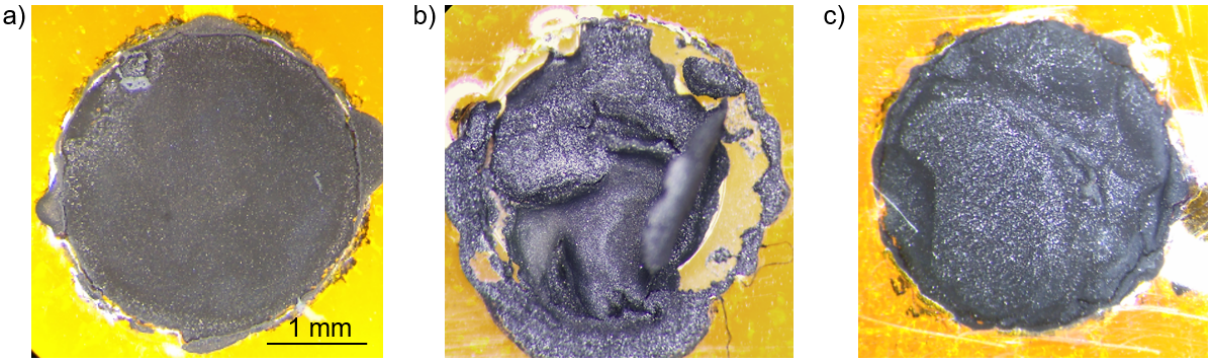


Figure II.9: Microscopy images of a) an unstructured, dried ink deposit (3 h at 80 ℃), b) a deposit structured under non-optimal conditions and c) a structured ink deposit obtained after optimising the protocol.

Equivalent microscopy images were evaluated during the project in order to estimate the geometric surface coverage of electrodes for the purpose of normalizing results.

### 2.3.2 Digital microscopy, porosity and volume change

#### 2.3.2.1 Sample preparation and measurement protocol

In a further step, the surface of structured electrodes was studied at higher magnification by means of a digital microscope capable of high magnification and high resolution image capture (VHX-7000, Keyence, USA). The inclinable sample stage allowed to image the deposits from the side and at an angle of 45 ° in order to benefit from the included

software measuring tools. In particular, the height of the ink deposits could be evaluated. Furthermore, a series of images could be realized while scanning the z-axis, allowing for an acquisition of images with different focal points, which were afterwards reconstructed to a 3D-model by the software. This allowed for a volume estimation and an idea of the total deposit porosity.

The sample preparation and measurement protocol is schematically presented in Figure II.10, including a colour scheme on how which information was derived. The utility of the four-electrode PCB was considered limited due to spatial restrictions on the microscope, hence structured ink deposits were prepared on fractures of microscope glass slides.
In order to study the effect of ink volume on the generation of structure, two electrodes were prepared per slide for each variation of process parameters. Further, two ink volumes were deposited for each set of parameters (1.0 and 1.5 µL), to confirm reproducibility of results and to highlight the creation of porosity. A larger volume of ink was thought to result in a larger pore volume, which is more distinctive. Double layered masks were used to contain the larger ink volumes. For the preparation of electrodes for electrochemical characterization, 1.3 µL of ink were deposited.

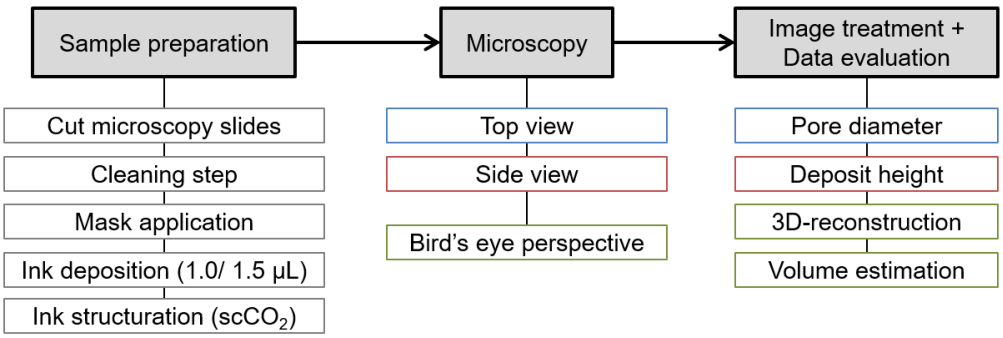


Figure II.10: Sample preparation and imaging protocol for structured ink deposits, prepared for digital microscopy. The color code indicates which type of information was gathered from which type of images.

## 2.3.3 Scanning electron microscopy, pore size and porosity

### 2.3.3.1 Realization of SEM images

In a further complementary technique, the structural changes were evaluated by means of scanning electron microscopy (SEM) (S-4100 field emission SEM, Hitachi, Japan). Samples were prepared analogous as for digital microscopy, but on conductive supports. Pieces of Au-sputtered silicon wafer were equipped with conductive carbon tape for increased mechanical adhesion and improved electrical contact. Polyimide masks were added as before to, contain the ink, see Figure II.11. The ink deposits were structured following the same protocol as earlier. Prior to imaging, the samples were transferred to an oven for several hours at 80 ℃ in order to remove residual solvent, respectively adsorbed moisture in case of older samples.
The SEM images were realized with an extraction voltage ($V_{extr}$) of 5.9 kV and an acceleration voltage ($V_{acc}$) of 30 kV. The working distance was around 8 mm.

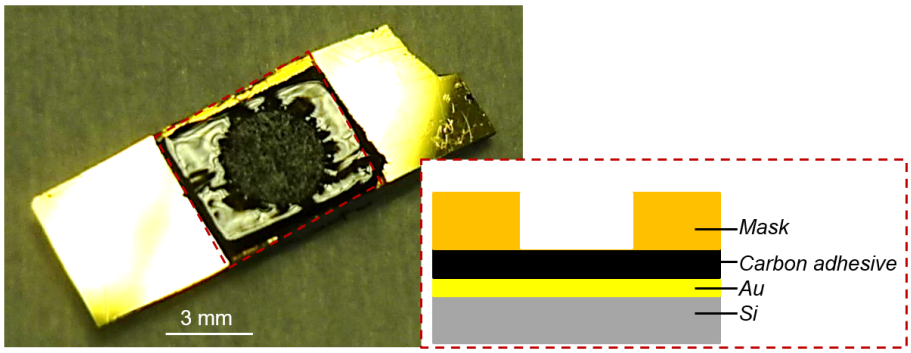


Figure II.11: Exemplary scanning electron microscope (SEM) sample on a support assembled as indicated in the cross-section.

In the following, exemplary SEM images of dried (undiluted and diluted) and structured ink deposits (undiluted and diluted) realized early in the project are compared at two different factors of magnification (Figure II.12). Based on series a) and b) it is concluded, that undiluted ink appears similar regardless of the applied process. On the macroscopic scale, the surface presents itself rather flat and even more so for the structured deposits. Some raised spots may indicate graphite flakes, which are typically between 10 to 40 µm in diameter. The high-resolution images seem to confirm this impression of absent pores, although it is interesting to observe the formation of a particular surface roughness for dried deposits.
Diluted, dried or structured ink deposits are compared in series c) and d). Drying the diluted ink resulted in the formation of a seemingly dense and unstructured deposit. Some roughly spherical surface features are discernible, potentially corresponding to the inks' carbon black particles instead of a structure developed during the treatment. It is thought, that dilution eventually induced a sedimentation of ink constituents during complete evaporation of EGDA.
Structuration of diluted ink, on the other hand, lead to an interesting observation. The deposit's surface is of inhomogeneous nature, with certain areas varying in "flatness". Some cracks are present. Upon their closer inspection, a structure consisting in connected pores/channels underneath the top layer was revealed. This small comparison confirmed the interest of diluting ink prior to structuration early on.

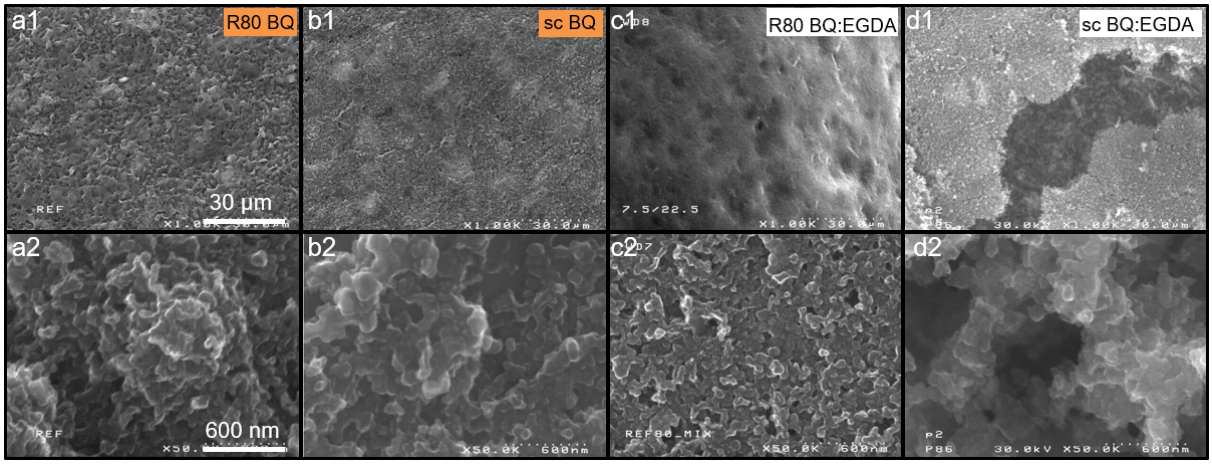


Figure II.12: SEM images of a) and c) dried, undiluted ink. In b) and d), ink was diluted and structured (ratio ink: EGDA = 1:10 w/w).

#### 2.3.3.2 SEM image treatment and data extraction

In order to extract further quantitative information from the SEM images, a treatment step based on the freeware "ImageJ" was applied. SEM images were transformed into monochrome by adjusting the three parameters "contrast", "threshold" and "blurr", such that the dark areas in the images corresponded to the porous parts of the deposits (by the software treated as particles). By means of the included particle analyser tool, the average pore size and total porosity of the surface were then estimated.
The differentiation between porous and non-porous sections, as well as the consideration of "a good fit" were carried out as objectively as possible, but remain open for discussion. Mainly due to this scientific limitation of the technique, a small series of image parameter studies was carried out. The intention was to verify, that reproducible and comparable data was extracted and to find optimum parameter settings for the supercritical $CO_2$ treatment. Figure II.13 displays the protocol.

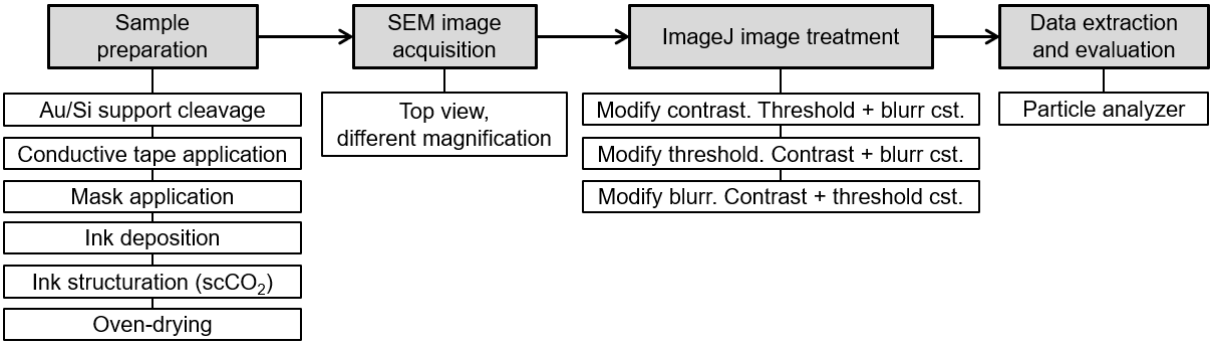


Figure II.13: SEM sample preparation and image treatment protocol.

The quantitative results, see the Table IV.5 in appendix section A.3, demonstrate no effect for the contrast values, which were tested, on the porosity-related information. Thus, the parameter remained constant. Image threshold and blurr appear to have an important effect, however due to the strong visual change of the images upon modifying the blurr, only a small operational range around 0.8 was identified. The application of an image threshold value between 78 and 76 was considered to yield the best representation of the dark areas considered as pores, so that the value 77 was used from there on.

## 2.3.4 Nitrogen adsorption for porosity estimation

#### 2.3.4.1 Sample preparation and experimental protocol

Another physical approach to obtain porosity-related data and specific surface area (SSA) consisted in nitrogen adsorption-desorption experiments[11] (ASAP™ 2420, Micromeritics Instrument Corp., USA). Diluted carbon ink was exposed to $scCO_2$ (80 bar, $t_{sep}$=20 min, $T_{sep}$=20 ℃, $t_{sat}$=30 min, $T_{sat}$=40 ℃) and characterized. The sample preparation is found in the appendix section A.2.

[11]Credits are given to Dr. Florence Ricoul under whose supervision and guidance the experiments were performed and further to Séverine Vignoud for her expertise in discussing the results.

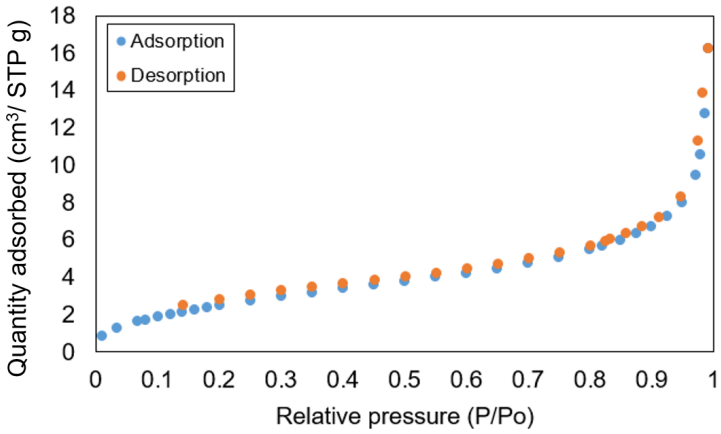


Figure II.14: Nitrogen adsorption-desorption isotherm (77 K) of structured carbon ink (80 bar, $t_{sep}$=20 min, $T_{sep}$=20 ℃, $t_{sat}$=30 min, $T_{sat}$=40 ℃).

After transferring the sample material into the corresponding glass vessel of the equipment, the degassing step was initiated (heating to 130 ℃ at 5 ℃ /min, then holding for 24 h), during which residual moisture was evacuated which could otherwise interfere with the measurement. The adsorption-desorption 77 K isotherm was started afterwards, yielding the curve seen in Figure II.14.

### 2.3.4.2 Data evaluation

The plot displays mainly characteristics of a type II isotherm according to IUPAC classification [105]. The adsorption isotherm shows a concave onset with respect to relative pressure. The following region of steady slope indicates the formation of an adsorbate monolayer, which appears complete at around 0.4 to 0.5 relative pressure, based on the start of the linear section. The continuously rising slope at higher relative pressure is a sign of (potentially partial) multilayer coverage. Based on these observations, the reversible type II isotherm indicates unrestricted monolayer-multilayer adsorption, which is commonly observed for non-porous or macroporous adsorbents (pores size larger than 50 nm).
Taking a second look, a slight degree of type IV [105] isotherm characteristic is potentially discernible, corresponding to some degree of mesoporosity (pore size between 2-50 nm). A very small, steep hysteresis loop is indicated when reaching 1 partial pressure. Practically speaking this would correspond to a monolayer formation, followed by multilayer adsorption and a small degree of capillary condensation in the smaller pores which causes the hysteresis. The location of the hysteresis loop at high partial pressure may be a sign of rather large mesopores. Its steepness ($H_1$ type hysteresis) could be conclusive for uniformly sized, well-connected pores.

Table II.2: Results of the nitrogen adsorption-desorption isotherms of a structured carbon ink.

| Parameter | Value |
|---|---|
| C | 26 |
| $SSA_{BET}$ | (10.18 ±0.05) $m^2$/g |
| $SSA_{Langmuir}$ | 15.30 $m^2$/g |
| $V_{pores,ads.,BJH}$ | 0.025 $m^3$/g |
| $D_{pores,ads.,BJH}$ | (10.4 ±10.6) $nm$ |
| $V_{pores,des.,BJH}$ | 0.024 $m^3$/g |

Quantitative results are summarized in Table II.2. The parameter C serves as qualitative indicator of the isotherm and is thought to allow identification of the end of monolayer formation if larger than 20, which is the case [105]. The SSA calculated via the BET theorem is around 10.2 $m^2/g$ and varies from the Langmuir SSA as expected[12].
The pore size D calculated by the software using the BJH method is 10.4 nm ($V_{ad}$) and 10.6 nm ($V_{des}$) during adsorption and desorption, respectively. The total pore volume calculated for the adsorption and desorption step is 0.025 and 0.024 $cm^3/g$, respectively, indicating a small amount of irreversible adsorption/chemisorption.

A selection of reference SSA of carbon blacks and carbon paste type electrodes are listed in Table II.3. Rezqita et al. compared the SSA of conductive graphite and Super C65 carbon black with values of 16.53 $m^2/g$ and 62.06 $m^2/g$, respectively, displaying an important difference in intrinsic porosity (0.88 nm vs. 2.74 nm) [106]. A higher value for a different type of carbon black was measured by Jiang et al. at 221.6 $m^2/g$ [107]. These findings indicate the range of SSA, which is to be expected for carbon precursor materials that are commonly incorporated in conductive inks.
In the same study, it was remarked that the preparation of a paste (mixing the carbon black with another component in a solvent, followed by deposition and drying) resulted in a 3-fold reduction of the SSA. The study underlines, that the use of high-SSA carbon precursors does not necessarily allow to prepare high-SSA ink-based electrodes. Specifically, particle agglomeration and the obstruction of the carbon particles' intrinsic porosity with other ink constituents are encountered.
Further values for unstructured carbon paste SSA are reported e.g. by Xu et al. [53] who compared a carbon paste material (graphite powder and mineral oil in a ratio 80/20 (w/w) against a similar paste containing calcium carbonate microspheres, which were dissolved out of the dried electrode, resulting in a porous structure. The unstructured carbon paste yielded a SSA of 8.52 $m^2/g$. Structured carbon electrodes attained 59.26 $m^2/g$.

Table II.3: Specific surface area and porosity data regarding porous carbon and carbon paste electrodes in comparison with this work.

| **Material** | **SSA ($m^2/g$)** | **Pore size (nm)** | **Reference** |
|---|---|---|---|
| Carbon paste electrode | 8.52 | | Xu et al. [53] |
| Porous carbon paste electrode | 59.26 | 2000-5000 | |
| Conductive graphite (MTI) | 16.53 | 0.88* | Rezqita et al. [106] |
| Super C65 carbon black (MTI) | 62.06 | 2.74* | |
| XC72R carbon black (Cabot) | 221.60 | - | Jiang et al. [107] |
| XC72R/hemin, 50/50 (w/w) | 74.80 | - | |
| Mersen RVC 2000 carbon felt | 0.70 | macrop. | [108] |
| Structured carbon ink via $scCO_2$ | 10.18 | 10.44* | This work |

*Pore sizes were calculated by means of the BJH method.

It is surprising, that the structured ink electrodes prepared in this work do not attain higher values, compared to unstructured carbon paste electrodes in literature. One hypothesis is the potentially unsuited technique of sample removal from the support in Figure IV.16 a) in the appendix section A.2. As the deposits were very fragile, the developed porosity was potentially destroyed and no longer accessible.

[12]The Langmuir model only assumes a monolayer formation and therefore overestimates the surface of the adsorbent.

## 2.4 The electrochemical characterization protocol

The schematic experimental protocol for characterization of the structured ink electrodes is displayed in Figure II.15. The particular methods are detailed in the following.

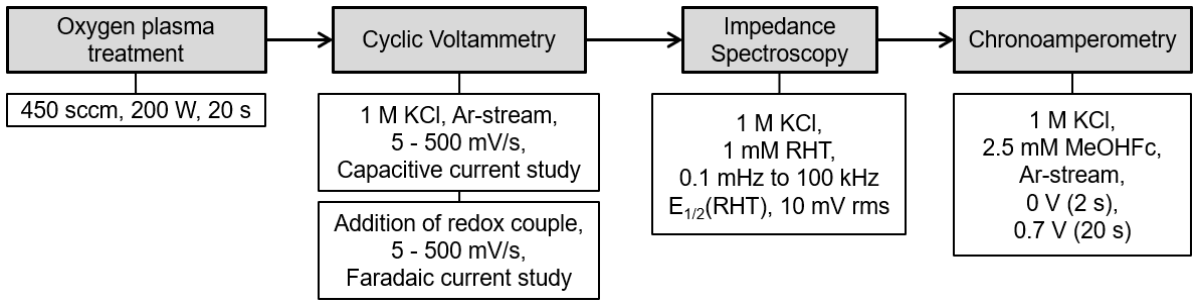


Figure II.15: General schematic protocol of the successive electrochemical measurements carried out to characterize structured carbon ink electrodes. RHT is short for ruthenium hexaamine trichloride.

### 2.4.1 Sample preparation and cell setup

#### 2.4.1.1 Oxygen plasma treatment

Whereas oven-dried, unstructured electrodes allowed for electrochemical measurements directly after preparation, a complete encapsulation by an air layer was observed when immersing structured electrodes into the aqueous electrolyte. This phenomenon is indicated by the reflected light in Figure II.16. The electrodes were considered highly hydrophobic, either due to surface tension of the electrolyte in combination with a small-scale surface structure or due to the change in surface chemistry induced by the treatment with supercritical $CO_2$.

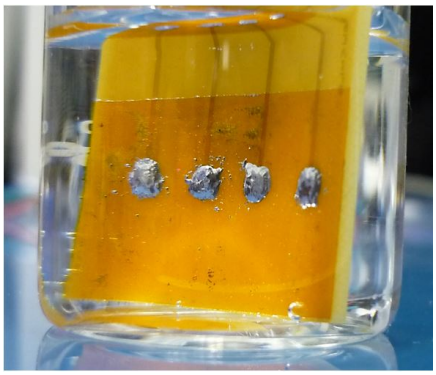

Figure II.16: Formation of an air layer around the structured ink electrodes in aqueous electrolyte, indicating a hydrophobic behaviour.

In order to increase surface hydrophilicity, electrodes were subjected to an oxygen plasma treatment directly after structuration. Due to technical reasons, two different equipments were used initially, namely an oxygen plasma generator (MDS 150, Plassys, France) and a molecular vapor deposition system (MVD 100, Applied Micro Structures, USA). The respective parameters are listed in Table II.4 and vary, as the adjustable ranges were different. Further, while the Plassys MDS operated under static conditions

and higher plasma power, the AMS MDV 100 made use of a plasma-flow and operated at lower power. However, the Plassys MDS was used exclusively during initial parts of the project.

Table II.4: Parameters during the oxygen plasma treatment.

| **Equipment** | **Power (W)** | **Oxygen pressure/ flow** | **Time (s)** |
|---|---|---|---|
| AMS MVD 100 | 200 | 450 sccm | 20 |
| Plassys MDS 150 | 600 | 130 mTorr | 100 |

Contrary to initial observations, the plasma exposure time was limited to 20 s during the project. This choice was supported by works of Garate et al. who employed a water-based ink containing CNT [109] for the preparation of amperometric sensors. The investigation of the duration of an oxygen-plasma exposure was part of the study (1 mbar pressure, other parameters not defined). Based on electrochemical results and SEM images it was reasoned, that oxygen plasma caused oxidation and subsequent partial removal of the polymeric binder present on the surface of CNT. This process lead to a better electrochemical accessibility of the CNT and reduced resistivity. Electrochemical behaviour, e.g. peak potential separation and peak current (studied using the redox couple $Fe(CN)_6^{3-/4-}$), remained mainly unaffected for short plasma exposure. However, a detrimental, damaging effect of prolonged plasma exposure was suggested. An optimum treatment time of 20 s was seen as a compromise between increased density of carboxylic surface groups and reduced electrochemical behaviour.
To verify the observations made in literature, the effect of different plasma exposure times up to 30 s was studied in this work and evaluated by means of contact angle measurements, see appendix section IV. Longer plasma exposure times seemed to improve wetting. However, aligning with literature, 20 s were set for the rest of the project, as the achievable wetting was considered sufficient[13].
It was not specifically studied, how long the structured electrodes could be characterized after the plasma-treatment. Electrodes, which were stored for 2 weeks in a dry atmosphere, rehydrated within several minutes.

#### 2.4.1.2 Realization of the electrochemical cell

The PCB were connected to the potentiostats (VMP-300 multichannel and SP-200 singlechannel, BioLogic, Seyssinet-Pariset, France) by means of a selfmade, soldered cable, prepared by using connectors, wiring, and heat-shrink tubing (RS Components, France). The cable was kept at rather short length for reduction of ohmic losses and was renewed several times during the project when the signal quality seemed to deteriorate.
In most of the experiments, each electrode was measured separately due to the requirement of using four channels of the potentiostat.

To complete the three-electrode setups, a hammered platinum (Pt)-wire served as counterelectrode (CE, A = 1 $cm^2$), with the exception of measuring the response of four electrodes at once. To provide a sufficient current, a CE of large surface was prepared by spreading and drying BQ242 carbon ink on a flexible polymer support, that was cut into shape (A = 4 $cm^2$) and inserted into the cell. In all cases, the electrical connection to the CE was established by means of an alligator clip. The reference electrode (RE) was a double junction Ag/AgCl electrode filled with 3 M KCl (DJ Ag/AgCl, Metrohm, Switzerland), to which all further potentials in this work will be referenced except when specified

[13]At a later point it is discussed, how far the plasma may have penetrated the structured electrodes.

otherwise.
A 50 mL glass vessel (6.1415.110, Metrohm, Netherlands) was used throughout the majority of EC experiments. In order to guarantee reproducible and comparable placements of the electrodes, a poly(methyl methacrylate) (PMMA) insert was designed. Based on own previous studies with differently designed inserts, several electrode placements were compared for signal stability in potentiometric measurements. The configuration demonstrated in II.17 a) was selected for all measurements presented in chapter III. For chronoamperometric measurements in chapter IV, the design was slightly modified as depicted in Figure II.17 b), since the noise level appeared to be reduced for closer distance between the CE and the structured working electrodes (WE). Figure II.17 c) shows the placement of the large-surface carbon ink CE.

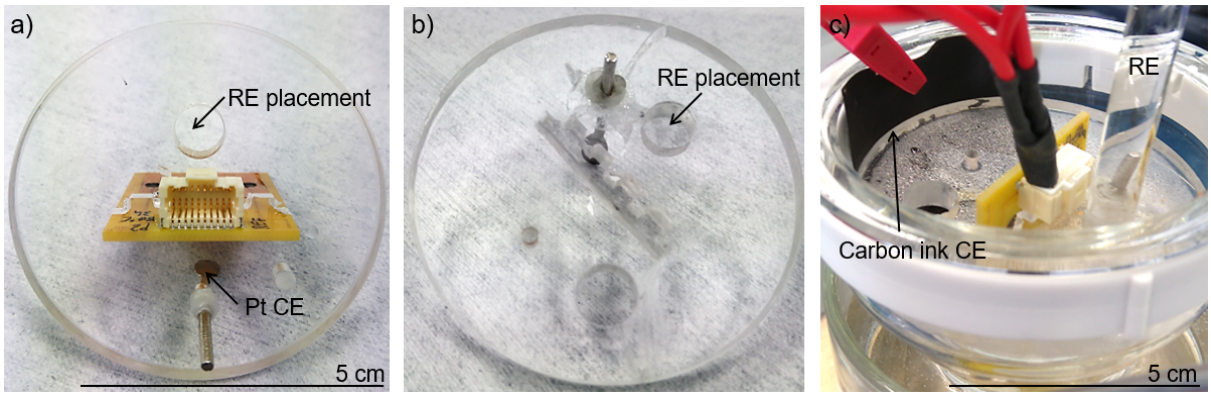


Figure II.17: Custom-made PMMA insert to assure a fixed placement of the electrodes in different configurations a) as used for characterizations in chapter III; b) as used for the single-electrode amperometric sensor characterizations in chapter IV; c) as used for the characterization of four electrodes simultaneously in chapter IV.

#### 2.4.1.3 Influence of the plasma treatment on the electrochemical response

While hydrophilicity was established successfully, an important aspect was to separate the effect of structuration from the effect of the plasma treatment. In particular, the introduction of carboxylic surface groups was thought to alter the electrochemical behaviour. Therefore, two equivalent PCB were prepared, as presented before, and dried. Then, one PCB was exposed to oxygen plasma (450 sccm, 200 W, 20 s). For characterization, electrodes were cycled in 1 M KCl at different scan rates, see Figure II.18, where series a) and c) refer to unmodified electrodes and series b) and d) refer to plasma-treated electrodes on the second PCB.
Without explaining the CV in detail at this point, the current response of electrodes at slow scan rates seems to be very similar, when neglecting minor general deviations between different PCB. Position 4 in Figure II.18 a1) presents an exception; incomplete ink coverage or contamination is suspected. For faster scan rates, the non-plasma-treated electrodes appear rather conductive. Plasma-treated electrodes, on the other hand, seem particularly capacitive or pseudo-capacitive. This is indicated by the gradual current onset in both scan directions, leading to plateau-like regions.
In conclusion, the qualitative comparison of CV suggests an increased capacitive or pseudo-capacitive nature of unstructured, plasma-treated electrodes. It is assumed, that structured electrodes behave likewise.

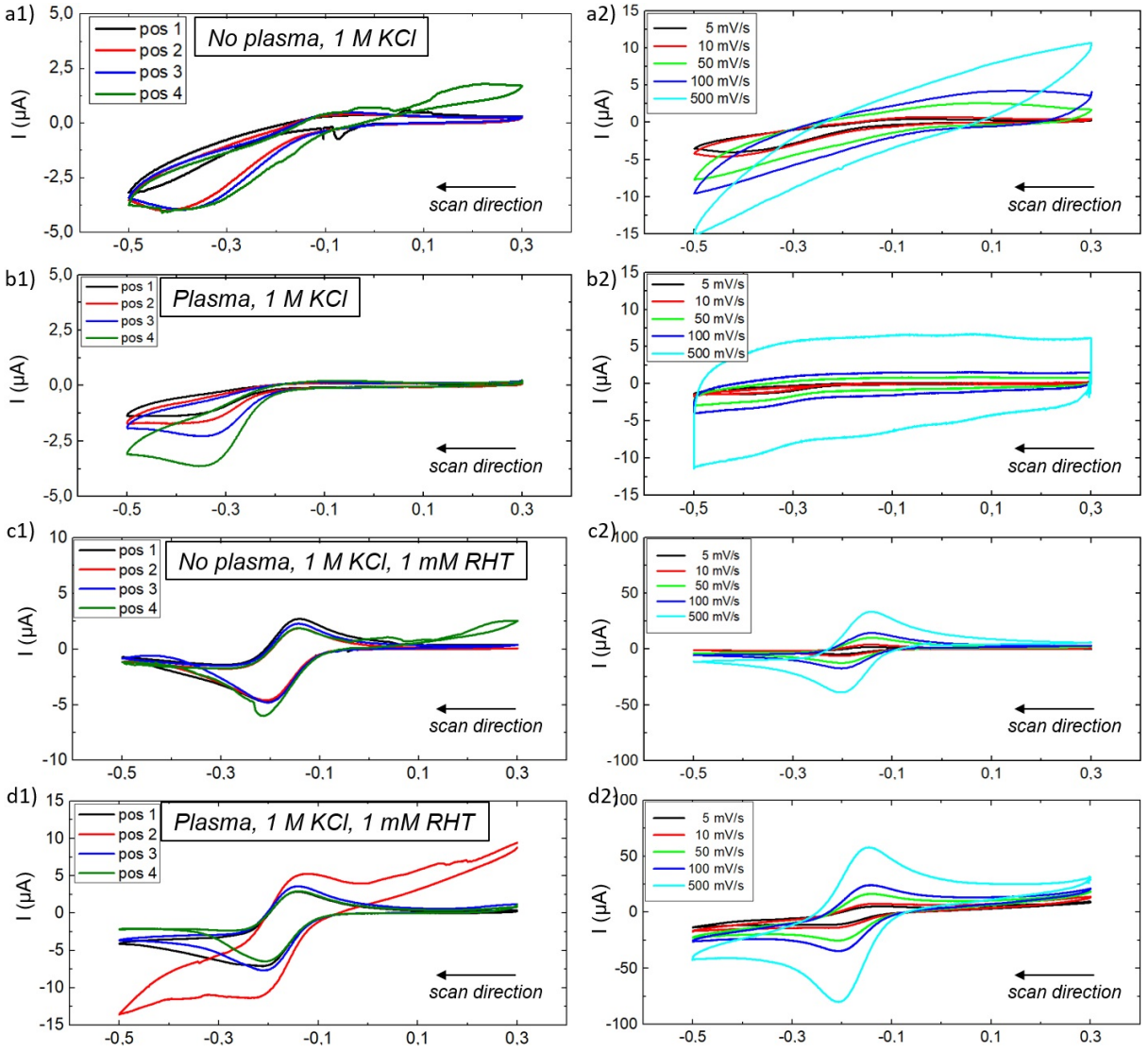


Figure II.18: Undiluted, dried electrodes in a) and c) without plasma treatment, in b) and d) after plasma treatment (450 sccm, 200 W, 20 s). In a1) and b1) at 5 mV/s in 1 M KCl; in c1) and d1) at 5 mV/s with 1 mM ruthenium hexaamine addition, background subtracted. In series 2) one of four positions is depicted for various scan rates, background subtracted. Origin at 0.3 V.

In a second step, the Faradaic responses of the same two sets of electrodes were measured in 1 M KCl and 1 mM ruthenium hexaamine, see Figure II.18 c) without plasma and d) after a plasma treatment. The background (in 1 M KCl) was subtracted in both cases for an easier interpretation. At small scan rates, the Faradaic response appears mainly unchanged, apart from an anomaly of position 2 in Figure II.18 d1). In comparison, for fast scan rates, the plasma-treated electrodes display currents, which have approximately doubled. The peak-to-peak separation of around 60 mV over all scan rates seems unchanged for plasma-treated electrodes. The results suggest a higher availability of electroactive sites due to the plasma treatment, but no kinetic limitation. The ratio of oxidation to reduction peaks is approximately one, suggesting a reversible or quasi-reversible charge-transfer.
In conclusion, this small investigation proposes to apply a plasma treatment to all electrodes, unstructured and structured, for a representative comparison of results.

## 2.4.2 Capacitive current studies

### 2.4.2.1 Experimental approach

Potassium chloride (KCl, $\geqslant$ 99 %, Sigma-Aldrich, Spain) was prepared as 1 M stock solution. Phosphate buffered saline solution (PBS) was purchased at 10x concentration (PBS 10x, Sigma, cell culture suited). Both solutions were used as base electrolytes for capacitive current studies after deaeration by an argon flow (15 min). A typical set of measurements consisted of cyclic voltammetry (CV) at scan rates of 5, 10, 50, 100 and 500 mV/s in a voltage range chosen depending on the equilibrium potential of the redox couple added afterwards.

### 2.4.2.2 Data evaluation

After the current response resulted in a stabilized curve, CV of the $5^{th}$ cycle were evaluated. The data was normalized to the geometric surface area of each electrode, resulting in $I_{norm}$ vs. E curves. Then, the normalized capacitance of the electrochemical double layer $C_{dl,norm}$ was calculated according to equation II.1, where $I_{capa,norm}$ is the normalized, capacitive current, read out at a potential of 0 V vs. RE and $\nu_{scan}$ is the scan rate. Care was taken to avoid regions of Faradaic side-reactions.

$$C_{dl,norm} = \frac{\Delta I_{capa,norm}}{2\nu_{scan}} \tag{II.1}$$

The electrochemically accessible surface area of the electrode was then estimated by dividing $C_{dl,norm}$ by the areal capacitance $C_{areal}$, obtained from reference works on carbon-based materials (see equation II.2)[14]. In a simplified approach, reference values for $C_{areal}$ were obtained from publications, in which the capacitance of unstructured electrodes made of comparable carbon materials and with a defined surface area is reported (see section III).

$$A_{dl,norm} = \frac{C_{dl,norm}}{C_{areal}} \tag{II.2}$$

## 2.4.3 Faradaic current studies

After adding a certain concentration of a redox couple to the base electrolyte, the CV protocol was repeated. Ruthenium hexaamine is involved in "outer sphere" charge transfer, meaning only physisorption occurs and the electrons are tunneling to the electrode surface. The advantage of this couple lies in an independence from the surface chemistry. Instead, it should primarily allow to monitor the development of surface area under the hypothesis, that mass transfer, i.e. diffusion is not a limiting factor.
Three different redox couples were used for studying the Faradaic current. A 10 mM ruthenium hexaamine trichloride (RHT, 98 %, Sigma-Aldrich, USA) solution was prepared and stored at 4 °C. For carrying out experiments, a suited volume was extracted for a dilution to 1 mM in 1 M KCl.

[14]The areal capacitance of a given material, measured in $F/m^2$, refers to the electric capacitance per unit surface area and deserves special attention due to the recent advances in electrochemistry on porous materials, where the exact estimation of the available physical surface is difficult [110]

### 2.4.3.1 Python script for CV data evaluation

Generally, potentiostats come with their own analytical software tools to evaluate the measured data. For example, peak evaluation can be carried out on a set of CV, yielding peak position, peak current and further details. It was found, however, that the software did not work as intended on subtracted data sets (the capacitive current CV were subtracted from the faradaic current CV for a better study of charge transfer processes).
For an equivalent evaluation of measurement data, a python script was written, yielding peak position, peak current and peak charge based on an adjustable baseline.
The peak position was determined by searching for the maximum/ minimum current values recorded during the CV and indicating the corresponding potential values. Afterwards, the baselines for the anodic and cathodic sweep were adjusted by selecting a suited, linear potential range which was extrapolated. The peak currents were calculated from the difference between the maximum/ minimum recorded current and the corresponding current from the baseline. The oxidation/ reduction peaks were modelled by fitting polynomials of degree 15 to the experimental data, which was essential to integrate the peak charge by means of the trapezoidal method, followed by a division by the scan rate.
A graphical representation of the subtracted CV, anodic/cathodic trend lines and modelled peaks was included in the script, which is provided in the appendix section A.4. An exemplary CV of a structured ink electrode, cycled in 1 mM ruthenium hexaamine, 1 M KCl base electrolyte, is shown in Figure II.19.

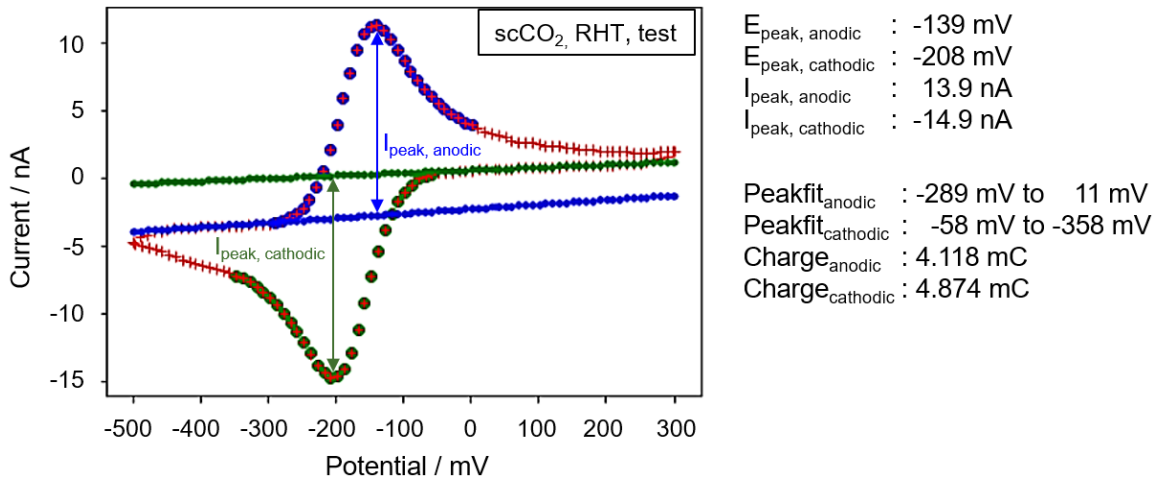


Figure II.19: Exemplary CV of a structured ink electrode cycled in 1 mM ruthenium hexaamine, 1M KCl at 5 mV/s, background subtracted. All steps carried out by the Python script are graphically indicated.

The accuracy of the Python script was confirmed by comparing results of the potentiostat software tool against a manual, Excel-based peak evaluation and against the result of the Python script. An exemplary, non-subtracted CV data set was chosen and the charge integrated.
Results are provided in Table II.5 and indicate a rather good correlation. The Excel-derived results display minor deviations of around 5 % for anodic and cathodic peak. A deviation of up to 8 % is observed for the Python-derived data, which may partially be explained by deviations in the slopes of trend lines, the choice of boundaries for the integration, and the density of data points of the modelled peaks and trend lines. Alternatively, an error in the mathematical approach of charge determination is not excluded. In any case, the uncertainty of the charge, determined by means of the Python script, has

to be kept in mind when using it for further calculation. The error plays a minor role, when focusing on a qualitative comparison of values in this project.

Table II.5: Comparison of the EC lab peak evaluation to manual data treatment in Excel and to a Python script.

| **Method** | **$Q_{ox}$(mC)** | **Deviation (%)** | **$Q_{red}$(mC)** | **Deviation (%)** |
|---|---|---|---|---|
| EC-lab | 0.21 | - | -0.166 | - |
| Excel | 0.205 | 5.854 | -0.176 | 5.682 |
| Python | 0.193 | 8.095 | -0.156 | 6.410 |

## 2.4.4 Chronoamperometry

### 2.4.4.1 Experimental approach

Chronoamperometric experiments were carried out on freshly prepared electrodes in order to exclude/avoid "memory" effects from previous voltammetric cycling. For a better comparison to the cycled electrodes, an oxygen plasma treatment was applied previously to the measurement.
By adapting the protocol proposed by Cummings et al., studies were performed in 2.5 mM hexacyanoferrate (II), 1 M KCl which was de-aerated by an argon stream (15 min) [111]. Structured electrodes were immersed in the electrolyte for 15 min to enhance wetting. Subsequently, an applied potential of 0 V vs. Ag/AgCl (vs. SCE in the publication) was maintained for 2 s, before switching to an oxidizing potential of 0.7 V for 20 s, during which the amperometric response was recorded every 100 ms or every 5 µA.

### 2.4.4.2 Data evaluation

Based on the peak current decay, data points corresponding to the first 0.5 s after the potential switch were selected for the preparation of I vs. $1/\sqrt{t}$ plots, on which further evaluation was based. After averaging the slopes of four electrodes for each PCB, the electrochemically active surface $A_{Cottrell}$ was calculated, based on rearranging the Cottrell equation II.3 [112]. The parameter $i$ is the decaying current, n is the number electrons transferred, F is the Faraday constant, $C_0$ is the bulk concentration of the redox agent and $D_{HexCN(II)6}$ is its diffusion coefficient ($6.3 \times 10^{-5}$cm$^2$/s in 1 M KCl [113]) and $t$ is the time. The application of the Cottrel equation is usually limited to planar electrodes exhibiting linear, semi-infinite diffusion. It was used to obtain approximative values, as no suitable equation for porous electrodes was found.

$$i = nFA_{Cottrell}C_0\sqrt{\frac{D}{\pi t}} \tag{II.3}$$

## 2.4.5 Electrochemical Impedance Spectroscopy

Electrochemical impedance spectroscopy (EIS) was employed to study the frequency-dispersed character of the charge transfer. Particularly for structured electrodes, the effect of limited diffusion was thought to be observable. To guarantee good wetting of the pores, electrodes were generally cycled in the respective electrolyte. The systems' stability was verified by performing OCP measurements of 3 to 5 minutes prior to EIS. Only in case of a stabilizing signal, it was proceeded with the characterization. The electrodes of one PCB were characterized one by one in the cell configuration displayed in Figure II.17 b).

Measurements were carried out in 1 M KCl, adding 1 mM of RHT in order to compare results with the other experimental techniques. Furthermore, it was thought, that the outer-sphere charge transfer might allow to study the structural development better than with a kinetically slower, inner-sphere redox probe[15]. The frequency was swept from 100 kHz to 0.1 Hz with a potential amplitude of 10 mV and at a bias of -0.18 V to study charge transfer at the half wave potential of the redox probe.
For some separate studies, 0.1 M PBS (pH 7.4) was used as electrolyte and EIS was carried out at OCP. Results are not mixed and conditions are indicated.

#### 2.4.5.1 Data evaluation and equivalent circuits

EIS results typically demand to verify the system's causality, i.e. an output signal must only be generated, when there is an input signal. Measurements were performed in a Faraday cage. Furthermore, systems are required to be what is called linear. Commonly, non-linearity is excluded by applying a Kramers-Kronig (KK) transform, which fits the measured spectrum with number $n$ of equivalent R/C circuits (so-called Voigt circuit) to confirm general "fittability". This step allowed to observe some deviation in the low- and high-frequency parts of the spectra. For data extraction and evaluation, the frequency range was narrowed accordingly.
In addition, a software tool proposed by BioLogic was available, allowing to verify a system's linearity by evaluation of the so-called total harmonic distortion (THD) [114]. The concept is based on the generation of harmonics in the output signal in case of non-linearity. An upper limit of 5 % is considered acceptable for a linear system.
The Nyquist and Bode plots were then compared qualitatively to match eventual visual tendencies with the change of structuration parameters. In a second approach, different basic equivalent circuits were fitted to the data by means of the provided software tools, before reading out the associated circuit-related information. Details are presented in the discussion of results.

[15] As mentioned before, outer-sphere charge transfer takes place via electron tunnelling, which is considered beneficial in order to measure results independently from the chemical state of the electrode surface. For example, the influence of oxygenated groups can generally be neglected, which simplifies the interpretation of results.

## 2.5 Conclusions of chapter II

A careful choice of electrode supports presented the base for this work, mainly guided by the compatibility of materials with the $scCO_2$ and the specifications of the supercritical fluid equipment. PCB with Au-collectors were identified to be ideal under the condition of complete coverage with ink, so as not to expose any underlying Au. In practical application, the PCB were advantageous due to their flat, sturdy but yet versatile design, allowing to prepare four electrodes according to the same protocol.

In the following, an electrode preparation protocol was identified consisting in a cleaning step, mask deposition and the deposition of diluted commercial DuPont$^{TM}$ BQ242 carbon ink prior to electrode drying or structuration. The identification of a particular structuration protocol was an empirical finding and difficulties were encountered due to the variety of different process parameters. The relevance of adding a step in process temperature was found by coincidence. For the further project, an important aspect was to maintain an equilibrium between detailed parameter studies to learn about the mechanisms and an evaluation of the practical application of the technique for preparing sensors.

The electrode characterization protocol primarily intended to find a means of studying the degree of structuration and porosity. Due to the nature of physical and electrochemical techniques, results give insight into different types of structural information. These can be surface-related, address surface and volume in parallel, or relate to the electrochemically active/accessible sites. Thus, it was considered essential to compare a variety of techniques to evaluate, whether results were displaying similar tendencies. Besides, the technical feasibility, reliability and ease of carrying out the measurements were of interest. Optical and digital microscopy were found to be ideal for a quick, visual verification of the general successful structuration. However, the estimation of pore-sizes requires highly advanced equipment and significantly increase measurement time. Physical techniques like SEM impose a particular sample preparation and technical knowledge, but represent the gold standard in order to visually descend to spatial resolutions in the nm-range. All image-generating techniques demand image treatment steps, to extract quantitative information. A particular disadvantage lies in limitation to surface-related information, which implies to fracture structured electrodes in order to access information related to bulk porosity.
Nitrogen-adsorption measurements were considered difficult to realize due to the requirement of large amounts of sample material. While this depends to some extent to the sample's SSA (low SSA materials imply to use a higher mass of material), the technique remains time-consuming. The $SSA_{BET}$ was estimated to 10 $m^2/g$ and suggested a low degree of structural development, compared to unstructured ink. A correlation with SEM-derived information was the presence of small macropores in the range of 50-100 nm in diameter. This potentially explains the hysteresis loop indicated in the adsorption-desorption isotherms. The technique provided an important additional insight, but was not further used in the project. There is a possible interest to repeat measurements using an adsorbent of lower vapour pressure, such as Krypton. An alternative technique, demanding higher levels of safety regulations, could be mercury porosimetry.

Electrochemical characterization techniques represent versatile and well-suited means for studying electrode behaviour, particularly when physical methods reach their limits. A large variety of techniques allows to conclude not only on the SSA, the nature of charge-transfer, but also to indirectly interprete the degree of structuration via the diffusion-related characteristics. As small changes in the sample preparation or treatment can significantly affect the results, special care is required to guarantee comparability of

the data.
As an example, the hydrophilic character of the structured electrodes required to improve wetting and in consequence an oxygen plasma treatment was carried out. A small range of experiments allowed to find suitable conditions. A set of comparative studies on non-structured, plasma-treated electrodes were prepared and served as reference.
Writing a Python script was considered necessary to extract quantitative data from the CV data. It is uncertain, why the software tool provided by the manufacturer of the potentiostat imposed limitations. The discussed level of uncertainty arising from the use of this script regarding the peak charges is to be kept in mind for a further quantitative discussion.
Chronoamperometry and EIS present further established methods for electrode characterization. In order to provide meaningful results on structured electrodes, complete wetting of the structured electrodes was essential. Therefore, in addition to the plasma treatment, a wetting time of several minutes was included in the characterization protocols.

# Chapter III

# Study of the structuration parameters

Chapter III outlines the results obtained from characterizing the structured electrodes, as well as the unstructured electrodes serving as reference. The influence of modified structuration parameters is studied by evaluating the change in porosity, pore size and calculated increase of specific and electroactive surface. The sections follow the pattern of a step-by-step improvement of the protocol, focusing on the effect of changing one selected process parameter and maintaining the identified optimum conditions during the study of the following parameter. The schematic structure of the chapter is depicted in Figure III.1.

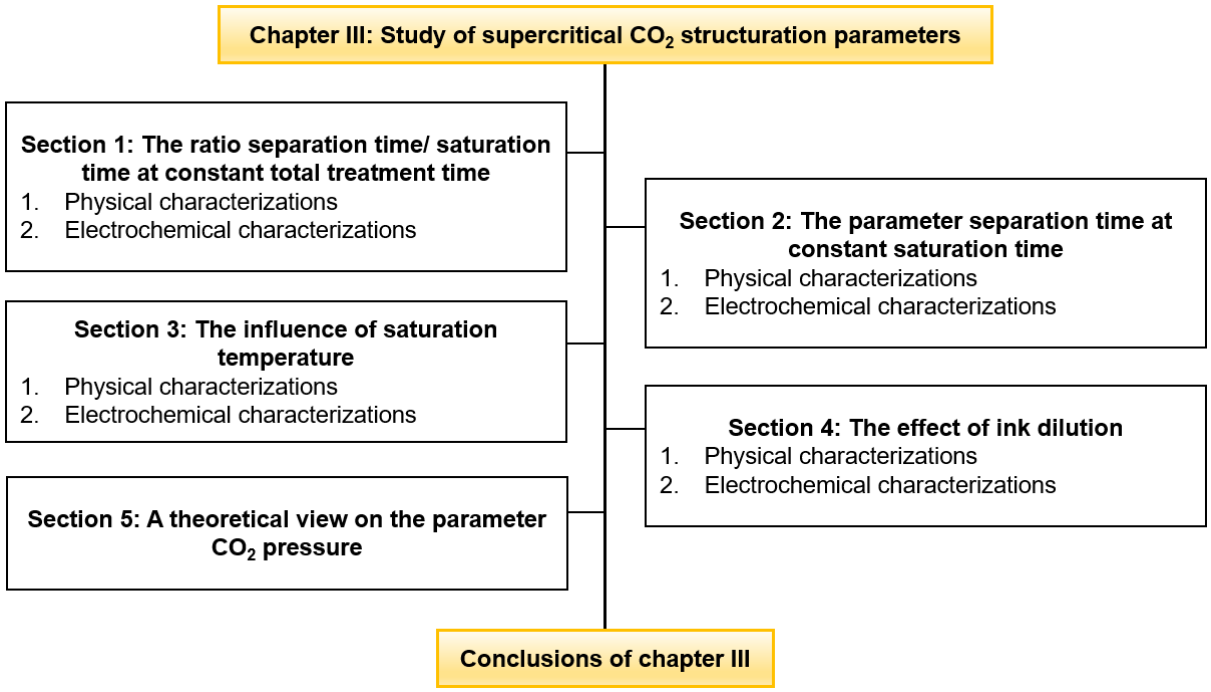


Figure III.1: The thematic outline of the chapter focused on the variation of process parameters.

Section one focuses on obtaining a general idea on the interplay between phase separation time where the $CO_2$ is in subcritical state and the saturation time with supercritical $CO_2$. To our knowledge, this has not yet been covered by literature. Specifically, different ratios of separation time and saturation time are compared, maintaining a constant total

treatment time. Results of physical and electrochemical characterization methods are presented, qualitatively discussed and quantitatively compared against literature values.

The parameter separation time is further studied in section two for a constant saturation time. Identical characterization protocols allow for a direct comparison with the previous section.

In section three, the influence of saturation temperature, thought to influence the polymer foaming during the saturation step of the treatment, is investigated within technical limits of the equipment.

Ink dilution, the focal point of section four, represents an important factor unrelated to the settings accessible with the supercritical fluid equipment but considered to be of importance specifically for the phase separation.

The supercritical $CO_2$ pressure has not been experimentally studied in this work, however it is thought to be of potential interest. Based on literature, a small discussion on the expected influence is displayed in section five.

The chapter ends with a conclusion on the process of optimizing the structuration within the range of experimentally accessible parameters. The results form the base of the following chapter IV.

# 3.1 Studying the ratio of separation to saturation time at constant total exposure time

A novelty of the approach is to unify the structuration mechanisms involving $scCO_2$, so far reported separately. In consequence, the exact influence of process parameters was vague and the initial protocol was mainly based on assumptions. A total process time of thirty minutes was selected in the beginning, generally aligning with works on the preparation of polymeric membranes by means of supercritical $CO_2$ [8]. Opposed to literature, two process temperatures ($T_{sep}$ and $T_{sat}$) were selected,, which allowed to work with $CO_2$ in both the subcritical and supercritical states during the respective times $t_{sep}$ and $t_{sat}$. In the following, the abbreviated sample description is given by the ratio $t_{sep}$ /$t_{sat}$. In the following sections, the results of different physical and electrochemical characterization methods are presented.

## 3.1.1 Physical characterization

### 3.1.1.1 Digital microscopy

Top view digital microscopy images of ink deposits are displayed in Figures III.2 and III.3 for 1.0 µL and 1.5 µL of ink volume (BQ:EGDA = 2:8 (w/w)). The locations surrounded by white boxes are presented at larger magnification scale.
The surface homogeneity of 1 µL deposits was found to be rather poor, displaying zones of different visual appearance. A central flat area was surrounded by a circular shaped fringe which features larger cavities. The 10/20 sample stands out, as the two zones seem particularly disconnected, generating a void. Potentially, this void is present in all cases but partially covered for the other deposits.

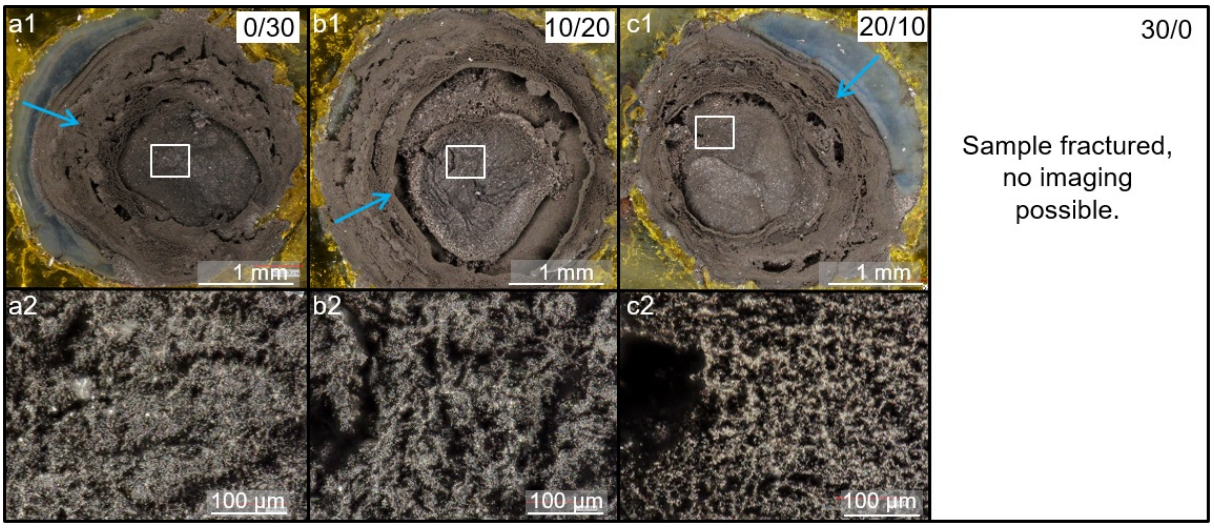


Figure III.2: 1 µL ink deposits (BQ242:EGDA = 2:8 (w/w)) for digital microscopy in top view; the 0/30 sample in a), 10/20 in b), 20/10 in c), the 30/0 sample was destroyed during the process. Arrows indicate the potential direction of $CO_2$ flow. Ratios refer to the parameters $t_{sep}/t_{sat}$. White boxes correspond to magnified locations.

Further, deposits appear slightly displaced and deformed, which is thought to be a consequence of the first $scCO_2$ process step. In particular, during the pressurization phase of the cell, a directional fluid flow may occur, imposing a force acting on the deposits. Blue

arrows indicate the direction of the fluid stream. The partial displacement is consequently explained by poor adherence of ink to the glass supports (fractures of microscopy slides were used).

The 1.5 µL deposits are of generally similar appearance. All zones generate the impression of being shifted in radial direction outwards from the centre, introducing an additional zone in form of a central indentation. Besides, the development of a meniscus at the boundary of the masks is suggested. Overall, the raised zones ("C"-shaped areas) appear to be mechanically less connected, resembling a thin and porous skin or membrane. This observation highlights the dynamic nature of the mechanism and in particular reinforces the expected mechanism to be a physical phase separation. Literature suggests this mechanism occurs rapidly, which locates it during the initial stages of the $scCO_2$ structuration.
No displacement is observed, eventually as the ink volume was increased by a factor of 1.5, while the mask thickness was doubled. Following this thought, ink deposits sat deeper in the cavities and were better protected from the directional force the during pressurization of the chamber. The idea is supported, as the deposits are not entirely displaced, but only the membrane-like top layer is deformed as indicated.

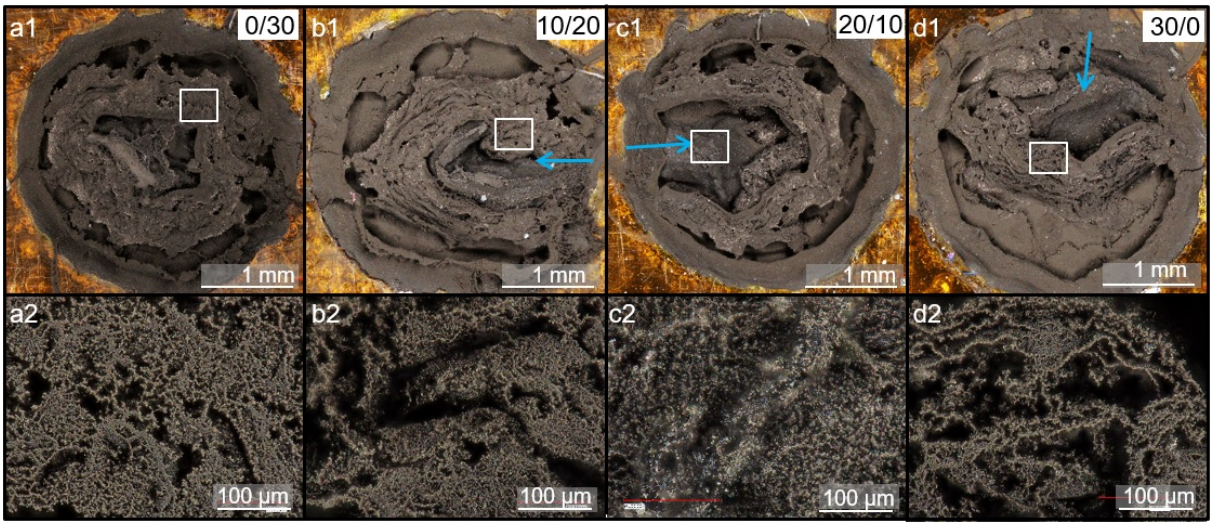


Figure III.3: Ink deposits (BQ242:EGDA = 2:8 (w/w)) for digital microscopy, 1.5 µL deposit volume, in top view; the 0/30 sample in a), 10/20 in b), 20/10 in c), 30/0 in d). Arrows indicate the potential direction of $CO_2$ flow. Ratios refer to the parameters $t_{sep}/t_{sat}$. White boxes correspond to magnified locations.

By focusing on a smaller location, images of larger magnification were thought to suppress the effect of an inhomogeneous surface structure. However, this was not always successful. It was therefore important to separate the remaining visual effect of the inhomogeneous surface from the created porosity.
A structure on the µm-scale can be observed, with one contribution from a surface-related porosity and a second contribution from seemingly deeper pores. For the most part, both types of pores are present in parallel, i.e. they are not separately located in particular zones. This complicated the extraction of quantitative information by only a simple visual comparison of the images.
It was attempted to further increase the magnification factor to suppress the visual effect of larger-scale features. However, the ink deposits were of very reflective behaviour, potentially as a consequence of the incorporated carbon particles. To compensate this effect,

the microscope's "anti-brilliance" mode in combination with low illumination was used, see Figure III.4 a). While the achieved optical resolution is impressive, the image suffers from overexposure/reflective artefacts which could not be sufficiently improved, despite successive image treatments. The images allowed only a rough estimation of pore sizes in the range of several µm.
As the presence of even smaller pores required confirmation, SEM imaging was employed. Particularly the conductive nature of deposits was thought to facilitate the sample preparation process.

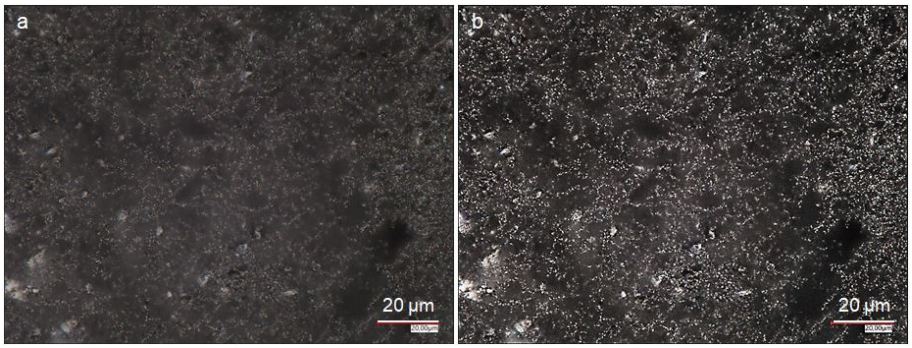


Figure III.4: Digital microscopy of a structured ink deposit (BQ242:EGDA = 2:8 (w/w)) at magnification factor 2000; a) raw image and b) treated image with enhanced contrast.

### 3.1.1.2 Height evolution of deposits

The evolution of height of ink deposits was considered to indicate the developed porosity. Since data was obtained from the same ink deposits as before, this time imaging from the side, see Figure III.5, an essential question was how to define the top surface. Specifically in series 2) for the larger ink volumes, it can be seen that deposits no longer appeared flat and the mentioned inhomogeneities limited the exact determination of height. For an estimative determination of values, a minimum, median and maximum height ($h_{min}$, $h_{mid}$, $h_{max}$) reading was carried out. Results are displayed in Table III.12.

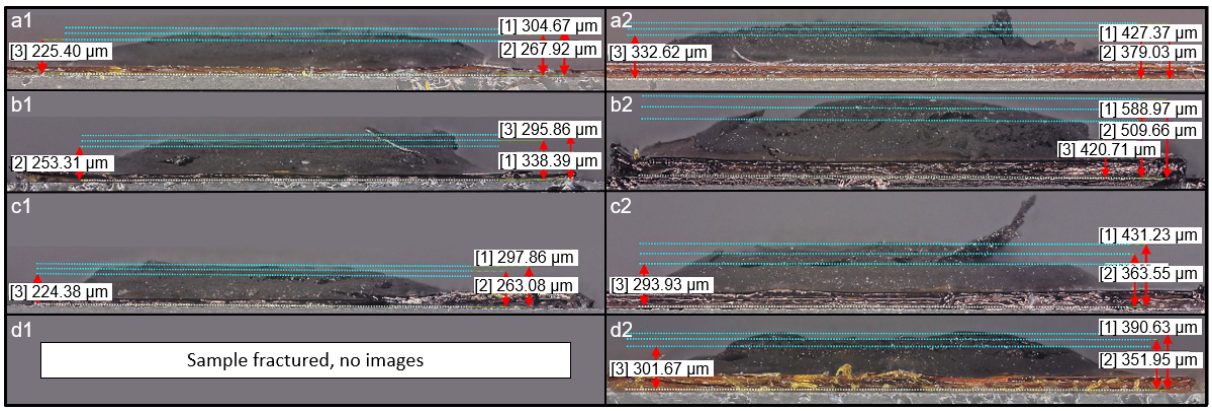


Figure III.5: Side view digital microscopy images of structured ink deposits (BQ242:EGDA = 2:8 (w/w)). 1 µL ink in series 1), 1.5 µL ink in series 2). Sample 0/30 in a), 10/20 in b), 20/10 in c) and 30/0 in d).

Table III.1: Height of ink deposits extracted from side view images in the study of separation and saturation time at constant total exposure time.

| $t_{sep}/t_{sat}$ | 1.0 µL | | | 1.5 µL | | |
|---|---|---|---|---|---|---|
| | $h_{min}$ (µm) | $h_{mid}$ (µm) | $h_{max}$ (µm) | $h_{min}$ (µm) | $h_{mid}$ (µm) | $h_{max}$ (µm) |
| 0/30 | 225 | 268 | 305 | 333 | 379 | 427 |
| 10/20 | 253 | 296 | 338 | 421 | 510 | 589 |
| 20/10 | 224 | 263 | 298 | 294 | 364 | 431 |
| 30/0 | - | - | - | 302 | 352 | 391 |

For both ink volumes, a tendency towards maximum deposit heights is observed for a ratio $t_{sep}/t_{sat}$ of 10/20 within the studied range. Further, the readings demonstrate an increased deposit height for larger ink volumes, which is important, since deposit height was initially assumed to result from the generation of a homogeneous porosity. The observation of a non-homogeneous surface and the presence of large voids were unexpected.

The observations can be explained when considering phase separation as part of the mechanism. When a classical ternary phase (polymer, solvent of the polymer and its non-solvent) reaches an unstable composition and undergoes demixing, one polymer-rich and one polymer-low phase are formed, as explained earlier. Based on the hypothesis, that the diluted ink follows a comparable process, areas of different polymer concentration and of varying size could be formed. The crystallization of polymer out of the highly concentrated phase could then form a solid, porous network. In the areas of low polymer concentration, a fragile structure would be created, consisting of polymer and conductive particles.
Areas which now resemble large pores or cavities were potentially filled with this loosely connected network directly after the phase separation. During the remaining structuration and in particular during dynamic steps pf the process, imposing a certain flow of $scCO_2$, detachment or destruction of this fragile network could have occurred.
To confirm the idea, an ink deposit was prepared in a small cavity (2.5 mm diameter, 2 mm depth) following a comparable structuration protocol, see Figure III.6. The visual appearance of the structured deposit is similar to ink deposits prepared earlier. Additionally, a filigree network distinguishes the sample, which confirms the hypothesis. Since the walls of the cavity were particularly high, compared to the earlier applied masks, a certain degree of protection from the lateral forces of the $scCO_2$ preserved this delicate structure.

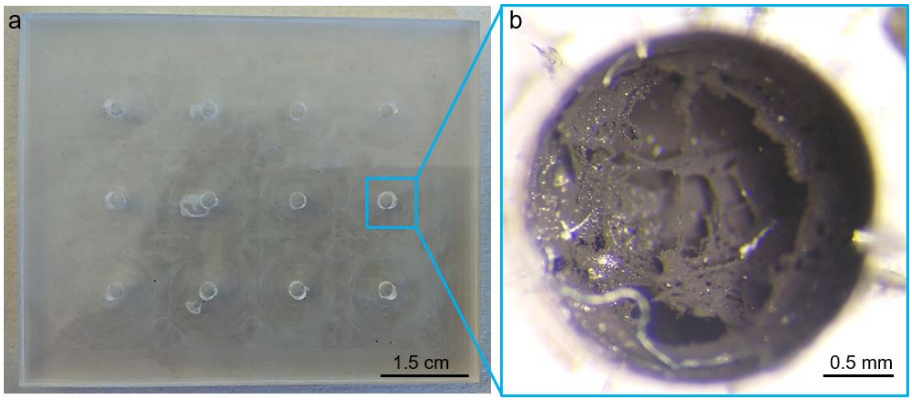


Figure III.6: Presentation of a PMMA plate with specifically deep cavities to study the protection from fluid flow-induced forces on the preservation of ink deposits.

#### 3.1.1.3 Evaluation of volume

Profiting from the microscope's software tools, images were taken at an angle of 45 ° to digitally reconstruct the deposit volume, see Figure III.7 series 1 for 1.0 µL and series 2 for 1.5 µL. Part of the approach was the indication of a base plane in z-direction, correlating with the height of the sample support. In order to solve the focusing problems which are common during the microscopy of transparent sample supports, black permanent marker was applied around the samples/masks which allowed to define the base-planes reasonably well. Still, it should be kept in mind that some uncertainty arises from this step. The areas of the deposits associated with structured ink ($A_{geo}$), based on which the volume was reconstructed, were selected as indicated by the red zones, and values extracted.

Results are listed in Table III.2 and include a normalized volume $V_n$ to compensate for variations in deposit coverage and for any potentially delaminated ink volume. In particular, $V_n$ was derived by dividing extracted volumes $V$ by $A_{geo}$, followed by an extrapolation to a unit surface □, which corresponds to a completely covered cavity. Thus, deposits of "identical" surface coverage could be compared.

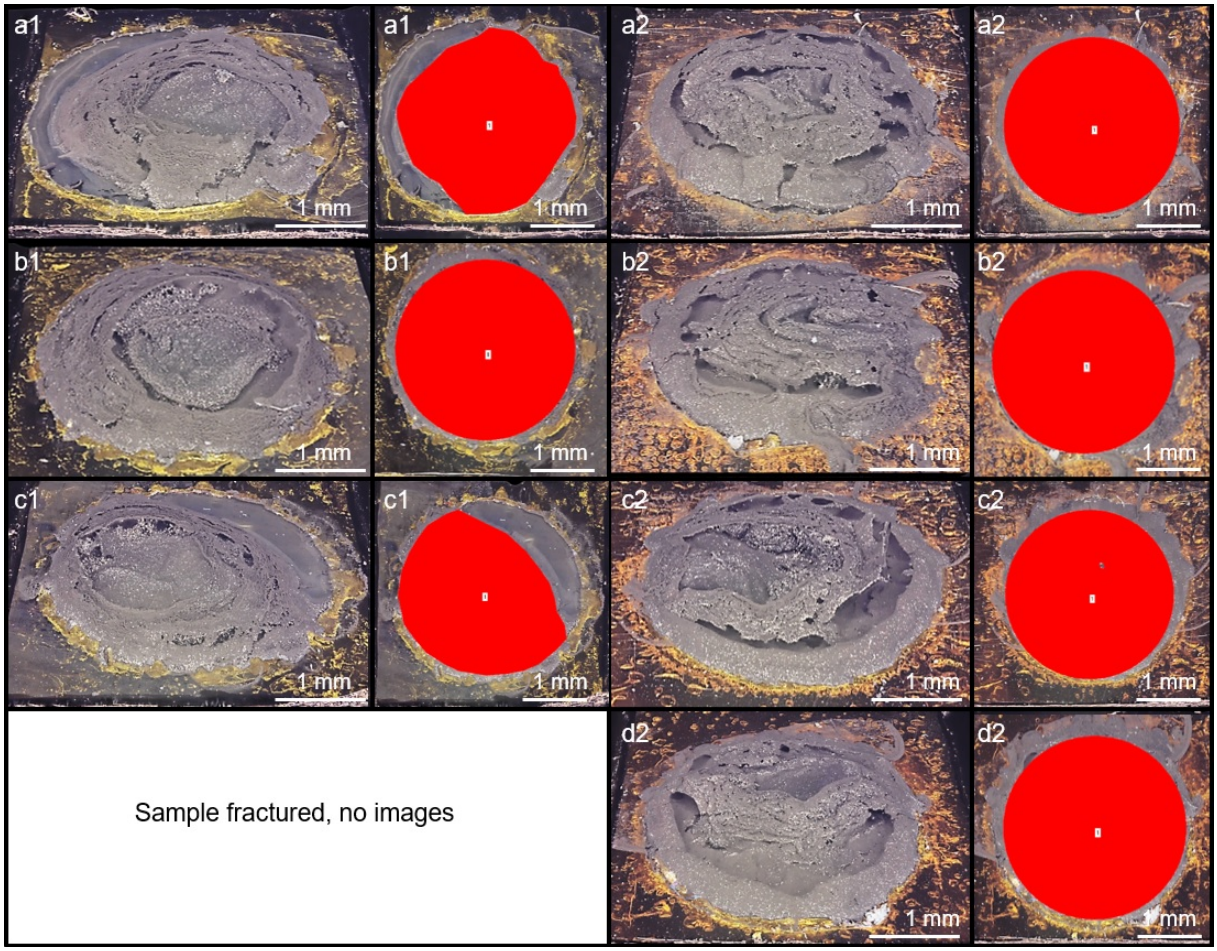


Figure III.7: Aerial view (45 ° and 90 °) digital microscopy of structured ink deposits (BQ242:EGDA = 2:8 (w/w)). 1 µL in series 1), 1.5 µL 2). The 0/30 sample in a), 10/20 in b), 20/10 in c), one 30/0 sample was destroyed. Ratios refer to the parameters $t_{sep}/t_{sat}$.

Table III.2: Volume of ink deposits extracted from aerial view images in the study of separation and saturation time at constant total exposure time, average for each PCB.

| $\mathbf{t_{sep}/t_{sat}}$ | **1.0 µL** | | | **1.5 µL** | | |
|---|---|---|---|---|---|---|
| | **V ($mm^3$)** | **$A_{geo}$ ($mm^2$)** | **$V_n$ ($mm^3/\square$)** | **V ($mm^3$)** | **$A_{geo}$ ($mm^2$)** | **$V_n$ ($mm^3/\square$)** |
| 0/30 | 1.24 | 6.67 | 1.32 | 2.06 | 7.66 | 1.90 |
| 10/20 | 1.21 | 7.55 | 1.13 | 2.17 | 7.28 | 2.10 |
| 20/10 | 1.12 | 6.22 | 1.27 | 1.87 | 8.53 | 1.55 |
| 30/0 | - | - | - | 1.33 | 1.28 | 1.28 |

Before discussing results, the uncertainty of the technique is addressed. The calculated volume depends on the angle and orientation at which each deposit was imaged, the precision of surface tilt correction and the correct indication of a base plane. The calculated volume then further depends on the correctly indicated area covered by the deposit. As a consequence of these factors, results have to be carefully interpreted. To reduce the error, images from opposite angles and orientations could allow to average results per deposit. The disadvantage would then consist in the extended experimentation time. Besides is shall be mentioned, that an intrinsic flaw of the technique is the extrapolation of 2-dimensional images into 3 dimensions. Artefacts in the 2-dimensional images are extrapolated as well and become larger. It was therefore essential, to critically sort out any non-representative images, before starting to evaluate the comparison of general tendencies (semi-quantitative analysis).

The general order of deposit volume is 1.2 $mm^3$ for 1.0 µL ink, implying an increase of 20 % relative to the deposited ink volume. For 1.5 µL ink deposits, the maximum estimated volume is 2.2 $mm^3$, corresponding to an increase of 44 %. Ideally the increase should be indicated relative to the dried ink volume, however, the thin layers were difficult to measure.
It is possible, that an extended $t_{sep}$ allows dissolution of ink constituents even in subcritical $CO_2$. As the non-normalized values display a tendency towards a decreased volume generation for large ratios of $t_{sep}/t_{sat}$, the 30/0 sample for 1.0 µL ink should have provided important information. The tendency was not reproduced after normalization.
For 1.5 µL ink, a maximum estimated deposit volume for the 10/20 sample was observed both for the calculated and the normalized volume, which indicates some degree of representability of results. Based on the assumption, that the maximum generated volume for 1.0 µL ink should equally occur for the 10/20 sample, the seemingly inverse tendency is curious. The 10/20 sample yielded the smallest volume instead, leading to the question, whether $V_n$ could be overestimated for the samples 0/30 and 20/10.

The practical interest of the study laid in the identification of process parameters, which allowed to maximize the generation of volume. Ideally, this correlated with the development the of specific or the electroactive surface. Under the assumption, that peak values indeed occurred for the 10/20 deposits, the approach of having a structuration protocol that included working with $CO_2$ both in the subcritical and the supercritical phase was supported. This hypothesis required validation by other characterization techniques.

#### 3.1.1.4 SEM images

To complement microscopy data, SEM images of specifically prepared samples were realized, see Figure III.8.

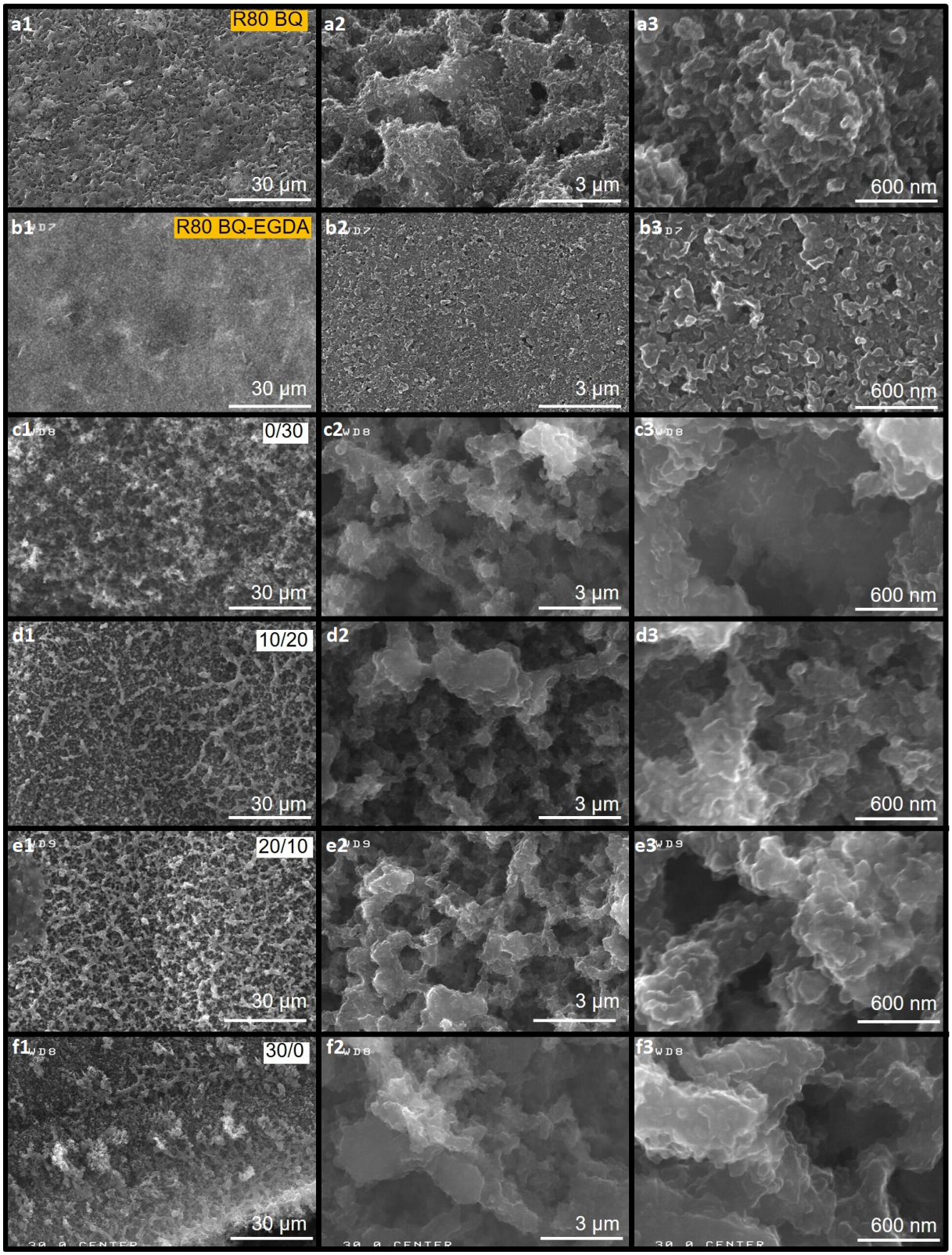


Figure III.8: SEM images of undiluted (a) and diluted (b) ink deposits after drying (orange labels, 3 h, 80 °) and structuration (d-f, white labels). The ratios refer to $t_{sep}/t_{sat}$ (in minutes), where $T_{sep}$ = 20 °and $T_{sat}$ = 40 °. Images display central sample locations.

Furthermore, the terms micro- and macrostructure are introduced, which refer to topographical features with dimensions of several µm and several tens of µm, respectively. In combination with the formerly presented terms nanostructure, as well as micro-, meso and macroporosity, a detailed description of the SEM images is possible.

Interestingly, the undiluted, dried deposits (R80 BQ) already display a certain degree of structuration, which was unexpected. While the deposits are flat on the scale of macrostructure-scale (tens of µm), some pore-like features on the microstructure-scale appear to be present in the near-surface region. Currently this is explained by solvent evaporation during drying, resulting in the creation of channels between agglomerations of carbon particles and binder. Further, a nanostructure is distinguishable consisting in particles of spherical shape up to approximately 100 nm in size, which resemble agglomerates. In addition, the surface displays a low degree of what appear to be macropores. Detailed studies are necessary to confirm up to which degree the structure extends into the volume. It is pointed out that the resolution of SEM images is insufficient for a clear identification of a potential nanostructure with micropores.

The diluted R80 BQ-EGDA deposits (Figure III.8 b)) show essentially no macro- or microstructure. On the scale of nanostructure, the surface again displays spherical features, however this time they do not seem to decorate any structure on the larger scale. A low number of macropores with approximate dimensions between 50 and 150 nm is present. The observations are potentially explained by the ink dilution, which reduces viscosity and increases evaporation time. Carbon particles, additives and binder may have undergone sedimentation towards the bottom of the deposit. The mechanism may have been supported by the higher amount of EGDA its elevated boiling temperature of (187 ℃), resulting in longer drying times.

The deposits treated by $scCO_2$ display an overall similar structure, composed by an open, sponge-like porosity that is generated by the interconnection of pores/ channels. The overall impression is that the structuration resulted in the formation of a microstructure (one to several µm), while the nanostructure, as observed on dried deposits, is replicated. In literature, this superposition of pores of different dimension is referred to as hierarchical structure and is considered of interest for electrochemical application [115].

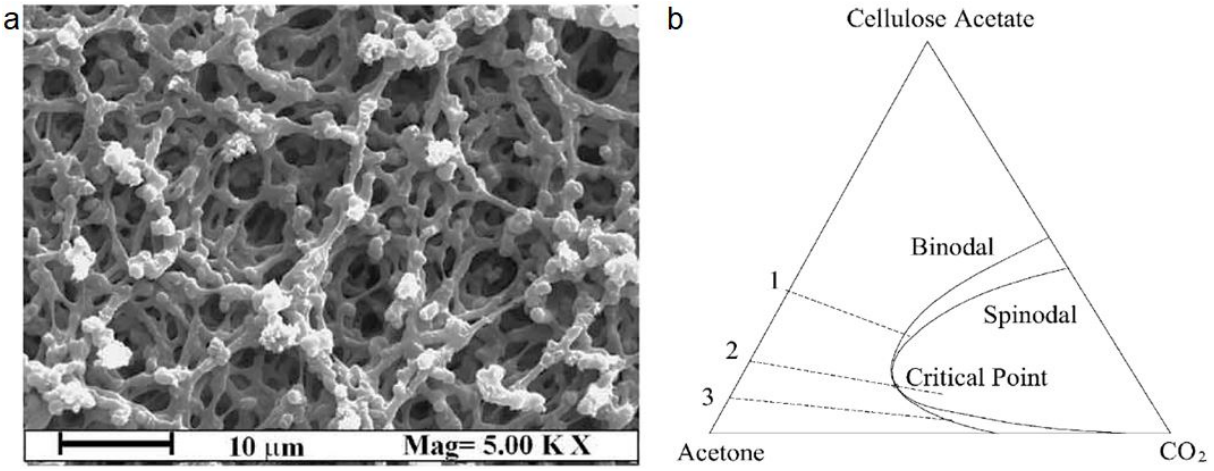


Figure III.9: a) SEM image of cellulose acetate-acetone solution (5 % w/w), exposed to supercritical $CO_2$ during 3 h at 100 bars and 45 ℃. b) The decomposition paths through the ternary phase diagram (polymer, solvent, non-solvent). Figure reproduced from [15].

For a better understanding of the mechanisms that occur during exposure of ink to

supercritical $CO_2$, the work of Reverchon et al. [15], is taken into consideration. In comparable manner to this project, a ternary system composed by cellulose acetate, acetone and $scCO_2$, which represented the non-solvent of the polymer, underwent phase separation. For this hypothesis to be valid, it is assumed that the conductive carbon particles and potentially unknown ink additives have no significant/particular effect on the phase separation.
A SEM image, depicting the surface of a structured cellulose acetate sample after phase separation, is reproduced from the publication, see Figure III.9 a). The structured carbon-ink deposits in this work are generally of similar appearance and structural features are of comparable size, which is particularly clear for the 20/10 deposit in Figure III.8 e). Reverchon et al. described the structure as "bicontinuous, beads-like" ("nodules" in [11]) and explained its generation by associating the path through the ternary phase diagram with a demixing according to path 2 or 3 in Figure III.9 b). These demixing paths are valid for systems of low polymer concentration, which is assumed to be the case for the diluted ink. In that case, so-called liquid-liquid demixing occurs either in form of spinodal decomposition, followed by the solidification of the phase of high polymer concentratio and resulting in a "bicontinuous membrane structure". Alternatively, the "nucleation and growth of droplets of the polymer-rich phase is followed by its solidification, which leads to the generation of the beads-like membrane structure" [15] [11].

In comparison, the macrostructures are visually similar, although of more homogeneous character in the reference, where the sample displays a well-defined (not ordered, though) network. This is less distinguishable in this project, but instead the resemblance to a decorated structure is underlined. This appearance may be either due to the presence of carbon particles or arise from the polymer foaming step. For the interpretation of the evolution of porosity depending on process parameters, an image treatment was proposed.

Table III.3: Extracted data from the ImageJ treatment of SEM (10 k) images in the study of separation and saturation time at constant total exposure time.

| **Description** | **Particle count** | **Total particle area ($\mu m^2$)** | **% Area** | **Pore diameter (nm)** |
|---|---|---|---|---|
| R80 | 540 | 17.1 | 17.2 | 32 |
| R80 BQ-EGDA | 625 | 2.7 | 2.7 | 4 |
| 0/30 | 197 | 17.1 | 17.3 | 87 |
| 10/20 | 287 | 25.3 | 25.5 | 88 |
| 20/10 | 250 | 20.9 | 21.1 | 84 |
| 30/0 | 130 | 18.9 | 19.6 | 145 |

Based on images of magnification factor 10k (series 2 in Figure III.8), the image treatment specified in the appendix section IV allowed for extraction of estimative pore dimensions. Results are depicted in Figure III.10 and corresponding summarized values are listed in Table III.3. However the interpretation requires several precautions.
1) The averaged pore size is a very basic derivation of information, obtained by dividing the total pore area by the pore number. It is however seen as a non-representative technique, ignoring potential populations of pore sizes.
2) The correct identification of pores is considered a limiting factor, as the software suggests to define pores as textural feature of high image contrast. The approach is somewhat controversial, as misinterpretations are probable.
3) Histograms of the pore populations were prepared, see Figure III.11. While being more representative than the mathematically averaged pore sizes, they are only an estimative interpretation of treated SEM images. For example, the histograms were limited to pores

of 750 nm in size, due to the low count of larger pores. The real microstructure, however, features pores of up to several µm in diameter.

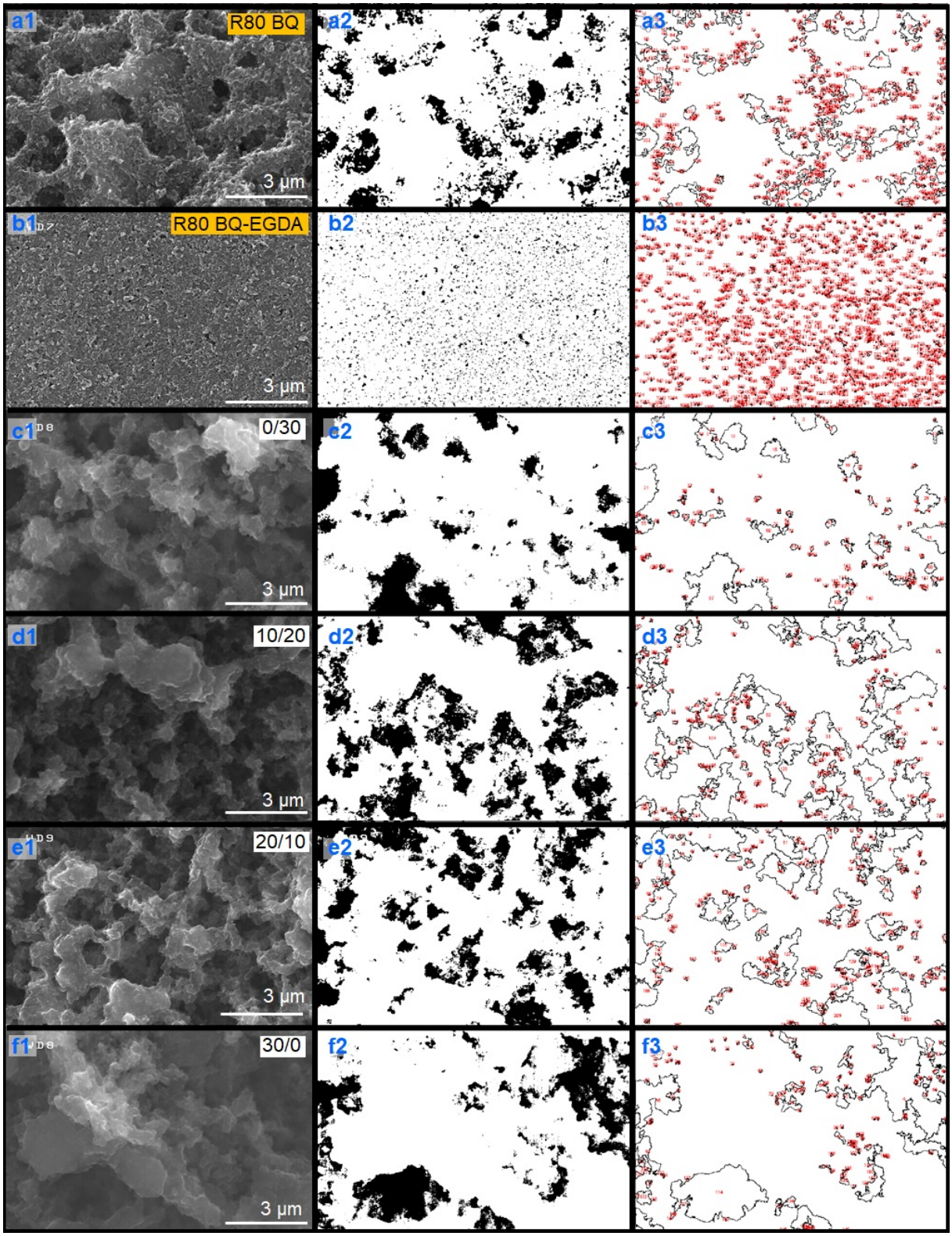


Figure III.10: SEM image treatment for ImageJ pore area determination and quantification in the study of separation and saturation time at constant total exposure time. The red markings originate from the automated particle counting in the software.

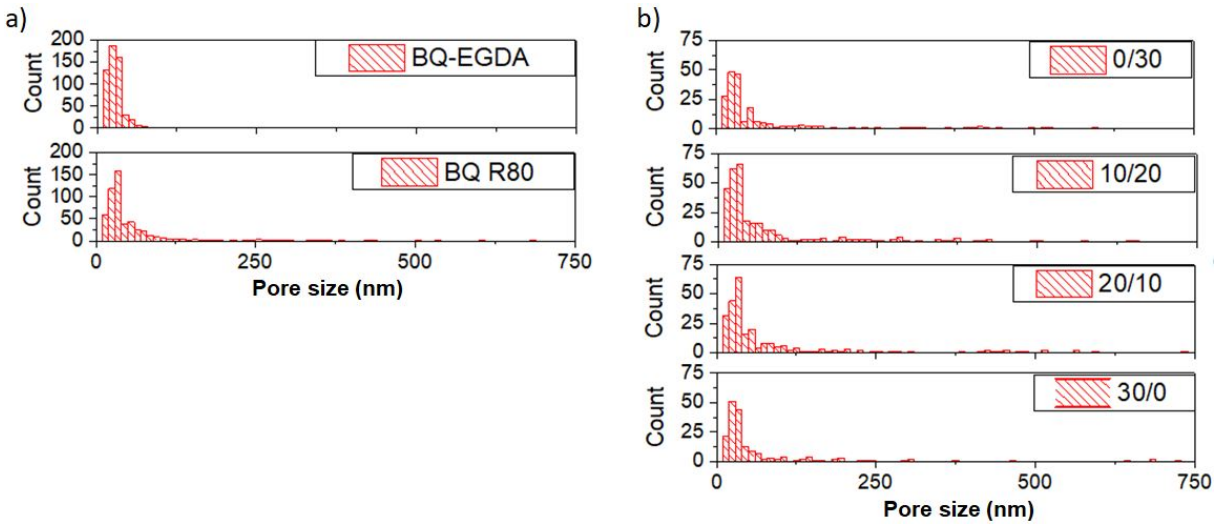


Figure III.11: Histograms of particle/pore populations based on treated SEM images in the study of separation and saturation time at constant total exposure time.

Comparing the pore count of the oven-dried deposits in Figure III.11 a) against each other, an increased number is observed for diluted BQ-EGDA deposits, relative to undiluted R80 BQ deposits. A visual evaluation of SEM images was unable to reveal this detail, in contrary the surface of BQ EGDA deposits was rather considered flat and non-porous.
The pore counts for structured deposits are reduced by a factor of around 2 to 2.5. A tendency towards maximum pore counts for the structuration parameters $t_{sep}/t_{sat}$ of 10/20 and 20/10 is indicated, which generally complements the tendency observed in the evaluation of deposit height.

For the non-diluted R80 BQ deposit, the total area covered by pores corresponds to 17.1 % of the imaged surface and the main pore populations measure 10 to 40 nm in size, peaking between 30 to 40 nm. Some small populations measuring up to 750 nm in size are present.
In contrast, the pore-coverage of diluted BQ EGDA deposits is only of 2.7 %, despite the higher total pore count, suggesting smaller pore dimensions. Therefore, this result fits to the expectation of a visually unstructured surface. The histogram reveals largest populations at smaller pore sizes between 20 to 30 nm with a high presence of pores smaller than 20 nm. Overall, the size distribution is narrow and pores larger than 80 nm are absent.
The structured deposits 0/30 and 30/0 have total pore areas comparable to the dried deposits and the populations appear distributed in similar manner as for the diluted BQ-EGDA deposit. A difference consists in the occurrence of populations up to 750 nm in size after structuration. Generally, the structuration appears to result in the creation of populations of larger size. This is particularly the case for the 10/20 sample, which matches previous observations for the same sample, see maximum deposit height. Further, the presence of populations measuring up to 500 nm is noticed. The maximum total pore area is equally assigned to the 10/20 sample, corresponding to 25.3 % of the deposit surface (an increase of factor 1.5 relative to the non-diluted BQ R80 deposit). This fits well to the range of estimated porosity, derived from the heights of deposits (20 to 44 %).

Considering the earlier presented results of nitrogen adsorption experiments, it is pointed out, that no particularly developed meso- and macroporosity was indicated. It is possible, that the sample collection resulted in considerable structural damage, as men-

tioned. Alternatively, the image treatment protocol could have resulted in an underestimation of the actual pore size ans may require further optimization in the future, to find optimum image treatment parameters.

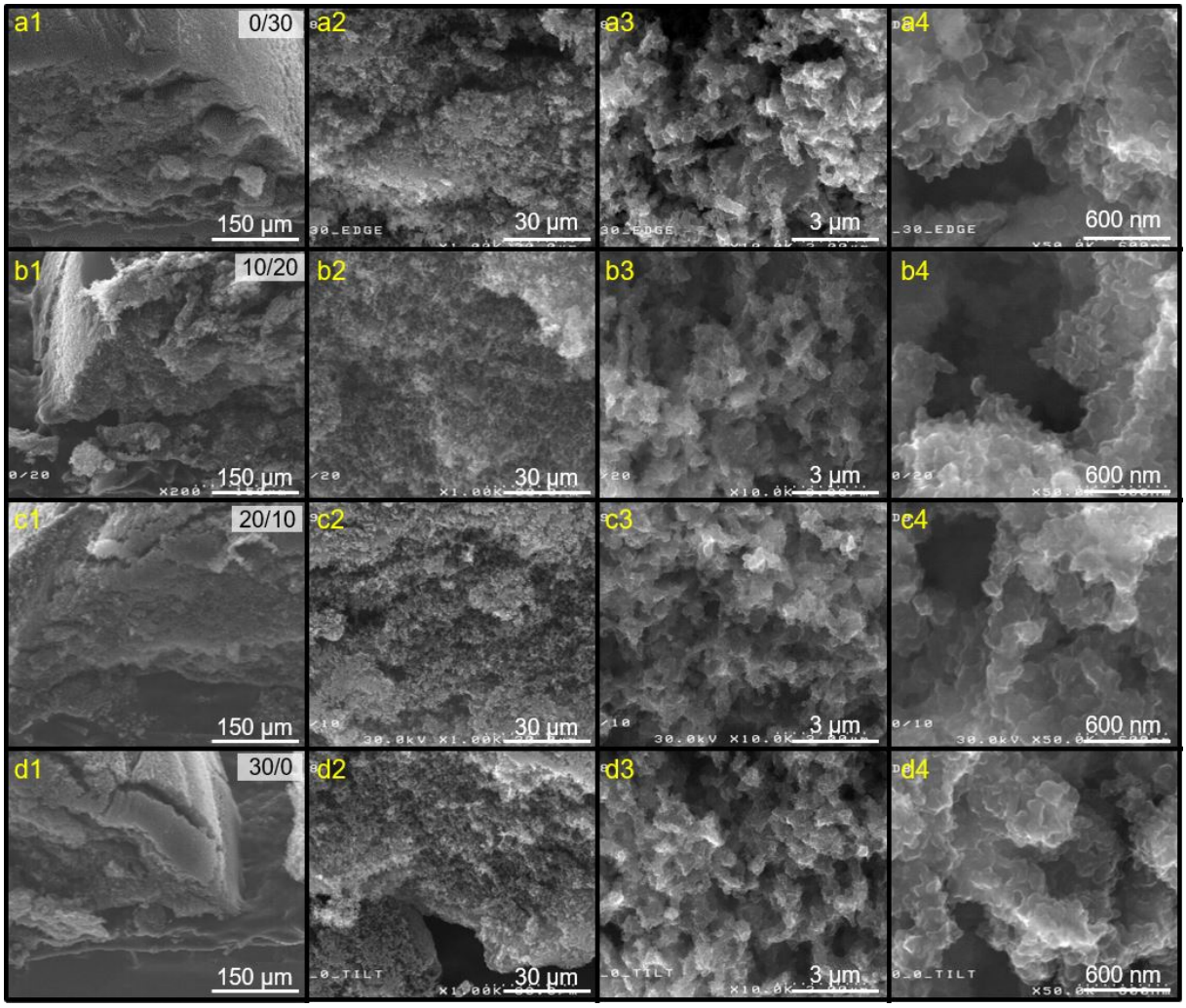


Figure III.12: Transversal SEM images of structured ink deposits in the study of the separation and saturation time at constant total exposure time, obtained by cutting the samples with a surgical blade. The ratios refer to $t_{sep}/t_{sat}$ as before. Images were taken at an angle of 45 ° at different magnifications. 0/30 deposits in a), 10/20 in b), 20/10 in c) and 30/0 in d).

Transversal samples, depicted in Figure III.12, realized at an angle of 45 °, were prepared by cutting and cleaving the structured deposits by means of a surgical blade. While the preservation of structure after cutting the samples, seems not ideal from a visual point of view, the technique was considered rather suited compared to other attempts. These included e.g. an inclusion of the deposits in resin, followed by cutting and polishing the exposed surface, which revealed inhomogeneous infiltration of the structures by resin and residual air in the pores. Digital microscopy failed to provide representative images and SEM imaging was not considered to be an option due to the non-conductive nature of the resin.
Due to the structural damage induced during the cutting step, care was taken to select areas for magnification. It was found, that the microstructure associated with the volume of deposits is specifically well represented in series 2) and 3). An overall resemblance

to the surface microstructure in Figure III.8 is apparent. A particular distinction of the volume structure lies in the absence of the "beads" described in literature and instead, the structure is rather homogeneous and could be described as a foam or sponge-like. Images at large magnification factor, see Figure III.12 series 4), are suited to study the nanostructure. Comparable to the deposits' surface, the porosity resembles a microstructure decorated by a nanostructure.

Similar visual differences between surface and bulk were observed in the work of Reverchon et al [15], which leads to the question how to correlate the observations with the structure-generating mechanisms. Specifically the interaction of solvent (EGDA) and non-solvent (supercritical $CO_2$) during the phase separation is thought to play a key role. During the exposure of ink deposits to $scCO_2$, their outside layer comes into contact with the supercritical fluid firt. Potentially, as a result of mutual diffusion of solvent and non-solvent, this could quickly change the ink composition to a polymer concentration that is lower than in the bulk. The thickness of said layer would then be a consequence of the velocity of diffusion and time. Although demixing is generally reported to advance rapidly, an unstable composition of the ternary system may still be achieved earlier in this outside layer, initiating demixing when the bulk of the deposits is still at a stable concentration.
The proposed phase separation mechanism, associated with solutions of low polymer concentration, which generates the characteristic, observed structure, is liquid-liquid (L-L) demixing [15] [11]. Upon extraction of the solvent, further mechanisms lead to a stabilization of the structure.

No tendencies regarding the evolution of pore size was observed in the bulk. However, as mentioned, the sample preparation technique is potentially unsuited to preserve the structure well enough for a detailed interpretation of the microstructure. The method was only used in this section to study the creation of structure in deposit volumes and no quantitative evaluation was carried out.

## 3.1.2 Electrochemical characterization

The interest of electrochemical studies was to link the variation of electrochemical behaviour to the generation of structure, particularly due to the experimental accessibility of bulk structure/porosity. The modification of treatment parameters were thought to affect the specific surface area, as well as the availability of electrochemically active surface.

### 3.1.2.1 Capacitive current studies

Cyclic voltammetry (CV) studies were carried out in 1 M KCl to study the evolution of capacitive current responses at different scan rates. Figure III.13 presents CV of both undiluted and diluted unstructured electrodes as well as the structured electrodes. All four positions per PCB are displayed at 5 mV/s scan rate (a1-f1), however only one electrode response per PCB is shown for cycling up to 500 mV/s (a2-f2). In all cases, five cycles were completed and the last one is displayed. All electrodes underwent a plasma treatment, including the unstructured electrodes, to facilitate comparison.
Electrode responses of the same PCB mostly follow a similar characteristic; however the scans at low scan rate reveal a certain degree of deviation which coincides with the visual differences of electrodes on one platform. Common observations are the oxygen reduction peak starting at around -200 mV during the cathodic potential sweep. Besides, a redox system with an equilibrium potential generally around 0 V vs. Ag/AgCl (around 210 mV vs. SHE) is observed for some electrodes.

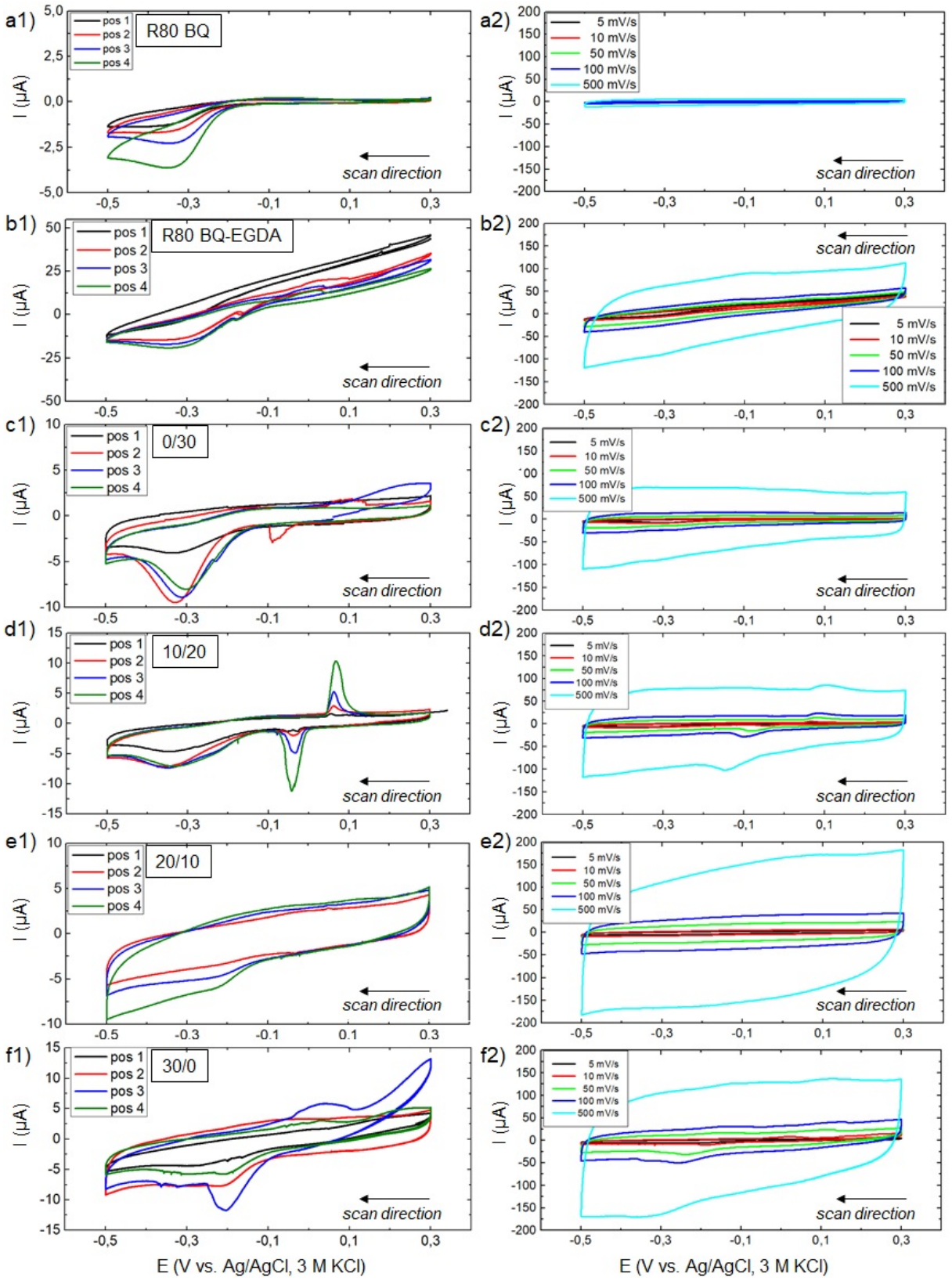


Figure III.13: Capacitive currents of structured ink in the study of separation and saturation time at constant total exposure time in 1 M KCl. Series 1 at 5 mV/s for all electrodes per PCB, series 2 for different scan rates of one electrode. a) R80 BQ, pos. 2 in detail; b) R80 BQ-EGDA, pos. 1 in detail (2:8); c) 0/30, pos 4 in detail; d) 10/20, pos.2 in detail; e) 20/10, pos. 3 in detail; f) 30/0, pos. 4 in detail. The ratios refer to $t_{sep}/t_{sat}$, where $T_{sep}$ = 20 °and $T_{sat}$ = 40 °C. Onset at 0.3 V. Note the different Y-axis in series 1. All electrodes were plasma-treated.

The unexpected redox system around 0 V potentially is the same observed earlier on bare Au electrodes. Based on the shape of CV, the exposure of Au collectors to the electrolyte as a consequence of poor mechanical contact between ink and Au is excluded for most electrodes. Respective CV display a steep current increase during the anodic potential sweep, e.g. seen for pos. 3 in Figures III.13 c1) and f1). Instead, the hypothesis of contamination of the Au collectors is underlined. Adsorbents on the collectors were eventually dissolved during deposition of the ink, or in the $scCO_2$. Thereby, they may have ended on the surface of ink deposits. The presence of this redox system did not limit the evaluation of capacitive currents, as readings were done in appropriate potential areas. The later evaluation of Faradaic current responses was not limited either. Background scans were subtracted from the CV acquired in presence of redox probes.

The CV for undiluted, non-structured ink, see R80 BQ in series a1), mainly display a low degree of capacitive/ pseudocapacitive behaviour in the studied potential range. Interestingly, a tendency towards an increased reduction of oxygen is shown.
The diluted ink, see R80 BQ-EGDA in b1), distinguishes itself by a more resistive behaviour, as indicated by the steeper slope of the curves. Upon faster cycling in b2) a pronounced pseudocapacitive character is apparent. An explanation is a potential orientation of graphite flakes. During drying, the reduced viscosity of the diluted ink and supposed sedimentation may have generated a parallel orientation of the flakes relative to the collector surface. Each flake may then have acted like a small capacitor. Further, when comparing the flakes to a classical two-plate capacitor, plate-spacing (the distance between two graphite flakes) is considerably smaller for the diluted, dried ink. According to equation I.1, the expected capacitance is then higher.
In comparison, the current response of structured electrodes, see c1)-f1), shows an increases capacitive character, represented by the surface included in the curves. Still, the behaviour does not match the rectangular shape that is typical for an electrochemical double layer capacitance. Instead, the gradual development of the current response upon switching the scan direction, particularly clear for faster scan rates in c2)-f2), suggests a pseudocapacitive character ("charging"). This is supported by the presence of broad, low intensity peaks, which correspond to oxidation and reduction reactions. Potentially, ink contamination or residual EGDA may have played a role. However, the pseudocapacitive character is likely a result of the oxygen-plasma treatment, known to create oxygenated, reactive surface groups.
As the effect of the plasma should be of comparable magnitude for all structured electrodes, it can theoretically be subtracted from the curves, allowing to conclude that the electrochemical double layer capacitance should be largest for the 10/20 or 20/10 deposit, see series d) and e). This general tendency matches earlier observations for other characterization techniques.

#### 3.1.2.2 Normalized double layer capacitance

The CV require a means of normalization for a meaningful comparison. For flat electrodes, metallic electrodes in particular, the measured capacitance is typically divided by $A_{geo}$, yielding the specific capacitance. For structured electrodes, this step is less sensible due to the difference between $A_{geo}$ and the SSA. Still, an eventual interest applied for a qualitative comparison of results within this project. The possibility to account for small variations in electrode size, resulting from ink overflowing the masks during the $scCO_2$ treatment, was advantageous.

On this base, the normalized capacitance $C_{norm}$ was calculated as presented in section II and is presented in Figure III.14 and Table III.4as a function of the scan rate. Data

points correspond to averaged results of electrodes belonging to the same PCB.
Before discussing the results, the overall trend of smaller capacitance values for higher scan rates requires clarification. In literature, this has been linked to non-ideally capacitive electrodes, e.g. when a pseudo-capacitive contribution is present, as suggested by the shape of CVs in this project. The measured "effective capacitance" is then composed by the double layer capacitance and an additional contribution, which can be modelled by a constant-phase-element (CPE)[1] [116].
In this project, one contribution potentially arises from the plasma-treatment. Ion diffusion may be another factor [117], since it is eventually limited for an electrode presenting meso- or microspores. The frequent anodic/cathodic polarization changes at fast scan rates could then hinder the complete formation of the electrochemical double layer.
For an easier evaluation, constant-phase elements are not introduced in the evaluation of results at this point. However the non-ideal character is taken into account by only focusing on the results for slow scan rates (5 mV/s), for which diffusion should not be limited.

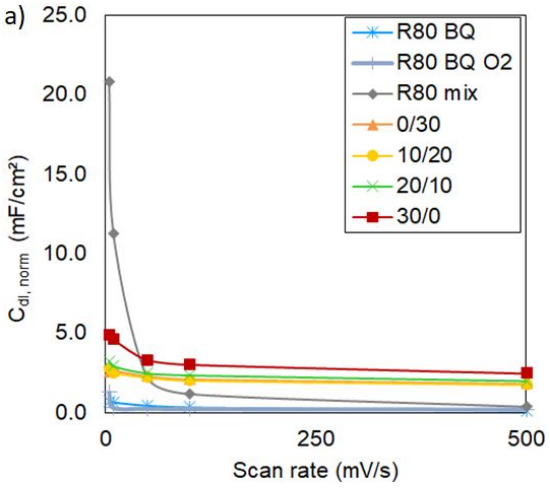


Figure III.14: Normalized capacitance as a function of the scan rate in the study of separation and saturation time at constant total exposure time. Each data point represents the average of up to four electrode responses.

Table III.4: Measured capacitance $C_{meas}$, normalized against the geometric surface of electrodes $C_{norm}$ and normalized to the response of non-structured R80 BQ electrodes in the study of separation and saturation time at constant total exposure time. Results originate from CV at 5 mV/s in 1 M KCl.

| **Description** | **$C_{meas}$ (mF)** | **$C_{norm}$ (mF/cm²)** | **Increase** |
|---|---|---|---|
| R80 BQ | 0.05 | 0.73 | 1.0 |
| R80 BQ $O_2$ | 0.09 | 1.26 | 1.7 |
| R80 BQ-EGDA | 2.36 | 20.79 | 28.7 |
| 0/30 | 0.18 | 2.58 | 3.6 |
| 10/20 | 0.20 | 2.74 | 3.8 |
| 20/10 | 0.36 | 3.24 | 4.5 |
| 30/0 | 0.41 | 4.85 | 6.7 |

[1]A CPE is a mathematical concept used to account for a frequency-dependent behaviour of the capacitance. It is commonly applied in impedance studies for modelling equivalent circuits.

Undiluted, dried R80 BQ electrodes without plasma treatment yield $C_{norm}$ displaying a low dependence on the scan rate. Following previous reasoning, this may indicate an ideally capacitive behaviour or a low degree of porosity. In that case, the structure observed in SEM images could be limited to the deposit surface. In comparison, for plasma-treated electrodes, a slightly higher maximum $C_{norm}$ was measured at 5 mV/s. However, a relatively strong reduction for faster scan rates was noted which may support the assumption of a pronounced pseudo-capacitive character.
Matching measured CV, R80 BQ-EGDA electrodes yielded highest normalized capacitances, increased by a factor around 29, linked either to altered material characteristics or to the increase of specific surface. Previous characterization based on SEM images suggested the creation of a low degree of porosity and the correlation with a large SSA requires validation. Alternatively, the hypothesis of graphite platelet orientation may explain the results. It is further noted, that $C_{norm}$ equally displays a pronounced decrease upon cycling at faster scan rates, which again points to pseudo-capacitive behaviour.
For structured electrodes, normalized capacitances are around 4 (0/30) to 7 times larger than for R80 BQ electrodes. A tendency towards larger values for longer separation times $t_{sep}$ is distinct. Despite electrodes having undergone a plasma treatment, a moderate scan rate dependence is displayed, corresponding to a more "linear" behaviour [116].

For a quantitative discussion of results, the effect of the plasma treatment is detailed first. A work from Okajima et al. on carbon fibres before and after plasma-activation (30 W, 66.7 Pa, gas feed concentration between 0 to 20 %) found the capacitive response to be increased by 28 % [118]. In contrast, the increase is estimated to approximately 57 % for structured electrodes. Fletcher confirmed the idea of increased current responses as consequence of an activated, pseudo-capacitive surface [44].
Focusing further on the plasma treatment, the rather short plasma exposure of 20 s is discussed. Potentially, a rather small surface-restricted zone of the structure was oxidized, instead of the entire available bulk structure. This could explain, why dried R80 BQ-EDGA electrodes attained significantly higher capacitive currents. Potentially, a longer plasma treatment of structured electrodes could result in even higher currents. The hypothesis presents an alternative to the earlier mentioned orientation of graphite platelets.

The specific capacitance of carbon materials typically falls in the range of 5-40 µF/cm$^2$, depending on the exact material and the characterization method. Shiraishi et al. studied conventional phenolic resin carbon fibres before and after steam activation by means of galvanostatic chronopotentiometry in 1 M $LiClO_4$/propylene carbonate. Results were in the range of 5.5 to 10 µF/cm$^2$ [119]. Graphite platelets, depending on their orientation, are referenced between 2 µF/cm$^2$ (basal plane) and 70 µF/cm$^2$(edge plane).
A second example are glassy carbon electrodes, which, depending on their degree of activation, yield very different results. A study by Rice et al. determined the specific double layer capacitance based on CV in 1 M KCl at 200 mV/s to 24-36 µF/cm$^2$ [120]. On the other extreme, Tang et al. determined 290 µF/cm$^2$ for bare glassy carbon (CV in 1 M KCl, 100 mV/s) [121].

The electrochemical comparability of pure carbon-based materials with the results of this study, however, is questionable, as the carbon particles are incorporated in a polymeric matrix. In a study by Harris et al., DuPont™BQ242 carbon ink was screen-printed and cured (1 h, 100 ℃) [122]. The double layer capacitance (15 nF) of obtained electrodes ($A_{geo}$ = 0.433 mm$^2$) was determined in 0.2 M KCl via Fourier transformed AC voltammetry, allowing to calculate the normalized capacitance to 30 µF/cm$^2$. Surprisingly, the published result is similar to the carbon fibres and glass-like carbon and deviates from results in this project (725 µF/cm$^2$), although the electrode preparation appears to be comparable. In particular, the carbon ink was dried under similar conditions and likely

displayed a comparable surface structure. Therefore, the deviating values potentially arise from different characterization methods.

This observation highlights a limitation for comparing structured electrodes, as the exact SSA is often unknown. Some research groups calculate the specific capacitance by dividing the measured capacitance by the separately determined SSA. Other works normalize the measured capacitance to the geometric surface of electrodes. Naturally, this step is prone to cause confusion and a conclusion on the development of SSA remains difficult. On the other hand, given the experiences gathered during this project, the exact surface area of porous electrodes is not always trivial to measure and often, the only available information consists in $A_{geo}$.
An example is the work of Garate et al., who determined the specific capacitance of water-borne CNT-ink on a platinum support to 1300 µF/cm$^2$ (CV in 1x PBS at 50 mV/s, normalized to the geometric surface (0.196 cm$^2$) [109].
Another valuable reference is the study of Lim et al., who prepared porous carbon electrodes via a wet phase inversion method of a carbon slurry. Activated carbon powder, dispersed in a PVDF solution, was cast and immersed in water, which created bimodal pore structures. By means of SEM images, smallest pores were determined to measure around 64 nm, a second population fell in the range of several hundred nm and the largest pores measured several micron in size. The reference is mentioned as potentially important comparative study, since capacitances were calculated based on CV at 1 mV/s in 0.1 M $Na_2SO_4$ according to the approach used in this project[2]. Results covered a range from 2180 to 4770 µF/cm$^2$, depending on the composition of the slurry [76]. The results obtained in this project match rather well, suggesting comparable pore sizes for structured electrodes in this project.
Furthermore, this could confirm the evaluation of SEM images via the ImageJ-protocol, since the smallest pores fall into a similar range.

[2]Measured currents were divided by the effective electrode surface (0.126 cm$^2$) and the scan rate.

### 3.1.2.3 Gravimetric capacitance

Alternatively, to better take the generation of surface in the bulk material into consideration, results for structured electrodes were normalized against their mass to obtain the gravimetric capacitance, see Figure III.15. This approach is commonly used for describing supercapacitor materials.
The mass of structured electrodes was derived from sample preparation for nitrogen adsorption experiments (3100 deposits of 314 mg total weight). The weight of non-structured, undiluted electrodes was estimated by measuring the weight of PCB with dried electrodes before and after removal of ink, dividing by the number of deposits [3].

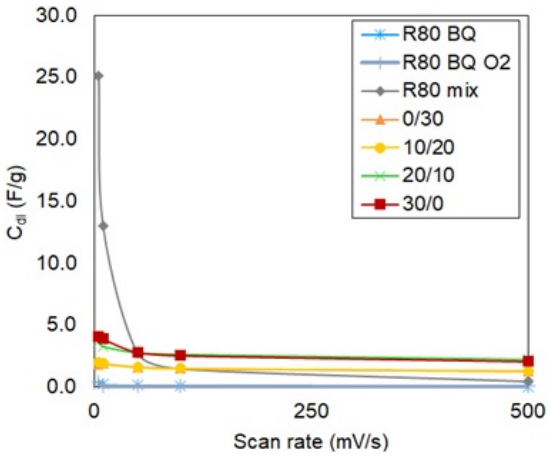


Figure III.15: Gravimetric capacitance as a function of the scan rate in the study of separation and saturation time at constant total exposure time. Data points were averaged for up to four electrodes per PCB.

Reference values cover several orders of magnitude as a function of the materials' specific/electroactive surface area. For SWCNT, Shiraishi et al. reported 45 F/g (galvanostatic chronopotentiometry in 1 M $LiClO_4$/propylene carbonate) [119]. Equally using SWCNT, 46 F/g were determined by Salinas et al. (CV in 0.5 M $H_2SO_4$, 50 mV/s) [123]. Porous carbon electrodes with high developed SSA cover a broad range of several 100 F/g [124] [125]. The order of magnitude diverges significantly from results in this project, suggesting that either the referenced values are not directly comparable, or that the specific/electroactive surface was rather small.

One particular aspect regarding the gravimetric capacitance is the custom of referencing the measured capacitance to the amount of active material, instead of the entire electrode weight [126] [125]. The solid fraction of carbon inks typically contains 82 to 95 % active material [44] [127][4]. The concentration of solvent is neglected, as it is extracted during electrode preparation. Applying the estimative correction to the calculation changes the gravimetric capacitance only marginally, however, see III.15 and Table III.5 with unchanged tendencies.

[3]For the dried R80 BQ ink, 0.225 mg/electrode were calculated and around 0.9 mg/deposit for diluted R80 BQ-EGDA.

[4]An approximate determination for the polymer using BQ242 ink composition is considered highly interesting for a potential future project aiming to identify an adapted ink composition.

Table III.5: Calculated gravimetric capacitance in the study of separation and saturation time at constant total exposure time for CV at 5 mV/s in 1 M KCl.

| **Description** | $\mathbf{C}_{gravimetric}$ **(F/g)** | $\mathbf{C}_{gravim.,corrected}$ **(F/g)** | **Increase** |
|---|---|---|---|
| R80 BQ | 0.219 | 0.231 | 1.0 |
| R80 BQ $O_2$ | 0.382 | 0.402 | 1.7 |
| R80 BQ-EGDA | 25.121 | 26.443 | 114.5 |
| 0/30 | 1.839 | 1.936 | 8.4 |
| 10/20 | 1.975 | 2.079 | 9.0 |
| 20/10 | 3.642 | 3.834 | 16.6 |
| 30/0 | 4.082 | 4.297 | 18.6 |

An impedance-based study from Suss et al. on porous carbon electrodes linked the capacitance to the pore size of electrodes, differentiating between larger "transport" pores with SSA smaller than 10 $m^2/g$ and smaller "storage" pores with SSA of several hundred $m^2/g$ [115]. In particular, the capacitance of transport pores was calculated to 2.5 F/g, whereas storage pores displayed capacitances of 46.0 F/g. Before comparing the values to results of this project, however, it is pointed out, that studied electrodes featured pores with diameters up to 1 nm before activation and up to 3 nm after activation. It is not clear, up to which extent this correlates with structured ink electrodes, as no confirmation of features on that particular scale of dimension was possible. Still, the cited literature is interesting for interpreting the calculated gravimetric capacitances. On the one hand, it could confirm the absence of a highly capacitive structure for undiluted R80 BQ electrodes, as gravimetric capacitances are low in comparison. For diluted R80 BQ-EGDA electrodes, results suggest the presence of a certain degree of micropores, comparable to storage pores in the publication. Structured electrodes exceed the gravimetric capacitance reported for transport pores, eventually due to mixed contribution by pores in the sub-µm and nm-range.

#### 3.1.2.4 Faradaic current studies

CV in 1 mM ruthenium hexaamine, 1 M KCl were carried out to study the electrodes' charge transfer characteristics. The background[5] was subtracted for an easier visual comparison of the current responses, e.g. in order to remove the capacitive contribution. Further, in most cases, the step helped suppressing redox peaks originating from contamination.
The CV are displayed as before, for four positions on one PCB for slow scan rates, to highlight the deviation of electrodes prepared during the same protocol (Figure III.16). CV of selected electrodes are shown at different scan rates. The small peaks in b1), c1) and d1) are a result of Faradaic peaks, resulting from contamination, which were not entirely cancelling out upon subtraction of the background.

[5]The background refers to CV measured in 1 M KCl under otherwise equivalent measurement conditions, electrode placement and temperature.

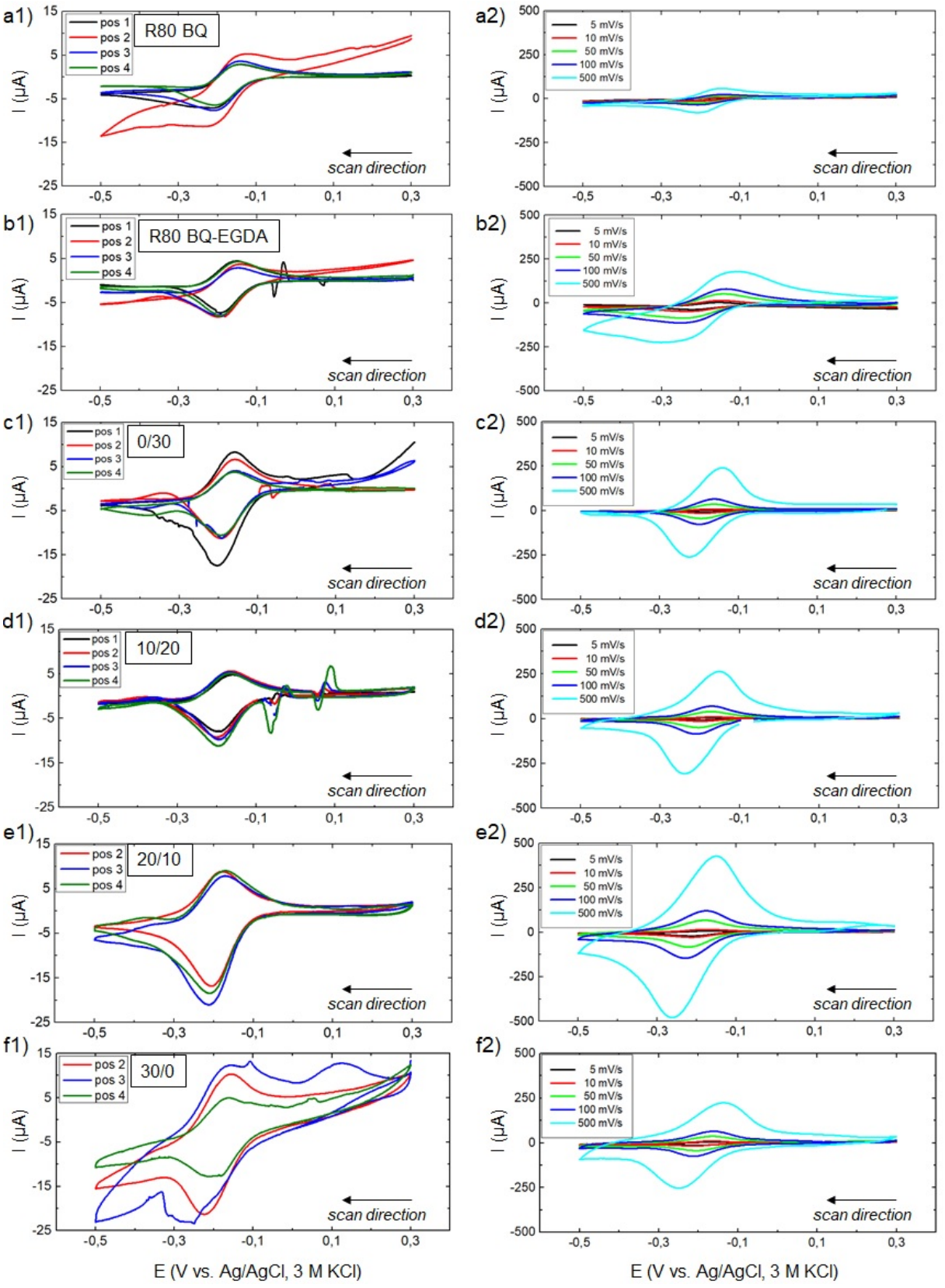


Figure III.16: Faradaic currents of structured ink at in 1 M KCl, 1 mM ruthenium hexaamine in the study of separation and saturation time at constant total exposure time. Series 1 at 5 mV/s for all electrodes per PCB, series 2 for different scan rates of one electrode. a) R80 BQ, pos. 2 in detail; b) R80 BQ-EGDA and pos. 1; c) 0/30 and pos. 4; d) 10/20 and pos. 2; e) 20/10 and pos. 3; f) 30/0 and pos. 4. The $5^{th}$ cycles are displayed. Onset at 0.3 V. All electrodes were plasma-treated.

A first visual impression is the homogeneity of current responses, which are mostly very similar for two to three electrodes per PCB. Deviating curves, e.g. position 2 in a1) or position 4 in f1) are not included in the further extraction of data. By means of the Python script, peak-to-peak separation ($\Delta E_{peak}$), peak height ($I_{ox}$ and $I_{red}$) and peak ratio ($I_{ox}/I_{red}$) were determined as presented in Table III.6, which is to be seen as supportive information. The values were normalized against the geometric surface, covered by the electrodes, to prepare the Figures III.17 and III.18.

Table III.6: Peak separation, peak current and peak ratio extracted from CV in 1 mM ruthenium hexaamine, 1 M KCl in the study of separation and saturation time at constant total exposure time.

| $v_{scan}$ (mV/s) | R80 BQ | R80 BQ $O_2$ | R80 BQ-EGDA | 0/30 | 10/20 | 20/10 | 30/0 |
|---|---|---|---|---|---|---|---|
| $\Delta E_{peak}$ (mV) | | | | | | | |
| 5 | 64.9 | 66.0 | 68.1 | 38.1 | 33.4 | 32.2 | 31.9 |
| 10 | 64.8 | 64.1 | 77.9 | 38.1 | 29.9 | 34.4 | 38.6 |
| 50 | 64.9 | 61.3 | 96.9 | 40.6 | 33.4 | 45.9 | 42.8 |
| 100 | 64.4 | 58.9 | 104.0 | 52.1 | 37.3 | 60.2 | 56.0 |
| 500 | 64.0 | 58.3 | 147.3 | 103.0 | 83.4 | 127.3 | 122.23 |
| $I_{ox}$ (µA) | | | | | | | |
| 5 | 4.3 | 4.8 | 17.1 | 9.1 | 5.8 | 10.5 | 9.6 |
| 10 | 6.1 | 6.8 | 26.9 | 13.5 | 10.1 | 17.8 | 11.0 |
| 50 | 12.9 | 15.4 | 36.2 | 40.8 | 33.2 | 69.0 | 45.8 |
| 100 | 17.8 | 22.0 | 43.6 | 75.2 | 60.9 | 132.7 | 79.0 |
| 500 | 39.4 | 51.5 | 83.7 | 252.7 | 214.7 | 444.0 | 195.4 |
| $I_{red}$ (µA) | | | | | | | |
| 5 | -4.6 | -4.9 | -18.9 | -11.7 | -8.8 | -17.0 | -11.9 |
| 10 | -6.1 | -6.8 | -28.6 | -16.0 | -13.9 | -25.8 | -13.9 |
| 50 | -12.7 | -15.3 | -40.5 | -44.3 | -44.9 | -79.8 | -52.6 |
| 100 | -17.8 | -22.9 | -47.2 | -76.9 | -85.1 | -133.7 | -87.9 |
| 500 | -40.3 | -61.1 | -108.2 | -259.9 | -270.3 | -411.5 | 237.8 |
| $I_{ox}/I_{red}$ | | | | | | | |
| 5 | -0.97 | -0.97 | -0.91 | -0.77 | -0.67 | -0.62 | -0.81 |
| 10 | -1.00 | -1.00 | -0.94 | -0.84 | -0.73 | -0.69 | -0.79 |
| 50 | -1.01 | -1.01 | -0.89 | -0.92 | -0.74 | -0.87 | -0.87 |
| 100 | -0.99 | -0.96 | -0.92 | -0.98 | -0.72 | -0.99 | -0.90 |
| 500 | -0.99 | -0.84 | -0.77 | -0.97 | -0.79 | -1.08 | -0.82 |

Undiluted, dried R80 electrodes without plasma treatment, see Figure III.16 a), present a reversible electron transfer, indicated by the ratio of anodic to cathodic peak current close to one. Further, quick charge transfer kinetics are interpreted based on the peak-to-peak separation, which is only slightly larger than for an ideal, reversible one-electron transfer and displays no dependence on the scan rate[6].
The plasma-treated R80 electrodes distinguish themselves by $\Delta E_{peak}$ values, which start at comparable values as the non-treated electrodes for slow scan rates. However, upon faster cycling, a decrease to 59 mV is observed. This is unusual, but possible within the error of the technique. Reductions of $\Delta E_{peak}$ following an oxygen plasma treatment of

[6]Shifted oxidation/ reduction potentials are generally linked to an increased activation energy, required for one of the charge transfers during oxidation/ reduction to take place. The oxidation peak, in consequence, is observed at higher polarization than ideally expected, which is 2.218 RT/F relative to the reduction peak for a reversible, single-electron transfer and translates to around 57 mV at 25 ℃ [128].

screen-printed carbon electrodes were reported by Wang et al. [129] and it was reasoned, that the impurities, oils and binder were partially removed from the electrode's surface, comparable to a plasma cleaning. Furthermore, the creation of basal-plane defects in the graphite flakes was proposed based on SEM images, potentially increasing the availability of oxygenated edge plane sites which exhibit faster electron transfer [7].

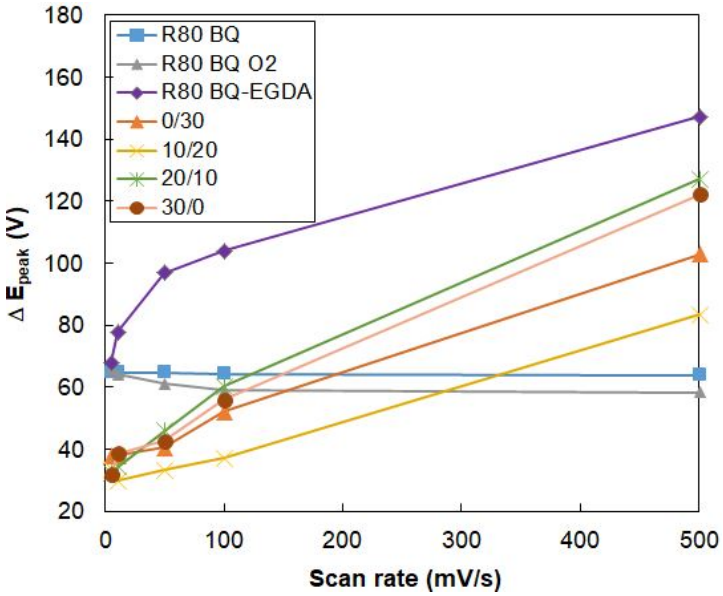


Figure III.17: Peak separation as a function of the scan rate in the study of separation and saturation time at constant total exposure time.

The curves for diluted, non-structured R80 BQ-EGDA electrodes show broadened oxidation and reduction peaks, which can be a sign of altered surface chemistry. Potentially, additional chemical processes are taking place before or after the electron transfer and modify the activation energy/ overpotential, required for the oxidation or reduction reaction [130]. This hypothesis coincides with the peak ratio, which is deviating from one. The reduction peaks are larger than the oxidation peaks, particularly for faster scan rates, suggesting that the reaction or one of its steps is of lowered electrochemical reversibility. The peak-to-peak separation allows for supporting observations in the form of increasing values between 68 mV (5 mV/s) up to 147 mV (500 mV/s). The development of values with increasing scan rate resembles the typical shape of a natural logarithm function, corresponding to the theory of peak-to-peak separation for an irreversible reaction, see equation III.1.
The electrochemical behaviour potentially supports the theory of graphite platelets aligning parallel to the electrode surface, as slower charge transfer is expected for basal-plane graphite. A proposed explanation is the requirement of different overpotentials for the initiation of charge transfer between graphite platelets. In addition, the variety of oxygenated groups on the basal planes, i.e. their (electro)chemical difference, may account for the increased peak width. In this context,

$$\Delta E_{peak} = \frac{RT}{F} ln(\nu) + cst \tag{III.1}$$

The structured electrodes display peaks of slightly increased width, compared to R80 BQ electrodes, but narrower than for diluted R80 BQ-EGDA electrodes. The oxidation

[7] From CV in 50 mM phosphate buffer and at 50 mV/s, the peak-to-peak separation was determined to 109 mV (pre-plasma) and 76 mV (post-plasma).

and reduction overpotentials thus appear well-defined. The peak ratios are slightly lower than for the diluted R80 BQ-EGDA electrodes, suggesting that the structuration limits electrochemical reversibility to a certain degree.
A particularity consists in the characteristic of structured electrodes, for which $\Delta E_{peak}$ displays lower onsets between 30 and 40 mV and remains largely unchanged up to 50 mV/s. At more than 100 mV/s, the 59 mV limit is passed. Other research groups have studied systems which displayed small peak-to-peak separations as low as 0 mV, reported as symmetric characteristic, for example on carbon nanotubes [131]. Alternatively, the behaviour is referred to as thin-layer type behaviour for a given scan rate, when the redox probes involved in the current response are located in the vicinity of the electrode surface. This can be explained by a certain degree of their confinement, adsorption or physical confinement in a structure. In consequence, a reduced activation energy/ overpotential is expected for the oxidation/reduction to occur and $\Delta E_{peak}$ follows accordingly. At fast scan rates, however, the charge transfer is rather limited in comparison to unstructured electrodes. One explanation are insufficient charge transfer kinetics, potentially caused by the addition of EGDA to the ink. Alternatively, restricted diffusion of analytes and supporting electrolyte could play a role[8]. Further, reduced electrical conductivity of the structured ink is likely due to larger spacings between graphite flakes.

Figure III.18 displays $J_{peak}$ vs. a) the root of the scan rate and b) vs. the scan rate. The Randles-Sevcik equation (III.2) describes the linear relation of $I_{peak}$ vs. the square root of the scan rate for an electrochemically reversible charge transfer involving $n$ electrons, the electroactive surface area $A_{Randles}$ and the diffusion coefficient $D_0$ (in the following $D_{HexRu(II)}$) for the redox probe with bulk concentration $C^0$.

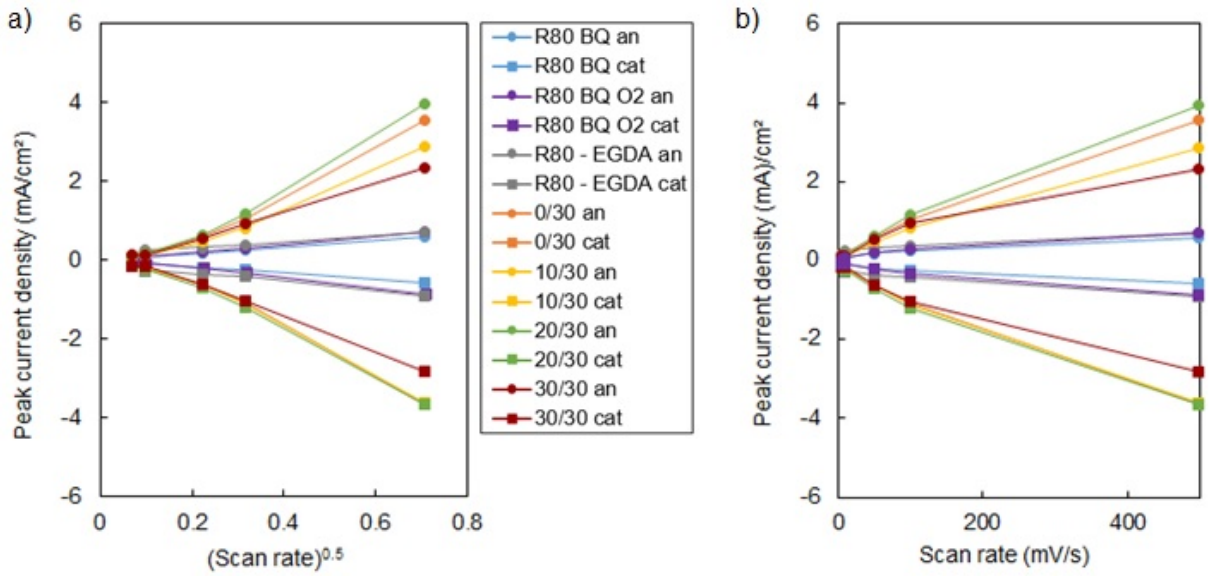


Figure III.18: Comparison of peak current densities in 1 mM ruthenium hexaamine, 1 M KCl in the study of separation and saturation time at constant total exposure time. Data extracted from CV in 1 mM ruthenium hexaamine, 1 M KCl.

$$I_p = 0.446nFA_{Randles}C^0\sqrt{\frac{nF\nu D_0}{RT}} \tag{III.2}$$

[8]The argument deserves discussion, as the $5^{th}$ cycles of CV are presented and analytes already have diffused/migrated into the pores.

Linearity of the plots is associated with unrestricted diffusion, whereas a low degree of linearity indicates limited diffusion. In the latter case, plotting $I_{peak}$ versus the scan rate allows to verify, whether the charge transfer involves surface-adsorbed species [132].
Linearity of the trend lines for anodic and cathodic peaks are averaged and listed in Table III.7. In this case, the current is replaced with the current density.

On this base, dried, undiluted electrodes exhibit a high degree of linearity for the plots versus the root of the scan rate, but a lower degree of linearity for the plot versus the scan rate. This implies unhindered diffusion of redox species and could confirm the hypothesis that the low degree of structure, observed previously, does not considerably extent into the bulk of the electrodes. An important conclusion for the non-structured R80 BQ electrodes is therefore the validity of applying the model of linear, semi-infinite diffusion on a planar electrode[9].
The addition of EGDA to the ink seems to slightly limit free diffusion, as indicated by the lower linearity in the plot against the square root of the scan rate. By considering the pronounced increase of $\Delta E_{peak}$ upon faster scan rates, it is possible to assign the addition of EGDA with a reduced reversibility (quasi-reversibility) of the charge transfer and to exclude adsorption [132].

Table III.7: Linearity of peak current density plots versus the scan rate and its root in the study of separation and saturation time at constant total exposure time. Data extracted from CV in 1 mM ruthenium hexaamine, 1 M KCl.

| | $\mathbf{R^2}$ **of** $\mathbf{J_{peak}}$ **vs.** $(\nu_{scan})^{0.5}$ | $\mathbf{R^2}$ **of** $\mathbf{J_{peak}}$ **vs.** $\nu_{scan}$ |
|---|---|---|
| **R80 BQ** | 0.999 | 0.958 |
| **R80 BQ O2** | 0.997 | 0.972 |
| **R80 BQ-EGDA** | 0.989 | 0.960 |
| **0/30** | 0.980 | 0.991 |
| **10/20** | 0.983 | 0.992 |
| **20/10** | 0.986 | 0.998 |
| **30/0** | 0.997 | 0.968 |

The structured electrodes behave generally inversely, displaying lower degrees of linearity in the plot against the root of the scan rate, which is a sign of altered mass transport, respectively limited diffusion. Correspondingly, high degrees of linearity are observed in the plot against the scan rate. However, as the formalism is intended for application on planar electrodes, no clear separation between the effect of adsorption and the effect of physical entrapment is possible from the curves alone. Under the hypothesis, that structured, diluted electrodes behave electrochemically similar to their non-structured counterparts, adsorption is considered not to play a major role. In consequence, the observations are explained by the generation of structure.
This is of particular interest when taking a closer look on the data derived from structured electrodes. A tendency towards more freely diffusing, less entrapped analytes is noticed for shorter saturation times $t_{sat}$, potentially indicating the importance of the saturation step for the generation of porosity.
In this context, a comparison of absolute peak current densities reveals a clear increase for structured electrodes (120 µA/cm$^2$, 5 mV/s, 20/10) compared to nonstructured electrodes (70 µA/cm$^2$, 5 mV/s, R80 BQ $O_2$). As all electrodes underwent plasma treatment, this confirms not only the generation of structure, but validates the increase in electroac-

[9]The electrode is considered as a solid surface from which the diffusion layer extends to one direction into the electrolyte.

tive surface area. The determination of a particular tendency as a function of process parameters, however, is not clear.

#### 3.1.2.5 Calculation of electroactive surface from Faradaic current studies

The charge transfer for non-structured, dried electrodes is considered to fulfill the criteria for (electro-)chemical reversibility, which are a peak-to-peak separation following the Nernst law, an independence of the peak-to-peak separation from the scan rate, a ratio of peak currents close to one and peak currents being of linear dependence to the square root of the scan rate. In consequence the electroactive surface area can be calculated by rearranging equation III.2. In literature, the diffusion coefficient of ruthenium hexaamine (II) is 6 $\times 10^{-6}$ cm$^2$/s in 0.1 M phosphate buffer and 0.1 M KCl[10] [133].
Alternatively it is taken into consideration, that data were extracted not from the first, but the fifth cycles of cyclic voltammetric experiments which already display a certain degree of stabilization, respectively of deviation from the initial shape of CV. The multi-scan cyclic voltammetry was mathematically studied in detail by Oldham and a modified formalism proposed for the "ultimate" CVs attained after an infinite number of cycles (III.3). The expression resembles the Randles-Sevcik equation except for a changing prefactor [134].
Assuming the fifth cycles of CV to be reasonably close to their ultimate form, the formalism was equally applied. Results are listed in Table III.18, including the factors of surface increase relative to $A_{geo}$ of electrodes for fast scan rates due to reasons detailed below.

$$I_p^O = 0.3708FAC^0\sqrt{\frac{F\nu D_0}{RT}} \tag{III.3}$$

Focusing on dried R80 BQ and R80 BQ-EGDA electrodes, a slight decrease in electroactive surface is observed for faster scan rates, similar to literature. Zhu et al. assumed, that the thickness of the diffusion space plays a major role and slow scan rates generally imply farther diffusion of analytes, which could lead to misinterpreting the results [135]. Thus, slow scan rates might eventually lead to an overestimation of the electroactive surface area of electrodes, which comply with the criteria for linear, semi-infinite diffusion.
Inversely, for porous electrodes it was shown, that slow scan rates are coupled with an underestimation of electroactive surface area. Specifically when the diffusion space of ions exceeds the dimension of pores, the electrode experimentally behaves rather like a planar electrode. Chan et al. [136] studied the simulation of voltammetric studies of complex, porous electrodes and concluded that theoretically, an infinitely fast scan rate would allow to reduce the diffusion layer to an infinitesimally thin, one-dimensional diffusion space orthogonal to the electrode's surface. In turn, this would allow applying the Randles-Sevcik equation.
Adopting the theory for both non-structured and structured electrodes, electroactive surfaces were estimated to correspond to the results for 500 mV/s.
For R80 BQ electrodes, results based on the Randles-Sevcik and Oldham formalisms are close to the geometric electrode surface with increases of 1.22 to 1.46. This aligns with expectations based on SEM images. The hypothesis regarding the influence of scan rate appears confirmed. Plasma-treated R80 BQ-EGDA electrodes yield an electroactive surface, which is 1.85 to 2.22 times larger than $A_{geo}$ and corresponds to an increase of around 50 %, exceeding the literature value of 30 % [118]. Interestingly, faster cycling lead to larger electroactive surface values for the plasma-treated electrodes, while the behaviour

[10]Wang et al. provided diffusion coefficients for 0.1, 0.3 and 0.5 M KCl, which were logarithmically fitted and extrapolated in this project, yielding the diffusion coefficient used for 1 M KCl.

was expected to be as for the R80 BQ electrodes. The exposure to plasma may therefore have resulted in a slight increase of porosity.

Another alternative approach was adopted, since ideal electrochemical reversibility of the electron transfer on diluted, structured electrodes was questioned. In literature, a modified Randles-Sevcik equation for irreversible charge transfer is reported [128], where $\alpha$ refers to the transfer coefficient which is assumed as 0.5 for an typical irreversible process, see equation III.4. Results are equally listed in Table III.18. As the formalism takes (potentially temporally) blocked electroactive sites into consideration, the estimated electroactive surface areas are larger than for the assumption of a reversible electrochemical charge transfer. The general form of the equation remains except for the prefactor.

$$I^R_{irrev.} = 0.496\sqrt{\alpha}FAC^0\sqrt{\frac{F\nu D_0}{RT}} \tag{III.4}$$

Just to obtain an idea, irreversible charge transfer is assumed and the electroactive surface calculates as 2.61 times $A_{geo}$ for diluted R80 BQ-EGDA electrodes. Surprisingly, this is far less than the development of SSA determined in the capacitive current studies. A comparison of the factors of surface increase (relative to the R80 BQ electrodes) suggests, that the addition of EGDA increases the specific surface around 29 times, while the electroactive surface is only multiplied by three. One explanation is the aforementioned hypothesis of graphite platelet orientation parallel to the electrode surface with basal sites facing the electrolyte. As these are thought to present less electroactive sites than graphite edge-sites, a rather small electroactive surface compared to the specific surface could be expected.
Furthermore, irreversible charge transfer was equally assumed for structured electrodes. Electroactive surfaces are one order larger than $A_{geo}$ and are increased by 6 to 10 times relative to R80 electrodes. A certain influence of structuration parameters is visible, with a largest increase of electroactive surface for 20/10 electrodes. In comparison to the development of SSA, the structuration appears to lead primarily, but not exclusively, to the generation of electroactive surface.

One aspect requiring particular discussion is the diffusion layer thickness $\delta$, which is calculated from equation III.5 [137] in combination with the expressions of peak current. Following the Randles-Sevcik formalism, 106.3 µm for 5 mV/s and 5.3 µm are obtained for 2000 mV/s. Using the Oldham equation, values are calculated as 127.8 µm for 5 mV/s and 6.4 µm for 2000 mV/s. Values increase slightly for irreversible charge transfer (135.0 µm for 5 mV/s and 6.8 µm for 2000 mV/s).

$$\delta = \frac{nFAD_0C^0}{i_{peak}} \tag{III.5}$$

Following the previous idea of an infinitesimally small diffusion space, cycling should have ideally been carried out as fast as possible. However, scans acquired at 1000 mV/s or more (not displayed) lacked the required quality or peak definition for a sensible extraction of data, which possibly originated from limited charge transfer kinetics. In consequence, the scan rate was limited to 500 mV/s, implying a diffusion space of 5-12 µm (depending on the expression of peak current). As it exceeds the dimensions of micro- and mesoporosity, a certain underestimation of the real electroactive surface is possible.

Table III.8: Electroactive surface areas calculated from cathodic peaks in CV experiments studying the separation and saturation time at constant total exposure time.

| $\mathbf{v}_{scan}$ (mV/s) | R80 BQ | R80 BQ $O_2$ | R80 BQ-EGDA | 0/30 | 10/20 | 20/10 | 30/0 |
|---|---|---|---|---|---|---|---|
| $\mathbf{A}_{Randles}$ ($\mathbf{cm}^2$) | | | | | | | |
| 5 | 0.098 | 0.105 | 0.405 | 0.252 | 0.188 | 0.365 | 0.256 |
| 10 | 0.092 | 0.103 | 0.434 | 0.242 | 0.210 | 0.391 | 0.210 |
| 50 | 0.086 | 0.104 | 0.275 | 0.300 | 0.304 | 0.541 | 0.357 |
| 100 | 0.086 | 0.110 | 0.226 | 0.369 | 0.408 | 0.641 | 0.421 |
| 500 | 0.086 | 0.131 | 0.232 | 0.557 | 0.579 | 0.882 | 0.510 |
| $\mathbf{A}_{Oldham}$ ($\mathbf{cm}^2$) | | | | | | | |
| 5 | 0.118 | 0.126 | 0.488 | 0.303 | 0.226 | 0.439 | 0.307 |
| 10 | 0.111 | 0.124 | 0.522 | 0.291 | 0.253 | 0.470 | 0.253 |
| 50 | 0.104 | 0.125 | 0.330 | 0.361 | 0.366 | 0.650 | 0.429 |
| 100 | 0.103 | 0.132 | 0.272 | 0.443 | 0.491 | 0.771 | 0.506 |
| 500 | 0.104 | 0.158 | 0.279 | 0.670 | 0.697 | 1.061 | 0.613 |
| $\mathbf{A}_{Randles,irrev.}$ ($\mathbf{cm}^2$) | | | | | | | |
| 5 | 0.125 | 0.133 | 0.516 | 0.321 | 0.239 | 0.464 | 0.325 |
| 10 | 0.117 | 0.132 | 0.552 | 0.308 | 0.267 | 0.497 | 0.267 |
| 50 | 0.110 | 0.132 | 0.349 | 0.382 | 0.387 | 0.687 | 0.454 |
| 100 | 0.109 | 0.140 | 0.288 | 0.469 | 0.519 | 0.815 | 0.535 |
| 500 | 0.110 | 0.167 | 0.295 | 0.708 | 0.737 | 1.122 | 0.648 |
| $\mathbf{A}_{charge,anodic.}$ ($\mathbf{cm}^2$) | | | | | | | |
| 5 | 0.158 | 0.198 | 0.619 | 0.359 | 0.304 | 0.557 | 0.370 |
| 10 | 0.157 | 0.194 | 0.744 | 0.362 | 0.293 | 0.597 | 0.341 |
| 50 | 0.142 | 0.175 | 0.477 | 0.381 | 0.436 | 0.804 | 0.552 |
| 100 | 0.140 | 0.180 | 0.362 | 0.541 | 0.544 | 0.976 | 0.602 |
| 500 | 0.134 | 0.104 | 0.351 | 0.868 | 0.835 | 1.485 | 0.830 |
| $\mathbf{A}_{Randles}/\mathbf{A}_{geo}$ | | | | | | | |
| 500 | 1.22 | 1.85 | 2.05 | 7.85 | 8.05 | 7.88 | 7.18 |
| $\mathbf{A}_{Oldham}/\mathbf{A}_{geo}$ | | | | | | | |
| 500 | 1.46 | 2.22 | 2.47 | 9.44 | 9.68 | 9.47 | 8.63 |
| $\mathbf{A}_{Randles,irrev.}/\mathbf{A}_{geo}$ | | | | | | | |
| 500 | 1.55 | 2.35 | 2.61 | 9.98 | 10.23 | 10.02 | 9.13 |
| $\mathbf{A}_{charge,anodic}/\mathbf{A}_{geo}$ | | | | | | | |
| 500 | 1.89 | 1.46 | 3.11 | 12.22 | 11.60 | 13.26 | 11.70 |
| **Factor of increase relative to R80, Randles-style equations** | | | | | | | |
| 500 | 1.0 | 1.5 | 2.7 | 6.5 | 6.7 | 10.2 | 5.9 |
| **Factor of increase relative to R80, $\mathbf{Q}_{anodic}$** | | | | | | | |
| 500 | 1.0 | 0.8 | 2.6 | 6.5 | 6.2 | 11.1 | 6.2 |

Zhu et al. published a detailed comparison of electroactive surface areas of nickel electrodes (pore diamater 10-1000 µm), determined based on peak current and peak charge in CV [135]. The calculated, electroactive surface increased by 10-30 %, when assuming a thin-layer diffusion model based on peak charge. It was advised, not to use semi-infinite models for scan rates implying a diffusion layer of more than one third of the pore radius. Interestingly, this criterion suggests not to work with equations for the semi-infinite case in this project at all, as the smallest pores should then measure around 15 µm. The proposed charge-based approach was equally used and electroactive surface areas calculated by means of rearranging expression III.6, inserting III.5 and values for peak current, respectively charge, from measured CVs.

$$Q_{peak} = \frac{n^2 F^2 A D_0 C^2}{2\ i_{peak}}. \tag{III.6}$$

While the former models were all rather consistent regarding the surface increase as a function of the scan rate for the non-structured R80 BQ electrodes, the peak charge model yields different results.
The structured electrodes, on the other hand, mostly follow a similar trend of consistently larger surface increase, which seems to fit expectations. In the end, though, the peak charge model was not used, as the introduction of this parameter equally increased the factor of uncertainty.

#### 3.1.2.6 Chronoamperometric studies

The chronoamperometric responses and selected sections of interest of the Cottrell plots are displayed in Figure III.19. For most electrodes per PCB, the curves are rather similar in shape and peak currents are comparable, besides for exceptions such as position 4 in Figure (d1), thought to correspond to a defective electrodes and excluded from further data evaluation.
Comparing the measured current decay, a clear difference between electrodes consists in the magnitude of the current peak, which is increased by a factor of approximately 10 for the structured electrodes. According to the Cottrell equation, the only factors influencing the peak current can be the electroactive surface area or the diffusion coefficient. Since the latter is generally not affected by porosity, only a surface increase can account for the increased peak current.
Focusing on the Cottrell plots in series 2), a remarkable difference between non-structured and structured electrodes is the linearity, respectively non-linearity of slopes within the first second of current decay. It is thought, that the porous nature of structured electrodes may have played a role, as the Cottrell equation is intended for application on systems showing linear, semi-infinite diffusion. Similar observations were reported in a study of Keeley et al. on glass-like carbon modified with porous films of SWCNT [131].

Instead, the Cottrell plots in this project display the influence of limited diffusion, which requires an adaptation of the observed time scale in order to assure compatibility of the diffusion length of analytes with the definition of semi-infinite diffusion. The steep slopes in the Cottrell plots are located within a short time-frame, thus expressing diffusion on the short time scale or short diffusion lengths, respectively. Therefore, trend lines were adjusted to include only half a second of peak current decay for non-structured electrodes. Even shorter 50 ms following the peak current were selected for the plots of structured electrodes (fits not displayed). Table III.9 lists the electroactive surfaces obtained at different observation times following the current peak. Results for electrodes of the same PCB were averaged. Geometric surface areas are equally included to estimate the factors of surface increase.
One more remark addresses curves in the Cottrell plots, which in some occasions display a shift of peak current on the x-axis. As experimental conditions were identical, the sampling rate during data acquisition could be the potential source for this observation.

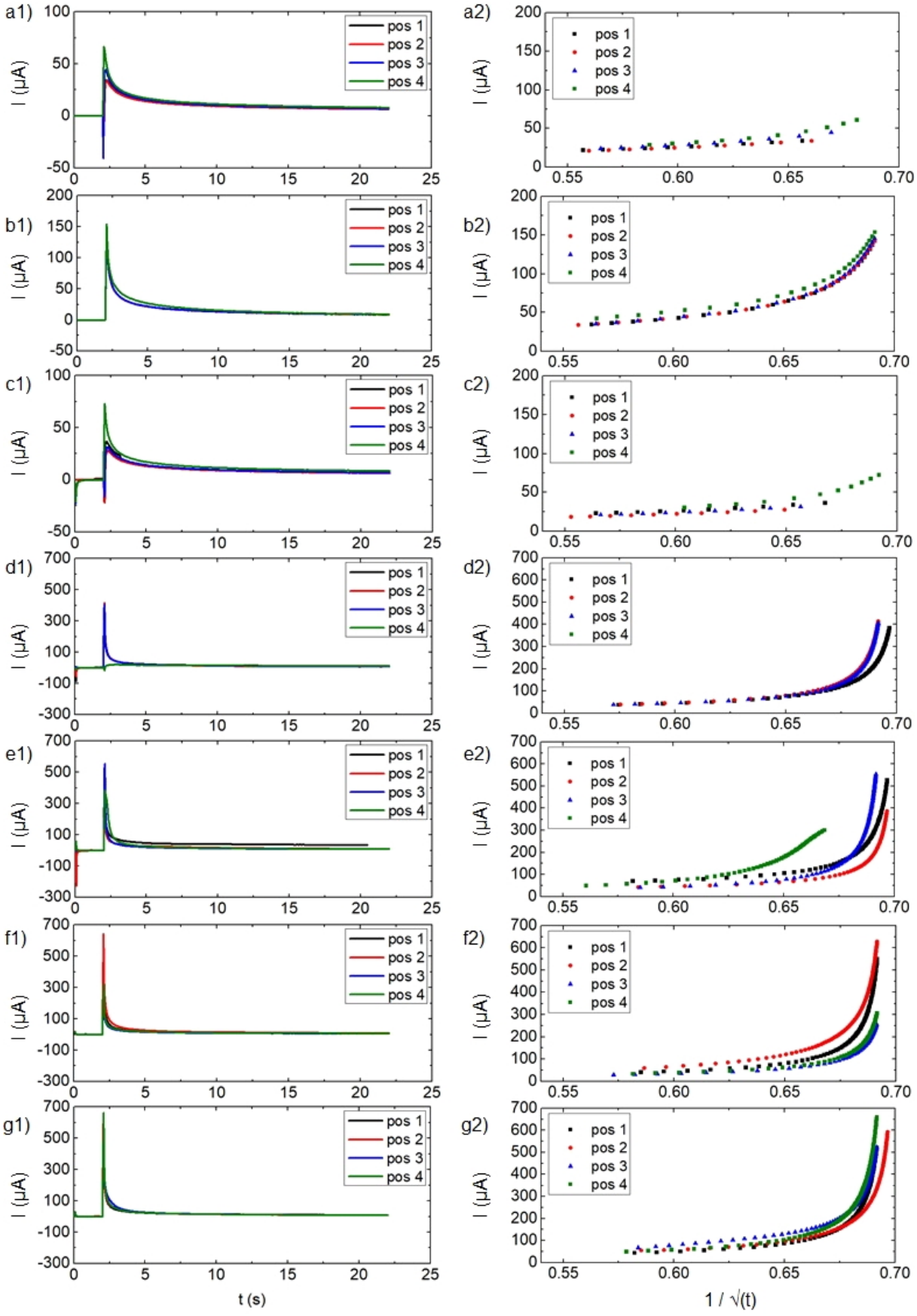


Figure III.19: Chronoamperometric responses in series 1)(0 V, 2 s and 0.7 V, 20 s in 2.5 mM hexacyanoferrate (II), 1 M KCl) in the study of separation and saturation time at constant total exposure time; a) R80 BQ; b) R80 BQ $O_2$; c) R80 BQ-EGDA; d) 0/30; e) 10/20; f) 20/10; g) 30/0. Electrodes were oxygen plasma-treated. The resulting Cottrell plots in series 2).

Table III.9: Cottrell slopes, calculated electroactive surface areas and specific surface areas for non-structured and structured carbon ink electrodes.

| | $\mathbf{A}_{geo}$ **(mm$^2$)** | $\mathbf{A}_{Cottrell}$ **(cm$^2$)** | $\mathbf{A}_{Cottrell}$ **(m$^2$/g)** | $\mathbf{A}_{Cottrell}/\mathbf{A}_{geo}$ |
|---|---|---|---|---|
| **R80 BQ, 1 s** | 7.1 | 0.18±0.08 | 0.079 | 2.5 |
| **R80 BQ $O_2$, 1 s** | 7.4 | 0.83±0.05 | 0.367 | 11.2 |
| **R80 BQ-EGDA, 1 s** | 11.3 | 0.17±0.11 | 0.045 | 1.5 |
| **0/30, 1 s** | 7.1 | 5.48±0.62 | 5.484 | 77.2 |
| **10/20, 1 s** | 7.2 | 3.81±0.86 | 3.808 | 52.9 |
| **20/10, 1 s** | 11.2 | 3.67±1.57 | 3.666 | 32.7 |
| **30/0, 1 s** | 8.4 | 4.62±0.62 | 4.619 | 55.0 |
| **R80 BQ, 0.5 s** | 7.1 | 0.17±0.05 | 0.076 | 2.4 |
| **R80 BQ $O_2$, 0.5 ms** | 7.4 | 1.45±0.07 | 0.645 | 19.6 |
| **R80 BQ-EGDA, 0.5 s** | 11.3 | 0.25±0.21 | 0.065 | 2.2 |
| **0/30, 50 ms** | 7.1 | 23.93±1.16 | 23.931 | 337.1 |
| **10/20, 50 ms** | 7.2 | 31.51±5.63 | 31.514 | 437.7 |
| **20/10, 50 ms** | 11.2 | 29.88±9.44 | 29.881 | 266.8 |
| **30/0, 50 ms** | 8.4 | 35.71±4.77 | 35.712 | 425.1 |

*****: The longer times, compared to structured electrodes, for the determination of trend lines are justified by the more linear character of Cottrell plots.

The non-structured R80 BQ and R80 BQ-EGDA electrodes yield electroactive surfaces (0.5 s observation time after peak current) of 0.172 and 0.245 cm$^2$, respectively. This corresponds to values which are, relative to the geometric surface, larger by a factor of 2.4 for R80 BQ and of 2.2 for R80 BQ-EGDA and was expected, given the somewhat structured electrode surfaces. The effect is pronounced after plasma-treating the R80 BQ electrodes, which leads to a 5-fold increase in calculated electroactive surface, possibly due to the activation of electroactive sites. The diluted R80 BQ-EGDA electrodes suggest either a lower number of electroactive sites, corresponding to their flat nature, or their electrochemical inaccessibility. The latter could in some way result from the addition of EGDA to the ink, eventually causing chemical modification.
The electroactive surface areas of structured electrodes are generally two orders of magnitude larger and no particular tendency is noted for the influence of parameter variation. Values range between 24 and 31.5 m$^2$/g, with the largest increase attained for the 10/20 electrodes. The increase of surface, relative to the geometric surface, is of factor 437, which is significantly higher than estimated by previous techniques.

By means of the averaged deposit weights determined earlier, specific surface areas were estimated (see the column in units of m$^2$/g). The values for dried R80 BQ, R80 BQ $O_2$ and R80 BQ-EGDA electrodes are up to two orders of magnitude smaller than what is referenced in literature based on nitrogen adsorption-desorption experiments (8.52 m$^2$/g in [53]), which can be explained by differences in electrode material, in electrode structure/porosity and different surface activation steps[11]. For structured electrodes, on the other hand, values range between 23.93 and 35.71 m$^2$/g which is in relatively good correlation with literature values for porous carbon ink (59.26 m$^2$/g) [53]. In addition, SSA are three times larger than what was estimated by means of nitrogen adsorption-desorption, which matches the idea of a difficult and non-representative sample preparation in that technique. Chronoamperometry, on the other hand, appears better suited.

[11]Specifically, the plasma treatment in this project was rather short, leading to the question whether longer exposure times could be beneficial and how other activation methods compare.

### 3.1.2.7 Electrochemical impedance studies

Impedance spectra (one electrode per PCB) are presented in Figures III.20 and III.21 in Nyquist and Bode plots for frequencies up to 10 kHz. As mentioned earlier, the KK-transform suggested potential non-linearity, non-stability or non-causality for the frequency range. Reducing the data set to a smaller frequency range was thought to allow for a better interpretation of the spectra, particularly as at 10 kHz the signal was thought to originate from the contact of Au collectors and ink. In the following, a general interpretation of results is given.
One common observation for all electrodes in the Nyquist plots is the small imaginary part of the impedance at high frequencies. At that end of the spectrum, the impedance is composed by mainly the electrolyte resistance, considered identical for all measurements here, plus the contact resistance between collector and electrode material, which is usually neglected. However, as the mechanical adhesion between collectors and structured ink was relatively low, some variation in contact resistance is possible and could explain the shifted 10 kHz "onsets" on the x-axis.

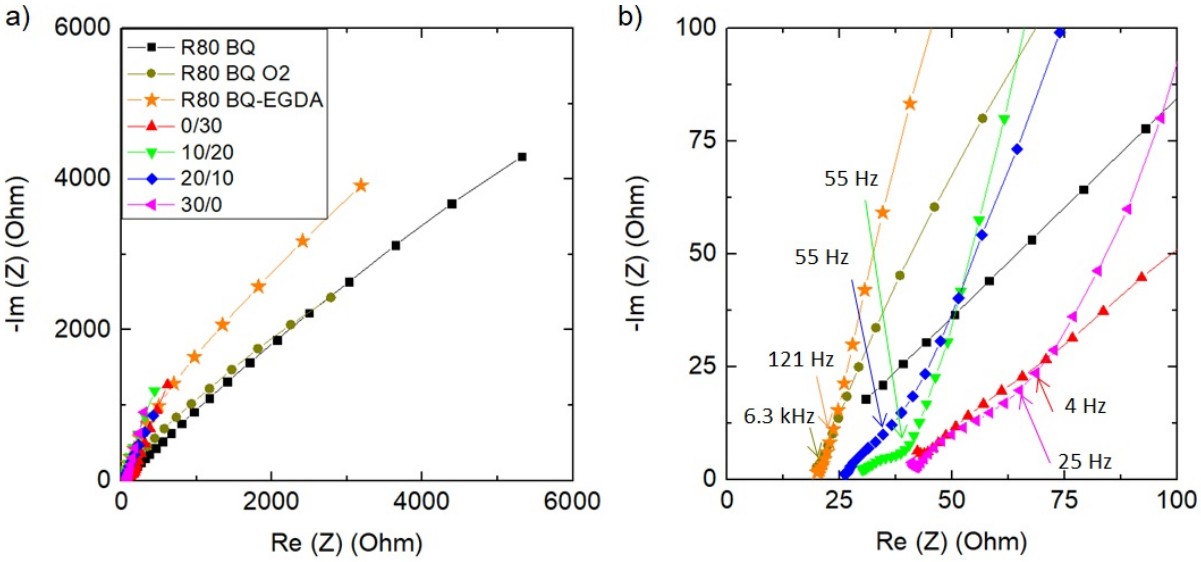


Figure III.20: (a) Nyquist plots with (b) high-frequency domains in 1 M KCl, 1 mM ruthenium hexaamine in the study of separation and saturation time at constant total exposure time.

For undiluted, R80 BQ electrodes the Nyquist plot interestingly shows no particular kinetically controlled character. Potentially, charge transfer at the dried electrodes is as fast as to result in insignificant R/C-semicircles, or requires to study the system at higher frequencies. The slope, which is seen instead over the entire frequency range, is a sign of mass-transport-related behaviour and its moderate inclination of around 45 ° suggests, diffusion of ions towards the electrode surface is the main response. In the Bode plot this is matched with an almost constant phase angle around -45 ° and a continuously curved increase of log(Z) towards lower frequencies, indicating a Warburg-impedance [138]. An exception is the high-frequency onset, with a phase angle around -30 °, which a sign of higher resistance. Ideal Warburg-type behaviour is commonly associated with (non-porous) electrodes that fulfill the criteria of linear, semi-infinite diffusion. However, R80 electrodes are slightly structured and potentially impose a diffusion limit, particularly at high frequencies. Slightly deviating phase angles may therefore be explained.

The visual difference of the plasma-treated electrode (R80 BQ $O_2$) is surprising, given that an outer-sphere redox probe was used. For high frequencies, in the Nyquist plot, a shift towards lower imaginary and lower real impedance values is observed. The mass-transfer region exhibits a steeper slope at moderate frequencies, potentially a sign of the double layer formation, before approaching 45 ° at lower frequencies.
In the Bode plot, corresponding information are the generally reduced impedance from 10 to 1 kHz, consisting in a plateau-like region with a phase angle tending towards low values.
Further, the presence of a capacitive component is indicated by the increasing phase angle below 1 kHz to around -60 °. This coincides with the end of the low-impedance plateau, also referred to as cut-off frequency of the capacitive component[12]. At low frequencies, the phase angle approaches -45 °, associated with a Warburg-character and linear, semi-infinite diffusion.
As the plasma treatment can not have lead to increased charge transfer of ruthenium hexaamine with oxygenated surface groups, the effect has to be of different nature. It is suspected, that the plasma treatment had a certain cleaning effect on the electrode/electrolyte interface and may have lifted off the outermost electrode layer. Potentially, this step may have revealed more carbon particles, leading to the increased capacitive behaviour.

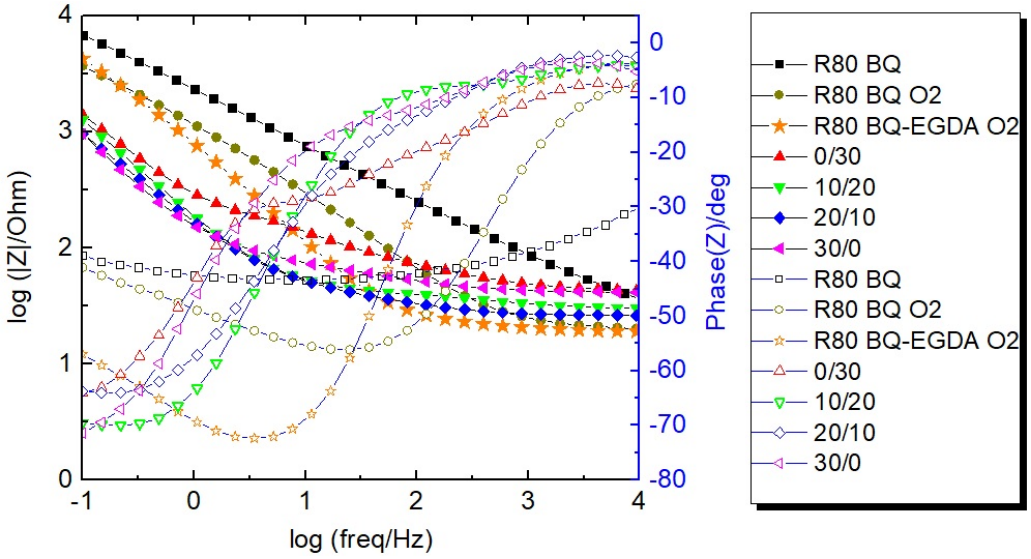


Figure III.21: Bode plot for electrodes in the study of separation and saturation time at constant total exposure time. EIS was performed in 1 M KCl, 1 mM ruthenium hexaamine.

The dilution of ink with EGDA, subsequently dried and plasma-treated (R80 BQ-EGDA $O_2$), resulted in Nyquist plots of similar $R_s$ and slope at high frequencies, as the R80 BQ $O_2$ electrodes. Towards lower frequencies, a different response is expressed by the steeper slope, before showing a mass-transport behaviour similar to the other non-structured R80 electrodes. The general impression is a "distortion" of the non-diluted R80 BQ $O_2$ response towards higher -Im(Z) values.
The Bode plot reveals, that the high-frequency, low-impedance domain is extended further, before charging effects occur (relative to R80 BQ $O_2$). Consequently, based on

[12]The expression applies, when discussing the impedance from low to high-frequencies in a R/C-circuit, for the frequency that shortens the capacitor, leading to current flowing over the resistance.

studying the phase angle, a shift of the cut-off frequency is noticed. Furthermore, a more pronounced capacitive character is distinguishable around 400 Hz, before decreasing at the low frequency end of the spectrum.

The structured electrodes present several differences. First, the high-frequency onset of spectra is shifted for each electrode/ set of parameters to higher real impedance values. Electrodes of the 0/30 and 30/0 protocol yield comparable onsets, while it is lowest for the 20/10 electrode. This trend appears to be in coherence with previous tendencies of other experiments, but no particular explanation has been identified so far. The high-frequency response of structured electrodes was expected to be rather similar.
Second, continuing towards lower frequencies, R/C semicircles are indicated, which appear to be largest for the 0/30 and the 30/0 electrodes and smallest for the 10/20 electrode. The R/C semi-circles are generally suppressed/overlapping with the mass-transfer region and their distinction is clearest for the 10/20 electrode. Besides for the obvious difficulty regarding the determination of charge transfer resistance values, the observation is potentially interesting. The curves qualitatively resemble works on porous electrodes with variations in pore geometry, size and levels of hierarchy [139].
Third, in the mass-transport range, slopes are of irregularly increasing steepness, starting at around 45 ° before adopting values which clearly exceed 45 °. While the latter suggests capacitive character (the transition for the 0/30 electrode is out of view), the different mass-transfer characteristics are similar to what has been assigned to anomalous diffusion [140], that varies from the semi-infinite case.
The Bode plots clearly display the near-ideal resistive character at high frequencies with phase angles smaller than -10 ° until 1000 to 100 Hz. No clear cut-off frequencies are extractable, as the transition from resisitive to capacitive character is rather continuous. Phase angles increase up to -70 ° at low frequencies, highlighting the pronounced capacitive contribution. At 100 mHz, impedance values are around one order of magnitude smaller than for dried electrodes.

The fit of equivalent circuits to the measured EIS data required a base model, from which on further adjustments could be done. Literature suggests, that the Randles-type cell is a simple and universal basic description for charge transfer on an electrode [141]. The first element consists of the series resistance $R_s$, representative for contributions from electrolyte, cabling and eventually from the collector/ink interface. The traditional R/C semicircle is formed by charge transfer resistance (also polarization resistance) on the electrode/electrolyte interface ($R_{CT}$) and capacitive behaviour, i.e. charging of the double layer ($C_{DL}$). In this case, the capacitance was exchanged by a constant phase element ($Q_{DL}$), to account for non-ideal/pseudocapacitive character [142]. To describe mass transfer on a porous surface of unknown behaviour, different diffusion elements were then introduced following $R_{CT}$.
Besides for a Warburg element for semi-infinite diffusion ($Z_W$)[13], restricted diffusion ($Z_M$) and anomalous diffusion ($M_g$) were studied. The resulting equivalent circuit (Figure III.22 a)) principally coincides with the order of complexity observed for the system, specifically the Bode plots show one plateau region for log(Z), which indicates one time constant [141], i.e. one semi-circle. The indicator of fit quality, $\chi^2$, is listed in Table III.10 for different equivalent circuits.

[13]The BioLogic equivalent circuit fitting tool distinguishes between two Warburg elements for an infinitely wide diffusion layer and semi-infinite diffusion.

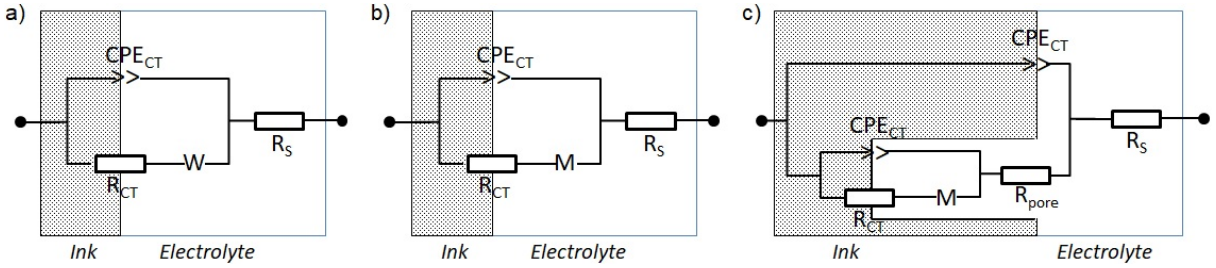


Figure III.22: Equivalent circuits proposed to describe the ink-based electrodes a) simple Randles-cell with Warburg impedance and b) for anormal diffusion, c) a more complex model proposed for porous electrodes and anormal diffusion.

The fits for the initial Randles-cell (a) are rather poor, as highlighted by $\chi^2$, which should approach zero for a good fit. Instead, a non-adapted equivalent circuit is indicated. With the Randles-type cell, best fits were obtained when assuming anomalous diffusion (b). As measured data for structured electrodes resemble impedance spectra published by Suss et al. on electrodes with hierarchical/bimodal porosity [115], the complexity of equivalent circuits was adapted likewise, as in Figure III.22 c). While the quality of fits improved, it is not advised to arbitrarily increase the number of circuit elements when the material-related characteristics of measured electrodes are unknown. Maintaining a better control over the physical relevance of the equivalent circuit, further data evaluation is limited to the less complex circuit b) and all interpretation is of estimative nature only.

Table III.10: Quality of fit for different equivalent circuits with values rounded to the nearest tens.

| **Description** | $\chi^2$ **fit a)** | $\chi^2$ **fit b)** | $\chi^2$ **fit c)** |
|---|---|---|---|
| **R80 BQ** | 7380 | 3350 | 2930* |
| **R80 BQ $O_2$** | 74580 | 5640 | 460* |
| **R80 BQ-EGDA** | 15330 | 8300 | 2770 |
| **0/30** | 446220 | 2430 | 750 |
| **10/20** | 15990 | 2200 | 800 |
| **20/10** | 13790 | 2130 | 520 |
| **30/0** | 74300 | 4690 | 1280 |

Equivalent circuits: a) $R_s$-Q//($R_{CT}$+W); b) $R_s$-Q//($R_{CT}$+M); c) $R_s$-$Q_{interface1}$//($R_{pore}$+$Q_{interface2}$//$R_{CT}$)

Parameters for the circuit elements are listed in Table III.11, which allows to compare $C_{DL}$ calculated from equation III.7 [143]. The CPE parameter $Q^0$ is linked to $C_{DL}$ via the frequency corresponding to the maximum of the half circle $f"_{max}$, where $\omega = 2\pi f$, and the CPE coefficient $\alpha$[14]. For better accuracy, $f"_{max}$ was read out from Bode plots at where the phase angle equals 45 °.

$$C = Q^0(\omega"_{max})^{\alpha-1} \tag{III.7}$$

[14]Ideally, the value for a smooth surface is 1, smaller than 1 for a rough surface and 0.5 for a porous surface. It is not certain that a value $\alpha$ smaller than 0.5 is valid and it may indicate the range of uncertainty.

Table III.11: Key circuit parameters determined from equivalent circuit b).

| | $R_s$ (Ω) | $Q^0$ (mF.s$^{(a-1)}$) | $\alpha$ | $f"_{max}$ (Hz) | $R_{CT}$ (Ω) | C (µF) | $C_{norm}$ (mF/cm$^2$)$^+$ |
|---|---|---|---|---|---|---|---|
| **R80 BQ** | 13.6 | Not determined* | | | | | |
| **R80 BQ $O_2$** | 19.8 | 0.29 | 0.4 | 9.7 | -* | 25 | 0.37 |
| **R80 BQ-EGDA** | 20.5 | 0.15 | 0.9 | 7.2 | -* | 87 | 0.77 |
| **0/30** | 39.4 | 0.58 | 0.6 | 1.0 | 120 | 257 | 3.60 |
| **10/20** | 28.0 | 0.56 | 0.6 | 1.7 | 14 | 216 | 3.00 |
| **20/10** | 25.5 | 1.13 | 0.7 | 1.6 | 30 | 514 | 4.57 |
| **30/0** | 40.2 | 0.67 | 0.7 | 1.3 | 35 | 355 | 4.33 |

*No R/C semi-circle distinguishable in Nyquist plot; $^+$ Normalized by the geometric surface of electrodes.

Before interpreting the results, it is pointed out, that the fit obtained for the R80 BQ $O_2$ electrode is considered poor, as the CPE coefficient should not be less than 0.5.
The results, although only estimations, eventually indicate interesting tendencies. The series resistance for structured electrodes is lowest for the 20/10 electrode. The charge transfer resistance is slightly increased for all structured electrodes, with a potentially erroneous value for the 0/30 electrode, when judging by the otherwise rather small values for longer separation times $t_{sep}$. Further, as the value is principally a function of the total electrode/electrolyte interface, the tendency of values approximately aligns with previous experiments, that indicated a maximum surface increase for the 20/10 electrode.
Calculated capacitances, thought to correspond to the total specific surface area, are increased by a factor of 10 to 20 for structured electrodes, corresponding rather well to what was determined based on capacitive current studies. A maximum development is seen for the 20/10 electrode.

### 3.1.3 Conclusion of studying the ratio separation to saturation time at constant total exposure time

This section served as detailed demonstration of the physical and electrochemical experimental techniques, employed to study the electrodes. During their preparation, the ratio of separation to saturation time was varied, refering to the exposure of ink to supercritical $CO_2$. Results were interpreted to obtain an idea about the development of porosity, as well as specific and electroactive surface.
Digital microscopy revealed a different visual appearance of electrodes when working with masks of different height to contain the ink. The lowest degree of surface homogeneity was attained for "well-contained" ink in deep cavities. During the dynamic step of phase separation, the phase of low polymeric content is potentially retained in deep cavities, leading to an irregular crystallization of the polymer upon $CO_2$ extraction. For future electrode preparation, despite the better preservation of a filigree structure, the use of sufficiently thin masks is advised, while ink overflow is to be avoided.
The development of height, associated with the generation of total porosity for a fixed volume of deposited ink, was observed to peak for the 10/20 electrodes for two different volumes of ink. The estimative determination of generated volume seemed to confirm this tendency, however the technique was found to display drawbacks related to the sample preparation and a potential lack in precision. A summary of the height and volume studies is presented in Figure III.23, illustrating the arc-shaped trend of results.

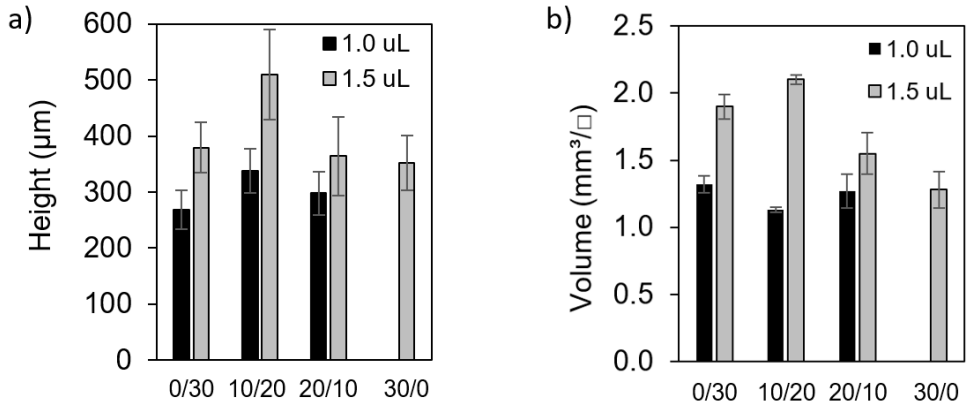


Figure III.23: Results for a) height (single measurements) and b) volume development for $scCO_2$-structured ink deposits (averages of 4 deposits). The ratio separation time ($t_{sep}$) to saturation time ($t_{sat}$) at constant total exposure time was studied. Two sets of deposits samples were prepared using different ink volumes.

SEM images confirmed the occurence of phase separation as primary structure-generating mechanism, increasing surface porosity. While all electrodes featured a structured surface with pores measuring several microns in diameter, the visual character after structuration is distinct, corresponding to a fast demixing process of electrodes' outer layer. Transversal images of electrodes display smaller pores in the volume, which aligns with expectations as the diffusion of fluids (solvents, non-solvent) is thought to limit the phase separation in the bulk. Interestingly, the generation of porosity peaked for 20/10 electrodes, suggesting that an extended exposure of ink to sub-critical $CO_2$ could be detrimental for creating maximum porosity. Alternatively, this observation could support the requirement of a certain minimum saturation time associated with the second structure-generating step (polymer foaming). A complementary study is part of the next section.
Estimative image treatments yielded multimodal pore size distributions with the main populations measuring less than 100 nm. Potentially, ink structuration slightly reduced the size of smallest pores. A second set of populations measuring several hundred nm was exclusively observed for structured electrodes. The technique generally allows semi-quantitative comparisons but has a major drawback consisting in the potentially incorrect identification of pores in the images. Furthermore, the preparation of transversal samples offers potential for optimization to better preserve the structure. On the other hand, results obtained based on capacitive current studies potentially confirmed the estimated values.

Electrochemical studies provided an access to non-destructively study the electrode volume and are thought to be particularly representative for a potential practical application. The introduction of an oxygen-plasma treatment was considered mandatory to compensate for the hydrophobicity and found to result in a pronounced pseudo-capacitive character of structured electrodes. While the qualitative comparison of results is unrestricted, literature values require attentive verification regarding comparable experimental conditions.
Structured electrodes were associated with increased capacitance values, which match what is reported in literature [76] [115], although the exact repartition in double layer capacitance and pseudo-capacitance remained unknown. The specific surface was found to increase up to 7 times, relative to the geometric surface. Longer phase separation times or shorter saturation times appeared beneficial. Interestingly, diluted, dried ink under some conditions attained a relatively large capacitance, which may have resulted from thin ink

coverage or the orientation of graphite particles. More specific studies (e.g. X-ray photoelectron spectroscopy) are required to reveal e.g. the prevalence of $sp^2$-hybridized carbon on the surface.
The development of electrochemically active surface was estimated by means of Faradaic current studies and equally increased for structured electrodes. Specifically, this reflects the potential for increasing the signal in a practical sensing application. The interpretation of peak current values suggested linear, semi-infinite character for non-structured electrodes, while structured electrodes were associated with limited diffusion. In particular, results for peak-to-peak separation suggested a certain degree of thin-layer type diffusion, which is of possible practical interest for the confinement of electroactive species, such as enzymes. Further, it was deduced that the reversibility of charge transfer remained unchanged after the plasma treatment, but was slightly affected by the addition of EGDA. Main results are summarized in Figure III.24.

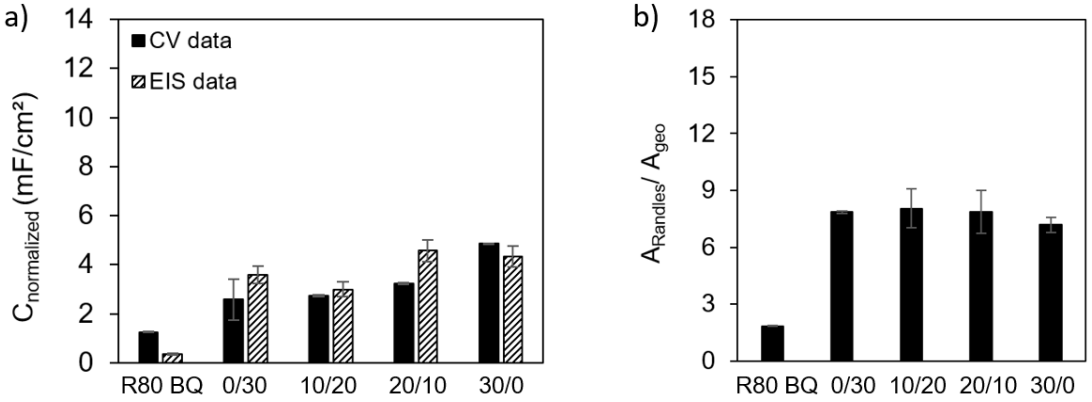


Figure III.24: a) Results for the development of capacitance of structured electrodes, normalized to the geometric electrode surface, determined from CV and EIS studies. b) The development electrochemically active surface for $scCO_2$-structured ink deposits. The ratio separation time ($t_{sep}$) to saturation time ($t_{sat}$) at constant total exposure time was studied. Average values of 4 structured electrodes are displayed. All electrodes were plasma-treated.

Chronoamperometric studies were carried out, to study the surface development more precisely. Results suggested the increase of electroactive surface to 400 times the geometric electrode surface. However, the uncertainty of results is to be discussed. Experimental conditions allowed short measurement times, highly interesting for a fast characterization, but diffusion characteristics of porous electrodes are limited in that case. Therefore, data based was evaluated based on a set of hypotheses, which may not be entirely representative. No tendency was observed regarding the structuration protocol.

The electrode characterization based on EIS was intended to compensate for the frequency-dispersed, non-linear nature of electrodes.
Structured electrodes displayed an extended domain of low impedance at high frequencies, which developed gradually and provided a clear visual impression of the effect of single electrode preparation steps.
Instead of applying KK-transforms, the validity of data was confirmed by plotting the total harmonic distortion, which suggested the potential to fit the spectra. Different equivalent circuit models were applied to the data, accounting for several scenarios of limited diffusion on a porous electrode. The capacitance was estimated and results and tendencies generally confirm previous observations of capacitive current studies based on

CV, see see Figure III.24 a).
As voltammetric studies on porous electrodes display certain limitations, EIS results could be considered more exact. On the other hand, the requirement of a physically representative equivalent circuit paradoxically implies a larger room for error. The general proportion between results, linked to non-structured and structured electrodes is comparable to other techniques, which appears to confirmation the validity of the data evaluation by means of EIS.

## 3.2 The study of variable separation time at constant saturation time

After obtaining a general idea about constant treatment time, the influence of both separation and saturation time was studied in detail. To reduce the potential presence of residual EGDA, suspected to limit reversibility of charge transfer, the saturation time was set to 30 min. Besides the higher chance of (non-)solvent extraction from the electrodes, a beneficial effect on the polymer foaming step was expected. Varying the separation time as before (0, 10, 20 and 30 min), the total exposure time thus varied between 30 and 60 min. The same characterization protocol was employed, allowing a direct comparison of results and a conclusion on the effect of structuration parameters.

### 3.2.1 Physical characterization

#### 3.2.1.1 Digital microscopy

Digital microscopy images in top view for 1.0 and 1.5 µL ink (BQ:EGDA = 2:8 (w/w)) are depicted in Figures III.25 and III.26. Compared to the previous section, surfaces for both ink volumes are of improved but not of ideal homogeneity. Further, higher structural uniformity is seen for smaller ink volumes. In particular, the membrane-like component is mostly absent (with exception for deposit 20/30 in Figure III.26 c1)). As mentioned earlier, the phase separation likely leads to the formation of a fragile top structure of high polymer content, which is of importance when considering studies on the interaction of polymers and supercritical $CO_2$. It is generally assumed, that after a swelling phase, during which a polymer saturates with supercritical $CO_2$, a dissolution of polymer in the supercritical fluid is taking place [144]. Applying the mechanism to a membrane-like top layer of presumably high polymer content, longer exposure times could then account for the visual difference.

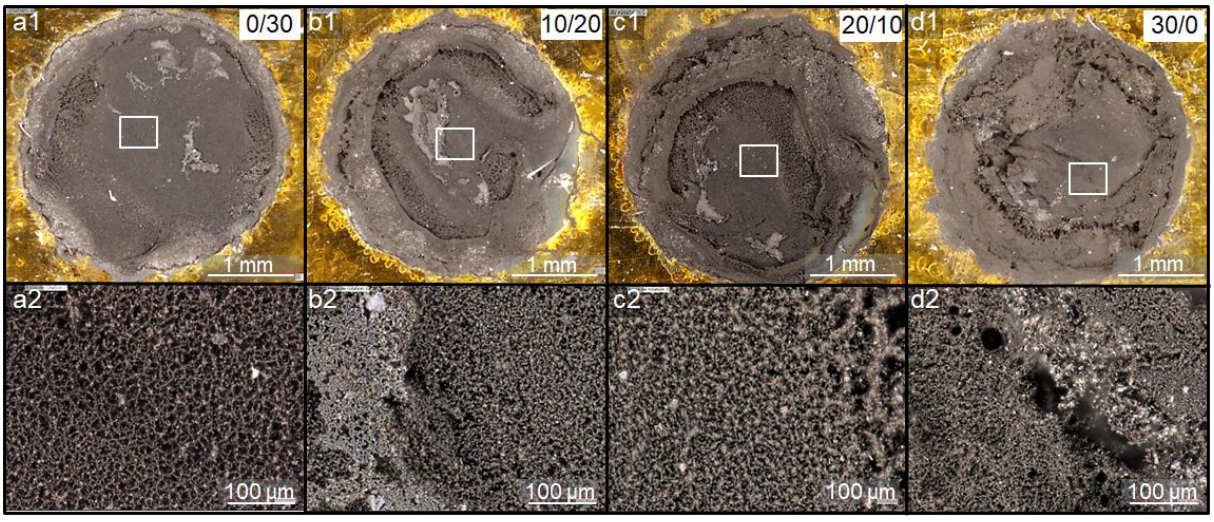


Figure III.25: 1.0 µL ink deposits (BQ242:EGDA = 2:8 (w/w)) for digital microscopy in top view in the study of separation time at constant saturation time; the 0/30 sample in a), 10/30 in b), 20/30 in c) and 30/30 in d). Ratios refer to the parameters $t_{sep}/t_{sat}$. White boxes correspond to magnified locations.

The magnified images clearly demonstrate the presence of a microstructure consisting of pores measuring up to several tens of microns, as well as larger cavities. Opposed to

the images obtained in the previous section, the structural quality allows distinguishing visual similarities with works on polymeric membranes prepared via phase separation. In particular, the study of Van de Witte et al. on membrane formation via phase separation processes describes a "cellular structure" which resembles the electrodes' visual appearance.
It is mentioned to carefully conclude on detailed demixing processes, when discussing ternary systems, as the temporal scale of diffusion processes and concentration gradients can vary importantly between the top layer and the volume [11]. However, this advice may eventually support the former hypothesis of the generation of a membrane-like surface layer, in parallel to the more homogeneous pore formation in the volume.
An interpretation of pore sizes by means of ImageJ or other suited techniques is considered possible, but not carried out since the quality of SEM images is superior.

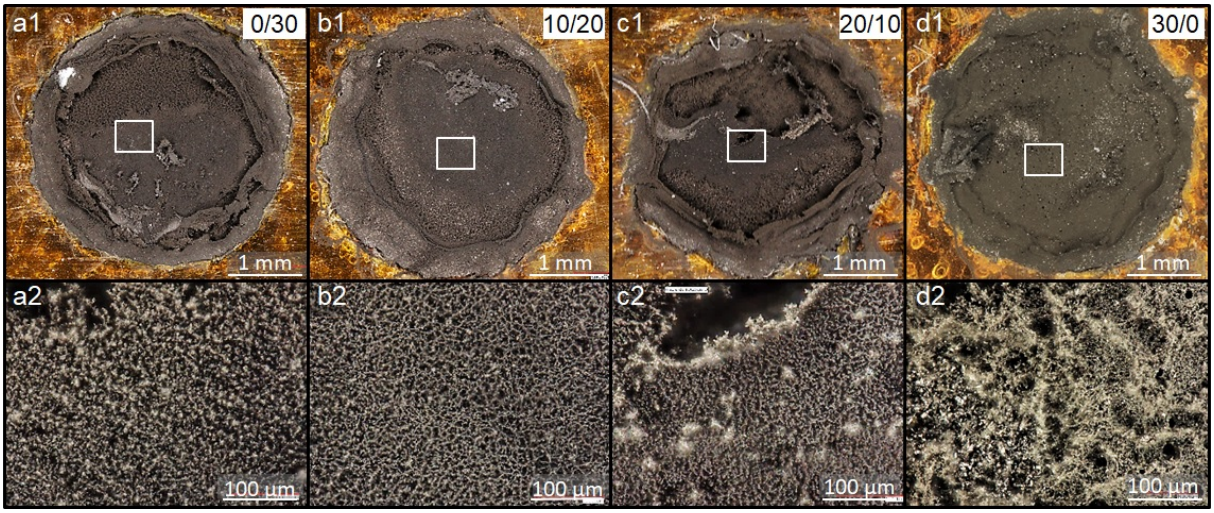


Figure III.26: 1.5 µL ink deposits (BQ242:EGDA = 2:8 (w/w)) for digital microscopy in top view in the study of separation time at constant saturation time; the 0/30 sample in a), 10/30 in b), 20/30 in c) and 30/30 in d). Ratios refer to the parameters $t_{sep}/t_{sat}$. White boxes correspond to magnified locations

### 3.2.1.2 Height of deposits

The deposit heights were evaluated in equivalent manner as before and are displayed in Figure III.27 with extracted values in Table III.27. For small ink volumes, tendencies exhibit a maximum deposit height for the 10/30 sample, which coincides with the 1.0 µL ink deposits in the study of $t_{sep}/t_{sat}$. It is specified, that the 30/30 deposit in d1) was slightly tilted, thus the apparent height did not correspond to the actual deposit height due to a visual, three-dimensional distortion. For 1.5 µL ink deposits, heights peak for the 20/30 sample (20/10 in the previous section).
Observing the general order of values, reductions between 27 and 48 % are noticed compared to the last section, applying for all deposits. Surprisingly, the 0/30 deposits, theoretically identical to the samples in the study of constant exposure time, equally yielded lower values
Eventually, the hypothesis of top-layer dissolution implies a loss in sample height and eventually a limited validity of quantitative results. The idea seems supported by the generally flatter visual appearance of deposits, compared to the more dome-like representations in the study of $t_{sep}/t_{sat}$. A further indicator is the roughness of edges of the deposit top-layers, which may correspond to the remains of said membrane-like structure.

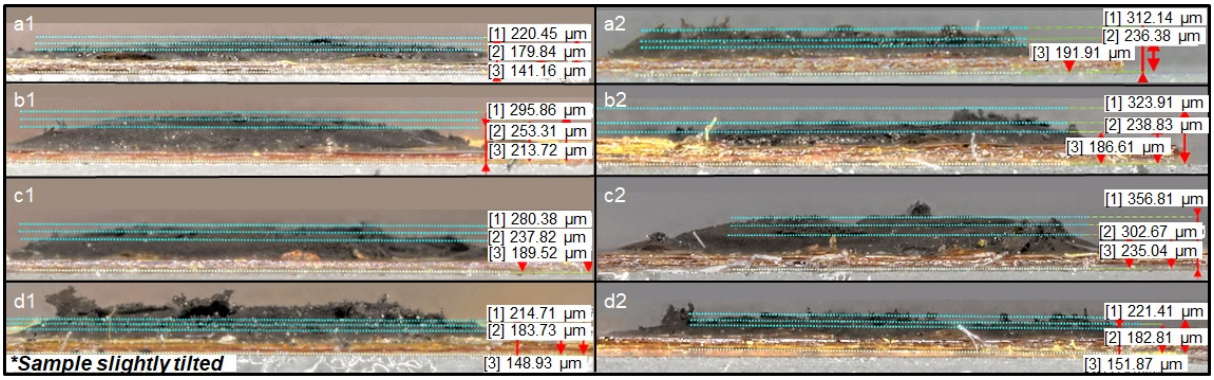


Figure III.27: Side view digital microscopy images of structured ink deposits (BQ242:EGDA = 2:8 (w/w)) in the study of separation time at constant saturation time. 1 µL ink in series 1), 1.5 µL ink in series 2). Sample 0/30 in a), 10/20 in b), 20/10 in c) and 30/0 in d).

Table III.12: Height of ink deposits extracted from side view images in the study of separation time at constant saturation time.

| $\mathbf{t_{sep}/t_{sat}}$ | **1.0 µL** | | | **1.5 µL** | | |
|---|---|---|---|---|---|---|
| | $\mathbf{h_{min}}$ **(µm)** | $\mathbf{h_{mid}}$ **(µm)** | $\mathbf{h_{max}}$ **(µm)** | $\mathbf{h_{min}}$ **(µm)** | $\mathbf{h_{mid}}$ **(µm)** | $\mathbf{h_{max}}$ **(µm)** |
| 0/30 | 141 | 180 | 221 | 192 | 236 | 312 |
| 10/30 | 214 | 253 | 296 | 187 | 239 | 324 |
| 20/30 | 190 | 234 | 280 | 235 | 303 | 357 |
| 30/30 | 149 | 184 | 215 | 152 | 183 | 221 |

#### 3.2.1.3 Evaluation of volume

Image acquisition in aerial view allowed to derive the sample volumes as earlier, see associated images in Figure III.28 and extracted values in Table III.13. In accordance with results of the determination of height, the magnitude of the values is generally slightly smaller, than in the study of $t_{sep}/t_{sat}$. Interestingly, the difference between both ink volumes is less pronounced, which is attributed to the potentially removed top layer of deposits. For 1.0 µL ink, a tendency towards maximum normalized deposit volumes is observed for the 20/30 sample. For 1.5 µL ink, the largest normalized deposit volume is determined for the 10/30 sample, which matches the tendency observed in the previous section (10/20 sample).
No correlation between the evolutions of deposit volumes was observed in the two studies. For one thing, this could oppose the earlier theory that both ink volumes should have followed the same development. Alternatively, the estimated uncertainty is eventually rather large and it is uncertain up to which point comparability is guaranteed. At the moment, the important conclusion consists in the repeated association of maximum results with separation times between 10-20 minutes. Additionally, in coherence with the first study, a trend towards smaller deposit volumes upon longer total exposure times is noted, which may again confirm the hypothesis of partial dissolution of the polymeric component.

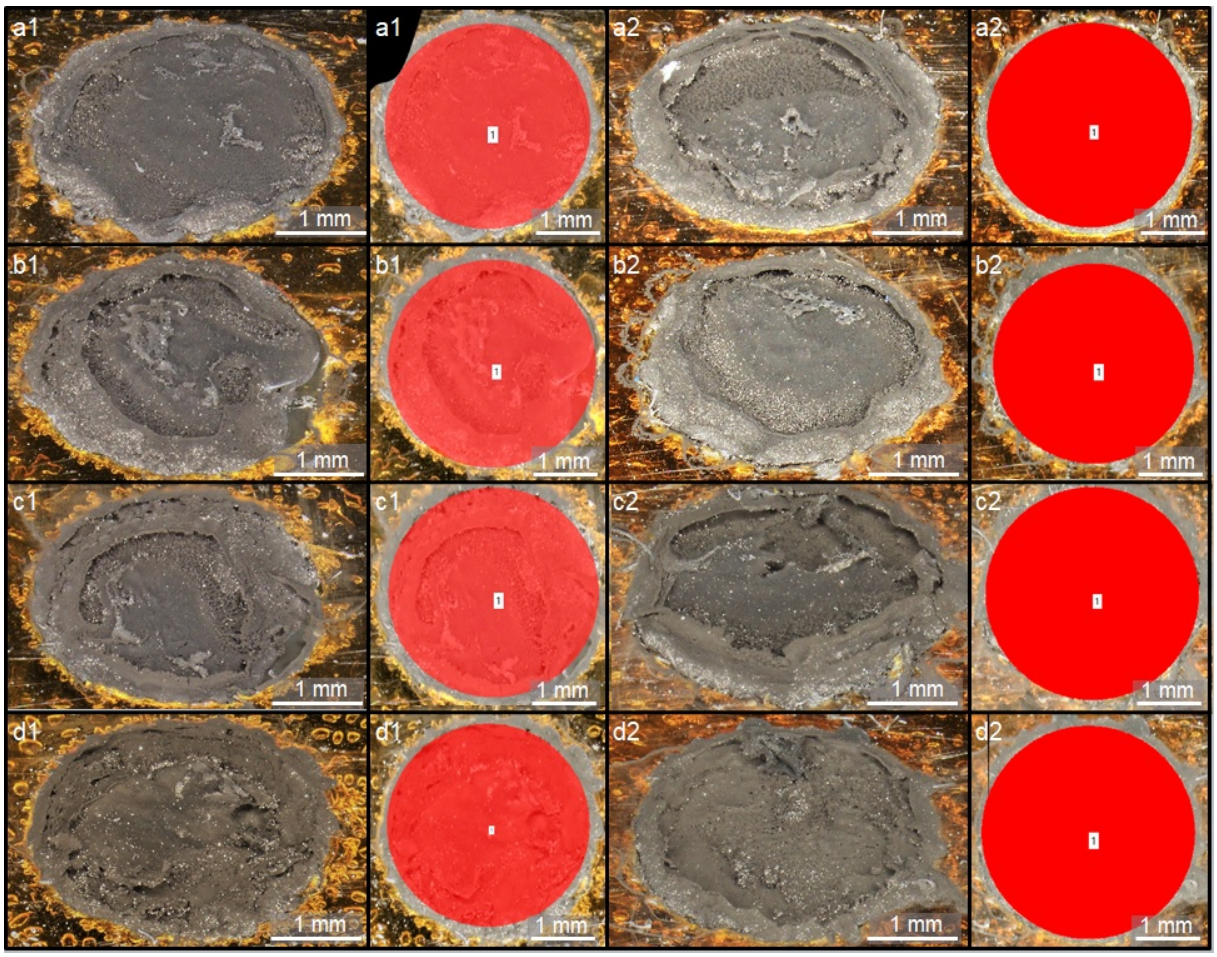


Figure III.28: Aerial view (45 ° and 90 °) digital microscopy of structured ink deposits (BQ242:EGDA = 2:8 (w/w)) in the study of separation time at constant saturation time. 1 µL in series 1), 1.5 µL 2). The 0/30 sample in a), 10/20 in b), 20/10 in c), one 30/0 sample was destroyed. Ratios refer to the parameters $t_{sep}/t_{sat}$.

Table III.13: Volume of ink deposits extracted from aerial view images in the study of separation time at constant saturation time with averaged values for each PCB.

| $t_{sep}/t_{sat}$ | 1.0 µL | | | 1.5 µL | | |
|---|---|---|---|---|---|---|
| | **V ($mm^3$)** | **A ($mm^2$)** | **$V_n$ ($mm^3/\square$)** | **V ($mm^3$)** | **A ($mm^2$)** | **$V_n$ ($mm^3/\square$)** |
| 0/30 | 1.19 | 6.62 | 1.27 | 1.52 | 6.85 | 1.57 |
| 10/30 | 1.48 | 7.07 | 1.48 | 1.73 | 6.76 | 1.81 |
| 20/30 | 1.94 | 6.45 | 2.12 | 1.53 | 7.23 | 1.50 |
| 30/30 | 1.05 | 6.64 | 1.12 | 1.17 | 7.77 | 1.06 |

#### 3.2.1.4 SEM images

A comparative view of SEM images is provided in Figure III.29. No clear influence of structuration parameters on the change of pore size is noticed. The visual appearance of deposits' surfaces is generally comparable to the previous study of $t_{sep}/t_{sat}$, presenting a slightly less "beads-like" and instead a more pronounced, interconnected, bicontinuous character. The parallel presence of these features has been reported in earlier studies with different degrees of expression.
Images at high factor of magnification allow to observe, that the decoration of the mi-

crostructure with a nanostructure is more expressed, than in the previous section. However, it is not clear, whether the visual difference could simply arise from improved image resolution. It is possible to identify structural features with dimensions around the transition of macro- to mesopores.

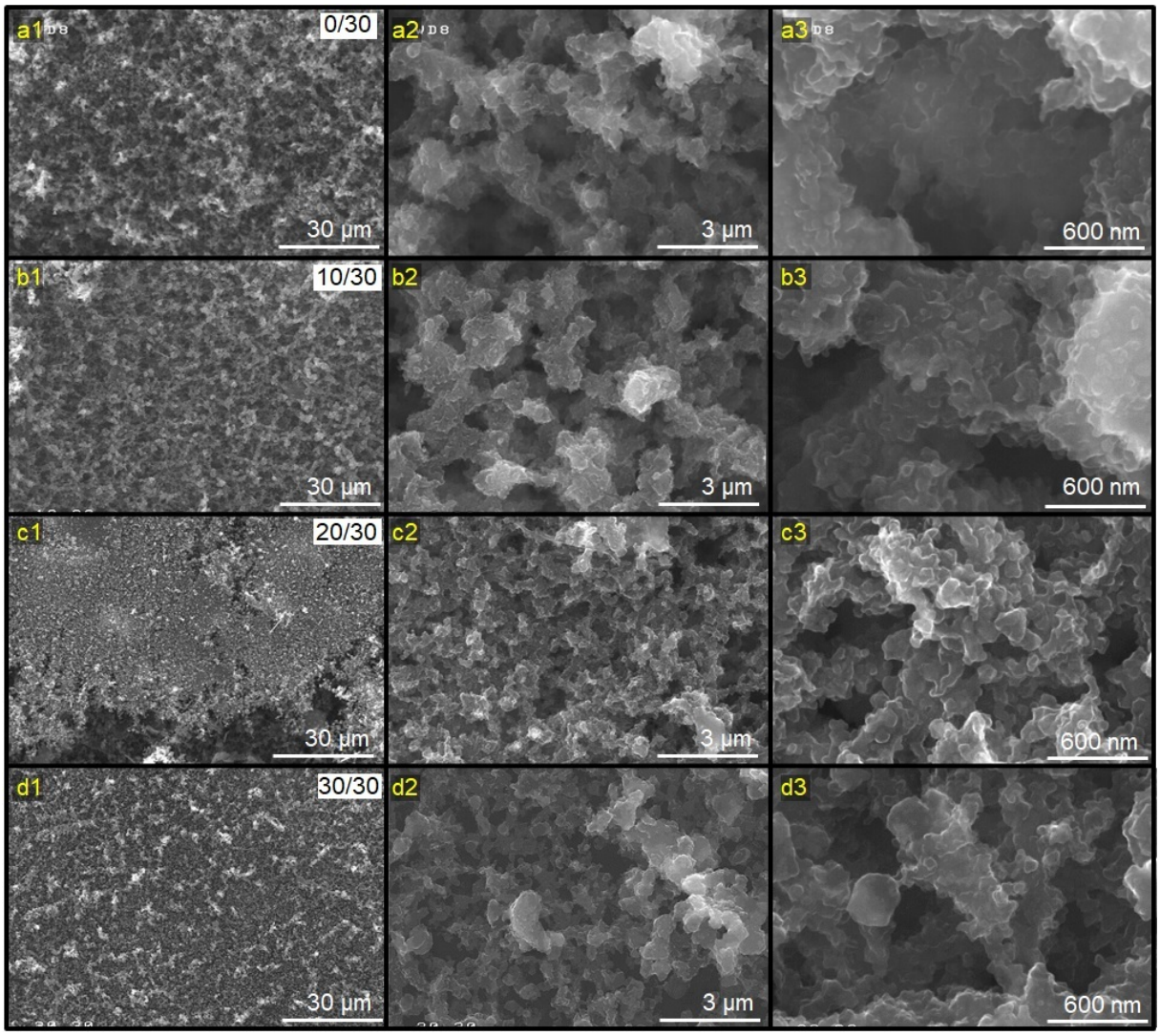


Figure III.29: SEM images of structured ink deposits in the study of separation time at constant saturation time. Ratios refer to $t_{sep}/t_{sat}$, where $T_{sep}$ and $T_{sat}$ were set to 20 and 40 ℃, respectively. The 0/30 sample is identical to the previous section (III.8). Images display central deposit locations.

The visual similarities with porous polymeric membranes lead to the idea, that the visible deposit surfaces contained a large polymer concentration. Further, the visual absence of larger graphite flakes (or similar carbon-based particles) is noted. Instead, a primary microstructure with nanostructural decoration is discernible for all samples. This observation has, to the author's knowledge, not been referenced in literature and indicates a potential spatial separation of large (in the volume) and small (near the surface) carbon particles. The theory further implies characteristic interactions of different carbon particles with the components of the "ternary" system. For example, carbon-based nanoparticles (i.e. carbon black) usually adhere to the larger carbon particles, but may be washed off to some extent by the combined exposure to EGDA and supercritical $CO_2$ in case of high ink dilution.

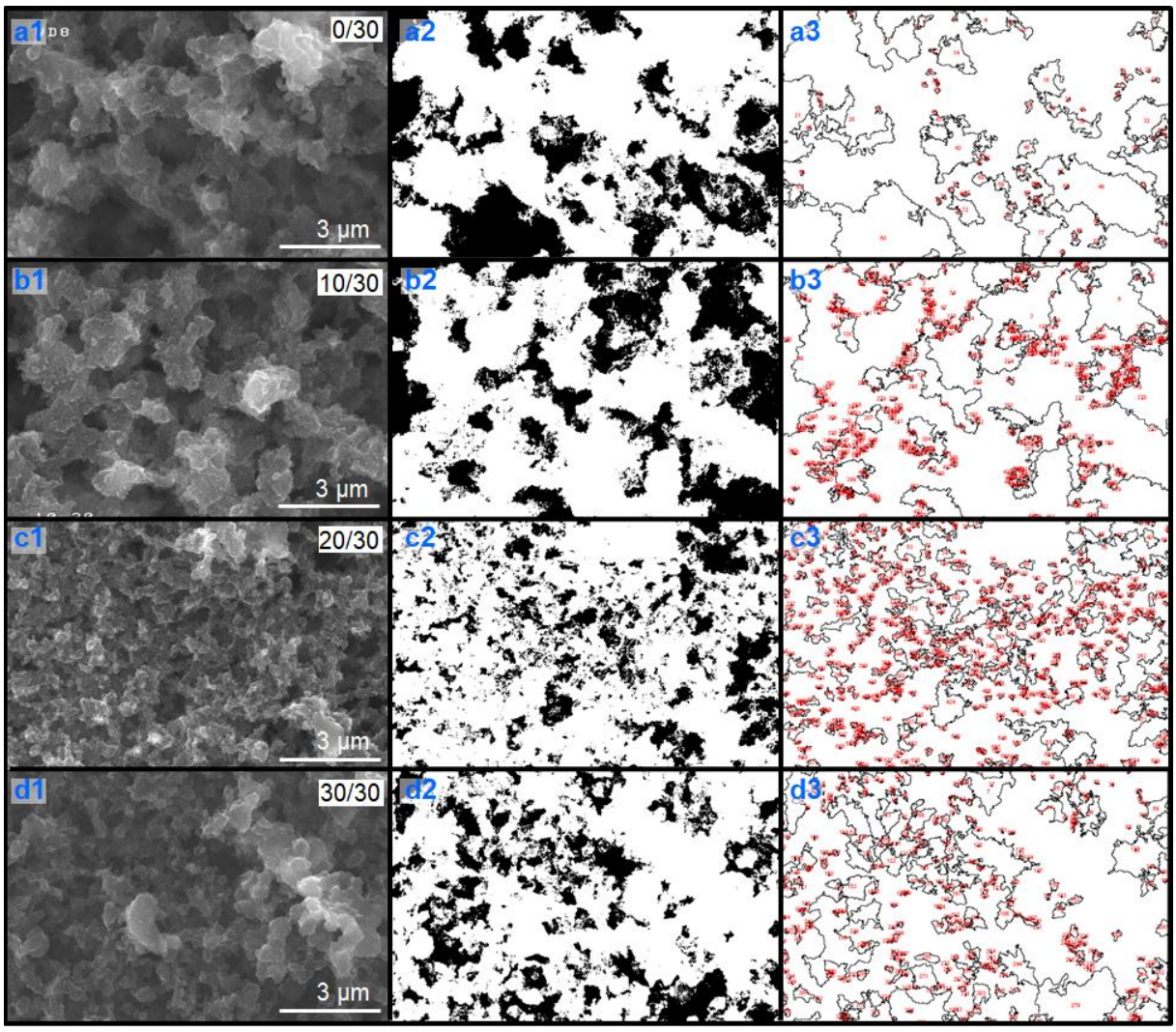


Figure III.30: SEM image treatment for ImageJ pore area determination and quantification in the study of separation time at constant saturation time. The red markings originate from the automated pore counting of the software.

Figure III.30 depicts the SEM image treatment. A minimum particle/pore limit of 5 nm was set for the extraction of values; a precaution, which intended to help separating actual pores from small-scale features in the images arising from strong image contrast. The effect is visible when comparing their presence/ absence in series 2) and 3). Extracted results are summarized in Table III.14 and it is reminded, that the mathematical averaged pore size, as specified earlier, potentially carries misleading information.
The first observation in this study is the pore count, which is consequently increased by a factor of two and more. The maximum pore count of 287 in the previous section was associated with the 10/20 deposit, while 544 and 690 pores were determined for the 10/30 and 20/30 deposits in this section. The difference suggests a link between increased porosity and either longer total exposure time of ink to supercritical $CO_2$ or to the longer saturation times.

The evolution of total pore areas is generally similar, with values that are increased by around 40 % for the 10/30 and 30/30 deposit. However, the overall evolution presents some irregularity for the 20/30 deposit, consisting in a local minimum. Eventually, this can be explained by a poor choice of the location for imaging the surface. In this context, the visual difference of the surface structures in Figure III.29 c) is pointed out, which

potentially supports the argument. As the area covered by pores is rather small, and in combination with the high pore count, the mathematically averaged pore size is smallest for the 20/30 deposit. Overall, the deposits in this study consistently attained smaller averaged pore sizes, than in the study of constant exposure times.

Table III.14: Extracted data from the ImageJ treatment of SEM images in the study of separation time at constant saturation time.

| **Description** | **Particle count** | **Total particle area ($\mu m^2$)** | **% Area** | **Pore diameter (nm)** |
|---|---|---|---|---|
| 0/30 | 197 | 17.1 | 17.3 | 87 |
| 10/30 | 544 | 34.6 | 34.0 | 64 |
| 20/30 | 690 | 21.7 | 21.4 | 31 |
| 30/30 | 293 | 26.8 | 26.4 | 68 |

Histograms of the pore size populations were prepared and are generally of comparable character, as in the last section. The overall range of pore sizes remained unchanged, with main populations measuring up to 150 nm. The distribution of pore sizes is equally comparable and largest populations are located around the upper limit of the macropore dimension. The 10/30 sample presents an exception, with a maximum population corresponding to the size of mesopores.

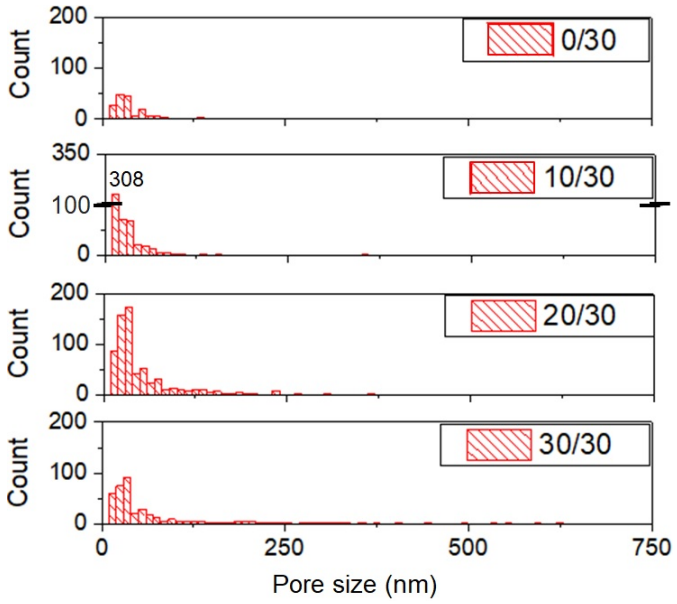


Figure III.31: Histograms of particle/pore populations based on SEM images in the study of separation time at constant saturation time.

The size of populations corresponding to 100 nm seems to follow an arc-shaped tendency with a maximum count for the 20/30 deposit, around four times the count of the 0/30 sample. Therefore, results suggest an interest to extend the factor of saturation time.

## 3.2.2 Electrochemical characterization

### 3.2.2.1 Capacitive current studies

The capacitive CV in 1 M KCl are depicted in Figure III.32 for structured electrodes 0/30 to 30/30. No particular qualitative changes were observed regarding their shape,

with exception for pos. 1 of the 10/30 electrodes. Although the surface of the electrodes could simply be structured above average and the response be particularly capacitive, it is excluded from a further evaluation of data.

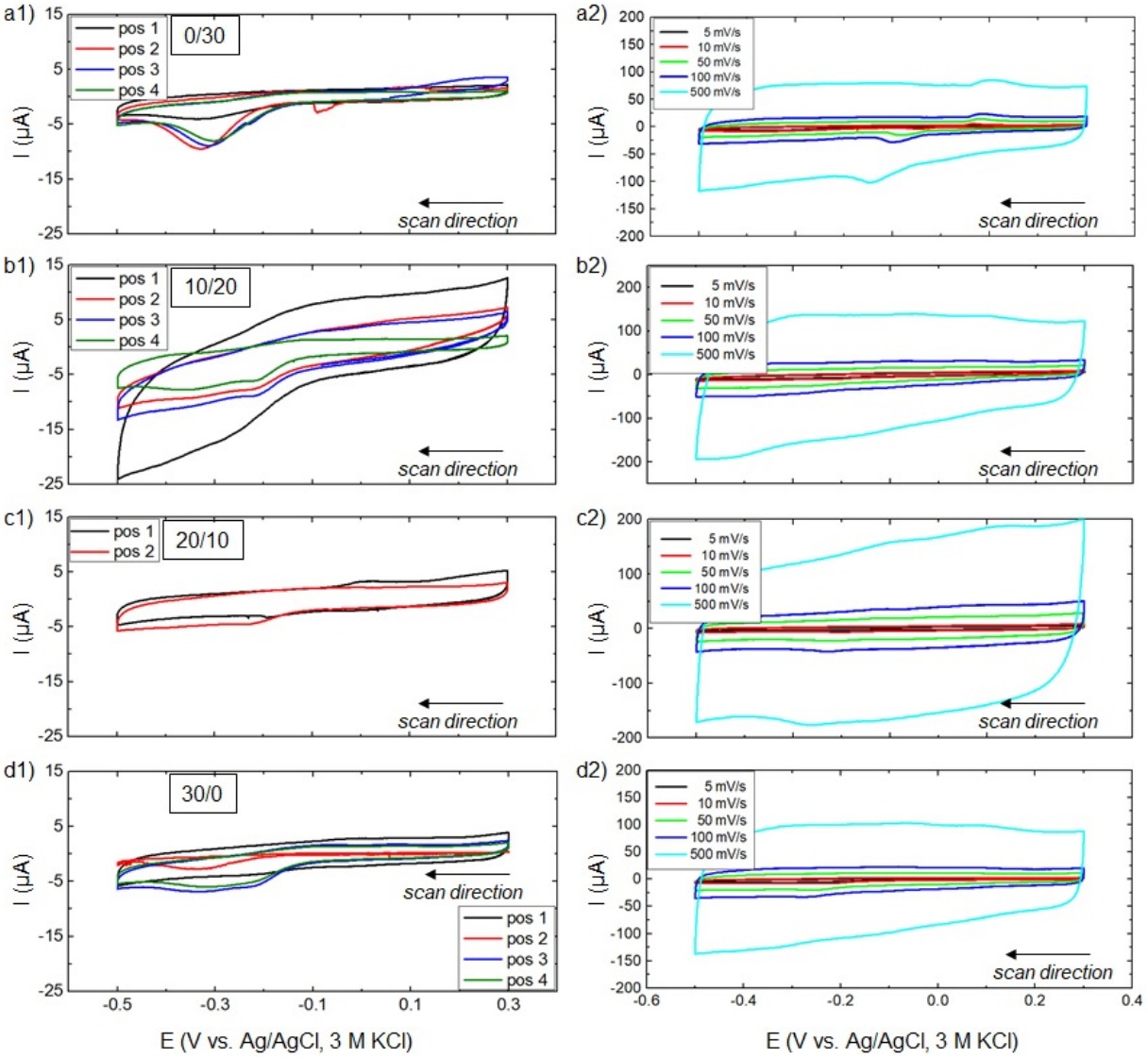


Figure III.32: Capacitive currents of structured ink in the study of separation time at constant saturation time at 5 mV/s in 1 M KCl. Series 1 at 5 mV/s for all electrodes per PCB, series 2 for different scan rates of one electrode. a) 0/30, pos. 4 in detail; b) 10/30, pos. 4 in detail; c) 20/30, pos. 1 in detail; d) 30/30, pos. 4 in detail. All electrodes were treated with an oxygen-plasma. The $5^{th}$ cycles are displayed. Onset at 0.3 V.

The less pseudocapacitive response during the anodic potential sweep is an interesting observation, indicated by the rapid achievement of a current plateau. The cathodic sweeps, on the other hand, are of pseudocapacitive nature, as indicated by the steady increase of current with small distinct peaks. Eventually, products of a Faradaic reduction reaction could require higher overpotentials to induce oxidation, resulting in a limited anodic current. In practical, this could originate from a lower reversibility of charge transfer, which is to be confirmed by means of complementary results. It is curious, that the electrode 20/30 seems to present an exception, see Figure III.32 c2). The described tendencies occur inversely for the cathodic and anodic scan.

### 3.2.2.2 Normalized and gravimetric capacitance

Opposed to the previous study at constant total exposure time, the determination of capacitance is presented in one subsection. Normalized capacitance values, relative to the geometric surface and relative to electrode weight are displayed in Figure III.33 a) and b), respectively. The data sets relating to dried electrodes are included for a better comparison. Results are listed in Table III.15.

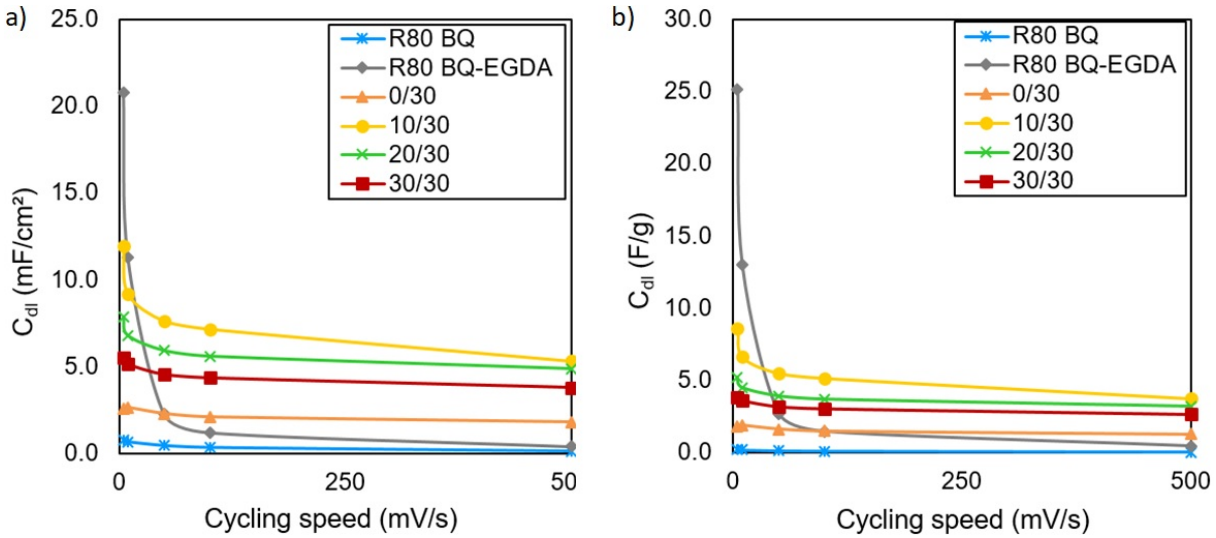


Figure III.33: a) Normalized capacitance and b) gravimetric capacitance in the study of separation time at constant saturation time, extracted from CV. All electrodes were plasma-treated.

Again, data represents averaged values of up to four electrode responses, which is a measure to increase significance. General tendencies are of similar character as in the study of total exposure time. Structured electrodes present increased capacitance values over the entire range of scan rates, compared with the dried R80 BQ electrodes. The particular behaviour of the dried, R80 BQ-EGDA electrodes at slow scan rates is pointed out, which was earlier explained by a potentially pronounced pseudocapacitive character. Structured electrodes in this study present a similar behaviour at slow scan rates in the form of increased capacitance, specifically for the 10/30 and 20/30 electrodes. The observation coincides with the larger macropore count estimated earlier. It could support the hypothesis, that the scan-rate dependence of capacitance values correlates with both a pseudocapacitive electrode surface and the presence of previously introduced pores with a certain "storage functionality".

Table III.15: Measured capacitance ($C_{meas}$) in the study of separation time at constant saturation time, normalized to $A_{geo}$ of electrodes ($C_{norm}$), to the mass of active material ($C_{gravimetric,corr.}$) and to the non-structured R80 BQ electrodes ($Increase$). Results originate from CV at 5 mV/s in 1 M KCl.

| **Description** | **$C_{meas}$ (µF)** | **$C_{norm}$ (mF/cm²)** | **Increase** | **$C_{gravim.,corr.}$ (F/g)** | **Increase** |
|---|---|---|---|---|---|
| 0/30 | 184 | 2.58 | 3.6 | 1.936 | 8.4 |
| 10/30 | 860 | 11.93 | 16.5 | 9.055 | 39.2 |
| 20/30 | 520 | 7.84 | 7.8 | 5.486 | 23.8 |
| 30/30 | 390 | 5.51 | 5.5 | 4.063 | 17.6 |

Interestingly, both normalized and gravimetric capacitances reproduce the tendencies displayed ealier with arc-like evolutions, peaking for the 10/30 electrodes. As the capacitive currents are thought to be connected to the specific surface area, the information of microscopy and SEM images on the generation of porosity can be used in a correlative manner. A link between electrodes' porosity and the surface development can be created. The largest determined, normalized capacitances are increased by a factor 16.5, relative to dried R80 electrodes, which is more than twice the increase observed in the previous section. Further, it is twice the value determined for the study of Lim et al., cited earlier, on porous electrodes based on carbon slurry [76]. The maximum gravimetric capacitance is increased by a factor of 39, which is equally twice the factor of increase found in the last section. So far, the modification of process parameters coherently indicates higher capacitive results for the longer saturation times.

#### 3.2.2.3 Faradaic current studies

The CV of structured electrodes, cycled in 1 mM ruthenium hexaamine and 1 M KCl, are depicted in Figure III.34 for different scan rates. The capacitive background were subtracted as before. However, while almost all electrodes were recovered in a functional state, the background correction could not always be carried out in a meaningful manner. In particular, some of the capacitive currents in CV in 1 M KCl exceeded the Faradaic currents, measured after the addition of the redox probe at the same potential, which is not fully understood. In consequence, some subtracted CV were distorted and are not displayed. Extracted values for peak-to-peak separation, peak currents and the peak current ratio are listed in Table III.16.
The general appearance of CV is comparable to the previous study with a clear definition of peaks, although their width seems increased, particularly at faster scan rates. Earlier, this was explained by a coupling of additional charge transfers to the oxidation/reduction of the redox agent and it may coincide with the suggested pronounced pseudocapacitive character.
The peak ratios are close to one for fast cycling and similar to dried R80 BQ electrodes. Compared to structured electrodes, in the study of constant exposure time, the reversibility for fast scan rates is slightly improved. For slow scan rates, the results of one PCB are of higher precision, but remain unchanged.

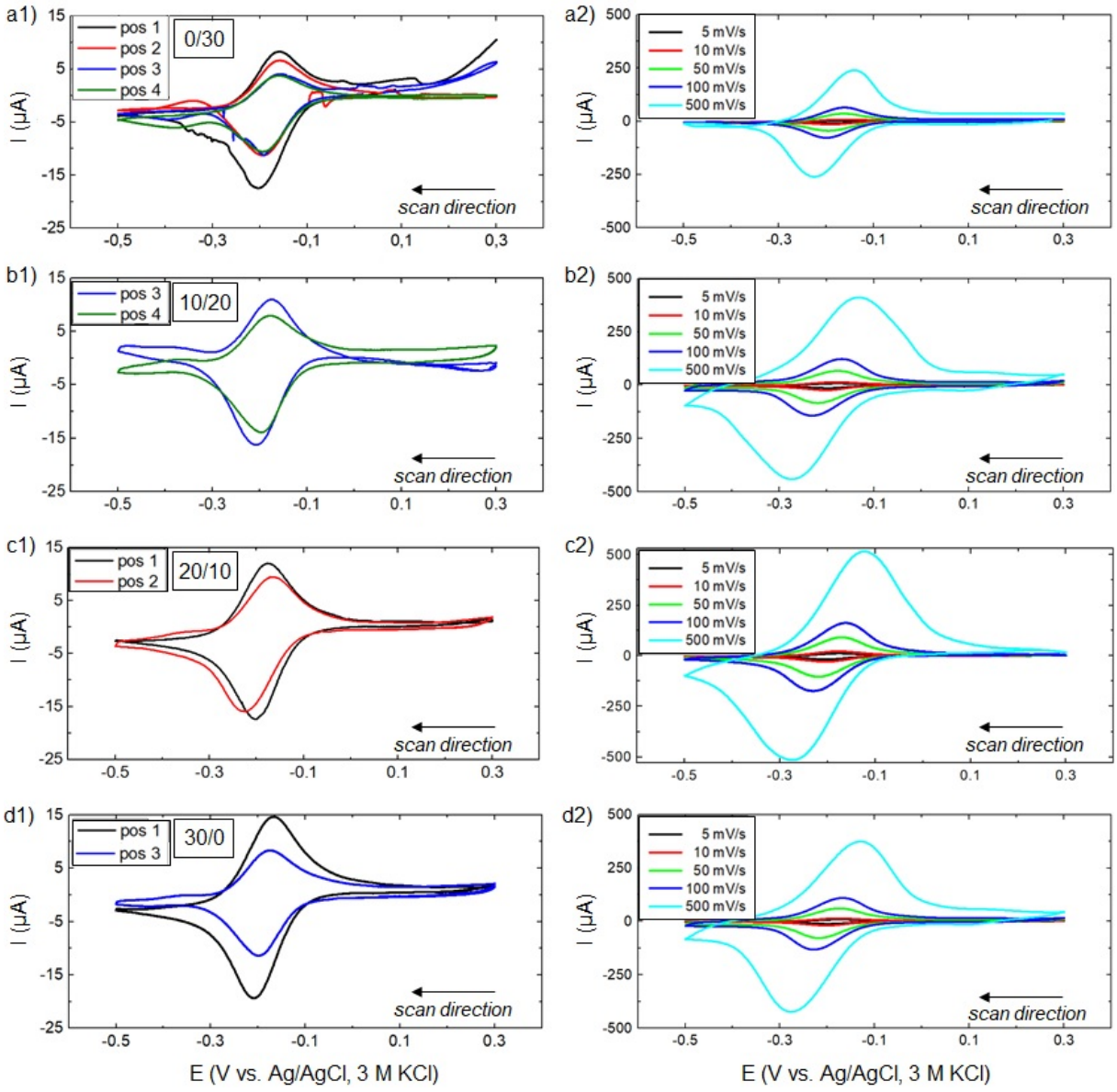


Figure III.34: Faradaic currents of structured ink electrodes in the study of separation time at constant saturation time at 5 mV/s in 1 M KCl, 1 mM ruthenium hexaamine. Series 1 at 5 mV/s for all electrodes per PCB, series 2 for different scan rates of one electrode; a) 0/30 and pos. 1 in detail, b) 10/30 and position 4 in detail, c) 20/30 and pos. 1 in detail, d) 30/30 and pos. 3 in detail. The $5^{th}$ cycles are displayed. Onset at 0.3 V. All electrodes were plasma-treated.

The peak separation for structured electrodes, see Figure III.35, is further reduced at slow scan rates to 25 mV (30 mV in the previous study), which may underline the validity of the thin-layer-type diffusion, proposed earlier. In that case, the assumption of redox species being trapped in the porous structure correlates well with the increased porosity, suggested based on imaging techniques. This would particularly be the case for pores/channels of small dimensions.

Table III.16: Peak-to-peak separation, peak current and peak ratio extracted from CV in 1 mM ruthenium hexaamine, 1 M KCl in the study of separation time at constant saturation time.

| $\mathbf{v}_{scan}$ **(mV/s)** | **R80 BQ** | **R80 BQ $O_2$** | **R80 BQ-EGDA** | **0/30** | **10/20** | **20/10** | **30/0** |
|---|---|---|---|---|---|---|---|
| | | | **$\Delta E_{peak}$ (mV)** | | | | |
| 5 | 64.9 | 66.0 | 68.1 | 38.1 | 24.5 | 25.3 | 31.3 |
| 10 | 64.8 | 64.1 | 77.9 | 38.1 | 35.6 | 28.2 | 36.4 |
| 50 | 64.9 | 61.3 | 96.9 | 40.6 | 50.8 | 48.9 | 74.0 |
| 100 | 64.4 | 58.9 | 104.0 | 52.1 | 77.0 | 70.3 | 111.0 |
| 500 | 64.0 | 58.3 | 147.3 | 103.0 | 141.2 | 150.2 | 147.3 |
| | | | **$I_{ox}$ (µA)** | | | | |
| 5 | 4.3 | 4.8 | 17.1 | 9.1 | 9.2 | 12.1 | 11.43 |
| 10 | 6.1 | 6.8 | 26.9 | 13.5 | 16.9 | 21.4 | 19.5 |
| 50 | 12.9 | 15.4 | 36.2 | 40.8 | 60.6 | 81.7 | 67.4 |
| 100 | 17.8 | 22.0 | 43.6 | 75.2 | 109.8 | 140.2 | 106.9 |
| 500 | 39.4 | 51.5 | 83.7 | 252.7 | 363.0 | 503.7 | 342.2 |
| | | | **$I_{red}$ (µA)** | | | | |
| 5 | -4.6 | -4.9 | -18.9 | -11.7 | -14.2 | -16.1 | -14.3 |
| 10 | -6.1 | -6.8 | -28.6 | -16.0 | -24.7 | -28.2 | -24.6 |
| 50 | -12.7 | -15.3 | -40.5 | -44.3 | -79.9 | -96.6 | -83.6 |
| 100 | -17.8 | -22.9 | -47.2 | -76.9 | -126.6 | -162.14 | -139.1 |
| 500 | -40.3 | -61.1 | -108.2 | -259.9 | -400.4 | -502.2 | -377.7 |
| | | | **$I_{ox}/I_{red}$** | | | | |
| 5 | -0.97 | -0.97 | -0.91 | -0.77 | -0.64 | -0.75 | -0.79 |
| 10 | -1.00 | -1.00 | -0.94 | -0.84 | -0.69 | -0.76 | -0.99 |
| 50 | -1.01 | -1.01 | -0.89 | -0.92 | -0.76 | -0.84 | -1.01 |
| 100 | -0.99 | -0.96 | -0.92 | -0.98 | -0.87 | -0.87 | -1.00 |
| 500 | -0.99 | -0.84 | -0.77 | -0.97 | -0.91 | -1.00 | -0.98 |

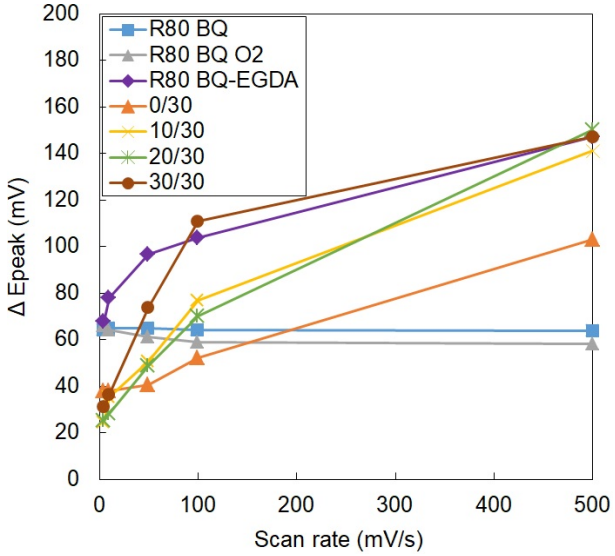


Figure III.35: Peak separation as a function of the scan rate in the study of separation time at constant saturation time, based on CV.

Interestingly, $\Delta E_{peak}$ now tends towards larger values at slower scan rates, comparable to diluted, dried R80 BQ-EGDA electrodes. In the study of constant total exposure time,

the peak-to-peak separation increased less rapidly with faster scan rates.
In addition, a tendency of larger $\Delta E_{peak}$ for longer separation times is noticed, with a small irregularity for the 10/30 and 20/30 samples. The observations suggest a correlation with limited charge transfer, although the exact mechanisms remain vague. In respect to earlier observations, the generation of porosity is not seen as a direct cause, as a pronounced expression would then have been expected for the 10/30 or 20/30 sample. Instead, the structuration may be linked to an increasing separation of carbon particles. The extended exposure to supercritical $CO_2$, which is known to partially dissolve the polymer and can potentially disperse the carbon particles, could simply cause a degradation of the connections between carbon particles in the porous structure. In that case, charge transfer is equally limited to fewer physical connections between the carbon particles. Thus, higher activation energies/ overpotentials would be required, to initiate the jump of electrons from one particle to another, much as in the blocking electrodes, known in impedance spectroscopy.

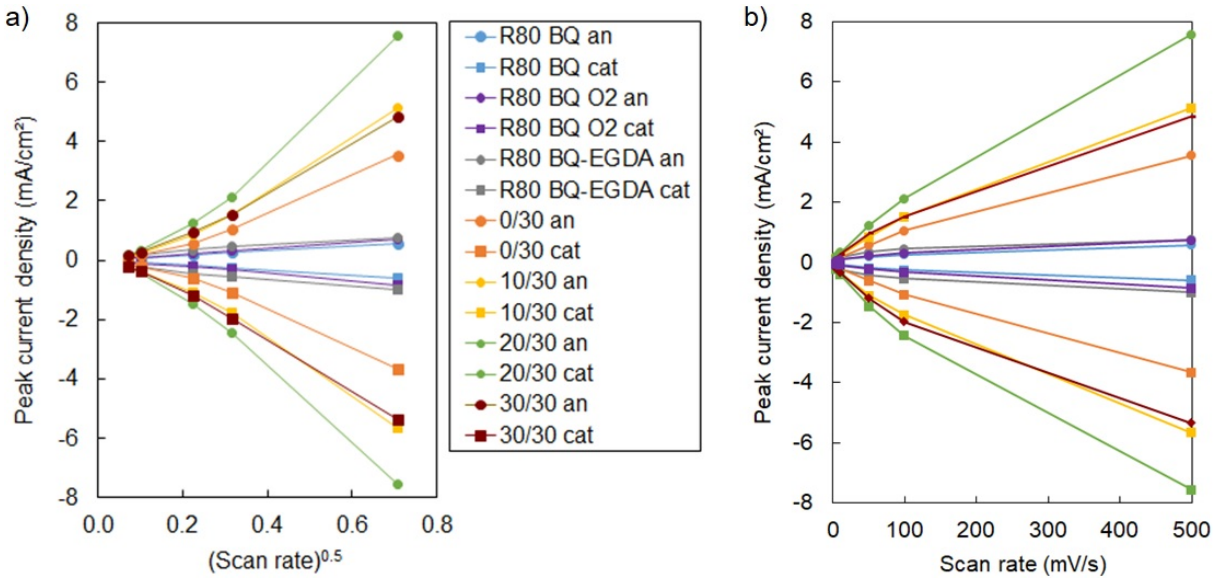


Figure III.36: Comparison of peak current densities in 1 mM ruthenium hexaamine, 1 M KCl in the study of separation time at constant saturation time. Data derived from CV.

Table III.17: Linearity of peak current plots versus the scan rate and the root of the scan rate in the study of separation time at constant saturation time. Data extracted from CV in 1 mM ruthenium hexaamine, 1 M KCl.

| | $\mathbf{R^2}$ **of** $\mathbf{I_{peak}}$ **vs.** $(\nu_{scan})^{0.5}$ | $\mathbf{R^2}$ **of** $\mathbf{I_{peak}}$ **vs.** $\nu_{scan}$ |
|---|---|---|
| **R80 BQ** | 1.000 | 0.958 |
| **R80 BQ O2** | 0.997 | 0.972 |
| **R80 BQ-EGDA** | 0.989 | 0.960 |
| **0/30** | 0.980 | 0.991 |
| **10/20** | 0.986 | 0.991 |
| **20/10** | 0.985 | 0.991 |
| **30/0** | 0.993 | 0.981 |

The evolution of peak heights is displayed in Figure III.36, with linearities of the evolutions listed in Table III.17. For fast scan rates, the first main observation is the general increase of peak current densities by a factor of approximately two (equally increased for

slow scan rates). Based on the Randles-type equations, this increase can potentially be linked to larger electrochemically active surface areas, which would match the assumed generation of smaller pores with higher surface-to-volume ratio.

Table III.18: Electroactive surface areas calculated from cathodic peaks in CV experiments studying the separation time at constant saturation time.

| $\mathbf{v}_{scan}$ (mV/s) | R80 BQ | R80 BQ $O_2$ | R80 BQ-EGDA | 0/30 | 10/30 | 20/30 | 30/30 |
|---|---|---|---|---|---|---|---|
| **$A_{Randles}$ ($cm^2$)** | | | | | | | |
| 5 | 0.098 | 0.105 | 0.405 | 0.252 | 0.311 | 0.345 | 0.306 |
| 10 | 0.092 | 0.103 | 0.434 | 0.242 | 0.375 | 0.427 | 0.373 |
| 50 | 0.086 | 0.104 | 0.275 | 0.300 | 0.542 | 0.656 | 0.566 |
| 100 | 0.086 | 0.110 | 0.226 | 0.369 | 0.607 | 0.777 | 0.665 |
| 500 | 0.086 | 0.131 | 0.232 | 0.557 | 0.858 | 1.076 | 0.810 |
| **$A_{Oldham}$ ($cm^2$)** | | | | | | | |
| 5 | 0.118 | 0.126 | 0.488 | 0.303 | 0.374 | 0.415 | 0.368 |
| 10 | 0.111 | 0.124 | 0.522 | 0.291 | 0.451 | 0.514 | 0.449 |
| 50 | 0.104 | 0.125 | 0.330 | 0.361 | 0.651 | 0.789 | 0.681 |
| 100 | 0.103 | 0.132 | 0.272 | 0.443 | 0.730 | 0.935 | 0.802 |
| 500 | 0.104 | 0.158 | 0.279 | 0.670 | 1.032 | 1.295 | 0.974 |
| **$A_{Randles,irrev.}$ ($cm^2$)** | | | | | | | |
| 5 | 0.125 | 0.133 | 0.516 | 0.321 | 0.396 | 0.438 | 0.389 |
| 10 | 0.117 | 0.132 | 0.552 | 0.308 | 0.477 | 0.543 | 0.475 |
| 50 | 0.110 | 0.132 | 0.349 | 0.382 | 0.689 | 0.834 | 0.720 |
| 100 | 0.109 | 0.140 | 0.288 | 0.469 | 0.771 | 0.988 | 0.848 |
| 500 | 0.110 | 0.167 | 0.295 | 0.708 | 1.091 | 1.369 | 1.029 |
| **$A_{charge,anodic.}$ ($cm^2$)** | | | | | | | |
| 5 | 0.158 | 0.198 | 0.619 | 0.359 | 0.472 | 0.478 | 0.426 |
| 10 | 0.157 | 0.194 | 0.744 | 0.362 | 0.517 | 0.610 | 0.308 |
| 50 | 0.142 | 0.175 | 0.477 | 0.381 | 0.784 | 0.929 | 0.827 |
| 100 | 0.140 | 0.180 | 0.362 | 0.541 | 0.929 | 1.135 | 1.030 |
| 500 | 0.134 | 0.104 | 0.351 | 0.868 | 1.526 | 1.969 | 1.330 |
| **$A_{Randles}/A_{geo}$** | | | | | | | |
| 500 | 1.22 | 1.85 | 2.05 | 7.85 | 11.92 | 16.21 | 11.55 |
| **$A_{Oldham}/A_{geo}$** | | | | | | | |
| 500 | 1.46 | 2.22 | 2.47 | 9.44 | 14.34 | 19.50 | 13.89 |
| **$A_{Randles,irrev.}/A_{geo}$** | | | | | | | |
| 500 | 1.55 | 2.35 | 2.61 | 9.98 | 15.16 | 20.62 | 14.69 |
| **$A_{charge,anodic}/A_{geo}$** | | | | | | | |
| 500 | 1.89 | 1.46 | 3.11 | 12.22 | 21.19 | 29.65 | 18.97 |
| **Factor of increase relative to R80, Randles-style equations** | | | | | | | |
| 500 | 1.0 | 1.5 | 2.7 | 6.5 | 9.9 | 12.5 | 9.4 |
| **Factor of increase relative to R80, $Q_{anodic}$** | | | | | | | |
| 500 | 1.0 | 0.8 | 2.6 | 6.5 | 11.4 | 14.7 | 9.9 |

For longer separation times, the evolutions of $J_{peak}$ with the square root of the scan rate exhibit higher degrees of linearity. The inverse is observed in the plot of peak current densities versus the scan rate, where the linearity for longer separation times is lower, which is typically associated with unrestricted diffusion of analytes. Comparison to the previous study at constant exposure time, the diffusion seems to be less surface-confined, matching the published works on supercritical fluid-assisted foaming, where the formation of larger pores was observed for higher temperatures.

In the following, the electroactive surface was calculated based on the results for a scan rate of 500 mV/s to allow for a comparison against results of the previous section. Only the structured electrodes 10/30, 20/30 and 30/30 require discussion, as the other samples serve for a comparative purpose.
For slow scan rates, calculated surfaces of all electrodes are of high coherence. Values fall into an equivalent range, as in the last section. Since this case corresponds to a large diffusion layer thickness, corresponding to the study of the macroscopic electrode surface, the result was expected. Still, values indicate a macroscopic surface which is largest for the 20/30 electrodes, measuring approximately four times $A_{geo}$. A primary influence is thought to be the developed surface structure.
Fast scan rates of 500 mV/s yield electroactive surface values, which are of arc-shaped character and peak for the 20/30 electrodes. When using Randles-style equations, the estimated results double in comparison with the study of constant exposure time, relative to the geometric electrode surface. This observation qualitatively matches earlier results within this study and is considered representative in consequence. Tendencies, relative to the R80 response, display less distinct increases, which is potentially due to not taking variations of $A_{geo}$ into consideration.

#### 3.2.2.4 Chronoamperometric studies

Figure III.37 displays the measured current responses in series 1). Compared to the previous section, peak currents are clearly increased. Assuming, that all other factors in the Cottrell equation remained unchanged, this can be a potential first (but on its own, insufficient) indicator of a larger electroactive surface. The corresponding Cottrell plots are shown in series 2) for a period of 300 ms after the current peak. The previously observed, pronounced time-dependence is replicated, again supporting the choice of a 50 ms time frame for the calculation of results.
Geometric, calculated and normalized surfaces areas are listed in Table III.19. Strongly deviating responses, such as pos. 2 in Figure III.37 d), are considered as erroneous and excluded from the extraction of data.
Again, an arc-like tendency with maximum values for the 20/30 electrodes is noticed, yielding electroactive surfaces around 98 $m^2/g$, which is three times as much as in the study of constant exposure time. Given the results are representative and valid, thex exceed literature values for carbon ink-based structured electrodes, see Table II.6 for comparison. In conclusion, this supports the choice of longer saturation times/ longer total exposure times in the further project. Relative to the geometric surface, the increase is estimated to a factor of 1476.

Table III.19: Cottrell slopes, calculated electroactive surface areas and specific surface areas for structured carbon ink electrodes in the study of separation time at constant saturation time.

| | $\mathbf{A_{geo}}$ **($mm^2$)** | $\mathbf{A_{Cottrell}}$ **($cm^2$)** | $\mathbf{A_{Cottrell}}$ **($m^2/g$)** | $\mathbf{A_{Cottrell}/A_{geo}}$ |
|---|---|---|---|---|
| **0/30, 50 ms** | 7.1 | 23.93±1.16 | 23.9 | 341.4 |
| **10/30, 50 ms** | 7.2 | 58.62±33.16 | 58.6 | 814.2 |
| **20/30, 50 ms** | 6.6 | 98.06±14.98 | 98.1 | 1476.8 |
| **30/30, 50 ms** | 7.0 | 39.02±5.90 | 39.0 | 556.6 |

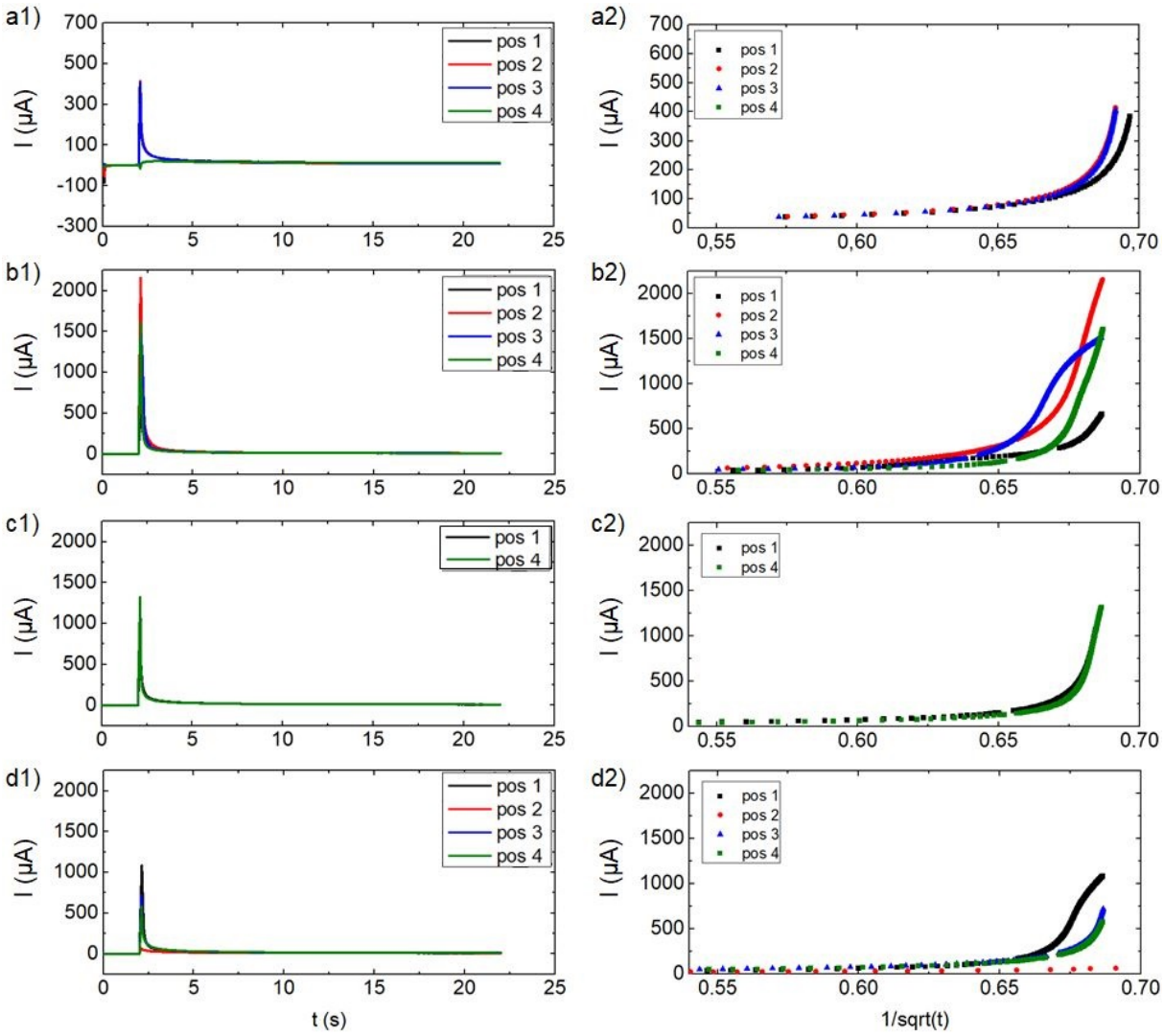


Figure III.37: Chronoamperometric responses in series 1) (0 V, 2 s and 0.7 V, 20 s in 2.5 mM hexacyanoferrate (II), 1 M KCl) in the study of separation time at constant saturation time; a) 0/30; d) 10/30; e) 20/30; f) 30/30. Electrodes were oxygen plasma-treated. The resulting Cottrell plots in series 2).

### 3.2.2.5 Electrochemical impedance studies

EIS was performed on electrodes considered functional as specified earlier and one specific electrode per PCB was selected for the presentation of Nyquist and Bode plots in Figure III.38 and III.39. Qualitatively, the spectra reproduce the distinct shapes previously indicated for structured electrodes more clearly. The visual impression is similar, to what is referenced as an electrode system with fractal porosity. More precisely, the spectra resemble the adaptation of de Levie's transmission line equivalent circuit model by Song et al. [145]. In their work, a porous electrode was modeled, taking pore size distributions into consideration, opposed to the uniform cylindrical pores in the approach of de Levie. In practical, this describes an electrode with a complex, multimodal porosity (several main pore sizes), which exhibits "mixed kinetically and charge transfer controlled" properties [141].

In the Nyquist plots, the indicated high-frequency R/C semi-circle (overlapping with a steep onset of the mass-transfer slope) is decreasing in diameter for longer separation times, or longer total exposure times respectively, up to the 20/30 electrode. This indicates

a smaller electrode charge transfer resistance[15], potentially linked to the partial dissolution of polymeric binder in supercritical $CO_2$. This, in consequence, explains the reduced impedance of the electrode surface. Small phase angles between 0 and 10 ° support the theory. In parallel, the dimension of high-frequency semi-circles are slightly larger than in the study of constant exposure time. This indicates a higher charge transfer capacitance, which is thought to arise from the increased surface area of the electrodes.
The cut-off frequency is of poor definition in both Nyquist and Bode plots, but a tendency towards higher frequencies up to the 20/30 electrode is observed. This coincides with smaller impedance values, suggesting facile charge transfer kinetics.

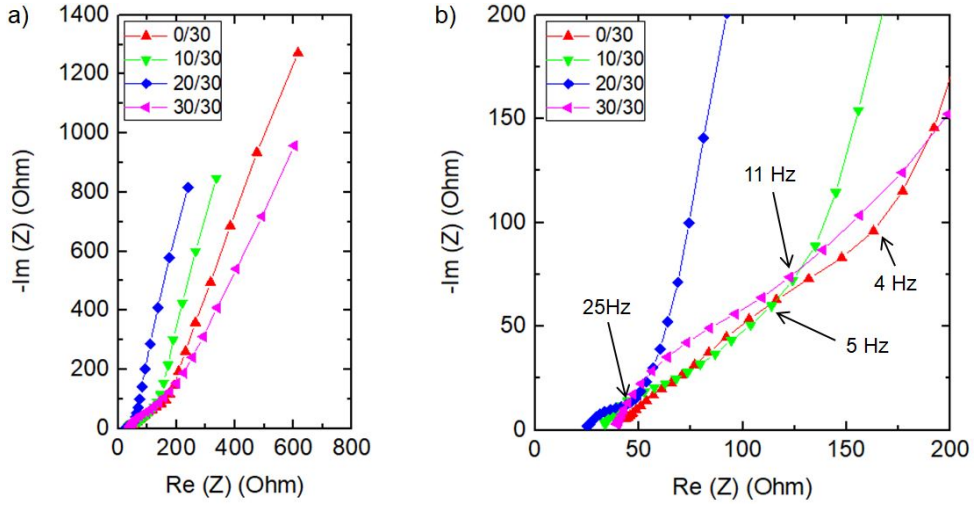


Figure III.38: a) Nyquist plots with b) high-frequency domains in 1 M KCl, 1 mM ruthenium hexaamine in the study of separation time at constant saturation time.

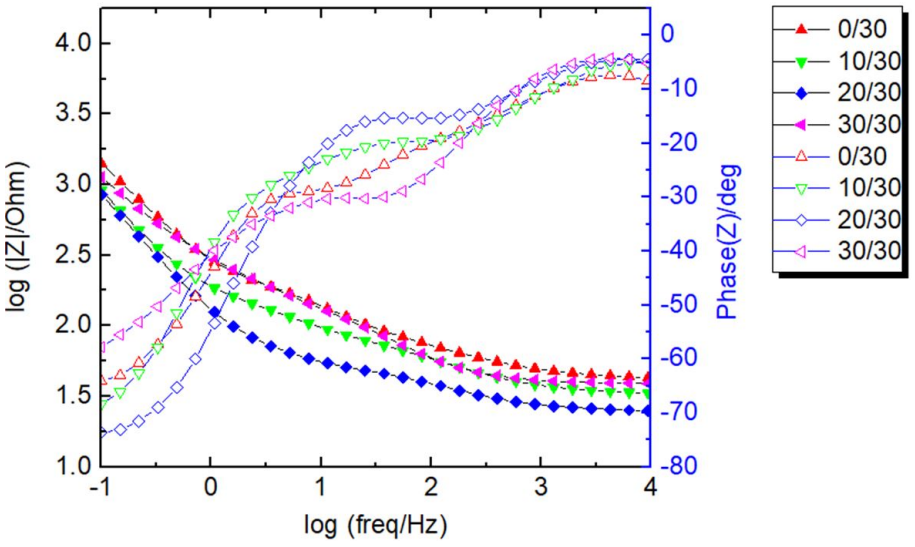


Figure III.39: Bode plot for electrodes in the study of separation time at constant saturation time. EIS was performed in 1 M KCl, 1 mM ruthenium hexaamine.

[15]A general deduction is made based on the formula R over C, or R/C.

The transition to the mass-transfer region/frequency range is different, compared to the previous section. It seems to display signs for the parallel influence of transfer mechanisms in a structured network electrode, depending on the pore size and resulting limitations of diffusion. The slopes in the Nyquist plots between 10 and 100 Hz are around 45 °, which indicates some extent of linear, semi-infinite diffusion. The idea is confirmed by the phase angles, which reach a plateau around 20-30 ° in the Bode plot. While this does not precisely satisfy traditional Warburg conditions, it is closer to 45 ° over a wider range of frequencies, than in the last section. The 20/30 electrode is of least semi-infinite character, which seems to confirm the previously discussed evolution of spectra as a function of structuration parameters and the interpretations regarding the generation of pores.
At frequencies below 1 Hz, the slopes in Nyquist and Bode plots indicate electrochemical double layer charging. Since the slopes are less inclined, a higher pseudo-capacitive behaviour may be confirmed. Interestingly, the 20/30 sample exhibits highest phase angles in the low-frequency region, corresponding to "most ideal" capacitive behaviour of the tested electrodes.

The equivalent circuits were fitted to the data, see $\chi^2$ in Table III.20. Compared to the last section, electrodes in this study attain significantly better fits, but the reason is unknown. Interestingly, all three circuits match the spectrum of the 20/30 electrode best.

Table III.20: Quality of fit for different equivalent circuits in the study of separation time at constant saturation time.

| **Description** | $\chi^2$ **fit a)** | $\chi^2$ **fit b)** | $\chi^2$ **fit c)** |
|---|---|---|---|
| **0/30** | 446220 | 2430 | 750 |
| **10/30** | 416198 | 1990 | 710 |
| **20/30** | 78160 | 350 | 70 |
| **30/30** | 119680 | 610 | 110 |

Equivalent circuits: a) $R_s$-Q//($R_{CT}$+W); b) $R_s$-Q//($R_{CT}$+M); c) $R_s$-$Q_{interface1}$//($R_{pore}$+$Q_{interface2}$//$R_{CT}$)

The extracted circuit parameters of fit b) are listed in Table III.21, demonstrating values of similar range as in the last section. An exception consists in $R_{CT}$, which is increased by one order for almost all electrodes, correlating with the larger dimensions of the R/C semi-circles. However, the 20/30 electrode deviates from the trend and presents small $R_{CT}$, which was reproduced for a second electrode ($R_{CT}$ determined to 74 ), which is not displayed here. For longer separation times, the constant phase coefficient $\alpha$ increases up to 0.73, which is seen as a sign of hierarchical or fractal porosity.
The estimated normalized capacitance values fall into the same range, as during the last study, with a slight increase for the 20/30 electrode. The observation may be coherent with results from the other characterization techniques. Interestingly, the evolution as a function of separation time follows the earlier observed, arc-shaped curve.

Table III.21: Key circuit parameters determined from equivalent circuit b) in the study of separation time at constant saturation time.

| | $\mathbf{R}_s$ **(Ω)** | $\mathbf{Q}^0$ **(mF.s$^{(a-1)}$)** | $\alpha$ | $f"_{max}$ **(Hz)** | $\mathbf{R}_{CT}$ **(Ω)** | **C (µF)** | $\mathbf{C}_{norm}$ **(mF/cm$^2$)** |
|---|---|---|---|---|---|---|---|
| **0/30** | 39.4 | 0.58 | 0.55 | 0.98 | 121 | 257 | 3.60 |
| **10/30** | 39.8 | 0.58 | 0.56 | 1.25 | 134 | 234 | 3.25 |
| **20/30** | 24.0 | 0.58 | 0.65 | 0.87 | 34 | 323 | 4.90 |
| **30/30** | 38.0 | 0.28 | 0.73 | 0.94 | 167 | 172 | 2.45 |

### 3.2.3 Conclusion of studying the separation time at constant saturation time

The intention of this section was to study the effect of longer saturation times on the generation of porosity and surface. Therefore, the same variations of separation time of the previous section was maintained. It is pointed out, that this implies in parallel an overlap with varying the parameter of total exposure time (between 30 to 60 min).

The quality of digital microscopy images was increased and deposits displayed higher surface homogeneity. It is suspected, that the membrane-like surface layer contains a high percentage of polymeric binder. In consequence, it is potentially partially dissolved during extended exposure times. This hypothesis requires confirmation in a future continuation of the project by means of surface-sensitive techniques, e.g. secondary ion mass spectrometry. Characteristic differences between the top layer and the underlying bulk structure are expected.
In the images, the top layer displayed irregularities, revealing the underlying bulk structure. The latter displayed an even distribution of pores with varying size. The study of generated height and volume allowed to distinguish an arc-shaped evolution with varying separation time, similar to the last section. A maximum total pore/volume generation was linked to 10/30 and 20/30 deposits, depending on the deposited ink volume. The reconstruction of deposit volumes confirmed maximum results for 10/30 or 20/30 samples as a function of ink volume. Overall, maximum values exceeded the results of the previous section. Figure III.40 illustrates main results regarding the generation of porosity.

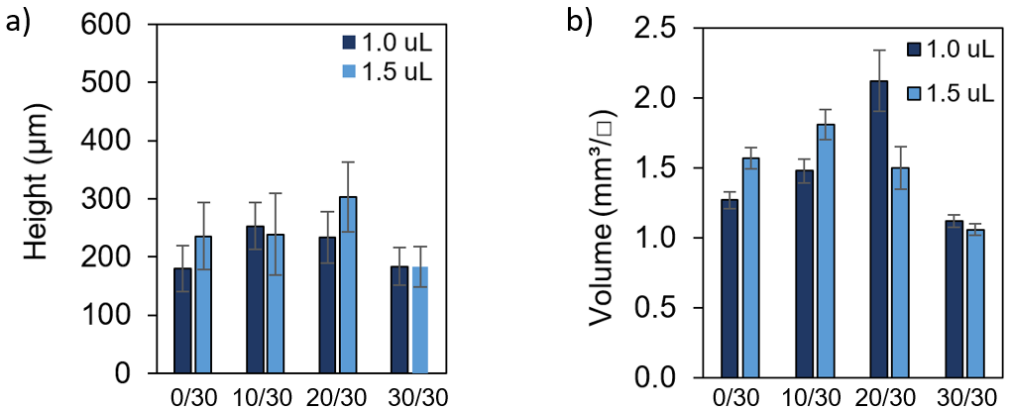


Figure III.40: Results for a) height (single measurements) and b) volume development for $scCO_2$-structured ink deposits (averages of 4 deposits). The separation time ($t_{sep}$) was studied at constant saturation time ($t_{sat}$). Two sets of deposits samples were prepared using different ink volumes.

SEM images provided a more detailed view of the exposed structure, which seemingly underlined the removal of the top-layer. In coherence with literature on phase separation, a bi-continuous structure was distinguishable, presenting a small contribution of beads or nodules. Generally, the structure resembled a "primary" microstructure, decorated with a nanostructure. The latter is possibly composed of carbon nanoparticles, commonly found in carbon inks, and polymeric binder. It could agglomerate around larger particles, such as graphite flakes, or microstructural features, respectively.
The image-based estimation of pore sizes on the surface of deposits yielded an arc-shaped evolution, with smallest pores linked to the 20/30 sample. This coincided with the smallest total pore area. Following previous reasoning, it is assumed that the pore formation in

the volume follows different tendencies. However, the verification of this hypothesis was limited by the difficulty to perform cross-section imaging.

Cyclic voltammetry studies yielded curves of pronounced pseudo-capacitive character. The determined normalized and gravimetric capacitances followed an arc-shaped tendency with maximum values for the 10/30 electrodes, corresponding to an increase by more than 10, relative to the unstructured electrode. The determined peak values increased significantly in comparison to the previous section, see Figure III.41 a). Literature values for the capacitance of porous, carbon-ink based electrodes were exceeded.
Faradaic studies displayed slightly lower reversibility of charge transfer, based on evaluating peak ratios, as for shorter saturation times. This may correlate with the increased pseudo-capacitive character. Largest electroactive surfaces were determined for the 20/30 electrodes and the overall trend again followed an arc-shaped evolution. Relative to the result of the unstructured electrodes, a maximum increase of factor 12.5 was calculated based on peak currents.

The chronoamperometric studies yielded very pronounced increases in electroactive surface, with peak values occurring for the 20/30 electrodes.
EIS studies are to be treated with care, but appear to equally follow an arc-shaped tendency as shown in Figure III.41 a). This observation further applied for almost all parameters of the equivalent circuit. The deviation between results extracted from CV and EIS studies are considered to potentially result from the difficulty to fit impedance spectra with reasonable equivalent circuits.

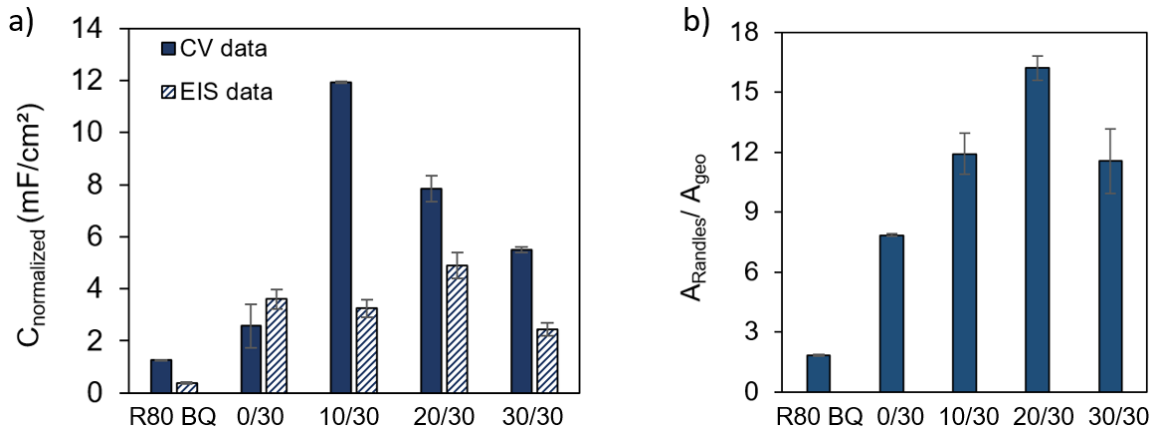


Figure III.41: a) Results for the development of capacitance of structured electrodes, normalized to the geometric electrode surface, determined from CV and EIS studies. b) The development electrochemically active surface for $scCO_2$-structured ink deposits. The separation time ($t_{sep}$) was studied at constant saturation time ($t_{sat}$). Average values of 4 structured electrodes are displayed. All electrodes were plasma-treated.

The results evolved very similar, as in the previous section, this may confirm the generation of a primary electrode structure by means of the phase separation mechanism. Further, the characterizations suggests a positive influence of longer saturation times on the generation of porosity and specific/electroactive surface. Particularly, this may confirm the theory of foaming of the polymeric binder. The further increase in electroactive surface is considered useful for a practical sensing application.
The results of this section highlight the potential of tailoring electrode properties to required specifications.

## 3.3 Study of saturation temperature

Based on the improved protocol, which confirmed an interest for longer saturation times and suggested to maintain a separation time around 10 to 20 min, the second phase during structuration was further investigated. Literature on the fabrication of porous polymeric membranes reports an interest to the adapt process temperature, which modifies the properties of supercritical $CO_2$ and lowers the glass transition temperature of the polymer. Together, this changes the achievable pore size. The aim of this part of the study was therefore, to conclude on the choice of saturation temperature for the further project.
As the previously used saturation temperature $T_{sat}$ (40 ℃) lies just above the critical temperature of $CO_2$ (31 ℃), a second temperature at 60 ℃ was selected in this section. Regarding the other structuration parameters, samples were prepared and characterized as before, justifying a direct comparison.

### 3.3.1 Physical characterization

#### 3.3.1.1 Digital microscopy

Figures III.42 and III.43 present the digital microscopy images in top view for 1.0 and 1.5 µL ink deposits, respectively. As first observation it is noted, that 0/30 deposits for both volumes display a homogeneous and seemingly "flat" surface structure. At higher magnification, the distinct porous "cellular" structure mentioned before is distinguishable. The visual difference to the other deposits is seen as confirmation for the general assumption, that phase separation does generally not take place for 0/30 deposits. A similar observation was noted for the 0/30 deposit, prepared with $T_{sat}$ equal to 40 ℃. in the previous chapter[16].

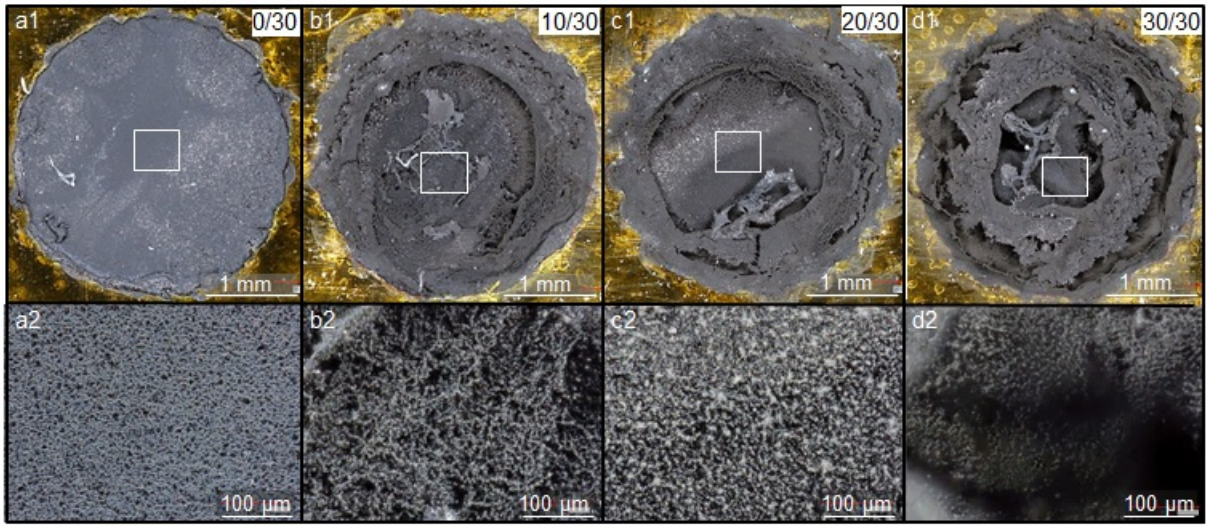


Figure III.42: 1.0 µL ink deposits (BQ242:EGDA = 2:8 (w/w)) for digital microscopy in top view in the study of saturation temperature; the 0/30 sample in a), 10/30 in b), 20/30 in c) and 30/30 in d). Ratios refer to the parameters $t_{sep}/t_{sat}$. White boxes correspond to magnified locations.

[16]In the study of the ratio of separation and saturation time, however, the 0/30 deposits did not reproduce this type of flat and regular surface. Earlier it was reasoned, that different cell pressurization times could have resulted in the difference, which remains to be confirmed.

It is further pointed out, that the surfaces of 0/30 deposits in FigureIII.42 present a remarkable homogeneity and regularity. Potentially, this is linked to the diminished non-solvent strength of supercritical $CO_2$ at higher temperatures [15]. As the transition between what is referred to as separation and saturation phase is not ideal, but in reality of continuous character, a short period of phase separation of unspecified time is expected even for 0/30 deposits, before the presumed foaming phase occurs. For higher temperatures (lower non-solvent strength), this mechanism is thought to be of different expression and may result in the different surface texture.
Reportedly, high non-solvent strength favours a rapid separation process (liquid-liquid demixing), that is limited by the mass-transfer kinetics of the components. In consequence, membranes with a thin top layer of beads-like/nodular type can be formed, that express a certain degree of porosity with underlying macrovoids [11]. Assuming comparable behaviour for the diluted ink, the less homogeneous nature of 0/30 deposits at low $T_{sat}$ could correspond to this case. On the other hand, low non-solvent strength is linked to slow demixing conditions (solid-liquid demixing), limited by thermodynamics. The generated membranes are considered to have a thick top layer of higher polymer content, but of less porous character [11]. In consequence, slow demixing may explain the surface of 0/30 deposits for a $T_{sat}$ of 60 °C.

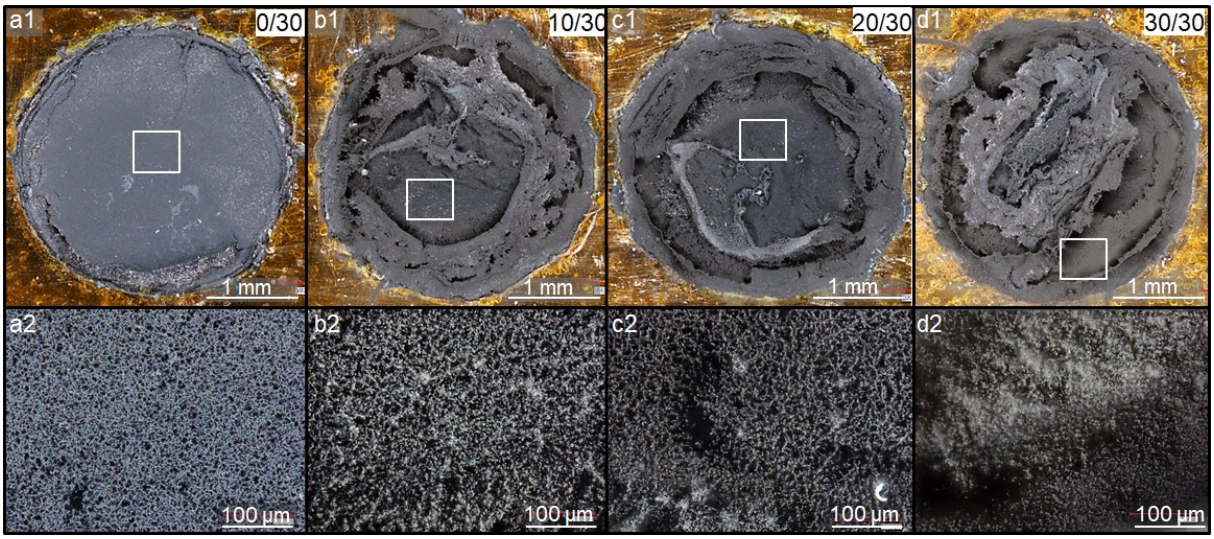


Figure III.43: 1.5 µL ink deposits (BQ242:EGDA = 2:8 (w/w)) for digital microscopy in top view in the study of saturation temperature; the 0/30 sample in a), 10/30 in b), 20/30 in c) and 30/30 in d). Ratios refer to the parameters $t_{sep}/t_{sat}$. White boxes correspond to magnified locations.

The phase separation in presence of subcritical $CO_2$ is initiated with certainty, once the separation time varies from 0. Under the assumption, that the dependence of non-solvent strength and temperature can be extrapolated for subcritical $CO_2$, lowering the temperatures (e.g. to ambient conditions) implies even higher non-solvent strength. The generation of a membrane-like top layer may hence be explained. The previously determined optimum $t_{sep}$ (10-20 min) could indicate the time-scale required for this process[17]. Up to this parameter setting, deposits should display a comparable structure, independent from $T_{sat}$. A re-dissolution of the polymeric component would then take place as suggested earlier. Phase separation may still be ongoing.

[17]However, some references state, that rapid phase separation potentially takes place even faster during a few minutes only.

In the following, the question is, how the presence of membrane-like top layers can be explained for higher $T_{sat}$ and two ideas are discussed. First, the earlier mentioned re-dissolution of polymer in supercritical $CO_2$ may in reality not easily take place, as $scCO_2$ is classified as a rather weak apolar and a weak polar solvent [146]. It is possible, that some types of polymer dissolve better at lower temperatures, where $scCO_2$ has more liquid-like properties.
Alternatively, the explanation could be linked to the polymer foaming step and particularly the depressurization of the cell. As the volume of $CO_2$ increases to a large extent, when transitioning from supercritical to gaseous state, the gain in volume is expected to be more pronounced for higher cell temperatures. In this context, expanding $CO_2$ could be trapped underneath a membrane-like top layer of low porosity, resulting in the partial rupture of electrode surfaces.

#### 3.3.1.2 Height of deposits

Heights of deposit are presented in Figure III.44, with values listed in Table III.22 for a better comparison. For both volumes, higher deposits are observed for longer separation times. The rather poor determination of the samples' top surfaces is compensated by assuming a large uncertainty. Particularly the 30/30 samples may not be representative, which raises the question, if detailed discussion of trends is of interest, or sensible. The previously observed, arc-shaped evolutions are not reproduced.

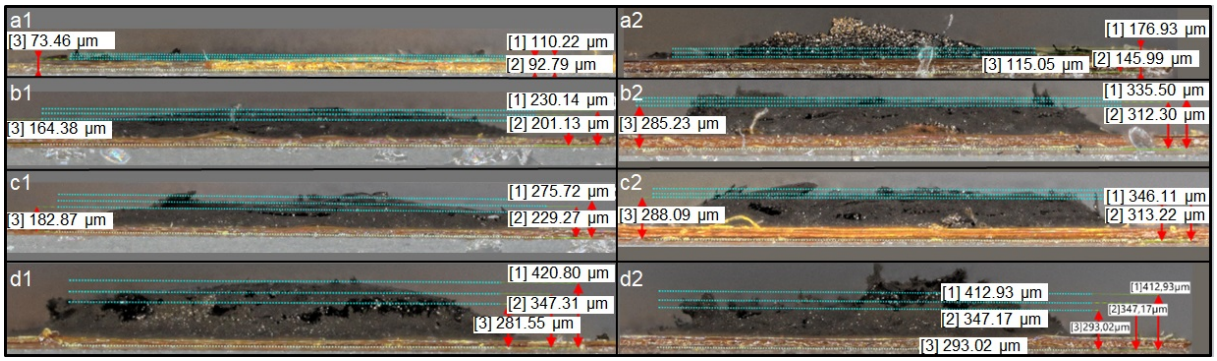


Figure III.44: Side view digital microscopy images of structured ink in the study of saturation temperature. 1 µL in series 1) and 1.5 µL in series 2). Sample 0/30 in a), 10/30 in b), 20/30 in c) and 30/30 in d).

Compared to the previous results for lower saturation temperature, the increase of $T_{sat}$ resulted in smaller height readings for short separation times and higher readings for long separation times. However, as top layers were potentially delaminated in the previous section, a direct comparison may not be sensible.
In addition and as above-mentioned, different structure-generating mechanisms apply for the 0/30 samples, compared to the other sets of parameters. In consequence, the consideration of height for 0/30 deposits should eventually be done separately from deposits undergoing phase separation. In that case, deposits for 1.5 µL ink are to some degree higher for $T_{sat}$ equal to 60 °C.
It is mentioned, that the comparison of side view images appears to be affected by a rather low deposit quality.

Table III.22: Height of ink deposits extracted from side view images in the study of saturation temperature.

| $\mathbf{t_{sep}/t_{sat}}$ | **1.0 µL** | | | **1.5 µL** | | |
|---|---|---|---|---|---|---|
| | $\mathbf{h_{min}}$ **(µm)** | $\mathbf{h_{mid}}$ **(µm)** | $\mathbf{h_{max}}$ **(µm)** | $\mathbf{h_{min}}$ **(µm)** | $\mathbf{h_{mid}}$ **(µm)** | $\mathbf{h_{max}}$ **(µm)** |
| 0/30 | 74 | 93 | 110 | 115 | 146 | 177 |
| 10/30 | 164 | 201 | 230 | 285 | 312 | 336 |
| 20/30 | 183 | 229 | 276 | 288 | 313 | 346 |
| 30/30 | 282 | 347 | 421 | 293 | 347 | 413 |

### 3.3.1.3 Evaluation of volume

Aerial views of the same deposits are shown in Figure III.45 and the correlating values for the estimated volumes are extracted in Table III.23, together with the geometric surface areas, to calculate the volume per unit surface $V_n$. The surface heterogeneity underlines the previous suggestion to interprete images with care, particularly for 30/30 deposits, series d), and eventually 10/30, b2), for 1.5 µL ink.

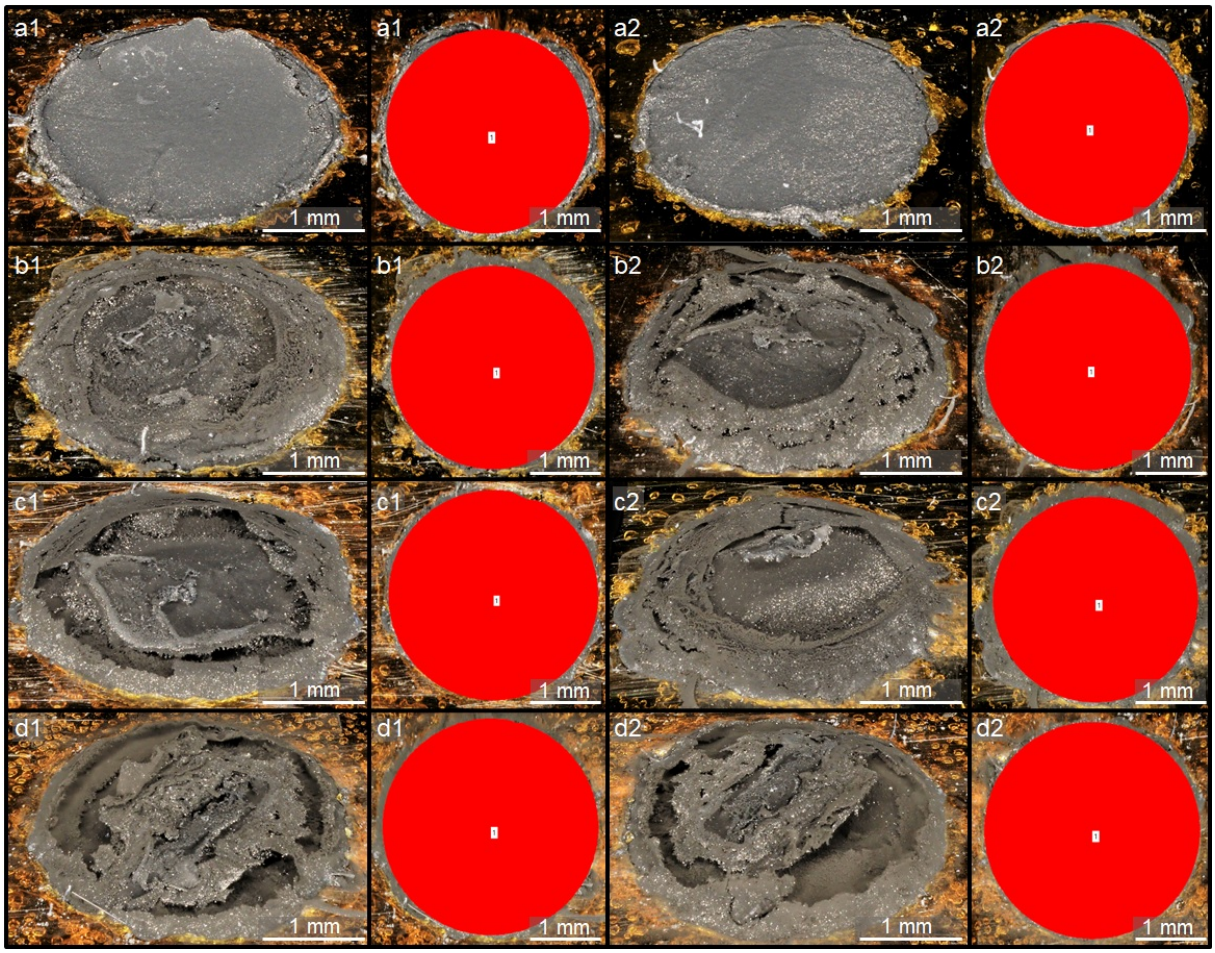


Figure III.45: Aerial view (45 ° and 90 °) digital microscopy of structured ink deposits (BQ:EGDA = 2:8 (w/w)). 1 µL in series 1), 1.5 µL in series 2). The 0/30 deposit in series a), 10/30 in b), 20/30 in c) and 30/30 in d).

Table III.23: Volume of ink deposits extracted from aerial view images in the study of saturation temperature with averaged values for each PCB and calculated volumes relative to a unit surface.

| $\mathbf{t_{sep}/t_{sat}}$ | **1.0 µL** | | | **1.5 µL** | | |
|---|---|---|---|---|---|---|
| | **V ($mm^3$)** | **A ($mm^2$)** | **$V_n$ ($mm^3/\square$)** | **V ($mm^3$)** | **A ($mm^2$)** | **$V_n$ ($mm^3/\square$)** |
| 0/30 | 0.45 | 6.78 | 0.47 | 0.58 | 7.19 | 0.57 |
| 10/30 | 1.95 | 6.89 | 2.00 | 1.58 | 7.48 | 1.49 |
| 20/30 | 1.54 | 6.13 | 1.78 | 1.21 | 6.94 | 1.23 |
| 30/30 | 1.44 | 8.09 | 1.26 | 1.72 | 8.36 | 1.45 |

The estimated, normalized volumes $V_n$ for 0/30 deposits are decreased by around three, compared to the previous section at lower $T_{sat}$, which is in correlation with the visual interpretation of top-view images and height evolutions. This supports the idea, that a higher $T_{sat}$ only allows to generate porosity/volume, when a phase separation step is included in the protocol. Compared to previous sections, the height values for all other deposits are in a similar range. Except for the 30/30 deposits, which attains higher values, results fall in a comparable range. For 1.0 µL ink, the general arc-shaped tendency is distinguishable with maximum values for the 10/30 deposit. For 1.5 µL ink, the 30/30 deposit appears to disrupt the trend.

#### 3.3.1.4 SEM images

The comparison of SEM images is depicted in Figure III.46. As a consequence of the membrane-like top layers with different expression of porosity, care was taken to find relatively central areas on the deposits, which gave the impression of exposing the "bulk" structure. The 30/30 deposit represents an exception and may potentially display said top layer. The texture resembles the visually denser areas in a1), c1) to somme degree, which were associated with the membrane.

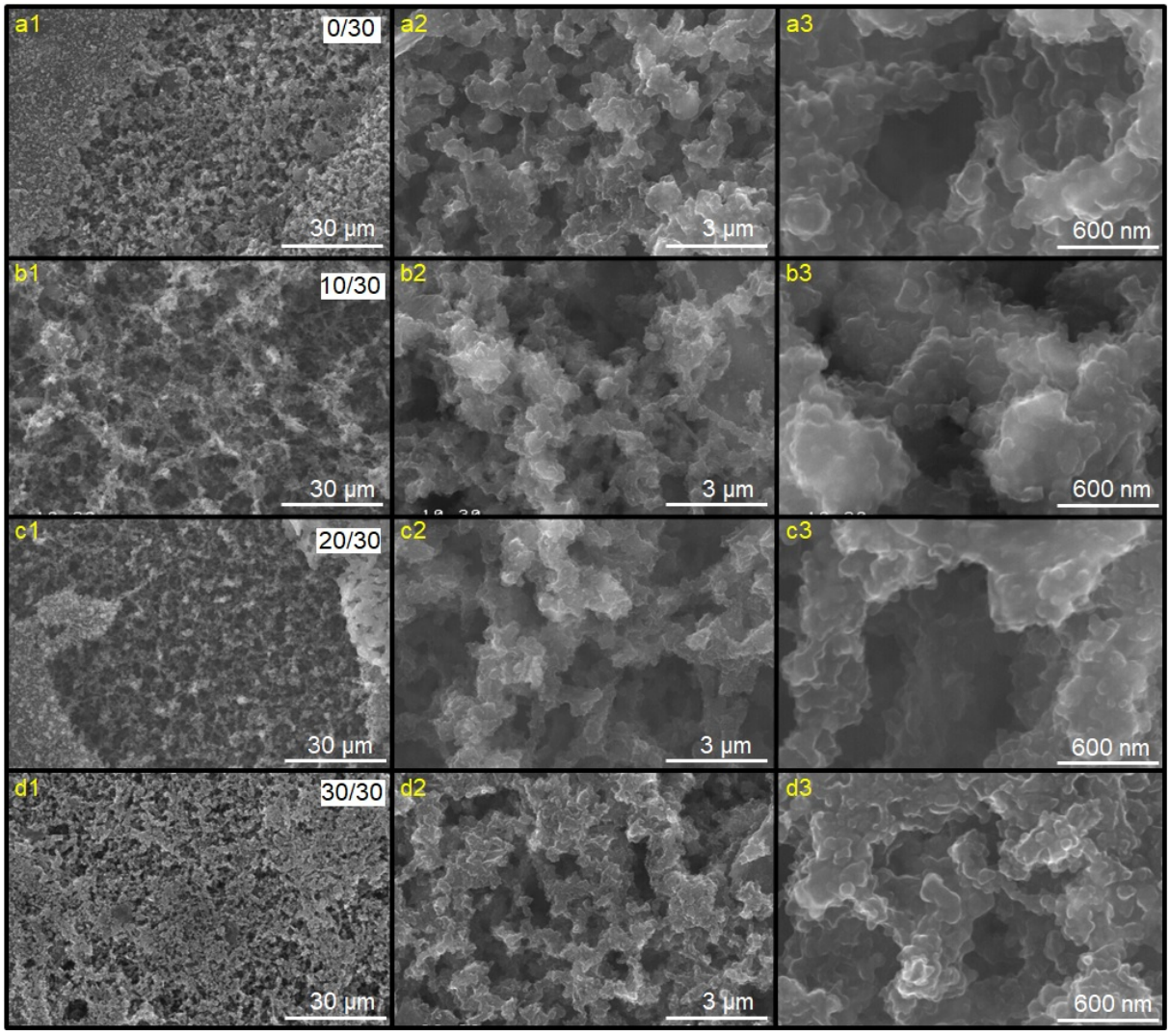


Figure III.46: SEM images of structured ink deposits in the study of saturation temperature $T_{sat}$ of 60 ℃. Images display central deposit locations.

Generally speaking, no principal, visual difference to SEM images in the previous sections was noticed. For a better identification of eventual structural differences, the ImageJ treatment was applied. The single steps are represented in Figure III.47 and results are extracted in Table III.24, forming the base for histograms of the pore size distributions. The latter are shown in Figure III.48.

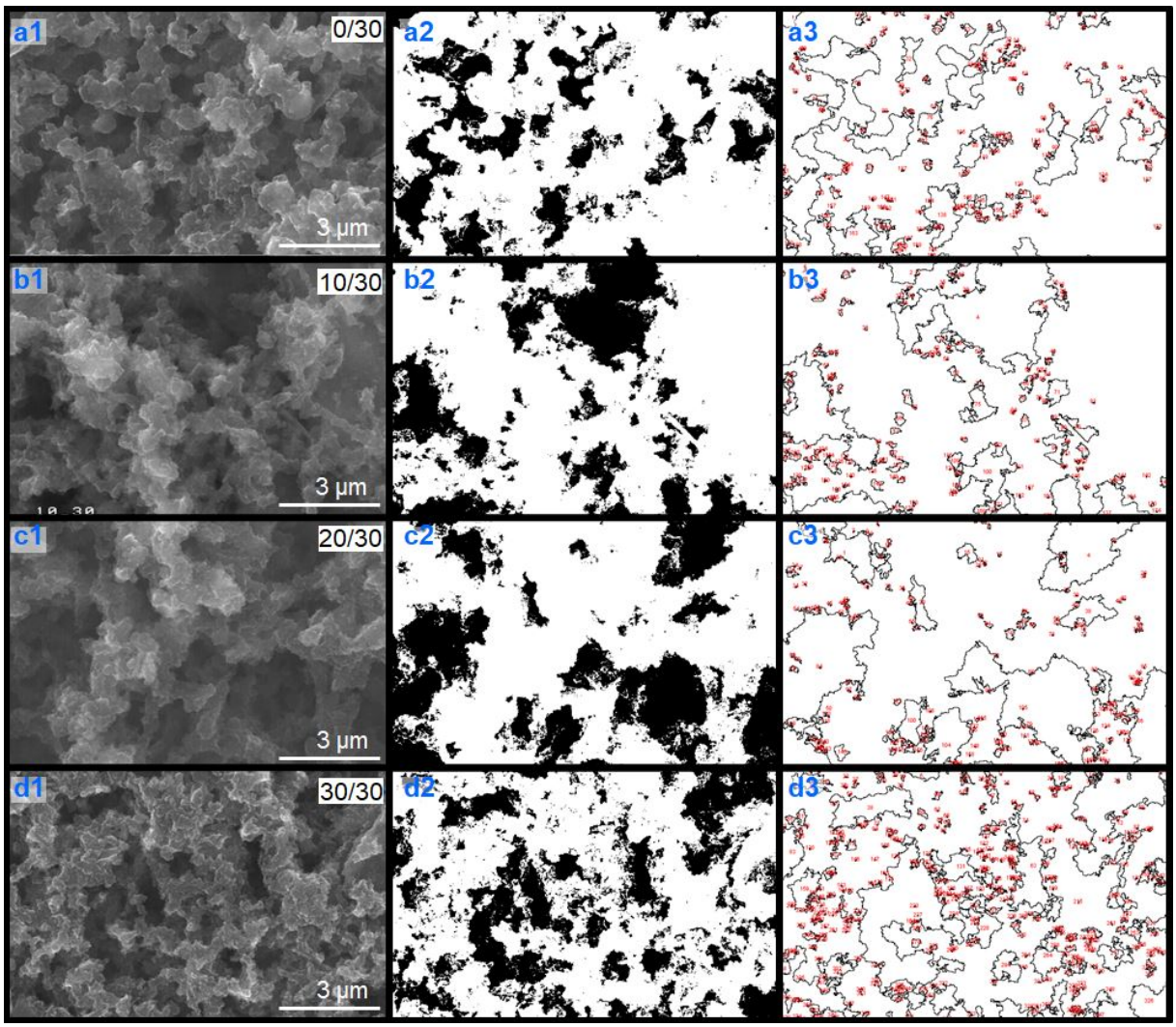


Figure III.47: SEM image treatment for ImageJ pore area determination and quantification in the study of saturation temperature. The red markings originate from the automatic pore count.

The non-structured 0/30 deposits are discussed first. It is reminded, that the studies of $t_{sep}/t_{sat}$ and of lower $T_{sat}$ contain the same data set for the respective deposit and values are copied.
The particle count for higher $T_{sat}$ is increased by 50 %; however, volume and the correlating porosity were previously estimated to be smaller. Therefore, while the surface covered by pores is estimated to be 20 % larger, the difference between volume and surface porosity is highlighted again.
The calculation of mathematically averaged pore sizes yields results, which are highly comparable to the previous study. In the histograms (for the 0/30 sample), the populations appear to be of similar size for pores up to around 100 nm, compared to lower $T_{sat}$. There is an eventual slight trend towards larger pore sizes around 50 nm.

The pore count for structured 10/30 and 20/30 deposits is halved and comparable to the study of $t_{sep}/t_{sat}$, while on average, the covered pore area is slightly increased. A difference lies in the maximum coverage, which is observed for the 30/30 deposit and which is of similar value, as the maximum result for lower $T_{sat}$. The potentially low representativity data derived from the 30/30 deposit was mentioned.
Earlier, the mathematically averaged pore size was considered to deliver information of

controversial quality. Given the comparable pore sizes for both $T_{sat}$, obtained for 30/30 deposits (70 nm), this statement is reconsidered. Potentially, some valuable information is extractable.
For higher $T_{sat}$, arc-shaped evolutions are noticed, with a maximum average pore size for the 20/30 deposit. The trend, is of inverse tendency, compared to the lower $T_{sat}$, where minimum values were associated with 20/30 samples. For lower $T_{sat}$, the averaged maximum pore size is around twice the value. In the histograms, the structured samples display population sizes, which are reduced up 3 times for pores up to 100 nm, in correspondance with the lower total pore count. While the distribution of populations is visually different for the 10/30 sample, 30/30 samples for both $T_{sat}$ are relatively comparable. Contrary to the mathematically averaged values and to initial expectations, no particular shift of populations towards larger pore diameters was observed for higher $T_{sat}$.

Table III.24: Extracted data from the ImageJ treatment of SEM images in the study of saturation temperature.

| **Description** | **Particle count** | **Total particle area ($\mu m^2$)** | **% Area** | **Pore diameter (nm)** |
|---|---|---|---|---|
| 0/30 | 250 | 21.7 | 21.3 | 87 |
| 10/30 | 216 | 28.1 | 27.7 | 130 |
| 20/30 | 214 | 32.7 | 32.2 | 153 |
| 30/30 | 466 | 33.1 | 32.6 | 71 |

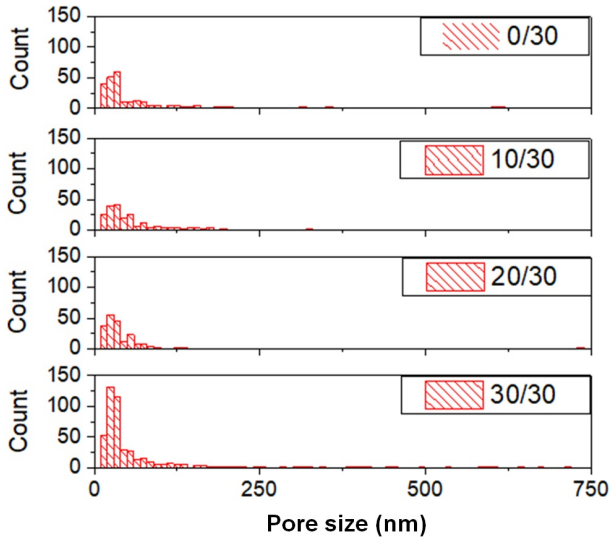


Figure III.48: Histograms of particle/pore populations based on treated SEM images in the study of saturation temperature.

During the polymer foaming step, the first mechanism to take place is the diffusion of supercritical $CO_2$ into the polymer matrix, forming a single phase. Besides for intermolecular interactions, the main parameters which alter the polymer's capacity of sorption (i.e. the capacity to contain supercritical $CO_2$) are process temperature and pressure [147]. Potentially, this is a consequence of the increased plasticity of the polymer, as detailed earlier. It is reminded, that no definitive, temporal separation between the primary structuration mechanism, phase separation, and the polymer foaming phase is possible. Saturation of the polymer with supercritical $CO_2$ may already start, while the phase separation mechanism is still ongoing and while $T_{sat}$ is still low. Reportedly, though, it is

more pronounced with increasing $T_{sat}$ [148]. In practical, this corresponds to a higher potential for generating a porous volume, once the supercritical fluid is extracted.
As increased temperature and pressure allow the system polymer-sc$CO_2$ to remain in a thermodynamically stable state, more $CO_2$ is dissolved in the polymer, than at lower temperatures. However, a rapid change in process conditions can induce the system to transition into a thermodynamically metastable state of supersaturation. Typically, for polymer foaming, this step is achieved by a rapid depressurization, which initiates nucleation. The experimental conditions determine, whether homogeneous or heterogeneous nucleation are favoured. Pores grow, once the clusters of nuclei exceed a certain critical radius which is linked to the activation energy/ Gibbs free energy of pore growth. The presence of nanoparticles, such as carbon black, is speculated to enhance foaming due to limitation of $CO_2$ diffusion and due to it acting as a nucleation agent, which increases the rate of heterogeneous nucleation. From a thermodynamic point of view, the formation of nuclei at a phase boundary requires less activation energy and an increased pore density/count is expected. In this context, higher process temperatures should further allow higher nucleation and growth rates, resulting in increased porosity.

A related work of Nikitine et al. on the extrusion of Eudragit E100, a thermoplastic copolymer derived from acrylic acid and methacrylate, is cited to support the theory of the generation of larger pores [92]. Supercritical $CO_2$ acts as plasticizer for polymers, decreasing its glass transition temperature and hence allows to optimize rheological properties in a given process. Further, its role as foaming agent, upon relaxation, is essential for this study. One of the studied parameters was die temperature, which is comparable to the cell temperature $T_{sat}$. In the study, a higher value was set (110 ℃), which implies lower polymer viscosity, in turn supporting pore growth [28 ip]. In addition, samples remain above the vitrification point of the polymer for a slightly longer time, until being cooled to laboratory conditions, than it is the case for lower $T_{sat}$ [63]. In consequence, the time available for pore growth is longer and the net expansion rate of the sample is increased. In the study, cross-sections allowed observing a distribution of pore sizes, with smaller pores on the outside and larger pores found in the bulk. Interestingly, the optimum foaming time was determined to 30 min for the given volume, which generally matches the order of parameters used in this project. The expansion of the sample was considered largest for 130 ℃.
Aside from the hypothesis, that delamination of the membrane-like top layer followed the expansion of $CO_2$, equivalent observations have not clearly been made in this work. The main interest for maintaining lower $T_{sat}$ is seen in the theoretical generation of smaller pores, which are of higher interest in electrochemical turns.

## 3.3.2 Electrochemical characterization

### 3.3.2.1 Capacitive current studies

Figure III.51 presents CVs recorded at different scan rates in 1 M KCl, cycled at 5 mV/s in series 1) and for scan rates up to 500 mV/s in series 2). Before entering a detailed discussion, the quality of curves is pointed out, which is lower than in previous chapters and is mainly distinguishable in the form of oscillating noise. As measurements were performed in a Faraday cage, the source of the interferences is unclear. Potentially, electronic noise emitted from other equipments in surrounding rooms was responsible. In particular, a shared ground connection in the laboratory building may have played a role. Due to the small amplitude of the noise signal, CV were still considered suited for a further evaluation.
Second, the 30/30 electrodes in Figure III.51 d) displays the redox peaks previously linked

to contamination, which is most visible for slow scan rates. The steeper slope expressed in these CV indicates a higher electrode resistance, which is superimposed with the expected pseudo-capacitive response. The electrodes 0/30 to 20/30 display CV of comparable shape, as in the study of lower $T_{sat}$.

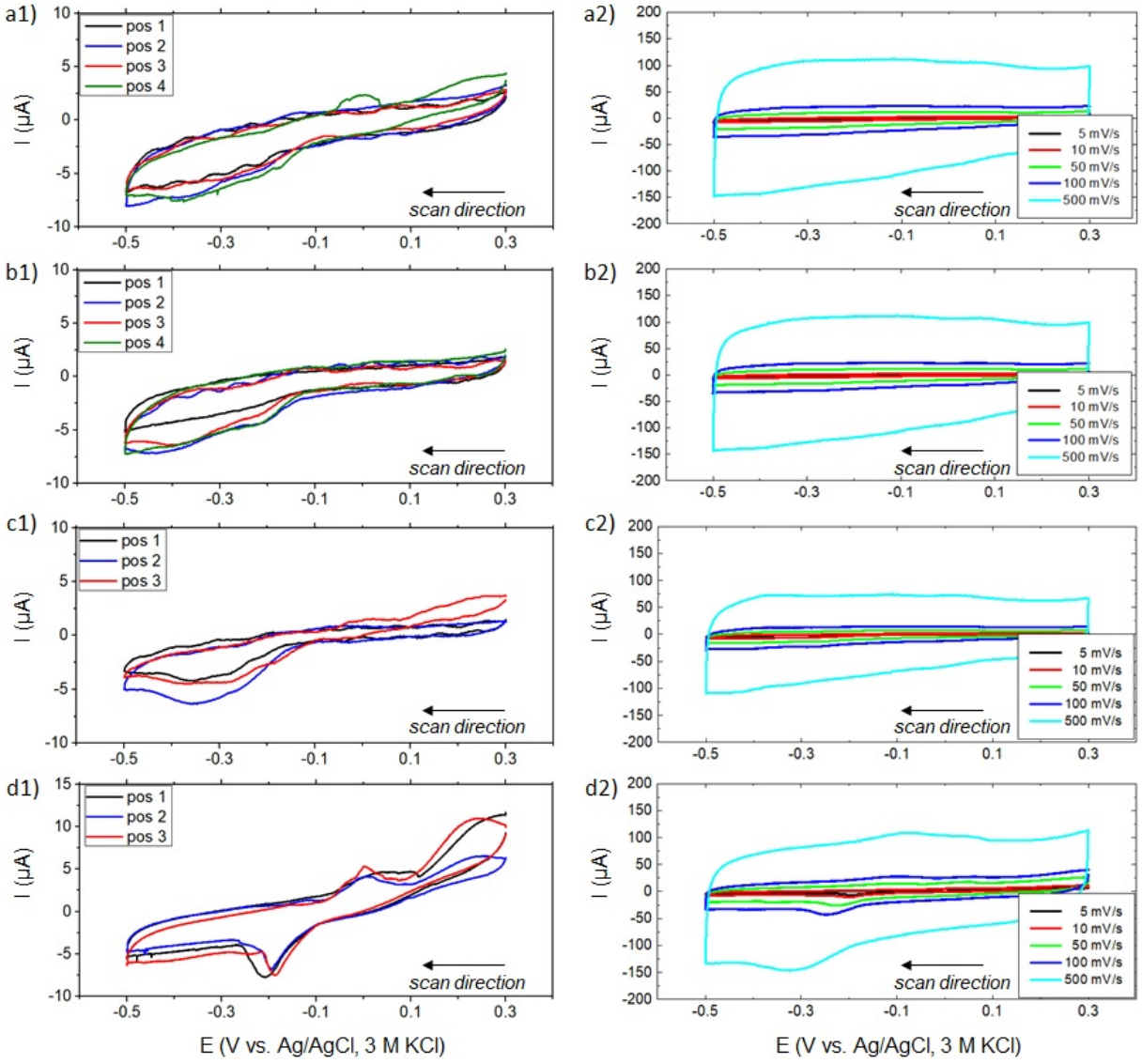


Figure III.49: Capacitive currents of structured ink in the study of saturation temperature in 1 M KCl. Series 1 at 5 mV/s for all electrodes per PCB, series 2 for different scan rates of one electrode. a) 0/30, pos. in detail; b) 10/30, pos. in detail; c) 20/30, pos. in detail; d) 30/30 pos. in detail. All electrodes were oxygen-plasma-treated. The $5^{th}$ cycles are displayed. Onset at 0.3 V.

Based on CV, the normalized and gravimetric capacitances were calculated, see III.50. Each data point represents the average of several electrodes per PCB, together with the results for non-structured electrodes for a better comparison. For scan rates of 5 mV/s, the extracted capacitances and corresponding factors of increase, relative to nonstructured electrodes, are listed in Table III.25. Interestingly, structured electrodes in this section exhibit a variety of different evolution of data as a function of scan rate.
The response of the 10/30 electrodes is rather independent from the scan rate. It resembles the characteristic of non-structured electrodes, but at higher capacitance values. As for the all other electrodes, the dependence on the scan-rate is similar to what was previ-

ously observed, the 10/30 data may be considered flawed. As all electrodes were visually inspected, visible delamination of the electrode is unlikely to have occurred. One explanation consists in small variations in process parameters, e.g. pressurization time, which has potentially affected phase separation and, in turn, the formation of the membrane-like top layer..
The dependence on the scan rate, in case of the other electrodes, is most pronounced for the PCB 0/30 and 30/30 and almost comparable to the R80 BQ-EGDA electrodes. In combination with the inclined CV, observed for these electrodes, see Figure III.51 a) and d), a pronounced pseudo-capacitive behaviour is possibly an explanation. Faradaic components, such as leakage currents, may overlap.

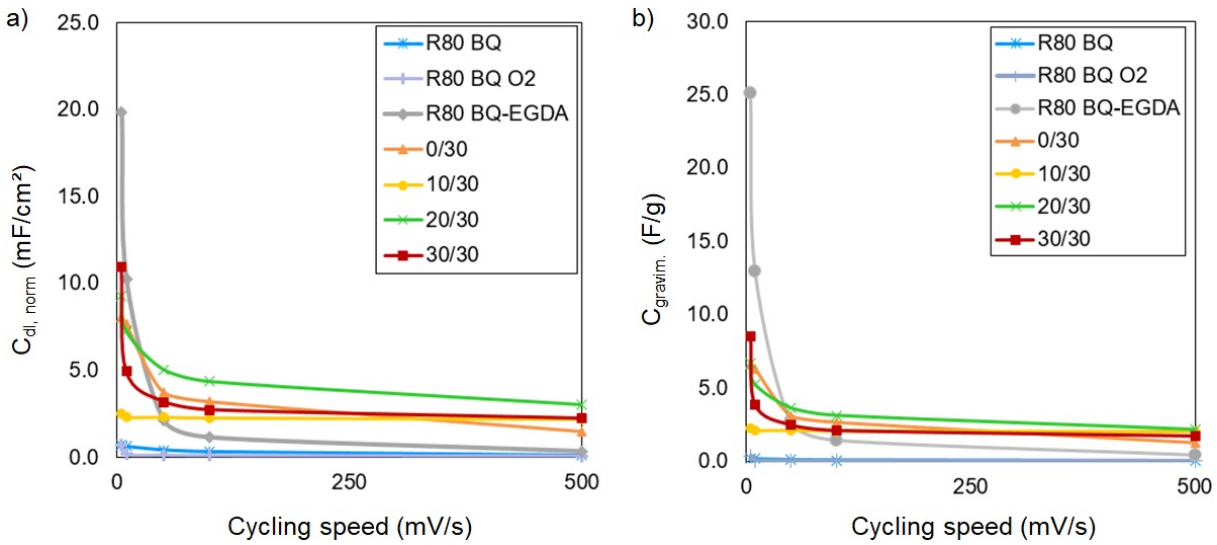


Figure III.50: a) Normalized capacitance and b) gravimetric capacitance in the study of saturation temperature, extracted from CV. Each data point corresponds to the average of up to 4 electrodes per PCB.

Table III.25: Measured capacitance ($C_{meas}$) in the study of saturation temperature, normalized to $A_{geo}$ of electrodes ($C_{norm}$), to the mass of active material ($C_{gravimetric,corr.}$) and to the non-structured R80 BQ electrodes ($Increase$). Results originate from CV at 5 mV/s in 1 M KCl.

| **Description** | **C$_{meas}$ (µF)** | **C$_{norm}$ (mF/cm$^2$)** | **Increase** | **C$_{gravim.,corr.}$ (F/g)** | **Increase** |
|---|---|---|---|---|---|
| 0/30 | 665 | 8.06 | 11.3 | 6.66 | 30.4 |
| 10/30 | 228 | 2.51 | 3.5 | 2.28 | 10.4 |
| 20/30 | 670 | 9.30 | 13.1 | 6.70 | 30.5 |
| 30/30 | 857 | 10.95 | 15.4 | 8.57 | 39.1 |

Comparing the measured capacitances, the 10/30 electrodes stand out due to the relatively low values, matching the visual impression. All other electrodes exhibited a tendency of larger capacitance values for longer t$_{sep}$, which is even more pronounced for normalized capacitances. Compared to the earlier section, this observation is incoherent, as an arc-shaped evolution was assigned to the results in the stud of lower T$_{sat}$. The general magnitude of values of both normalized and gravimetric capacitance is very similar to the previous section, with increases up to 15 and 39, relative to the R80 BQ electrodes. It is noticed, however, that the capacitances for the study of higher T$_{sat}$ are increased on average.

### 3.3.2.2 Faradaic current studies

Following earlier sections, CV were repeated in presence of 1 mM ruthenium hexaamine and fifth cycles are shown in Figure III.51. For the following discussion, the qualitative impression of the curves is complemented by data listed in Table III.26.

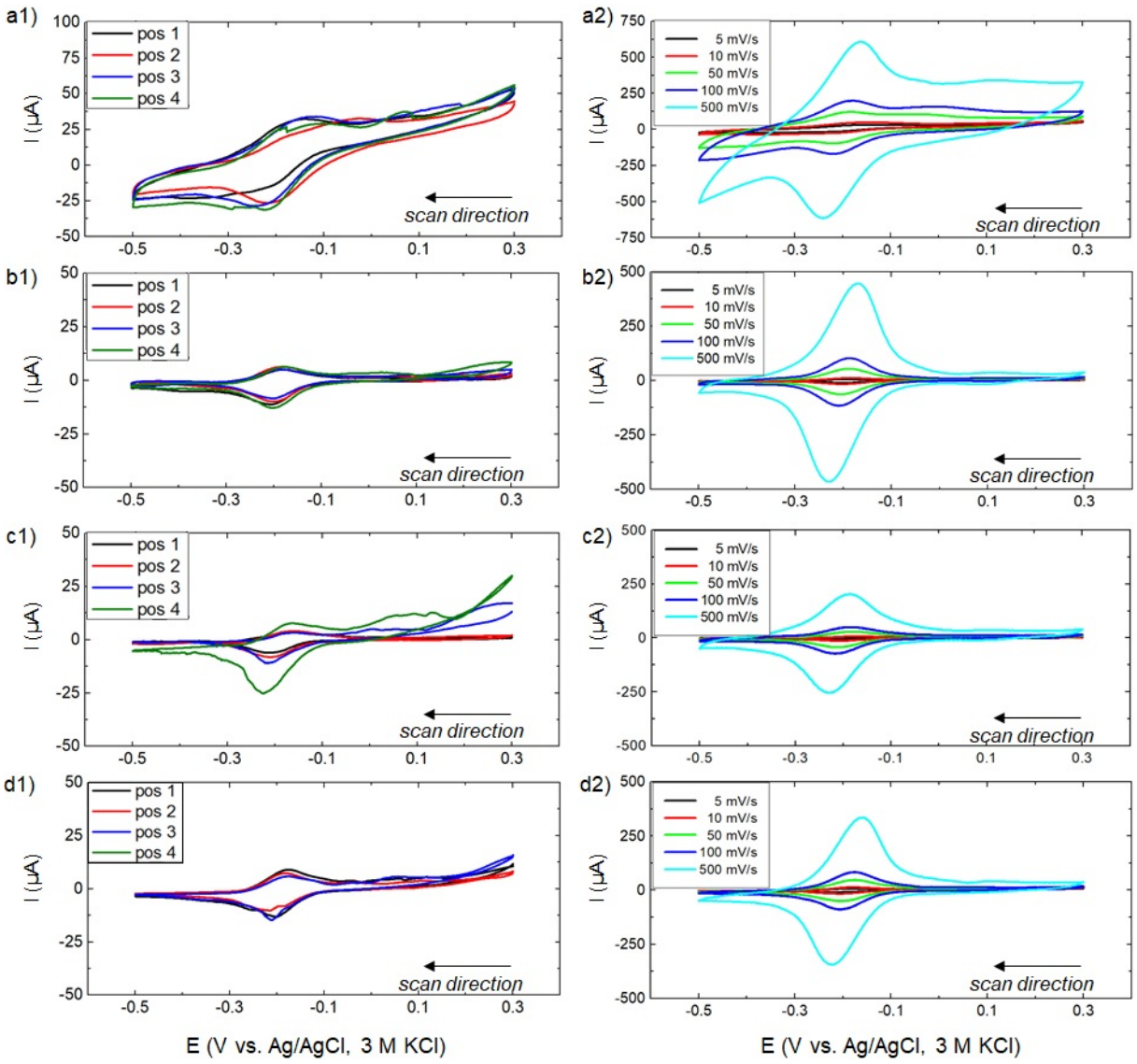


Figure III.51: Faradaic current response of structured electrodes in the study of saturation temperature in 1 M KCl, 1 mM ruthenium hexaamine. Series 1 at 5 mV/s for all electrodes per PCB, series 2 for different scan rates of one electrode. a) 0/30 and pos. 2 in detail; b) 10/30 and pos. 2 in detail; c) 20/30 and pos. 2 in detail; d) 30/30 and pos. 2 in detail. All electrodes were oxygen-plasma-treated. The $5^{th}$ cycles are displayed. Onset at 0.3 V.

For the 0/30 electrodes, the different scale of the y-axis is pointed in a). The corresponding CV are of different overall impression, displaying a steeper slope, which is seen as a consequence of higher electrode resistance. The volume enclosed by the curves again results from the relatively high pseudo-capacitive base response, as explained earlier. This may equally explain, why the CV are not resembling the often encountered "duck shape", despite the subtraction of background currents. Pseudo-capacitive currents linked to the structured ink, may eventually have been comparably low during the capacitive current studies, but higher in the Faradaic current studies.

Table III.26: Peak-to-peak separation, peak current and peak ratio extracted from CV in 1 mM ruthenium hexaamine, 1 M KCl in the study of separation time at constant saturation temperature.

| $\mathbf{v}_{scan}$ **(mV/s)** | **R80 BQ** | **R80 BQ $O_2$** | **R80 BQ-EGDA** | **0/30** | **10/30** | **20/30** | **30/30** |
|---|---|---|---|---|---|---|---|
| **$\Delta E_{peak}$ (mV)** | | | | | | | |
| 5 | 64.9 | 66.0 | 68.1 | 50.8 | 17.7 | 45.7 | 29.7 |
| 10 | 64.8 | 64.1 | 77.9 | 40.8 | 18.8 | 43.2 | 35.2 |
| 50 | 64.9 | 61.3 | 96.9 | 49.0 | 17.8 | 40.8 | 45.9 |
| 100 | 64.4 | 58.9 | 104.0 | 35.8 | 20.6 | 37.2 | 43.9 |
| 500 | 64.0 | 58.3 | 147.3 | 72.5 | 56.5 | 44.3 | 72.5 |
| **$\mathbf{I}_{ox}$ (µA)** | | | | | | | |
| 5 | 4.3 | 4.8 | 17.1 | 11.1 | 6.1 | 5.3 | 9.1 |
| 10 | 6.1 | 6.8 | 26.9 | 22.7 | 10.7 | 7.3 | 14.8 |
| 50 | 12.9 | 15.4 | 36.2 | 58.8 | 44.1 | 19.9 | 45.6 |
| 100 | 17.8 | 22.0 | 43.6 | 80.5 | 85.4 | 31.5 | 77.2 |
| 500 | 39.4 | 51.5 | 83.7 | 444.0 | 378.6 | 105.4 | 274.9 |
| **$\mathbf{I}_{red}$ (µA)** | | | | | | | |
| 5 | -4.6 | -4.9 | -18.9 | -3.5 | -8.9 | -7.7 | -18.8 |
| 10 | -6.1 | -6.8 | -28.6 | -31.4 | -15.2 | -11.1 | -26.9 |
| 50 | -12.7 | -15.3 | -40.5 | -83.7 | -56.4 | -27.1 | -60.5 |
| 100 | -17.8 | -22.9 | -47.2 | -104.8 | -103.4 | -42.7 | -95.5 |
| 500 | -40.3 | -61.1 | -108.2 | -402.7 | -407.4 | -138.2 | -320.2 |
| **$\mathbf{I}_{ox}/\mathbf{I}_{red}$** | | | | | | | |
| 5 | -0.974 | -0.974 | -0.905 | -0.678 | -0.690 | -0.722 | -0.542 |
| 10 | -1.001 | -0.996 | -0.940 | -0.957 | -0.704 | -0.672 | -0.573 |
| 50 | -1.012 | -1.008 | -0.893 | -0.703 | -0.782 | -0.737 | -0.751 |
| 100 | -0.996 | -0.962 | -0.922 | -0.763 | -0.825 | -0.732 | -0.808 |
| 500 | -0.978 | -0.842 | -0.774 | -1.089 | -0.932 | -0.760 | -0.861 |

A second important difference is the relatively small peak-to-peak separation, which is observed for all electrodes up to fast scan rates. Figure III.52 provides a visual representation, highlighting the relatively symmetrical appearance of CV, compared to earlier sections. For the 10/30 electrodes, at slow scan rates, $\Delta E_{peak}$ smaller than 18 mV were determined. The value remained relatively constant up to a scan rate of 100 mV/s and only exceeded 59 mV for 500 mV/s.

According to an earlier discussion, two theories could apply to explain the observation. First, the elevated temperatures during the process could cause a more complete removal of EGDA from the samples, in turn favouring a faster transfer of electrons. This theory may be supported by the oxidation and reduction peaks being more narrow, than observed for low $T_{sat}$[18].

The confirmation of the potential presence of EGDA by means of an adapted chemical analysis, e.g. Fluorescence Spectroscopy, could be of interest. In particular, chemical bonds associated with the organic solvent are thought to be characteristic, in comparison with the carbon-polymer matrix.

Alternatively, the polymer foaming step could benefit from higher process temperatures, resulting in an altered creation of porosity. Potentially, this could favour thin-layer type diffusion due to the confinement of analytes.

As the visual inspection of samples confirmed the presence of relatively large pores on

[18]Earlier, the wider redox peaks in CV were thought to arise from interactions between residual EGDA and the redox probe.

the deposit surface, the membrane-like top layer is thought not to impose a significant diffusion limit.

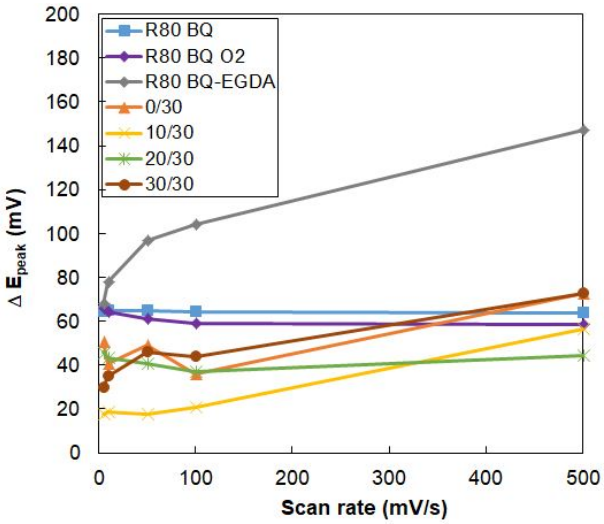


Figure III.52: Peak separation as a function of the scan rate in the study of saturation temperature, derived from CV.

In the recorded CV, a tendency of inverted arc-like character was observed. Against expectations, minimum values were associated with the 20/30 electrodes. The evolution of peak current densities, see Figure III.53, requires a closer look, since extracted values confirm this observation. Compared to the other structured electrodes, the values associated with the 20/30 electrodes are clearly reduced. The overall evolution of results as a function of the scan rate is more similar to the non-structured electrodes. The same statement applies for the linearity of the curves.

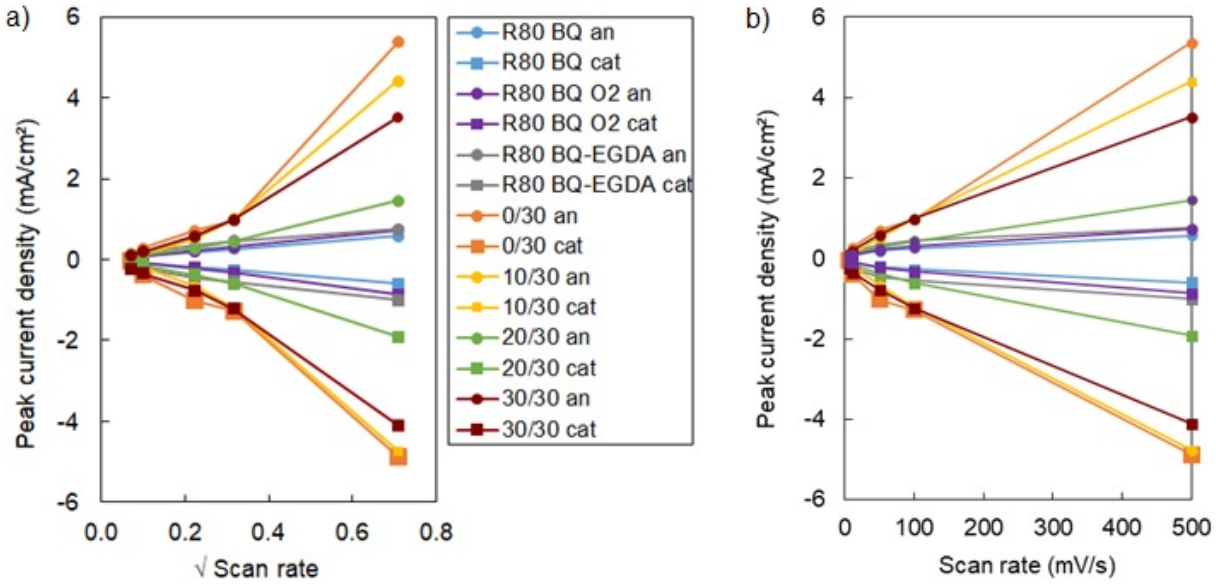


Figure III.53: Comparison of peak current densities in 1 mM ruthenium hexaamine, 1 M KCl in the study of saturation temperature.

For the other electrodes, peak current densities are of almost identical order as observed for lower $T_{sat}$. The only evident differences are the inverse tendency as a function of longer

$t_{sat}$, as well as the lower linearities in the plot versus the square root of the scan rate, compared to lower $T_{sat}$ (see Table III.27). The linearities in the plot versus the scan rate, on the other hand, are increased. According to earlier interpretation, this indicates limited mass transport. In combination with the small values of $\Delta E_{peak}$, it seems credible to conclude on a more pronounced thin-layer type diffusion with confined redox analytes. For an explanation, it is referred to the altered generation of porosity following polymer foaming. It is assumed, in consequence, that e.g. diffusion is equally affected, causing the observations of inverse tendencies of peak currents and of linearities. In particular, as explained earlier, the generation of larger pores was expected, based on the increase in process temperature. However, the results rather suggest the formation of small pores with diameters below what would be required for unrestricted diffusion.

Table III.27: Linearity of peak current plots versus the scan rate and the root of the scan raate in the study of separation time at constant saturation temperature. Data extracted from CV in 1 mM ruthenium hexaamine, 1 M KCl.

| | $\mathbf{R^2}$ **of** $\mathbf{I_{peak}}$ **vs.** $(\nu_{scan})^{0.5}$ | $\mathbf{R^2}$ **of** $\mathbf{I_{peak}}$ **vs.** $\nu_{scan}$ |
|---|---|---|
| **R80 BQ** | 1.000 | 0.958 |
| **R80 BQ O2** | 0.997 | 0.972 |
| **R80 BQ-EGDA** | 0.989 | 0.960 |
| **0/30** | 0.960 | 0.997 |
| **10/20** | 0.968 | 0.997 |
| **20/10** | 0.982 | 0.996 |
| **30/0** | 0.978 | 0.993 |

The calculation of electroactive surface area followed the previously employed approach, using three different formulas. Results for fast cycling were then normalized against the geometric electrode surface and against the result of the non-structured R80 BQ electrode, for comparison. Values are listed in Table III.28.
As expected, results exhibit an inverse, arc-shape evolution when varying $t_{sep}$, which is a consequence of the proportionality to both peak curent and peak charge. For 0/30 and 30/30 electrodes, results are largest (generally peaking for 0/30 electrodes), while surface areas estimated for the 20/30 electrodes are around three times smaller. As in the previous section at lower $T_{sat}$, surfaces are determined larger, when calculation is based on the peak-charge.
Relative to the geometric surface, the increase of values can be roughly quantified as 4.5 to 15.6 for current-based methods (increases between 7.9 and 20.6 were found for lower $T_{sat}$), while increases for charge-based calculation range between 6.7 and 17.7 (6.5 to 29.7 for lower $T_{sat}$). Relative to the response of the R80 BQ electrodes, higher maximum increases were found here.

Comparing the calculated values with the last section suggests a 50 % lower development of electroactive surfaces for electrodes, prepared at higher $T_{sat}$. At a first glance, this appears to match the theoretically larger pore size, according to the foaming theory. Digital microscopy images had confirmed this idea, although the technique is limited to the observation of the electrodes' surface only. Further, the capacitive and Faradaic current studies, providing a more representative view on the bulk generation of porosity, seem to yield mostly corresponding results. The lower surface-to-volume ratio of larger pores could in particular explain the overall lower calculated specific and electroactive surface areas.

Table III.28: Electroactive surface areas calculated from cathodic peaks in CV experiments studying the separation time at constant saturation temperature.

| $\mathbf{v}_{scan}$ (mV/s) | R80 BQ | R80 BQ $O_2$ | R80 BQ-EGDA | 0/30 | 10/30 | 20/30 | 30/30 |
|---|---|---|---|---|---|---|---|
| $\mathbf{A}_{Randles}$ ($cm^2$) | | | | | | | |
| 5 | 0.098 | 0.105 | 0.405 | 0.474 | 0.190 | 0.166 | 0.402 |
| 10 | 0.092 | 0.103 | 0.434 | 0.456 | 0.231 | 0.169 | 0.408 |
| 50 | 0.086 | 0.104 | 0.275 | 0.543 | 0.382 | 0.184 | 0.410 |
| 100 | 0.086 | 0.110 | 0.226 | 0.549 | 0.496 | 0.205 | 0.458 |
| 500 | 0.086 | 0.131 | 0.232 | 0.871 | 0.873 | 0.296 | 0.686 |
| $\mathbf{A}_{Oldham}$ ($cm^2$) | | | | | | | |
| 5 | 0.118 | 0.126 | 0.488 | 0.570 | 0.229 | 0.199 | 0.484 |
| 10 | 0.111 | 0.124 | 0.522 | 0.549 | 0.278 | 0.203 | 0.491 |
| 50 | 0.104 | 0.125 | 0.330 | 0.653 | 0.460 | 0.221 | 0.493 |
| 100 | 0.103 | 0.132 | 0.272 | 0.660 | 0.596 | 0.246 | 0.550 |
| 500 | 0.104 | 0.158 | 0.279 | 1.048 | 1.050 | 0.356 | 0.825 |
| $\mathbf{A}_{Randles,irrev.}$ ($cm^2$) | | | | | | | |
| 5 | 0.125 | 0.133 | 0.516 | 0.603 | 0.242 | 0.211 | 0.511 |
| 10 | 0.117 | 0.132 | 0.552 | 0.580 | 0.294 | 0.214 | 0.519 |
| 50 | 0.110 | 0.132 | 0.349 | 0.690 | 0.486 | 0.234 | 0.522 |
| 100 | 0.109 | 0.140 | 0.288 | 0.698 | 0.630 | 0.261 | 0.582 |
| 500 | 0.110 | 0.167 | 0.295 | 1.108 | 1.111 | 0.377 | 0.873 |
| $\mathbf{A}_{charge,anodic.}$ ($cm^2$) | | | | | | | |
| 5 | 0.158 | 0.198 | 0.619 | 0.721 | 0.262 | 0.221 | 0.540 |
| 10 | 0.157 | 0.194 | 0.744 | 0.698 | 0.312 | 0.230 | 0.569 |
| 50 | 0.142 | 0.175 | 0.477 | 0.825 | 0.517 | 0.270 | 0.568 |
| 100 | 0.140 | 0.180 | 0.362 | 0.743 | 0.667 | 0.305 | 0.676 |
| 500 | 0.134 | 0.104 | 0.351 | 1.255 | 1.213 | 0.443 | 1.029 |
| $\mathbf{A}_{Randles}/\mathbf{A}_{geo}$ | | | | | | | |
| 500 | 1.22 | 1.85 | 2.05 | 12.27 | 12.13 | 4.46 | 9.79 |
| $\mathbf{A}_{Oldham}/\mathbf{A}_{geo}$ | | | | | | | |
| 500 | 1.46 | 2.22 | 2.47 | 14.76 | 14.59 | 5.37 | 11.78 |
| $\mathbf{A}_{Randles,irrev.}/\mathbf{A}_{geo}$ | | | | | | | |
| 500 | 1.55 | 2.35 | 2.61 | 15.60 | 15.42 | 5.67 | 12.45 |
| $\mathbf{A}_{charge,anodic}/\mathbf{A}_{geo}$ | | | | | | | |
| 500 | 1.89 | 1.46 | 3.11 | 17.67 | 16.85 | 6.67 | 14.68 |
| **Factor of increase relative to R80, Randles-style equations** | | | | | | | |
| 500 | 1.0 | 1.5 | 2.7 | 10.1 | 10.1 | 3.4 | 8.0 |
| **Factor of increase relative to R80, $\mathbf{Q}_{anodic}$** | | | | | | | |
| 500 | 1.0 | 0.8 | 2.6 | 9.4 | 9.1 | 3.3 | 7.7 |

#### 3.3.2.3 Chronoamperometric studies

With the intention of finding complementary results on the evolution of electroactive surface, which would allow to conclude on pore sizes, chronoamperometric measurements were carried out as before. The chronoamperometric responses of up to four electrodes per PCB are displayed in Figure III.54 series 1, with generated Cottrell plots in series 2. Table III.29 lists the extracted, averaged results.

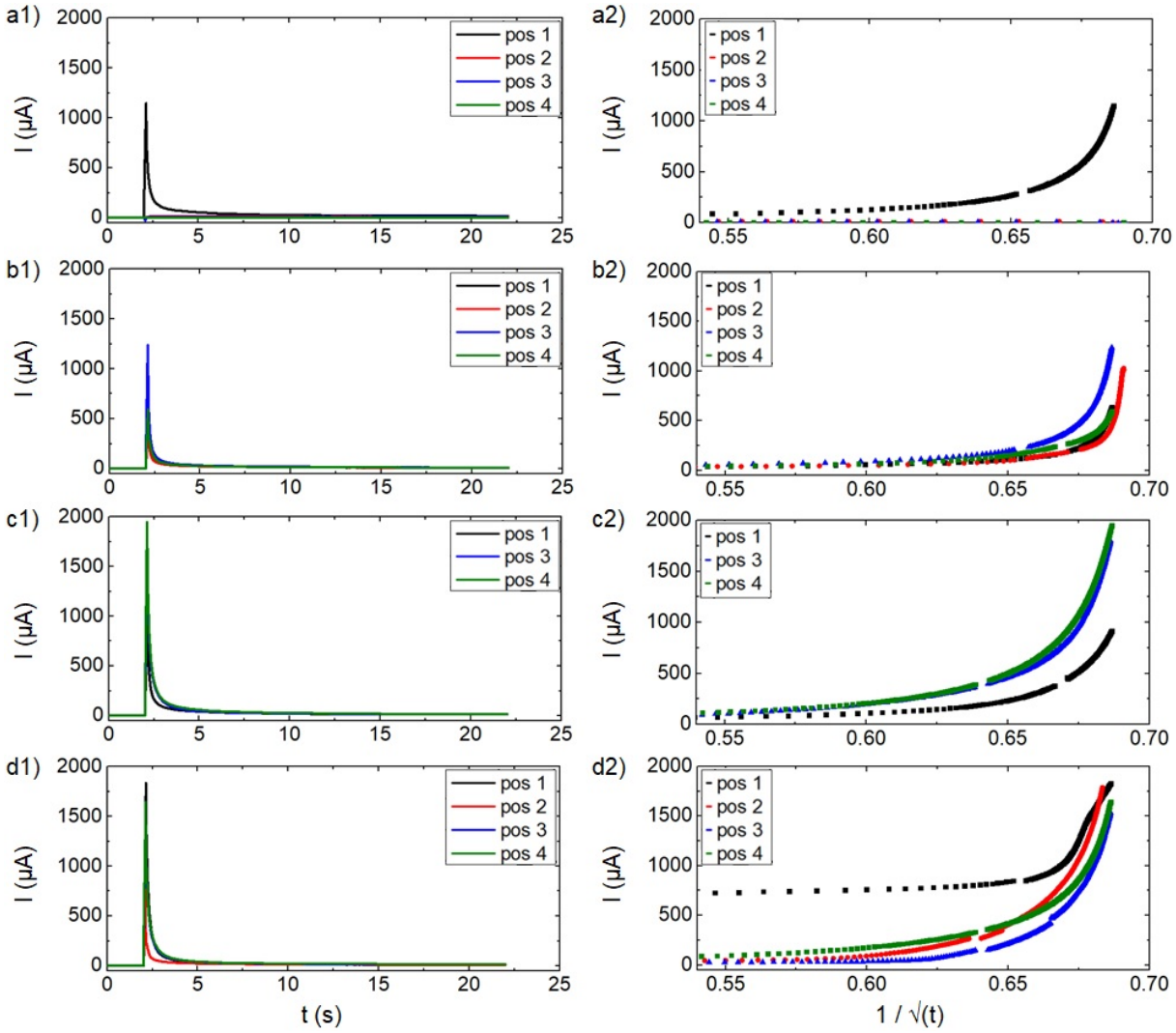


Figure III.54: Chronoamperometric responses in series 1 (0 V, 2 s and 0.7 V, 20 s in 2.5 mM hexacyanoferrate (II), 1 M KCl) in the study of saturation temperature; a) 0/30; d) 10/30; e) 20/30; f) 30/30. Electrodes were oxygen plasma-treated (450 sccm, 200 W, 20 s). The resulting Cottrell plots in series 2.

The chronamperometric responses are an interesting indicator of changed electrode character, compared to the study of lower $T_{sat}$. Specifically, identical applied voltages resulted in overall higher current spikes, except for electrodes 10/30 in the previous section, for which recorded currents are of comparable height. As all experimental conditions were considered to be equivalent, a potential origin is suggested by the Cottrell equation. Increased electrode area could account for the difference in this section, in particular for 20/30 and 30/30 electrodes (position 1 of the 30/30 electrode was excluded from the evaluation). Longer $t_{sep}$ were found to correlate with increased peak currents, however the values require normalization to the geometric electrode surface for a better enhanced validity.
Characteristic differences are assigned to the Cottrell plots for each change in preparation condition and allow distinguishing the earlier explained non-linear slope that follows the current peak in the plot. The first 50 ms were averaged as before to simulate data evaluation corresponding to a thin diffusion layer.

Calculated electroactive surfaces range between 56 and 75 $m^2/g$, which is more accurate, than for lower $T_{sat}$. However, the maximum estimated surface is lower by around 25 %

(98 $m^2/g$ for higher $T_{sat}$). In consequence, the increase in electroactive surface, relative to the geometric surface, is to some extent smaller. An interpretation of tendencies depending on longer $t_{sep}$ seems not entirely clear.
One interpretation of results is based on the hypothesis, that the density of electroactive sites remains constant at both $T_{sat}$. In that case, the generation of larger pores with bigger surface-to-volume ratio could explain, why smaller electroactive surfaces were estimated.

Table III.29: Cottrell slopes, calculated electroactive surface areas and specific surface areas for structured carbon ink electrodes in the study of saturation temperature.

| | $A_{geo}$ ($cm^2$) | $A_{Cottrell}$ ($cm^2$) | $A_{Cottrell}$ ($m^2/g$) | $A_{Cottrell}/A_{geo}$ |
|---|---|---|---|---|
| **0/30, 50 ms** | 0.083 | 56.62 ±22.03 | 56.6 | 685.3 |
| **10/30, 50 ms** | 0.086 | 73.03 ±23.38 | 73.0 | 850.9 |
| **20/30, 50 ms** | 0.072 | 57.81 ±22.51 | 58.8 | 802.2 |
| **30/30, 50 ms** | 0.078 | 74.94 ±7.89 | 74.9 | 957.6 |

### 3.3.2.4 Electrochemical impedance studies

EIS spectra of one selected electrode per PCB are displayed in Figure III.55 in the Nyquist plots, where a) provides a general view and b) represents a magnification of the high-frequency regions. The high-frequency regions of the spectra are different, compared to the electrodes prepared at low $T_{sat}$, as no overlapping R/C semicircles are distinguishable. Further, the earlier observed slope of 45 ° is no longer visible, which potentially indicates that electrodes don't comply to semi-infinite diffusion. Instead, the spectra start with steep slope in the high-frequency region. Similar behaviour has been linked to electrochemical double layer charging and may complement the theory of the formation of a different type of porosity.

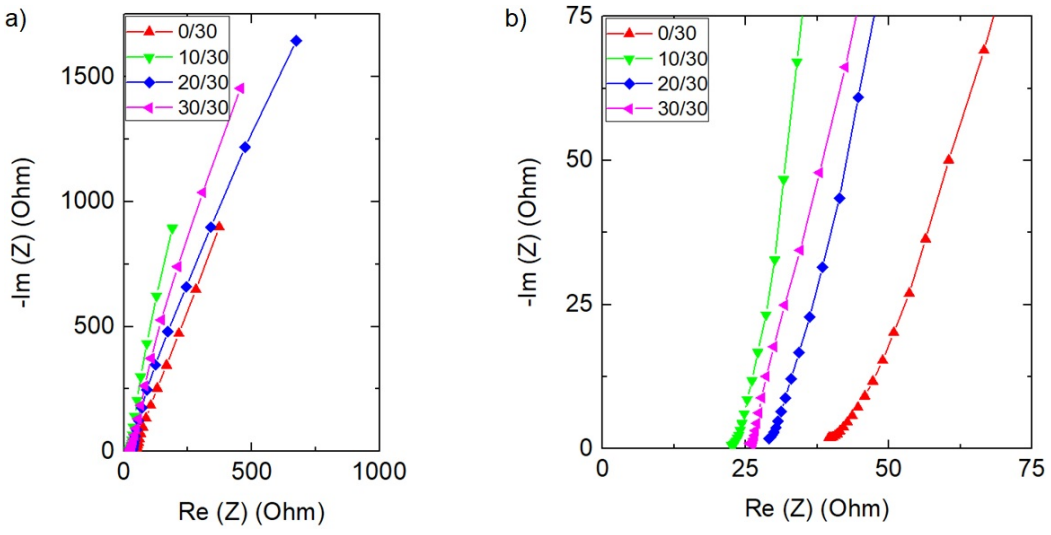


Figure III.55: a) Nyquist plots with b) high-frequency domains in 1 M KCl, 1 mM ruthenium hexaamine in the study of saturation temperature.

Based on visual comparison, the electrolyte resistance for the 0/30 electrode is comparable to the last section (40-45 Ω). The other electrodes show reduced values of around 25 Ω, which is equally similar to the last section. However, no correlation with $t_{sep}$ is observed. No particular difference is observed in the low-frequency end of the spectra for

higher $T_{sat}$ and no clear evolution with $t_{sep}$ seems to apply.
The study of spectra in Bode plots, see Figure III.56, is considered interesting, as differences to the previous section are more pronounced. At high-frequencies from 10 to 0.1 kHz, the phase angle approaches 0 °, indicating resistive behaviour. In the curve for log (Z), this corresponds to the low-impedance plateau, which is more extended than for low $T_{sat}$. Further, the transition around the cut-off frequency of capacitive circuit elements (see earlier explanation) into the mass-transport region is of clear definition, opposed to the previously observed "shoulder". For electrodes prepared at low $T_{sat}$, this was linked to a small region of frequency, governed by linear, semi-infinte diffusion. Its absence is considered to confirm the theory of changed pore formation. In particular, the hypothesis of thin-layer diffusion with confined analytes could explain the measurements. For low frequencies, the electrode responses are of relatively capacitive character, with phase angles closer to 90 °, than in the study of lower $T_{sat}$. Further, the inversion frequencies are shifted to higher values and (pseudo-)capacitive character is assigned to a wider frequency range. These interpretations match the earlier interpretation of CV.

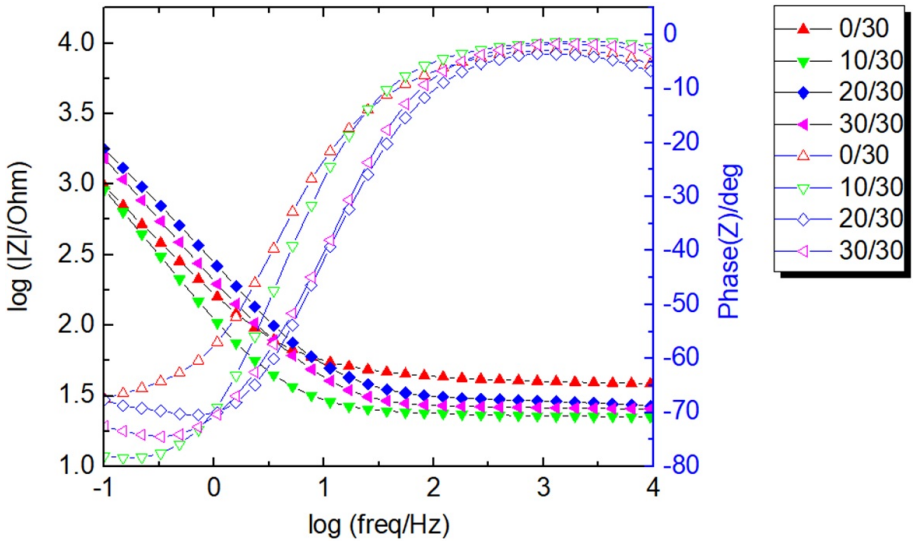


Figure III.56: Bode plot for electrodes in the study of saturation temperature. EIS was performed in 1 M KCl, 1 mM ruthenium hexaamine.

Table III.30 lists the quality of fit for the different equivalent circuits. On average, compared to the study of lower $T_{sat}$, fits are better for circuits b) and c). At the same time, certain inconsistencies with the evolution of $t_{sat}$ suggest a potentially limited interpretation of results. A repeated iteration of the fits didn't resolve this point.

Table III.30: Quality of fit for different equivalent circuits in the study of saturation temperature.

| **Description** | $\chi^2$ **fit a)** | $\chi^2$ **fit b)** | $\chi^2$ **fit c)** |
|---|---|---|---|
| **0/30** | 2560 | 940 | 810 |
| **10/30** | 3810 | 180 | 190 |
| **20/30** | 1730 | 690 | 1280 |
| **30/30** | 2340 | 6570 | 200 |

Equivalent circuits: a) $R_s$-Q//($R_{CT}$+W); b) $R_s$-Q//($R_{CT}$+M); c) $R_s$-$Q_{interface1}$//($R_{pore}$+$Q_{interface2}$//$R_{CT}$)

Table III.31 displays the results extracted from the fit with the modified Randles-equivalent circuit. The series resistance $R_s$ follows the above description with small values for $t_{sep}$ of equivalent or longer than 10 min. The CPE parameter $Q^0$ is generally of smaller value, than for electrodes prepared at lower $T_{sat}$, with an exception for electrode 0/30. It requires clarification, whether this observation can be associated with recorded spectra. Particularly the low-frequency-data for the 0/30 electrode in the Bode plot suggests least capacitive behaviour.
The CPE coefficient $\alpha$ potentially displays an arc-shaped evolution with a minimum for the 10/30 electrode. However, as the values descend below 0.5, this potentially indicates non-representable fits. The range of frequencies, at which the transition to the mass transfer regime is observed, is higher than for low $T_{sat}$ and follows a linear evolution with longer $t_{sep}$. As previously mentioned, diffusion mechanisms are limited in pores of smaller diameter, particularly for elevated frequencies. For electrodes in this section, therefore, the observation could indicate the generation of larger pores.
The charge transfer resistances are more than one order of magnitude smaller, compared to low $T_{sat}$ and show an inconsistency for the 10/30 electrode, which requires further verification.
Estimated capacitances are 1.6 times larger for the 0/30 electrode in this section, but considerably smaller for all other electrodes. Further, a potential inverted arc-like trend suggests smallest values for the 10/30 electrode. While the evolution is not understood in detail, the results eventually match the evolution of calculated capacitances. One interpretation consists in the generation of smaller specific surface areas at higher $T_{sat}$, which would confirm the theory of the formation of larger pores.

Table III.31: Key circuit parameters determined from equivalent circuit b) in the study of saturation temperature.

| | $\mathbf{R_s}$ (Ω) | $\mathbf{Q^0}$ ($\mathbf{mF.s^{(a-1)}}$) | **a** | $f"_{max}$ **(Hz)** | $\mathbf{R_{CT}}$ (Ω) | **C (µF)** | $\mathbf{C_{norm}}$ ($\mathbf{mF/cm^2}$) |
|---|---|---|---|---|---|---|---|
| **0/30** | 38.1 | 0.96 | 0.64 | 1.60 | 6 | 420 | 5.07 |
| **10/30** | 22.2 | 0.21 | 0.21 | 1.75 | 1 | 31 | 0.36 |
| **20/30** | 24.1 | 0.39 | 0.39 | 2.44 | 5 | 72 | 1.00 |
| **30/30** | 23.6 | 0.31 | 0.63 | 2.42 | 3 | 112 | 1.43 |

### 3.3.3 Conclusion of the study of saturation temperature

Within the technical limits of the supercritical fluid equipment, the saturation temperature was increased to study its effect on the polymer foaming mechanism. Although the strict separation of phase separation and foaming is a simplified way for describing the complex structuration mechanism, the increase in temperature was expected to have a characteristic effect on the foaming mechanism.

Digital microscopy images revealed a clear structural difference for 0/30 electrodes, compared to longer separation times. Specifically, electrodes displayed rather homogeneous and flat surfaces.
The study of deposit height and the reconstructed volume allowed to associate separation times of 0 min with the formation of rather thin deposits, opposed to longer $t_{sep}$. The results are highly interesting and confirm the potential to directly manipulate the polymer foaming mechanism. Still, in this case, the deposits prepared at lower $T_{sat}$ yielded higher estimated volumes.
Further, for low $T_{sat}$, the absence of the thin membrane-like layer may be of practical benefit. The latter was found to be relatively brittle, leading to the question of mechanical

integrity of the entire electrodes. For higher $T_{sat}$, the electrodes were prone to delaminate and to break more frequently. This observation is thought to be a consequence of altered porosity. in consequence, the electrode's utility is considered limited for a practical sensing application.
For a potential future continuation of the project, the identification of an own ink formulation is seen as an essential task. The choice of polymeric binder with respect to its glass transition temperature could mainly influence the cohesion exhibited by the structured electrodes.
Main results of height and volume evolution are presented in Figure III.57.

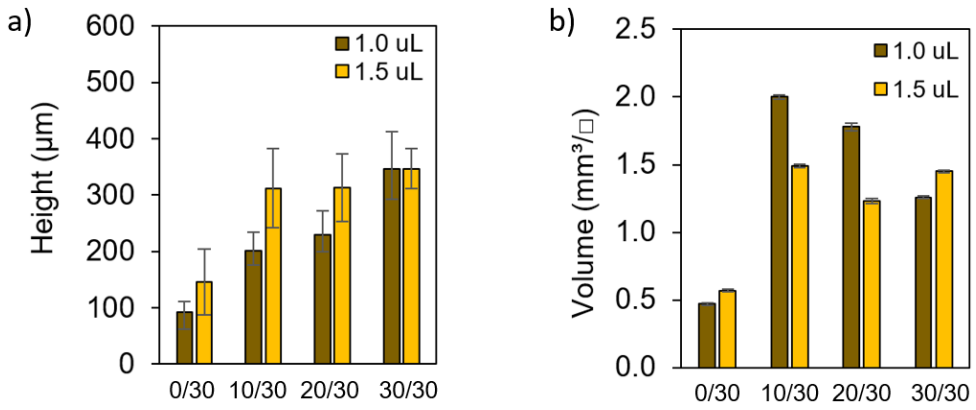


Figure III.57: Results for a) height (single measurements) and b) volume development for $scCO_2$-structured ink deposits (averages of 4 deposits). Maintaining the protocol of the previous section, the influence of saturation temperature was studied. Two sets of deposits samples were prepared using different ink volumes.

SEM images provided similar visual impressions, as in the study of lower $T_{sat}$. However, the visual similarity of all deposits was higher in this section. The image treatment yielded lower pore counts, while the total pore areas were slightly larger. For elevated $T_{sat}$, this observation may confirm the generation of larger pores on the surface of electrodes. Largest pore sizes were observed for 10/30 and 20/30 deposits.

The study of capacitive currents and estimated normalized and gravimetric capacitances indicated a relatively similar character of electrodes, compared to lower $T_{sat}$. However, the assignment of tendencies as a function of separation time is not clear. In particular, for 0/30 and 30/30 electrodes a distinct pseudo-capacitive character is observed. On average, values were slightly larger than for lower $T_{sat}$, while peak values remained lower.
Faradaic current studies highlighted the small peak-to-peak separation. The peak current evolution deviated from what is known for electrodes that exhibit linear, semi-infinite diffusion. Instead, thin-layer type diffusion due to confined redox analytes played a role. Potentially, a different polymer foaming mechanism resulted in the generation of pores on a different scale. Results suggest the formation of smaller pores, contrary to expectations (see Table I.3 in chapter I). It is likely, however, that the distribution of pore size on the surface of electrodes diverges from the volume.
The calculation of electroactive surfaces, see Figure III.58 b), yielded overall smaller increases than in the study of lower $T_{sat}$. This observation could confirm the formation of larger pores, due to a lower surface-to-volume ratio, and align with literature. It is pointed out, however, that the interpretation of results in this section presented difficulties. It is assumed, that the interpretation of a combined phase separation and polymer foaming

mechanism is complex.

Compared to the previous study, the electroactive surfaces, based on chronoamperometric studies, attained smaller values for higher $T_{sat}$. This is equally thought to align with the generation of larger pores with reduced surface-to-volume ratio.

EIS studies proved to be very interesting. Despite the generally different order of magnitude of estimated electrode capacitance, compared to results based on CV, a similar tendency of results is noted, see Figure III.58 a). In particular, this appears to confirm the different pore development in the electrode bulk at elevated $T_{sat}$.
As a result, the low-impedance plateau region in Bode plots was extended by more than one order of frequency. The pseudo-capacitive character was found to be close to an ideally capacitive element, opposed to electrode prepared at low $T_{sat}$.

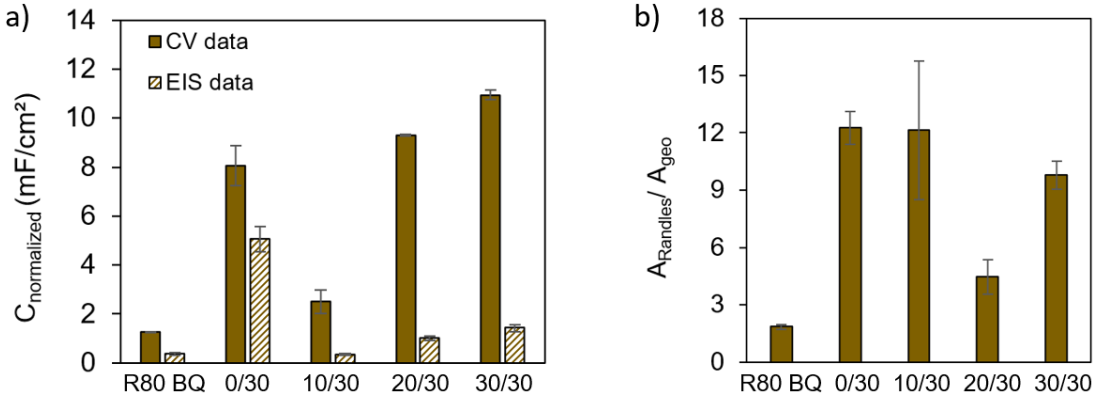


Figure III.58: a) Results for the development of capacitance of structured electrodes, normalized to the geometric electrode surface, determined from CV and EIS studies. b) Maintaining the protocol of the previous section, the influence of saturation temperature was studied. Average values of 4 structured electrodes are displayed. All electrodes were plasma-treated.

## 3.4 Study of ink dilution

Ink dilution was a practical solution to extent manipulation time between deposition of the ink and the start of the structuration process. The lowered viscosity of the ink was essential for measuring exact quantities of deposited volumes, particularly for undiluted inks. In last sections, the ratio of ink to Ethylene glycol diacetate (EGDA) was based on a practical choice. As the mechanical properties of deposits lead to the partial delamination and fracturing of some electrodes upon handling, it was intended to improve their practical reliability by studying the ink dilution. In parallel, the identification of membrane-like top layers raised the question, to which extent the diluted inks behaved like polymeric solutions during the phase separation. In literature, the capability to manipulate the porous structure by adapting the polymer content is suggested.

Process parameters were chosen based on previous results and comprised in particular a process pressure of 8 MPa and $T_{sep}$ of 23 ℃. The lower saturation temperature was chosen, as the interpretation of results for $T_{sat}$ of 40 ℃ was more conclusive and the mechanical properties of deposits/electrodes were superior than for higher $T_{sat}$. The study of specific and electroactive areas repeatedly suggested maximum results for the 20/30 deposits. In consequence, $t_{sep}$ was set to 20 min and $t_{sat}$ maintained at 30 min.
The dilution ratios of DuPont™BQ242 ink varied, creating a range of viscosities. While a focus was set on the criterion of practical manipulation of ink, i.e. on overall stronger dilutions, low ink dilutions were tested for comparative reasons. In Table III.32, dilutions and a conversion to the ink concentration are listed. Further, an approximative determination of the polymer concentration is included, to compare results to literature, as no data is provided by DuPont.
A quantity of 76 mg of undiluted ink was spread on a suitable support and dried at 80 ℃ for 10 h to guarantee removal of the solvent. The weight of the dried ink was determined to 33 mg, implying a weight loss of 57 %. In conclusion, the solid fraction at 80 ℃ corresponds to 43 %, which corresponds approximately to the suppliers data (38 to 40 % at 150 ℃).
For an estimation of upper and a lower limits of the solid fraction, both values are considered. The determined polymer content is relatively low, compared to what was studied in some references on phase separation and foaming (up to 40 % w/w). There, the solid fraction typically contains polymeric binder in the range of 20 to 30 % w/w [149]. The percentages of solid fraction and polymer content were multiplied to yield the approximative polymer content in undiluted ink and, after further calculation, for diluted inks, see Table III.32.

Table III.32: Ratios of ink to Ethylene glycol diacetate (EGDA) and estimative range of polymer concentrations (20 % lower threshold, 30 % upper threshold) in the study of ink dilution. The approximative value of the solid fraction was 38 to 43 %.

| **ink:EGDA** | **ink (wt-%)** | **20 % polymer** | | **30 % polymer** | |
|---|---|---|---|---|---|
| | | **38 % solids** | **43 % solids** | **38 % solids** | **43 % solids** |
| 1:10 | 9 | 0.7 | 0.8 | 1.0 | 1.2 |
| 3:17 | 15 | 1.1 | 1.3 | 1.7 | 1.9 |
| 2:8 | 20 | 1.5 | 1.7 | 2.3 | 2.6 |
| 3:7 | 30 | 2.3 | 2.6 | 3.4 | 3.9 |
| 4:6 | 40 | 3.0 | 3.4 | 4.6 | 5.2 |
| 1:1 | 50 | 3.8 | 4.3 | 5.7 | 6.5 |
| 1:0 | 100 | 7.6 | 8.6 | 11.4 | 12.9 |

A more precise determination of the polymeric fraction is regarded essential for a potential continuation of the project, particularly in the context of ink formulation. Thermogravimetric analysis is suggested for studying the weight loss of a dried sample of undiluted ink during thermal decomposition of the polymeric binder. Alternatively, it is proposed to redissolve a given mass of dried ink in solvent and to repeatedly certrifuge and decant the liquid phase. Subsequently, drying and weighing of the solid fraction is proposed to deduce the weight loss, ideally corresponding to the polymer weight.

## 3.4.1 Physical characterization

### 3.4.1.1 Digital microscopy

Digital microscopy images of 1.0 and 1.5 µL deposits are presented in Figures III.59 and III.60 for high ink dilution in a) towards undiluted ink in g). All deposits underwent a supercritical $CO_2$ structuration. The yellow areas in the images display the mask material, which partially delaminated for the deposits in a1), c1) and f1). Dilutions 1:0 and 1:1 were highly viscous and limited the exact deposition by means of a pipette, hence the attained heights and volumes are potentially erroneous.

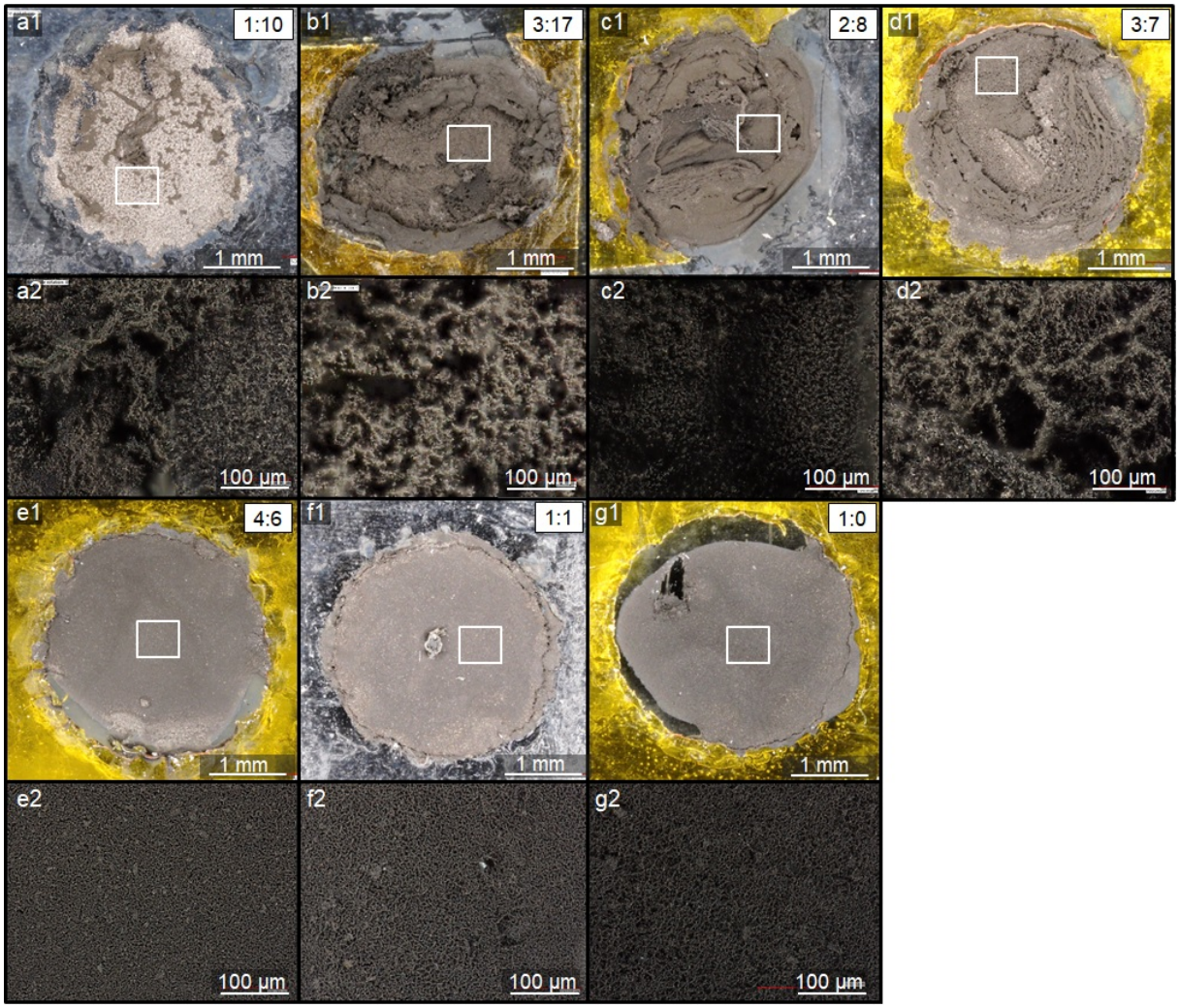


Figure III.59: Digital microscopy of deposits in top view, 1 µL ink volume, in the study of ink dilution. Ratios indicate ink:EGDA (w/w); a) 1:10; b) 3:17; c) 2:8; d) 3:7; e) 4:6; f) 1:1; g) 1:0.

The visual impressions vary strongly and seem to confirm the creation of filigrane structures of lower mechanical integrity for deposits of high ink dilution. For example, the 1:10 (ink:EGDA) deposit in Figure III.59 a) appears mainly delaminated. The areas of high reflection are interpreted as sedimented ink constituents, while the areas of higher light absorbance correspond to structured ink.
Inversely, less diluted deposits are considered relatively mechanically stable and it is eventually possible, to investigate the deposition of ink without masks. In particular, as no meniscus formed, masks could be removed without physically damaging the electrodes.
Surfaces of less diluted inks gradually change to higher uniformity and integrity. The observation is reproduced for deposits of large ink volume. A transition towards deposits with homogeneous surface is particularly associated with the sample of dilution 4:6.
A supplementary view on the structural changes is provided by images of larger magnification. Surfaces of highly diluted ink display pores and cavities on a broad range of dimension, aside from the formation of a membrane-like layer. On the other hand, less diluted ink deposits display a homogeneous generation of porosity/structure on the scale of approximately 10 µm.

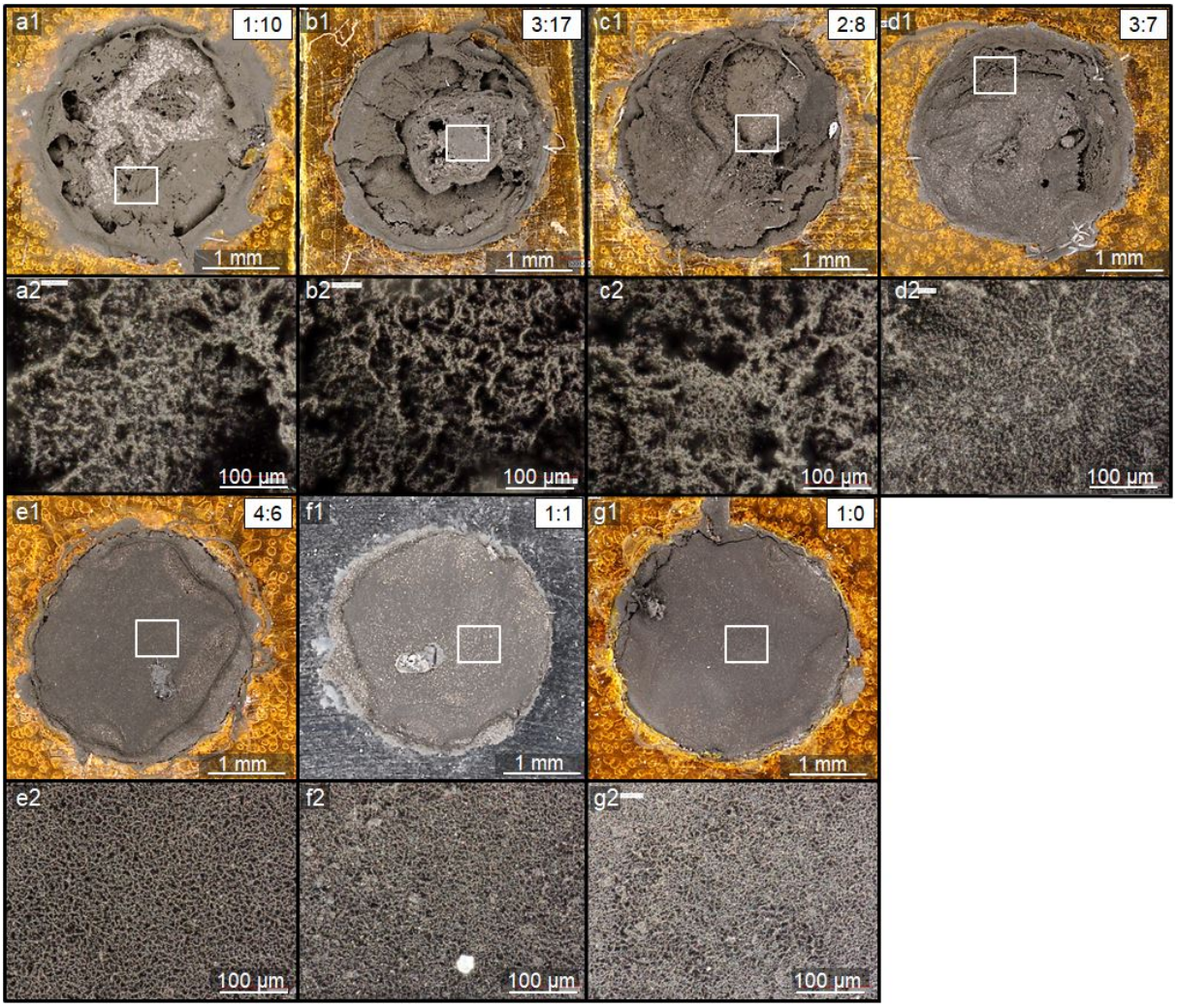


Figure III.60: Digital microscopy of deposits in top view, 1.5 µL ink volume, in the study of ink dilution. Ratios indicate ink:EGDA (w/w); a) 1:10; b) 3:17; c) 2:8; d) 3:7; e) 4:6; f) 1:1; g) 1:0.

The observations are linked primarily to the changes in phase separation, i.e. the starting points in the ternary phase diagram, according to the polymer content as schematized by the paths 1-3 in Figure III.9 b). In their work on the preparation of porous, polymeric membranes by means of a phase separation mechanism, Reverchon et al. varied the concentration of cellulose acetate in acetone from 5 to 40 % (w/w). Assuming similar demixing mechanisms for the diluted ink, this is partially comparable to the lower range of polymer concentration in the reference. It is pointed out, that different cell temperatures applied (45 ℃ compared to 23 ℃ in this project). Further, the $CO_2$ pressure was higher (20 MPa instead of 8 MPa in this project), suggesting an increased non-solvent strength of $CO_2$. Furthermore, the detailed comparison is potentially limited due to the different components of the system, implying a changed phase diagram. The slow depressurization rate indicates the absence of foaming.
Despite these differences, the visual similarity of samples is relatively close, compared to membranes prepared from solutions of low polymer content, which are marked by a loss of surface homogeneity. A transition from "flat" surfaces to filigree structures is equally observed. Similar to the images of structured electrodes in this project, a resemblance agglomerated spherical or beads-like particles is noted. The cross-sections of membranes in the published works support the idea, that samples prepared from solutions of low polymer content present lower bulk connectivity, resulting in higher mechanically instability.

Matsuyama et al. studied the concentration of polystyrene in toluene (15 to 30 % w/w) during the formation of porous membranes via phase separation [79]. Compared to this project, the process parameters varied, with a temperature set to 35 ℃, a pressure of 13 MPa and a slow depressurization rate. SEM images of membrane cross-sections suggested an increased thickness of top-layers, as well as a reduced pore size, when increasing the polymer content. Potentially, this was due to the overall smaller volume of the polymer-lean phase after phase separation. In consequence, surface-related porosity was less interconnected for polymer-rich solutions. No images were provided to compare the structures.

#### 3.4.1.2 Height of deposits

Electrode height was determined based on side-view images of deposits of different ink dilution, see Figure III.61 a) and b) for 1.0 and 1.5 µL deposits. Table III.33 lists minimum, average and maximum height. An exception is undiluted, sc$CO_2$-treated ink, for which only one height per sample could be determined.
Deposit quality is discussed first, as samples for stronger diluted inks exhibit the tendency of a partial delamination. Specifically, deposits in Figures III.61 b), d) and e) indicate a fractured top-layer. For the strongest factor of dilution 1:10 (ink:EGDA) in series a), top-view images suggest the removal of a major part of deposits. The validity of samples in e2) and g), for which side-view images give the impression of significant delamination, could equally be confirmed.

The comparison of average deposit heights supports the visual impressions and particularly underlines the low heights obtained for ink dilution 1:10 due to partial delamination. Besides, the height of undiluted ink deposits could not be precisely estimated.
The evolution of average sample heights exhibits maxima for higher dilutions. This is interpreted as an elevated generation of volume, potentially matching the theory of pore generation during phase separation. A lower quantity of solid phase implies the formation of larger zones, low in polymer, during phase separation, which have a higher potential for expansion. Alternatively, the demixing process could follow a different path through the phase diagram. It could thus be linked to faster and more "dynamic" demixing, gen-

erating a larger volume.
While scientifically interesting, it is concluded that the practical interest in the structuration of highly diluted inks remains low. The fabrication of electrodes in sensors requires electrodes to be of high mechanical stability and homogeneity. In particular, this was observed for lower dilutions of 4:6 (ink:EGDA) and less.

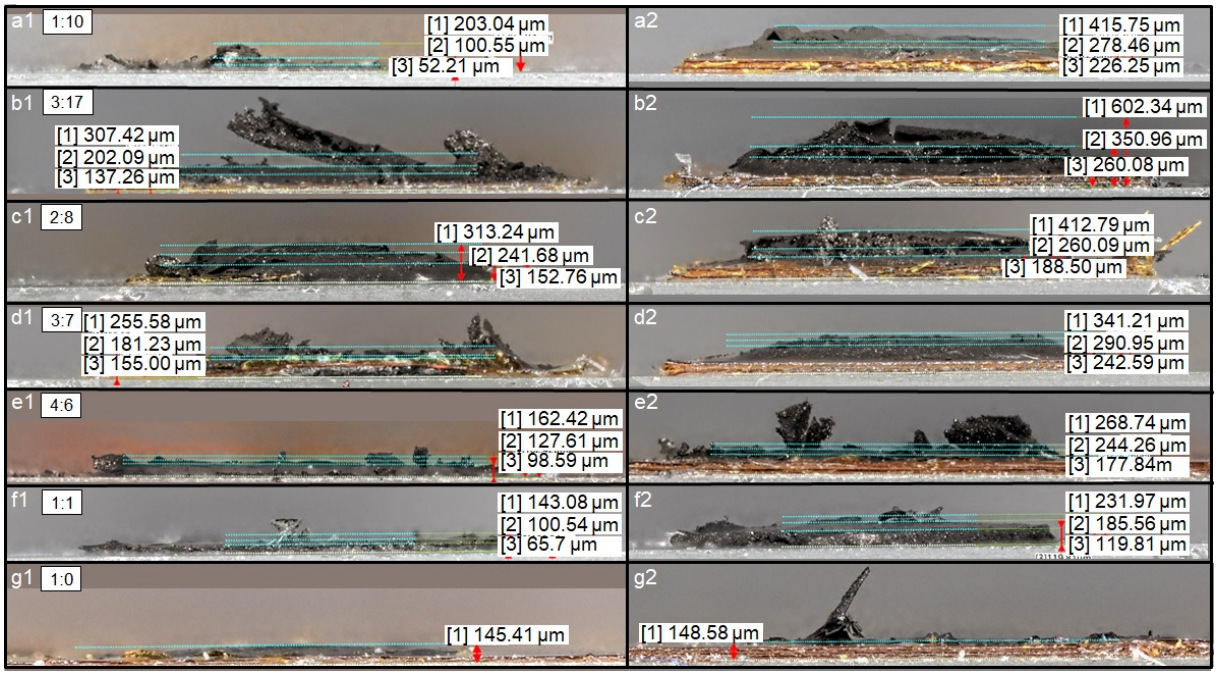


Figure III.61: Side view digital microscopy images of structured ink in the study of ink dilution. 1 µL in series 1) and 1.5 µL in series 2). Sample a) 1:10; b) 3:17; c) 2:8; d) 3:7; e) 4:6; f) 1:1; g) 1:0. Ratios indicate ink:EGDA (w/w).

Table III.33: Height of ink deposits extracted from side view images in the study of ink dilution. Ratios indicate ink:EGDA (w/w).

| $\mathbf{t_{sep}/t_{sat}}$ | **1.0 µL** | | | **1.5 µL** | | |
|---|---|---|---|---|---|---|
| | $\mathbf{h_{min}}$ **(µm)** | $\mathbf{h_{mid}}$ **(µm)** | $\mathbf{h_{max}}$ **(µm)** | $\mathbf{h_{min}}$ **(µm)** | $\mathbf{h_{mid}}$ **(µm)** | $\mathbf{h_{max}}$ **(µm)** |
| 1:10 | 52 | 101 | 203 | 226 | 279 | 416 |
| 3:17 | 137 | 202 | 307 | 260 | 351 | 602 |
| 2:8 | 153 | 242 | 313 | 189 | 260 | 413 |
| 3:7 | 155 | 181 | 256 | 243 | 291 | 341 |
| 4:6 | 99 | 128 | 162 | 178 | 244 | 269 |
| 1:1 | 66 | 101 | 143 | 120 | 186 | 232 |
| 1:0 | - | 145 | - | - | 149 | - |

### 3.4.1.3 Evaluation of volume

The estimation of volumes was based on aerial view images of the same samples, as presented in Figure III.62, including the areas assigned to the deposits as indicated in red. The yellow and black backgrounds result from mask material and black permanent. The extracted volumes, geometric areas and volumes per unit surface are listed in Table III.34.

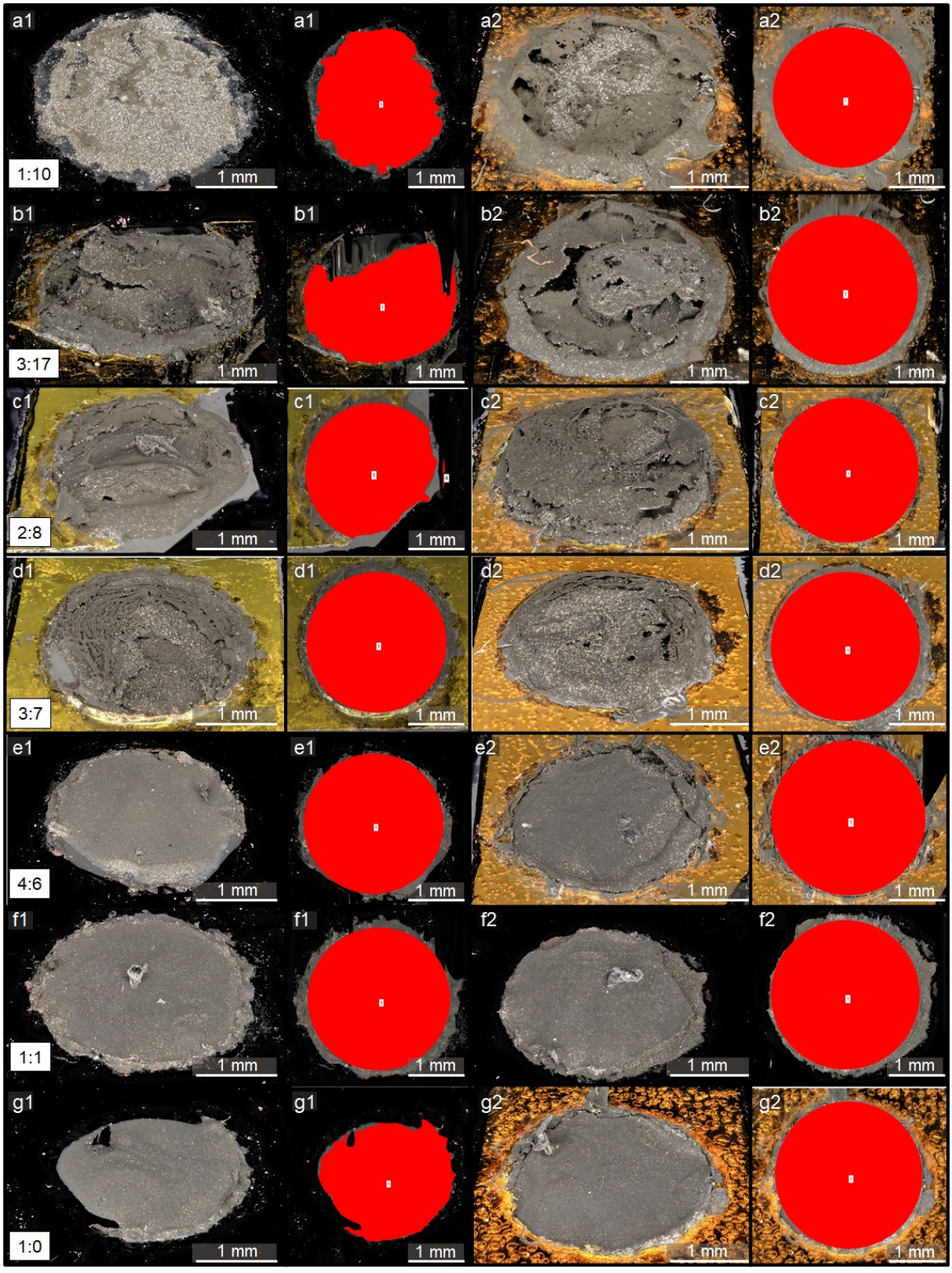


Figure III.62: Aerial view (45 °) digital microscopy of structured ink deposits in the study of ink dilution. 1 µL in series 1), 1.5 µL in series 2). Ratios of ink:EGDA (w/w) were a) 1:10; b) 3:17; c) 2:8; d) 3:7; e) 4:6; f) 1:1; g) 1:0.

Besides for the lack of precision of reconstructed volumes, the volume evaluation requires to exclude the deposits of 1:10 (ink:EGDA) dilution from the discussion. The visual impression and the small determined volumes support the idea of delaminated deposits.

The 4:6 (ink:EGDA) deposit for 1.0 L ink yielded a relatively small volume, deviating from the overall trend and presenting a second inconsistency. The corresponding 1.5 µL deposit behaves differently and is considered representative.
Aside from these points, a general trend of larger reconstructed volumes is identified, with maximum values for higher dilutions of 2:8 and 3:17 (ink:EGDA). This matches the previously stated generation of larger volumes during phase separation. At the same time and in agreement with literature, images confirm that this is not necessarily identical to the generation of homogeneous porosity. Images suggested to need of dilutions of 4:6 (ink:EGDA) and less. For the latter concentration, the 1.5. µL ink deposit attained a volume, which approximately doubled relative to the structured, undiluted ink. No data is available for dried, undiluted ink, as the deposit thickness was too small for data extraction.

Table III.34: Deposit volumes extracted from aerial view images in the study of ink dilution with averaged values for each PCB and volumes normalized to a unit surface.

| $\mathbf{t}_{sep}/\mathbf{t}_{sat}$ | **1.0 µL** | | | **1.5 µL** | | |
|---|---|---|---|---|---|---|
| | **V ($mm^3$)** | **A ($mm^2$)** | **$V_n$ ($mm^3/\square$)** | **V ($mm^3$)** | **A ($mm^2$)** | **$V_n$ ($mm^3/\square$)** |
| 1:10 | 0.16 | 8.36 | 0.14 | 1.27 | 7.32 | 1.22 |
| 3:17 | 1.15 | 9.17 | 0.89 | 1.82 | 7.99 | 1.61 |
| 2:8 | 0.85 | 5.85 | 1.03 | 1.85 | 8.59 | 1.53 |
| 3:7 | 0.97 | 6.93 | 0.99 | 1.39 | 7.07 | 1.39 |
| 4:6 | 0.59 | 14.29 | 0.29 | 1.47 | 10.42 | 1.00 |
| 1:1 | 1.02 | 16.90 | 0.43 | 1.39 | 9.09 | 1.08 |
| 1:0 | 0.51 | 6.76 | 0.53 | 0.58 | 7.65 | 0.54 |

#### 3.4.1.4 SEM images

SEM images are depicted in Figure III.63 for the range of concentrations in question, with high ink dilutions in the top and undiluted ink in the bottom of the image. The SEM deposits were prepared separately from digital microscopy samples in one single treatment[19], except for sample 2:8 in Figure III.63 c), for which the previously acquired images were used.

For deposits of low ink dilutions, at low magnification, the similarity of surfaces is rather low, compared to equivalent microscopy images. These display clearly distinguishable, cellular structures, as seen in Figure III.63 series e) to g). The different generation of image contrast in scanning electron microscopy could account for this variation.
Meeting the expectations, surfaces of highly diluted deposits 1:10 and 3:17 (ink: EGDA) exhibit a more filigree character, than deposits studied in sections 1-3 for dilution 2:8. Series c) is of particular interest, as the membrane-like top layer remained largely intact. The underlying bulk-structure appears comparable to the samples of comparable dilution.

Interestingly, needle/platelet-like features of high image contrast in series b) and d) are distinguishable for deposits of dilutions 3:17 and 3:7. Carbon particles, e.g. graphite platelets or carbon fibres, are thought to be visually similar. It is possible, that phase separation mechanisms in this range of dilution are too rapid for significant sedimentation effects to occur, opposed to higher dilution. In consequence, said particles could remain near in the surface region of deposits. In addition, the low polymer content may limit the coverage of carbon particles, allowing for their better visibility, compared to deposits of low dilution.

[19]Ink deposits on their supports were placed in a circle, approximately 5-7 cm apart from each other in the pressure cell.

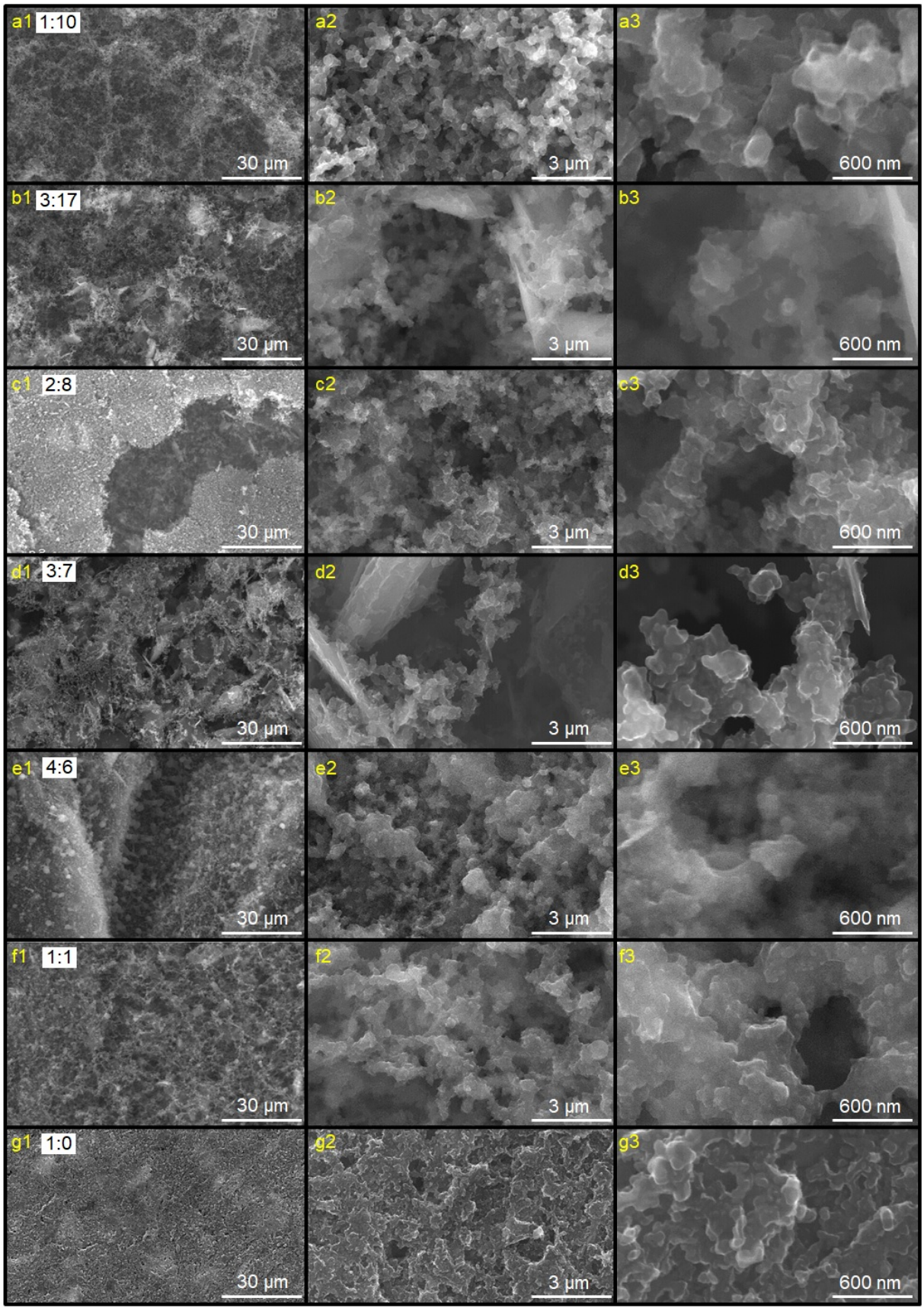


Figure III.63: SEM images of central locations of structured ink deposits in the study of ink dilution. Ratios of ink:EGDA (w/w) were a) 1:10; b) 3:17; c) 2:8; d) 3:7; e) 4:6; f) 1:1; g) 1:0.

In this context, the work of Reverchon et al. on the formation of porous polymer membranes is mentioned again [15]. It is referred to the schematic ternary phase diagram in Figure III.9 and the accompanying explanation. The three paths are assigned to polymer solutions of different concentrations, to some degree comparable to this study. For a solution rich in polymer, path 1 suggests binodal demixing, which consists in the nucleation and subsequent coarsening of the polymer-lean phase, while the polymer-rich phase solidifies and generates the cellular structure. The demixing dynamics are considered to be slow and the top layer membranes are found to be thicker. Correspondingly, samples in this study were linked to a continuous top layer for dilutions 1:0 and 1:1 (ink:EGDA). Digital microscopy images confirmed the cellular appearance, which was less visible in SEM images.
Solutions of low polymer concentration, see path 3 in Figure III.9, undergo a rapid binodal demixing process, marked by the absence of a continuous membrane. The structure is dominated by beads-like agglomerates, formed by the nucleation and coarsening of the phase high in polymer, from which the polymer solidifies. Further, the degree of pore interconnection decreases with lower polymer content. While deposits of dilution 1:10 and 3:17 correspond well to this description, deposit 2:8 seems to fall into the transition of low to intermediate polymer concentration, as the bulk structure is similar. However, the membrane-like top layer indicates a slightly higher total polymer content.

For intermediate polymer concentrations, the missing knowledge of the exact polymer concentration and location of the miscibility gap limits the possibility to distinguish between a binodal or spinodal demixing process. While Reverchon et al. proposed a path through the phase diagram along path 2 in Figure III.9 b), other researchers argue, that spinodal demixing during the phase separation is unlikely [150] or difficult to distinguish from binodal demixing. It is highlighted, that deposits of dilution 4:6 and 3:7 display structures, which stand out from the deposits of lower and higher dilution at low magnification. In particular, the nodules observed for dilution 4:6 are characteristic. Their formation, however has not been explained to satisfaction, as discussed in [11].

The treatment of SEM images in series 2) was carried out as before, see Figure III.64. Pore count, pore area and the averaged pore size are listed in Table III.35.
The pore count for the undiluted ink deposit is up to five times larger, than for diluted ink. For the latter, an interesting trend is observed. Increasing ink dilution is linked to a growing number of pores up to dilution 3:17, after which a slight decrease occurs. Based on the above explained mechanism of pore formation in polymer solutions of low polymer content, the generally higher pore count appears natural. The area, corresponding to pores, is lowest for the undiluted ink deposit and around twice as large for dilutions 3:7 and 4:6. For higher dilutions the total pore area decreases, which is unexpected.
Following a similar but more pronounced tendency, the average pore diameter for the undiluted ink deposit yields 41 nm. This is approximately four to nine times smaller, than for all other diluted ink deposits, for which the maximum averaged pore size exceeds 350 nm. Interestingly, the largest average pores are determined for relatively low ink dilutions between 1:1 and 4:6. Reverchon et al. reported an inverse observation during the formation of porous polymer membranes via phase separation by means of supercritical $CO_2$. In particular, the pore size decreased from 50 to 2 µm for polymer concentrations from 10 to 40 % (w/w). A similar result was obtained by Matsuyama et al., who found a decrease in pore size from 14 to 11 µm for increased polymer concentrations from 15 to 30 %. However, a limited comparability could apply due to the different ternary system used in this work, along with the addition of the polymer foaming mechanism.

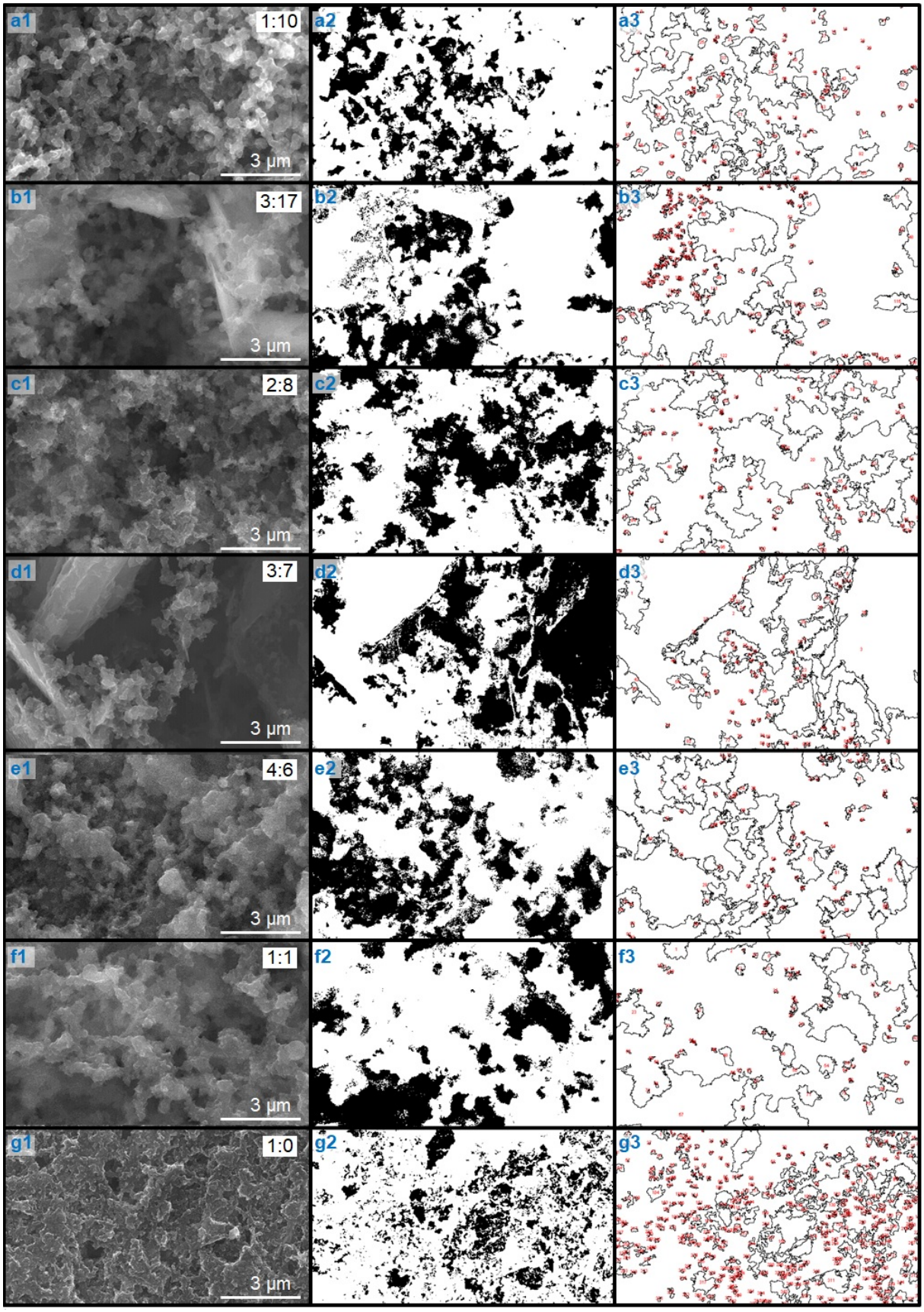


Figure III.64: SEM image treatment for ImageJ pore area determination and quantification in the study of ink dilution. Red dots in series 3) originate from the automatic particle counting. Ratios of ink:EGDA (w/w) were a) 1:10; b) 3:17; c) 2:8; d) 3:7; e) 4:6; f) 1:1; g) 1:0.

Table III.35: Pore count, pore area and mathematically averaged pore radius extracted from the ImageJ treatment of SEM images in the study of ink dilution.

| **Description** | **Particle count** | **Total particle area ($\mu m^2$)** | **% Area** | **Pore diameter (nm)** |
|---|---|---|---|---|
| 1:10 | 144 | 27.2 | 26.8 | 189 |
| 3:17 | 170 | 28.2 | 27.8 | 166 |
| 2:8 | 141 | 33.1 | 32.6 | 234 |
| 3:7 | 115 | 39.3 | 38.7 | 342 |
| 4:6 | 111 | 36.8 | 36.3 | 332 |
| 1:1 | 91 | 32.1 | 31.6 | 353 |
| 1:0 | 501 | 20.3 | 20.0 | 41 |

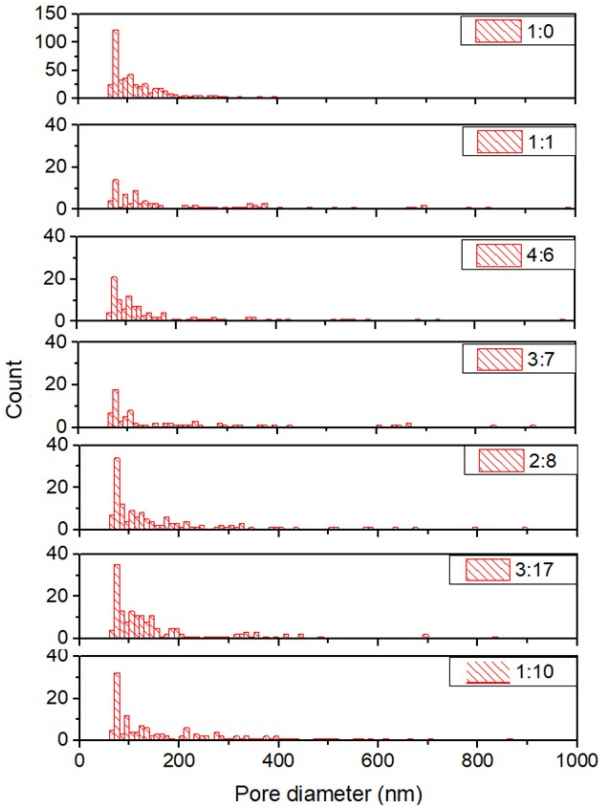


Figure III.65: Histograms of particle/pore populations based on treated SEM images in the study of ink dilution with 60 nm lower threshold pore size. Ratios of ink:EGDA were a) 1:10; b) 3:17; c) 2:8; d) 3:7; e) 4:6; f) 1:1; g) 1:0.

The detailed study of pore size distributions, see the histograms in Figure III.65, reveals pores up to 300-400 nm in diameter for the deposit of dilution 1:0. In contrast, pore diameters of at least one micron are observed for all other dilutions, although the count of these larger pores is extremely low.
The lower threshold of pore diameters corresponds to 60 nm. No valid or sensible separation of actual pores from image contrast artefacts was possible for smaller values. Indifferent from ink dilution, the largest populations are located around 100 nm in diameter. For diluted ink of dilutions 1:10 to 2:8, this population is around twice the size as for dilutions 3:7 to 1:1. For undiluted ink, this population is increased by a factor three. This tendency matches the variation in average pore size in Table III.35. In conclusion, the higher dilution of inks appears to favour the generation of smaller pores.

## 3.4.2 Electrochemical characterization

### 3.4.2.1 Capacitive current studies

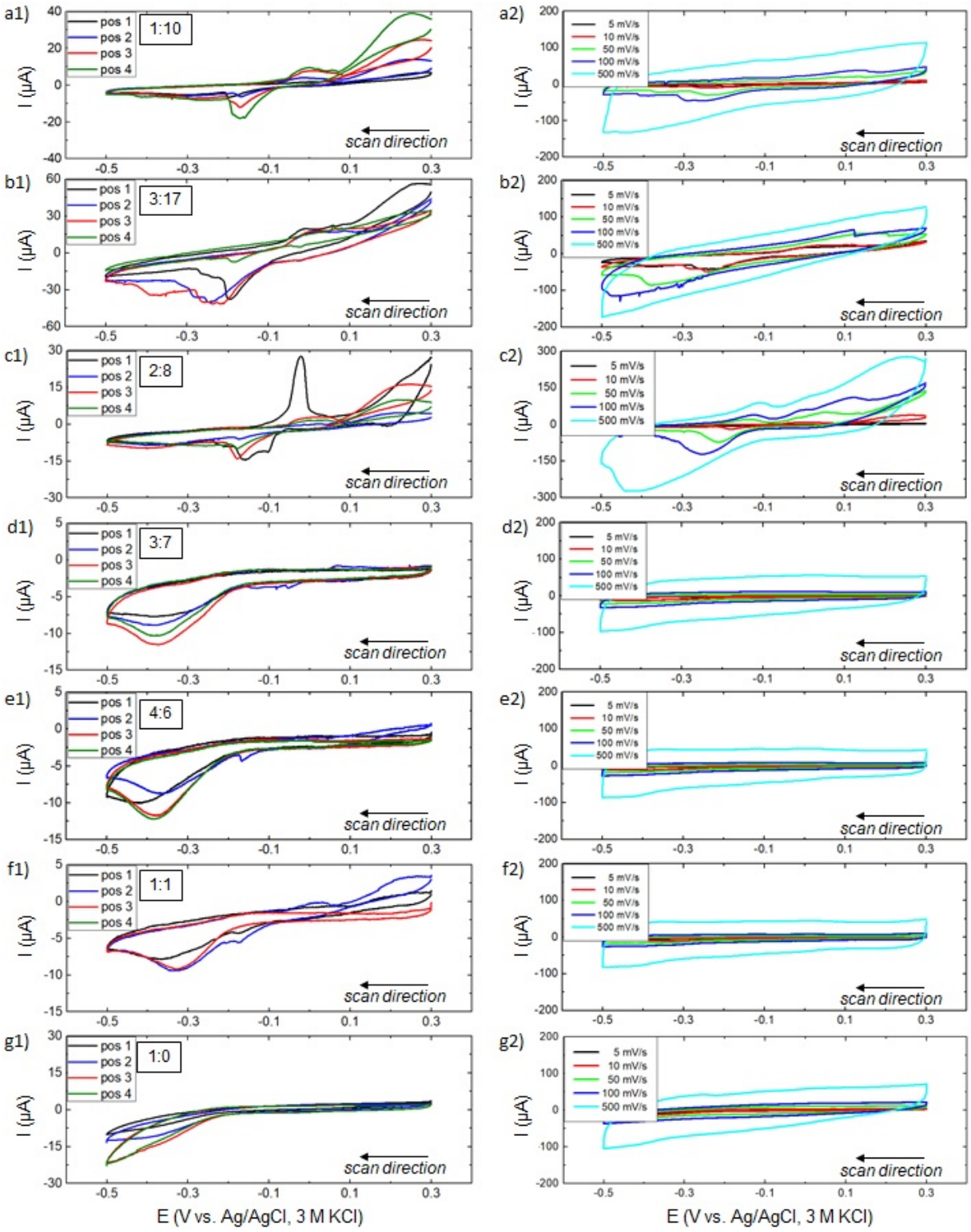


Figure III.66: Capacitive response of structured, plasma-treated electrodes in the study of ink dilution in 1 M KCl. Series 1 at 5 mV/s and different scan rates in series 2. The ratios ink:EGDA (w/w) were a) 1:10, pos. 1 in a2); b) 3:17, pos. 3 in b2); c) 2:8, pos. 2 in c2); d) 3:7, pos. 1 in d2); e) 4:6, pos. 3 in e2); f) 1:1, pos. 3 in f2); g) 1:0, pos. 2 in g2). The $5^{th}$ cycles are displayed. Onset at 0.3 V.

The measured CV of structured and plasma-treated electrodes are displayed in Figure III.66 and the different scales of the y-axis pointed out. Further, the general appearance of curves requires a note of caution. The CV of dilutions 1:0 to 3:7 (ink:EGDA), see Figures d) to g), were of similar shape, compared to earlier sections and of expected capacitive or pseudo-capacitive character. However, the curves corresponding to higher ink dilutions 3:7 to 1:10 (ink:EGDA) diverge at both slow and fast scan rates and resemble more the earlier presented response of a contaminated electrode. Besides for an intrinsic resistive component, indicated by the generally inclined slope of the curves, the presence of an additional redox couple is noted[20].

For the extraction of capacitive currents, this implied the choice of a suited location on the potential scale for the electrodes in question and in consequence, values were read out at -100 mV for all electrodes (opposed to 0 V in previous sections). The determined capacitances, normalized against the geometric surface and against the electrode mass, are presented in Figure III.67 as a function of the scan rate. Table III.36 lists extracted results for the 5 mV/s data sets, including the factors of increase relative to the undiluted, unstructured electrode.

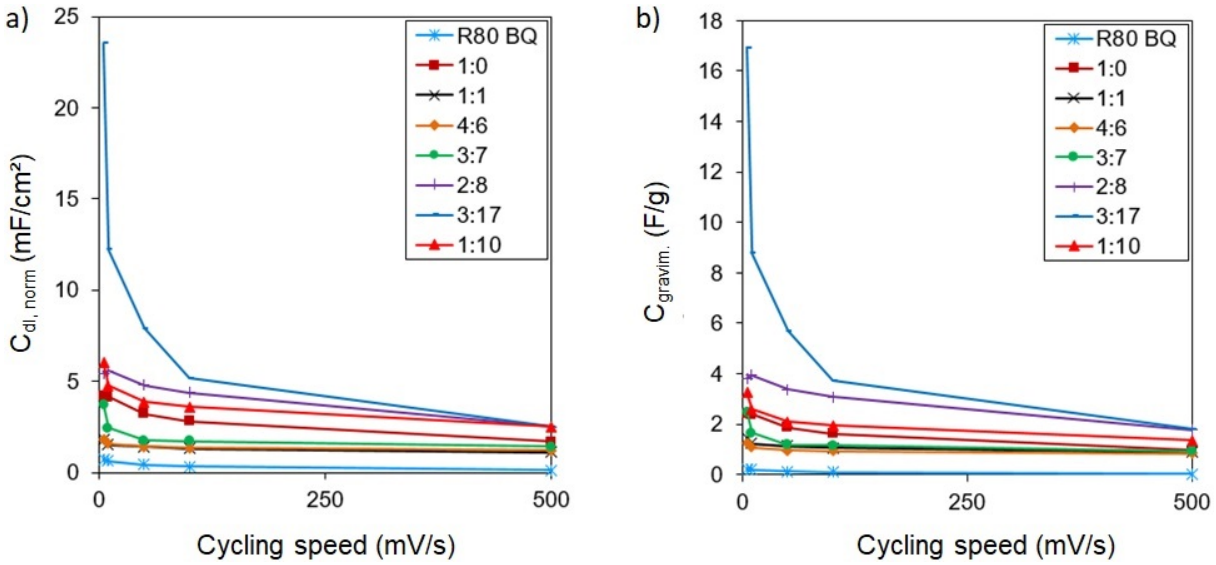


Figure III.67: a) Normalized capacitance relative to $A_{geo}$ and b) gravimetric capacitance in the study of ink dilution, derived from CV. Ratios represent ink:EGDA (w/w).

Compared to the undiluted and dried R80 BQ electrode, all structured electrodes in this section exhibit increased capacitance values. As earlier, results are higher for slow scan rates. The electrodes representing high ink dilution appear to be particularly interesting. Maximum values are observed for the 3:17 (ink:EDGA) electrode with 23.5 mF/cm$^2$ and 16.9 F/g, which corresponds to increases of 33 or 77, respectively. As this is supposedly linked to the larger specific surface areas, the corresponding dilutions seem to generate particularly structured or porous electrodes.
The result is supported by the determination of large pore populations at the upper threshold of macropores and by the coinciding small average pore diameter. Further, the estimated deposit heights and volumes peaked for dilutions 2:8 and 3:17 (ink:EGDA).

[20]The asymmetry/distortion of the oxidation and reduction peaks is a sign of varying overpotential required for the charge transfer, potentially indicating coupled chemical side reactions. The lower viscosity of highly diluted ink may favour diffusion of the contaminants, increasing their presence on the surface in contact with electrolyte.

Electrodes prepared from low ink dilutions, on the other hand, yielded rather low increases in capacitance and results are smallest for electrodes prepared from dilutions 1:1 and 4:6. The results found in previous characterization support the observation, as the populations of small pores were low, the average pore diameter was large and the generated heights and volumes were inferior. The seemingly controversial data on total pore area, which presents an opposed trend, is explained by the surface-related interpretation, which neglects the generation of structure in the bulk.

A detail worth mentioning is the relatively high capacitance, determined for the undiluted, structured electrode (1:0), in comparison with the dilution 1:1 (ink:EGDA). Eventually, the effect of sedimentation of ink constituents in the short time frame before structuration occurs may play a larger role than assumed. This theory implies an optimization of electrode fabrication approaches, to further reduce the manipulation time.
Aside, the evolution of capacitance with the scan rate as a function of ink dilution is curious. Values are highest for dilution 3:17 (ink:EGDA), but no clear tendency is seen. The capacitance is rather constant and independent from the scan rate for dilutions 1:1 and 4:6. Following earlier reasoning, this may indicate a pronounced pseudo-capacitive character.

Table III.36: Measured capacitance ($C_{meas}$) in the study of ink dilution, normalized to $A_{geo}$ ($C_{norm}$), to the electrode mass ($C_{gravimetric}$) and to the non-structured R80 BQ electrodes ($Increase$). Results originate from CV at 5 mV/s in 1 M KCl.

| **Dilution** | **C$_{meas}$ (µF)** | **C$_{norm}$ (mF/cm$^2$)** | **Increase** | **C$_{gravimetric}$ (F/g)** | **Increase** |
|---|---|---|---|---|---|
| 1:10 | 326 | 6.03 | 1.4 | 3.26 | 1.3 |
| 3:17 | 1691 | 23.52 | 33.1 | 16.91 | 77.1 |
| 2:8 | 383 | 5.44 | 7.6 | 3.83 | 17.4 |
| 3:7 | 249 | 3.72 | 5.2 | 2.49 | 11.4 |
| 4:6 | 123 | 1.79 | 2.5 | 1.23 | 5.6 |
| 1:1 | 146 | 1.82 | 2.6 | 1.46 | 6.7 |
| 1:0 | 244 | 4.23 | 5.9 | 2.44 | 11.1 |
| R80 BQ | 49 | 0.71 | 1.0 | 0.22 | 1.0 |

#### 3.4.2.2 Faradaic current studies

Faradaic currents were recorded using the same electrodes, however the subtraction of capacitive currents was limited in this study due to two reasons. First, specifically at slow scan rates, the peaks of charge transfer that originated from the additional redox system were sometimes higher during the capacitive current study. The subtraction of curves then lead to "inverse" peaks, i.e. positive subtracted peaks during the cathodic potential sweep. Second, for some electrodes the recorded capacitive currents towards 0.3 and -0.5 V exeeded the currents recorded during Fardaic studies, which generated deformed subtracted CV and hindered the proper determination of baselines.
In consequence, Figure III.68 displays the recorded CV, in which capacitive and Faradaic currents are superimposed. All measured positions per PCB at a scan rate of 5 mV/s are shown in a) and one selected position up to 500 mV/s in b). Curves with a clearly overlapping Faradaic response from ruthenium hexaamine and the additional redox system, such as in Figure III.68 c1) pos. 1 and pos. 4, were excluded from the extraction of data. However, associated peaks shifted at faster scan rates, allowing to collect data from almost all electrodes except for slow scan rates.

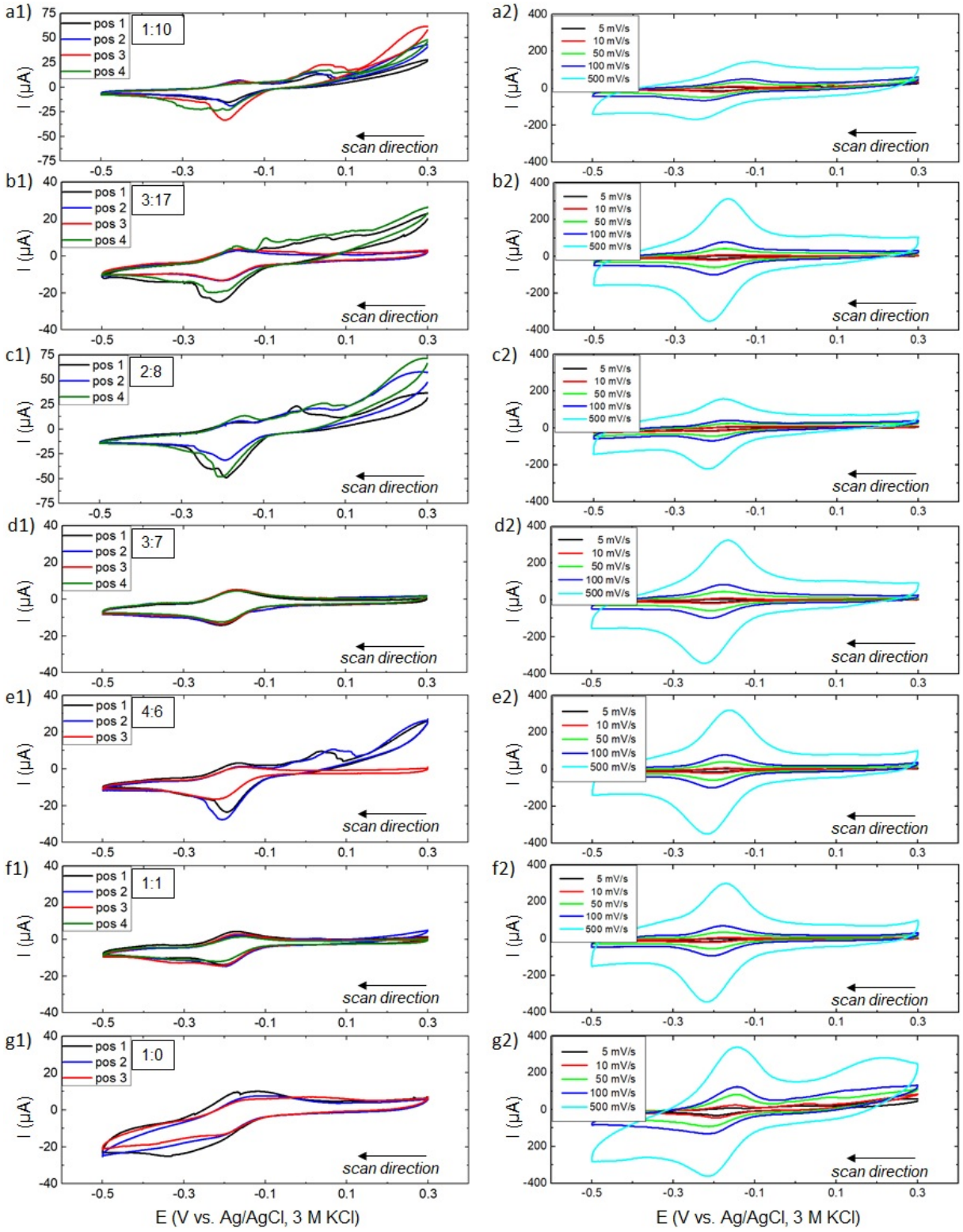


Figure III.68: Faradaic currents of structured, plasma-treated electrodes in the study of ink dilution in 1 M KCl. Series 1 for 5 mV/s and different scan rates in series 2. The ratios ink:EGDA (w/w) were a) 1:10, pos. 1 in a2); b) 3:17, pos. 3 in b2); c) 2:8, pos. 2 in c2); d) 3:7, pos. 4 in d2); e) 4:6, pos. 2 in e2); f) 1:1, pos. 3 in f2); g) 1:0, pos. 3 in g2). The $5^{th}$ cycles are displayed. Onset at 0.3 V.

The further, visual impression of CV is comparable to earlier sections, with a rather small peak-to-peak separation and seemingly similar peak width.
To determine evolutions of electrochemical properties as a function of ink dilution, peak current [densities], peak-to-peak separation and peak ratios were read out and are listed in Table III.37.

Table III.37: Peak-to-peak separation, peak current and peak ratio extracted from CV in 1 mM ruthenium hexaamine, 1 M KCl in the study of ink dilution. Ratios indicate ink:EGDA (w/w).

| $\mathbf{v}_{scan}$ | **1:10** | **3:17** | **2:8** | **3:7** | **4:6** | **1:1** | **1:0** |
|---|---|---|---|---|---|---|---|
| | | | | $\Delta E_{peak}$ **(mV)** | | | |
| 5 | 28.9 | 38.2 | 40.1 | 35.4 | 35.4 | 42.1 | 38.5 |
| 10 | 41.7 | 33.5 | 51.2 | 30.0 | 26.1 | 37.4 | 49.2 |
| 50 | 83.1 | 31.4 | 67.7 | 33.0 | 21.4 | 32.5 | 34.4 |
| 100 | 89.1 | 32.0 | 64.3 | 37.1 | 23.6 | 30.6 | 33.1 |
| 500 | 118.9 | 44.2 | 66.5 | 58.8 | 49.5 | 47.7 | 35.6 |
| | | | | $\mathbf{I}_{ox}$ **(µA)** | | | |
| 5 | 6.2 | 6.0 | 11.6 | 6.3 | 5.8 | 6.1 | 3.9 |
| 10 | 9.8 | 11.0 | 23.6 | 10.8 | 9.5 | 11.2 | 8.7 |
| 50 | 24.7 | 34.3 | 65.2 | 37.8 | 33.7 | 32.3 | 18.6 |
| 100 | 32.5 | 55.1 | 95.9 | 65.4 | 59.9 | 54.3 | 26.9 |
| 500 | 76.5 | 209.9 | 286.4 | 240.7 | 241.9 | 216.3 | 87.9 |
| | | | | $\mathbf{I}_{red}$ **(µA)** | | | |
| 5 | -15.3 | -8.3 | -33.3 | -8.3 | -8.3 | -15.3 | -4.1 |
| 10 | -21.0 | -14.3 | -46.9 | -13.5 | -12.4 | -20.0 | -8.9 |
| 50 | -35.7 | -37.6 | -82.1 | -44.5 | -41.0 | -44.2 | -22.2 |
| 100 | -41.0 | -60.9 | -106.9 | -73.9 | -72.3 | -70.9 | -38.4 |
| 500 | -86.8 | -218.3 | -275.1 | -236.5 | -264.5 | -241.1 | -128.9 |
| | | | | $\mathbf{I}_{ox}/\mathbf{I}_{red}$ | | | |
| 5 | -0.337 | -0.742 | -0.359 | -0.753 | -0.699 | -0.417 | -0.955 |
| 10 | -0.400 | -0.778 | -0.521 | -0.797 | -0.766 | -0.579 | -0.960 |
| 50 | -0.475 | -0.919 | -0.832 | -0.849 | -0.821 | -0.735 | -0.832 |
| 100 | -0.535 | -0.918 | -0.923 | -0.886 | -0.826 | -0.767 | -0.699 |
| 500 | -0.570 | -0.970 | -1.044 | -1.019 | -0.911 | -0.896 | -0.682 |

For a better visualisation, $\Delta E_{peak}$ (mV) is plotted against the scan rate in Figure III.69, together with the earlier response of undiluted, dried R80 BQ electrodes.
For slow cycling speeds, peak-to-peak separations of structured electrodes all range between 30 to 40 mV, including electrodes prepared from low ink dilutions, which shows a clear difference to the dried R80 BQ electrodes. In conformity with earlier explanation, this is attributed to the generation of pores in a dimension, which changes the electrode's diffusion characteristics from linear, semi-infinite to a thin-layer type diffusion.
Upon increasing the scan rate, two principal behaviours seem to emerge. For high dilutions 1:10 and 2:8, a relatively fast increase of $\Delta E_{peak}$ (mV) is observed for faster scan rates. For the electrodes corresponding to dilution 3:17, the behaviour varies. Overall, the inconsistency for high ink dilutions could arise from the overlap of charge transfer reactions in the CV, hindering the exact extraction of data. This aspect is addressed again below.
For low dilutions, $\Delta E_{peak}$ (mV) generally remains below the 57 mV threshold, but without any particular link to ink dilution. Smallest $\Delta E_{peak}$ (mV) of 21 mV were associated with 4:6 ink dilution, while the peak-to-peak separation for 1:0 dilution remained

rather constant over the entire range of scan rate. The results suggest the generation of a diffusion-limiting structure for all structured electrodes and confirm particularly fast charge transfer kinetics for the undiluted, structured ink. In the context of earlier theories, this confirms the limiting effect of EGDA on the charge transfer kinetics.

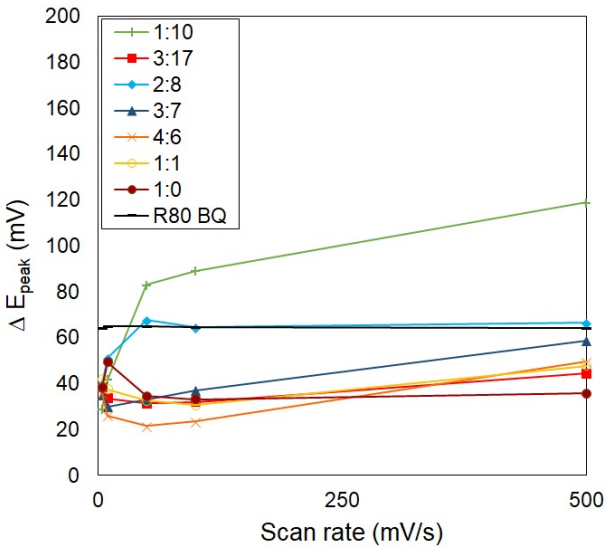


Figure III.69: Peak separation as a function of the scan rate based on CV in 1 mM ruthenium hexaamine, 1 M KCl in the study of ink dilution. Ratios indicate ink:EGDA (w/w).

The interpretation of peak current ratios is interesting, as it equally suggests two generally different electrode characteristics. As for non-structured, undiluted R80 BQ electrodes, which were considered as reference in this context, peak ratios were close to 1 for all scan rates, a reversible charge transfer with negligible absorption is suggested.
For structured, undiluted electrodes, the peak ratio decreased from close to 1 at slow cycling to less than -0.7 for fast scan rates. While this indicates a comparable oxidation and reduction reaction at slow scan rates, it proposes an imbalance at faster scan rates. As the diffusion coefficients for the oxidized ruthenium hexaamine ion are smaller, than for the reduced ion [133], limited diffusion in a porous structure would lead to a depletion of the reduced form specifically at fast scan rates[21]. The resulting smaller oxidation peaks and the relatively large reduction peaks then explain the smaller negative peak ratios. The theory matches the evolution of peak currents and densities of the 1:0 electrodes, which increase more importantly for the reduction than for the oxidation, see Table III.37.
For structured, diluted electrodes, an inverse trend is observed, consisting in small negative peak ratios for slow scan rates and ratios closer to one for faster scan rates. In addition to the above-detailed mechanism, the earlier mentioned theory of trapped analytes is assumed, which in particular limits the diffusion length of reduced species. In consequence, more reduced analytes undergo oxidation, resulting in the observed larger oxidation peak currents at fast scan rates.

In the following, the evolution of peak currents is briefly discussed, based on the plots of peak current densities in Figure III.70 and the extracted linearities of curves in Table III.38. It is reminded, that the criterion of a reversible, or quasi-reversible charge transfer

[21]Reported are $D_{HexRu(III)} = 0.547 \times 10^{-9} m^2/s$ and $D_{HexRu(II)} = 0.77 \times 10^{-9} m^2/s$ for a measurement in 0.5 M KCl. Similar tendencies apply for smaller concentrations. It is assumed, the trend can be extrapolated for 1 M KCl

applied despite the diffusion limit, justifying the approach.
Peak current densities describe an arc-shaped evolution with ink dilution. Highest values were obtained for dilutions 2:8, 3:7 and 4:6, potentially highlighting the generation of largest electrochemically active surfaces of the electrodes in study. For structured electrodes, lowest values were determined for dilutions 1:0 and 1:10 with very similar results.

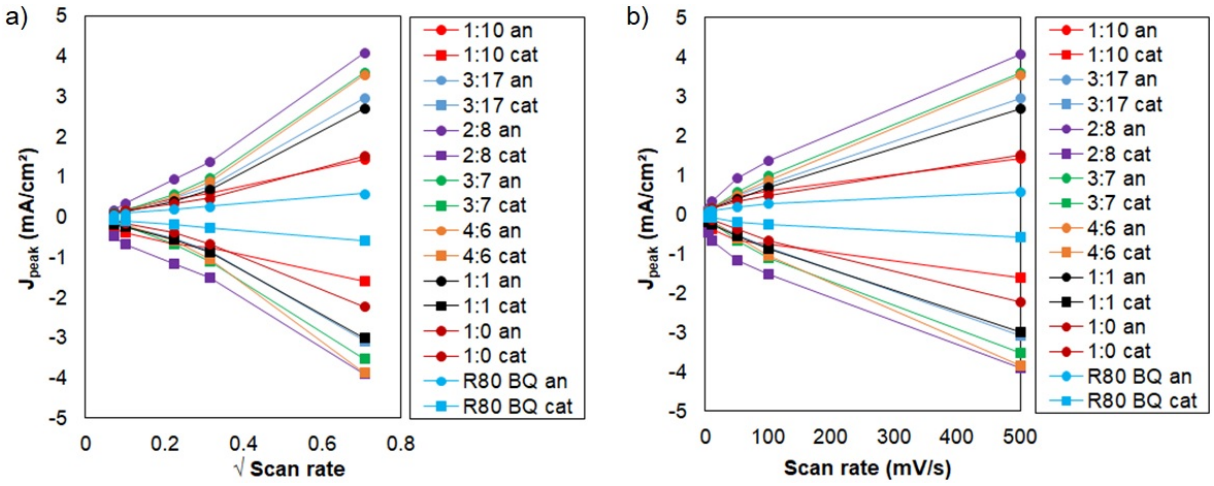


Figure III.70: Comparison of peak current densities based on CV in 1 mM ruthenium hexaamine, 1 M KCl in the study of ink dilution. Ratios indicate ink:EGDA (w/w).

For high ink dilutions (except 3:17), pronounced linearities of $J_{peak}$ against the square root of the scan rate are attained, as well as for the unstructured R80 BQ electrodes. Inversely, lower linearities apply for the plot against the scan rate, which is an indicator of unrestricted (linear, semi-infinite) diffusion, usually observed on flat electrodes.
A smooth transition is visible towards electrodes of lower ink dilutions, for which lower linearities in the plot of $J_{peak}$ against the root of the scan rate were determined. Correspondingly, linearities are higher in the plot against the scan rate, which is interpreted as a charge transfer involving electrode-absorbed species [132]. In combination with the conclusions of the peak-to-peak separation, the results confirm the thin-layer-type diffusion, specifically for electrodes prepared from dilutions 4:6 and 1:1.

Table III.38: Linearity of peak current density plots versus the scan rate and the root of the scan rate in the study of ink dilution based on CV in 1 mM ruthenium hexaamine, 1 M KCl. Ratios indicate ink:EGDA (w/w).

| **Dilution** | **$R^2$ of $J_{peak}$ vs. $(\nu_{scan})^{0.5}$** | **$R^2$ of $J_{peak}$ vs. $\nu_{scan}$** |
|---|---|---|
| **1:10** | 0.997 | 0.954 |
| **3:17** | 0.976 | 0.997 |
| **2:8** | 0.992 | 0.984 |
| **3:7** | 0.983 | 0.993 |
| **4:6** | 0.973 | 0.997 |
| **1:1** | 0.972 | 0.998 |
| **1:0** | 0.982 | 0.993 |
| **R80 BQ** | 0.999 | 0.958 |

An estimative calculation of the electrochemically active surface was done as before, relying on both peak current and peak charge. The results are presented in Table III.39, together with the factors of increase relative to the geometric electrode surface and relative to the non-structured R80 BQ electrodes.

Table III.39: Electroactive surface areas calculated from cathodic peaks in CV experiments studying the ink dilution. Ratios indicate ink:EGDA (w/w).

| $\mathbf{v}_{scan}$ | **1:10** | **3:17** | **2:8** | **3:7** | **4:6** | **1:1** | **1:0** |
|---|---|---|---|---|---|---|---|
| $\mathbf{A}_{Randles}$ **(cm$^2$)** | | | | | | | |
| 5 | 0.327 | 0.178 | 0.714 | 0.179 | 0.178 | 0.328 | 0.087 |
| 10 | 0.319 | 0.217 | 0.711 | 0.205 | 0.189 | 0.304 | 0.134 |
| 50 | 0.242 | 0.254 | 0.556 | 0.302 | 0.278 | 0.299 | 0.151 |
| 100 | 0.196 | 0.292 | 0.512 | 0.354 | 0.347 | 0.340 | 0.184 |
| 500 | 0.186 | 0.468 | 0.590 | 0.507 | 0.567 | 0.517 | 0.276 |
| $\mathbf{A}_{Oldham}$ **(cm$^2$)** | | | | | | | |
| 5 | 0.394 | 0.214 | 0.859 | 0.215 | 0.214 | 0.394 | 0.105 |
| 10 | 0.384 | 0.261 | 0.855 | 0.247 | 0.227 | 0.365 | 0.161 |
| 50 | 0.291 | 0.306 | 0.669 | 0.363 | 0.335 | 0.360 | 0.181 |
| 100 | 0.236 | 0.351 | 0.616 | 0.426 | 0.417 | 0.409 | 0.221 |
| 500 | 0.224 | 0.563 | 0.709 | 0.610 | 0.682 | 0.622 | 0.332 |
| $\mathbf{A}_{Randles,irrev.}$ **(cm$^2$)** | | | | | | | |
| 5 | 0.416 | 0.226 | 0.908 | 0.227 | 0.336 | 0.417 | 0.111 |
| 10 | 0.406 | 0.276 | 0.904 | 0.261 | 0.240 | 0.386 | 0.171 |
| 50 | 0.308 | 0.324 | 0.708 | 0.384 | 0.354 | 0.381 | 0.191 |
| 100 | 0.250 | 0.371 | 0.651 | 0.451 | 0.441 | 0.432 | 0.234 |
| 500 | 0.237 | 0.595 | 0.750 | 0.645 | 0.721 | 0.657 | 0.351 |
| $\mathbf{A}_{charge,anodic.}$ **(cm$^2$)** | | | | | | | |
| 5 | 0.386 | 0.219 | 0.789 | 0.255 | 0.233 | 0.386 | 0.120 |
| 10 | 0.401 | 0.285 | 0.781 | 0.254 | 0.256 | 0.383 | 0.183 |
| 50 | 0.339 | 0.361 | 0.730 | 0.427 | 0.369 | 0.410 | 0.194 |
| 100 | 0.284 | 0.422 | 0.714 | 0.513 | 0.464 | 0.470 | 0.242 |
| 500 | 0.281 | 0.683 | 0.907 | 0.772 | 0.803 | 0.728 | 0.372 |
| $\mathbf{A}_{Randles}/\mathbf{A}_{geo}$ | | | | | | | |
| 500 | 2.62 | 6.59 | 8.30 | 7.14 | 7.98 | 7.28 | 3.89 |
| $\mathbf{A}_{Oldham}/\mathbf{A}_{geo}$ | | | | | | | |
| 500 | 3.15 | 7.93 | 9.99 | 8.59 | 9.60 | 8.75 | 4.68 |
| $\mathbf{A}_{Randles,irrev.}/\mathbf{A}_{geo}$ | | | | | | | |
| 500 | 3.33 | 8.38 | 10.56 | 9.08 | 10.15 | 9.26 | 4.95 |
| $\mathbf{A}_{charge,anodic}/\mathbf{A}_{geo}$ | | | | | | | |
| 500 | 3.95 | 9.61 | 12.78 | 10.88 | 11.31 | 10.26 | 5.23 |
| **Factor of increase relative to R80, Randles-style equations** | | | | | | | |
| 500 | 2.2 | 5.4 | 6.8 | 5.9 | 6.6 | 6.0 | 3.2 |
| **Factor of increase relative to R80, $\mathbf{Q}_{anodic}$** | | | | | | | |
| 500 | 2.1 | 5.1 | 6.8 | 5.8 | 6.0 | 5.4 | 2.8 |

Again, electrodes follow two different tendencies. The calculated electroactive surfaces increase with scan rates as expected, except for ink dilutions 1:10 and 2:8, which shown an inverse trend. Similar behaviour was observed for R80 BQ and R80 BQ-EGDA electrodes in previous sections and an overestimation of the surface for slow scan rates was suspected. The peak-charge-based calculation yielded slightly larger values (increased up to 20 %), compared to earlier sections.

The calculated electroactive surfaces followed an arc-shaped evolution with ink dilution. The largest increase was associated with ink dilution 2:8, yielding the factors 12.8 and 6.8, relative to $A_{geo}$ and to the dried, R80 BQ electrodes. A second, local maximum with somewhat lower values was observed for dilution 4:6.

### 3.4.2.3 Chronoamperometric studies

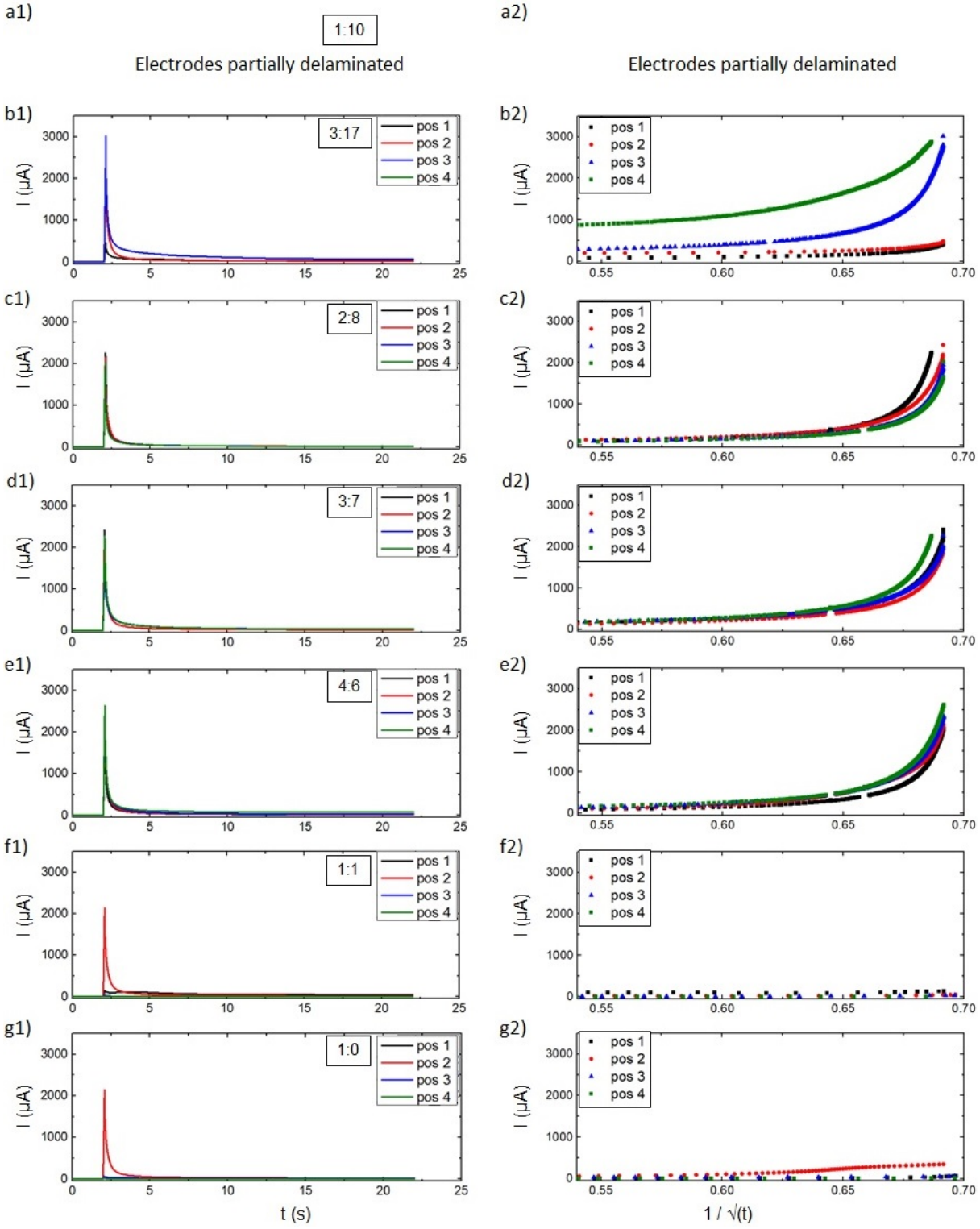


Figure III.71: Chronoamperometric responses in series 1 (0 V, 2 s and 0.7 V, 20 s in 2.5 mM hexacyanoferrate (II), 1 M KCl) in the study of ink dilution; a) 1:10; b) 3:17; c) 2:8; d) 3:7; e) 4:6; f) 1:1; g) 1:0. Ratios indicate ink:EGDA (w/w). The resulting Cottrell plots in series 2.

Chronoamperometric measurements on structured electrodes, prepared from differently diluted inks, were carried out in 2.5 mM hexacyanoferrate (II), 1 M KCl as before. The

recorded curves and Cottrell plots are presented in Figure III.71 1) and 2).
The electrodes of PCB corresponding to dilution 1:10 were partially delaminated due to repeated handling, as the experiments were chronologically carried out after all other techniques. Similar reasons of low mechanical stability are assumed for the inhomogeneous curves for dilution 3:17. Cottrell plots of position 1 and 2 are relatively linear and may indicate diffusion according to the linear, semi-infinite case.
For the electrodes of "moderate" dilutions 2:8 to 4:6, reponses per PCB appear rather homogeneous, while responses of PCB corresponding to low dilutions are of unexpectedly varying character. This difference is equally visible in the Cottrell plots, where electrodes of dilution 1:1 and 1:0 visually diverge.

Employing the Cottrell equation allowed for an estimative calculation of electroactive surfaces, which are listed in Table III.40, together with geometric surface areas and relative surface increase.
Comparing electrodes of dilution 2:8 with the earlier results, comparable values were expected. The deviation of around 18 % (98 $m^2/g$ vs. 116 $m^2/g$) is considered an important indicator of uncertainty and could have been influenced by different wetting/hydration times prior to the start of the experiments. The relatively low surface increases of electrodes 1:0 and 1:0 could potentially be explained likewise.
The electroactive surfaces evolve with ink dilution in an arc-shaped manner, with maximum electroactive surfaces of 122 $m^2/g$ determined for electrodes of dilution 4:6, which is approximatley 1670 times $A_{geo}$. In agreement with earlier results, a second local maximum is noted for electrodes of dilution 2:8.

Table III.40: Cottrell slopes, calculated electroactive surface areas and specific surface areas for structured carbon ink electrodes in the study of ink dilution. Ratios indicate ink:EGDA (w/w)

| | $\mathbf{A_{geo}}$ **(mm$^2$)** | $\mathbf{A_{Cottrell}}$ **(cm$^2$)** | $\mathbf{A_{Cottrell}}$ **(m$^2$/g)** | $\mathbf{A_{Cottrell}/A_{geo}}$ |
|---|---|---|---|---|
| **1:10, 50 ms** | - | - | - | - |
| **3:17, 50 ms** | 7.1 | 52.04 ± 46.82 | 55.5 | 733 |
| **2:8, 50 ms** | 7.0 | 108.74 ± 14.08 | 116.1 | 1545 |
| **3:7, 50 ms** | 6.7 | 99.77 ± 9.32 | 106.5 | 1489 |
| **4:6, 50 ms** | 6.9 | 114.49 ± 8.39 | 122.2 | 1669 |
| **1:1, 50 ms** | 8.1 | 0.74 ± 0.46 | 0.8 | 9.2 |
| **1:0, 50 ms** | 5.8 | 1.72 ± 1.04 | 1.7 | 29.8 |

#### 3.4.2.4 Electrochemical impedance studies

The EIS spectra of one electrode per PCB are displayed in Nyquist plots in Figure III.72 with a view on a) the entire spectrum and b) a representation of the high-frequency region. Electrodes corresponding to dilution 1:10 are missing due to the partial delamination.
All spectra present the previously identified response of structured electrodes, varying from linear, semi-infinite diffusion. The high-frequency domains are marked by the visual absence of defined R/C semicircles. Instead, the slopes are of steep inclination, which was linked to double layer charging.
The general similarity of high-frequency responses is pointed out, which is a potential confirmation of a certain structural similarity. However, spectra display a shift regarding the real part of the impedance as a function of ink dilution. For undiluted, $scCO_2$-structured electrodes, the value is around 20 , while it is increasing up to 33  for higher ink dilution. Eventually, this is explained by the larger total pore volume to be expected for inks of

lower solid content. A higher dilution reduces charge transfer bridges between the carbon particles.
The low-frequency regions of the spectra follow a slightly curved shape, potentially caused by the diffusion characteristics. The last recorded impedance value for each electrode follows an evolution with ink dilution, with minimum values for the dilution 4:6. In particular, this observation could be linked to the diffusion-related resistance in the structure and, in consequence, could be affected by pore size. In that case, electrodes corresponding to dilution 4:6 appear interesting and of low diffusion resistance.

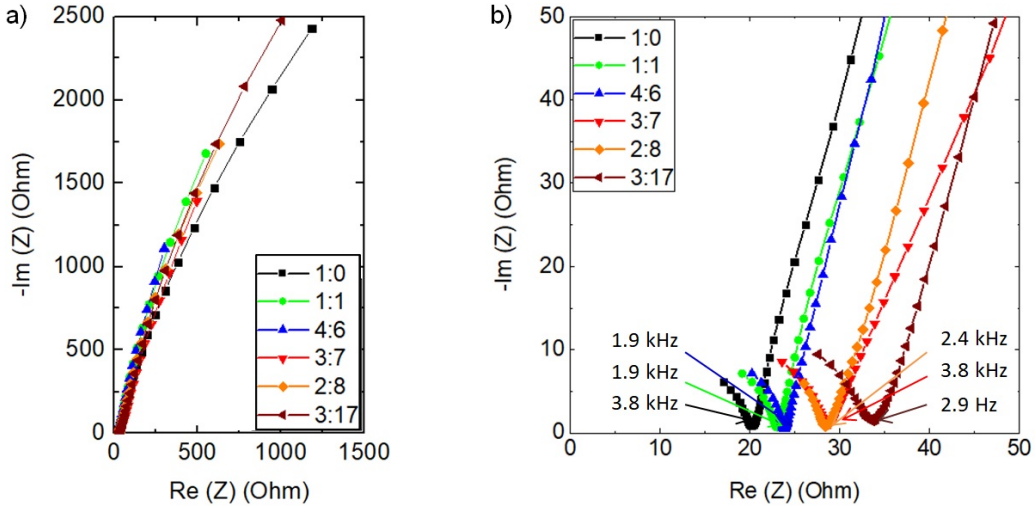


Figure III.72: a) Nyquist plots with b) high-frequency domains in 1 M KCl, 1 mM ruthenium hexaamine in the study of ink dilution. Ratios indicate ink:EGDA (w/w).

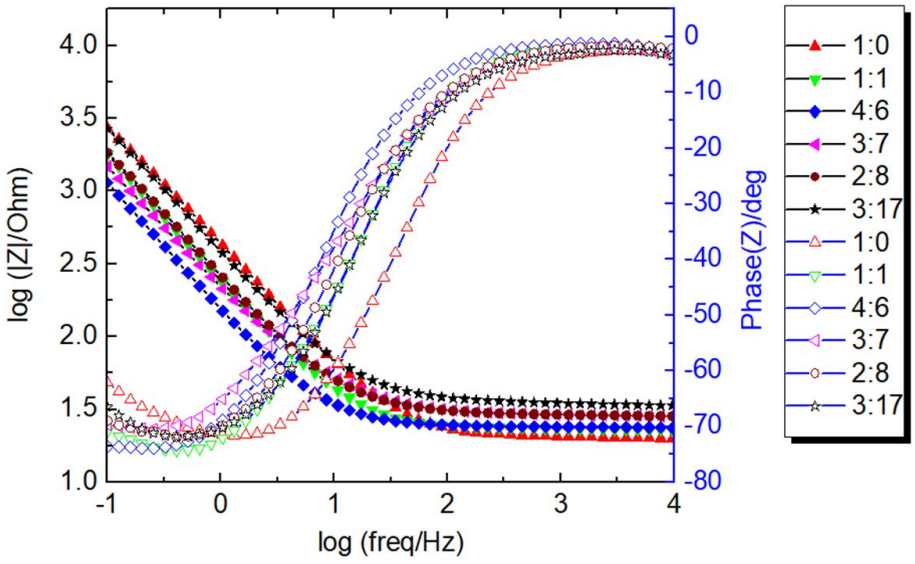


Figure III.73: Bode plot for electrodes in the study of ink dilution. Ratios indicate ink:EGDA (w/w). EIS was performed in 1 M KCl, 1 mM ruthenium hexaamine.

Figure III.73 provides Bode plots, which support the theory of almost purely resistive behaviour at high frequencies of 10 to less than 1 kHz, as the phase angle is close to 0. More specific, when considering phase angles smaller than 10 °, the resistive low-impedance region extends over more than two orders of frequency. A clear tendency

towards lower impedance is noticed for less diluted inks, although the overall difference is less remarkable, than for changed process times in earlier sections.
At the cut-off frequencies, electrodes adopt a capacitive character. Interstingly, the shoulder shown in the Bode plot of electrodes in earlier sections is not expressed and the behaviour of electrodes is thought to deviate from Warburg-type diffusion. The observation is somewhat curious, as the PCB of dilution 2:8 was theoretically prepared under equivalent conditions, as the 20/30 sample in an earlier section. Further, in comparison, the electrode prepared with undiluted ink reaches this point at highest frequencies.
The phase angle in the capacitive low-frequency region is comparable for all electrodes and no particular tendency is observed.

Table III.41 lists the quality of fit, extracted from the application of equivalent circuits to the Nyquist plots. As in previous sections, circuit b) yields better fits than circuit a). Comparing total values, however, $Xi^2$ for circuit b) in this section is twice the value, suggesting a careful interpretation of results. Best matches for circuit b) were linked to electrodes of dilution 4:6 and 1:0.

Table III.41: Quality of fit for different equivalent circuits in the study of ink dilution. Ratios indicate ink:EGDA (w/w).

| **Description** | $\chi^2$ **fit a)** | $\chi^2$ **fit b)** | $\chi^2$ **fit c)** |
|---|---|---|---|
| **1:10** | - | - | - |
| **3:17** | 7130 | 7130* | 6750 |
| **2:8** | 2960 | 2960* | 300 |
| **3:7** | 10200 | 5600 | 340 |
| **4:6** | 1990 | 2020 | 20 |
| **1:1** | 3470 | 6100 | 140 |
| **1:0** | 2560 | 2200 | 1260 |

Equivalent circuits: a) $R_s$-Q//($R_{CT}$+W); b) $R_s$-Q//($R_{CT}$+M);
c) $R_s$-$Q_{interface1}$//($R_{pore}$+$Q_{interface2}$//$R_{CT}$); *the same values were obtained for fits with the very similar circuits.

Parameters correlating with fit b) were extracted, see Table III.42, and used to calculate the double layer capacitance of electrodes. The series resistance $R_s$ falls into a similar range as for previous sections and exhibits a clear tendency towards larger values for inks of higher dilution, as mentioned and explained in the qualitative description of Nyquist plots.
The evolution of the CPE parameter $Q^0$ is arc-shaped and displays a maximum value for electrode 4:6, while dilution 3:17 and the undiluted electrode express only half the value. No tendency is assigned to the CPE coefficient $\alpha$. Here, it has a rather constant value of around 0.84, indicating a capacitive electrode experiencing diffusion processes. Further, the overall similar structure of electrodes submitted to the same structuration protocol is suggested.
The estimated charge transfer resistances are, with exception of electrodes 3:7 and 4:6, considerably larger than expected. An arc-shaped tendency is indeed observed, with smallest resistance for the electrode corresponding to dilution 4:6. Still, the need to optimize the higher equivalent circuit elements is suspected.

Table III.42: Key circuit parameters determined from equivalent circuit b) in the study of ink dilution. Ratios indicate ink:EGDA (w/w).

| | $R_s$ (Ω) | $Q^0$ (mF.s$^{(a-1)}$) | a | $f"_{max}$ (Hz) | $R_{CT}$ (Ω) | C (µF) | $C_{norm}$ (mF/cm$^2$) |
|---|---|---|---|---|---|---|---|
| **1:10** | - | - | - | - | - | - | - |
| **3:17** | 34.4 | 0.54 | 0.85 | 2.2 | 21761 | 299 | 5.15 |
| **2:8** | 29.1 | 0.80 | 0.86 | 2.9 | 19516 | 575 | 7.10 |
| **3:7** | 28.8 | 0.91 | 0.80 | 2.2 | 302 | 608 | 8.82 |
| **4:6** | 23.6 | 1.00 | 0.82 | 2.5 | 2 | 540 | 8.05 |
| **1:1** | 23.2 | 0.84 | 0.87 | 2.8 | 16201 | 527 | 7.53 |
| **1:0** | 20.2 | 0.48 | 0.86 | 4.1 | 10186 | 365 | 5.14 |

Prior to and after normalization to the geometric electrode surface, results follow the same arc-shaped tendency with largest values obtained for the electrode corresponding to dilution 3:7 (8.8 mF/cm$^2$), followed by dilution 4:6 (8.1 mF/cm$^2$). For highest and lowest dilution, results around 5 mF/cm$^2$ quantitatively resemble the largest normalized capacitances obtained in previous sections and highlight the increase achieved by studying inks of different dilutions. It is considered, that the results are representative for the development of specific surface area. However, is is curious, that the coherence with results based on capacitive current studies is low. A large discrepancy regarding the results is noted and instead, the tendency matches the development of specific surface area.

### 3.4.3 Conclusion of the study of ink dilution

Digital microscopy images indicated the generation of fragile, voluminous structures for high ink dilutions, which were prone to fracture and delamination. Moderate ink dilutions yielded structured deposits topped by thin membranes. Low ink dilutions resulted in homogeneous, porous surfaces of macroscopically flat appearance. The structural differences correlate with height and volume evolutions, see Figure III.74. Particularly, the observations confirm a causality between higher ink dilution and a lower density of the obtained deposit. In consequence, their mechanical integrity is reduced.

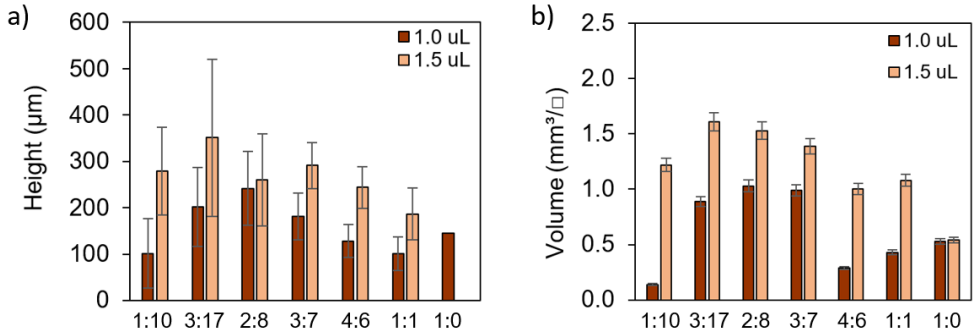


Figure III.74: Results for a) height (single measurements) and b) volume development for $scCO_2$-structured ink deposits (averages of 4 deposits). The parameter of ink dilution (ink:EGDA, w/w) was studied at otherwise constant prepraration of deposits. Two sets of deposits samples were prepared using different ink volumes.

The deposits prepared for SEM imaging presented different surfaces, depending on the degree of ink dilution. In agreement with literature, the structural generation could be linked to different phase separation mechanisms, reinforcing the validity to compare structured polymer solutions to structured, diluted ink. In particular, fast phase separation

kinetics could apply for highly diluted inks. For low ink dilutions, slow phase separation could occur as a function of the starting point in the ternary phase diagram.
It is advised to conduct further studies on the exact interaction of carbon particles with other components of the system during the phase separation mechanism.
The estimated generation of pores on the surface of deposits, based on image-evaluation, followed overall arc-shaped tendencies. Maximum pore areas were observed for dilutions 3:7 and 4:6. Interestingly, the average pore diameter was found to increase for low ink dilutions (i.e. high polymer concentration), against expectations (see Table I.3 in chapter I). Considering the evolution of deposit volumes, this suggests an independent generation of surface and bulk porosity.
The pore sizes are of smaller diameter, compared to works on porous polymer membranes prepared via phase separation. This can be a sign of the additional foaming step, or result from the particular interactions of components of the ternary system.

Based on capacitive current studies, the generation of large specific surface areas for high ink dilutions was confirmed. Results peaked for electrodes 3:17 with an estimated increase of 33, relative to the non-structured R80 BQ electrodes, as displayed in Figure III.75 a). Inversely, the inferior results for electrodes of low ink dilution potentially confirmed the less pronounced generation of porosity.
Faradaic current studies were of particular interest, as peak-to-peak separations suggested a changed diffusion behaviour for most electrodes. For low and moderate ink dilution, electrodes experienced thin-layer-type diffusion. Electrodes of dilution 4:6 and 1:0 stood out due to specifically small peak separations and fast charge transfer kinetics. The effect of captured redox species in the porous structure was underlined in form of changed peak ratios.
The evolution of peak current (density) as a function of the scan rate supports the theory on electrode-adsorbed redox probes for moderate to low ink dilution. This was not the case in previous chapters.
Equivalent tendencies were observed for the calculation of electroactive surfaces, which yielded maximum values for ink dilutions of 2:8 and 4:6, see Figure III.75 b). Relative to the geometric surface, factors of increase ranged between 10 and 11, depending on whether peak current or peak charge was used for the calculation.

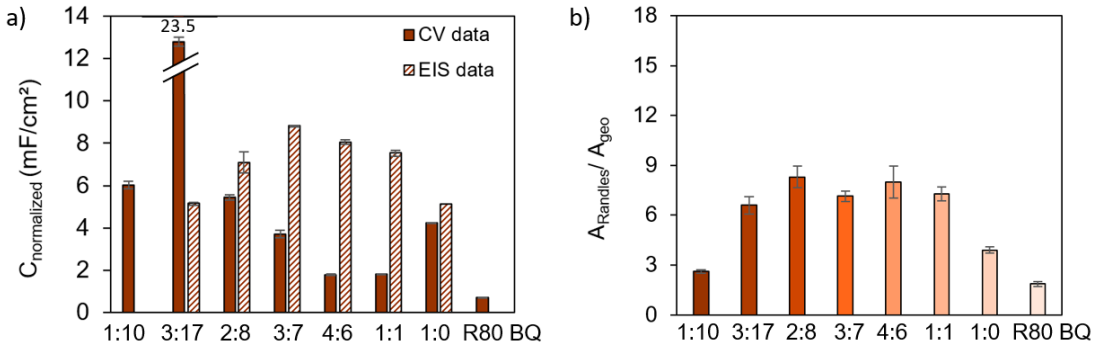


Figure III.75: a) Results for the development of capacitance of structured electrodes, normalized to the geometric electrode surface, determined from CV and EIS studies. b) The development electrochemically active surface for $scCO_2$-structured ink electrodes. The parameter of ink dilution (ink:EGDA, w/w) was studied at otherwise constant prepraration of deposits. Average values of 4 structured electrodes are displayed. All electrodes were plasma-treated.

The generation of electroactive surface by means of chronoamperometric experiments

yielded comparable results. It is thought, that electrodes corresponding to dilutions 1:1 and 1:0 could eventually profit from longer hydration times prior to electrochemical characterization, but this is considered impractical from an experimental point of view. Electrodes of dilution 4:6 and 2:8 yielded the largest factors of increase in electroactive surface observed throughout the studies.

Impedance spectroscopy allowed recording a homogeneous set of data, which suggested a link between series resistance and ink dilution. A second relation was assigned to double layer capacitance and ink dilution. Electrodes generally exhibited functional similarities to earlier sections. At the same time, a characteristic difference consisted in the changed mass transfer/diffusion-related response. Results propose a maximum development of electroactive surface for the electrodes corresponding to dilutions 3:7.

# 3.5 A theoretical view on the parameter $CO_2$ pressure

The last process parameter, which is accessible via the supercritical fluid equipment, is the supercritical $CO_2$ pressure. Several works in the field of phase separation and polymer foaming of polymer solutions have been published over the years, of which a small excerpt is presented.
While the rate of depressurization technically is a separate parameter, it is mentioned as well in the following.

## 3.5.1 $CO_2$ pressure in phase separation of polymeric solutions

Reverchon et al. studied the phase separation of cellulose acetate in acetone with $CO_2$ pressures between 10 and 20 MPa at a comparable temperature of 45 ℃. The surface of membranes prepared at lower pressure visually resemble the deposits/electrodes in this project, in particular for polymer concentrations below 5 %. It is described as bicontinuous and composed by "beads-like elements". Less comparability was assigned to the membranes prepared at high $CO_2$-pressure.
The different structural generation is explained by the increased density of the supercritical fluid at high pressure[22], which reportedly accelerates the demixing process and favours the formation of cellular structures. Slower demixing, inversely, is linked to lower $CO_2$ pressures.
Despite this interesting insight, the influence on pore size was not evaluated in particular [15]. Judging by the rapidity of demixing alone, an increased process pressure could be favourable to prevent sedimentation effects.

Knutson et al. carried out a similar study to investigate the similarity of supercritical fluid-assisted immersion precipitation and phase separation[23] in the formation of porous polymer membranes.
The study is cited while pointing out the lower pressurization/depressurization rate, limited to 0.7 MPa/min. In this project, 20 MPa/min allowed for kinetically driven demixing, which was presumably not the case in the reference.
It was argued, that increased pressure corresponds to higher non-solvent strength of the $CO_2$, which in turn supports kinetically favoured, fast liquid-liquid demixing. In the publication, this was linked to the generation of a slightly more cellular and interconnected network. However, the formation of a dense surface layer was equally observed. Inversely, the reduction of process pressure (implying lower non-solvent strength) was found to favour thermodynamically-driven, slow solid-liquid demixing. This applied in particular for rapidly crystallizing polymers such as the polymer in question, leading to the advise to select a slowly crystallizing polymer to reinforce the generation of structural differences.
Another highly interesting observation consists in the influence of the pressurization rate. Knutson et al. reported, that no phase separation seemed to be initiated below cell pressures of 5.6 MPa. Instead, samples were covered by a dense film. This, in particular, allows to assign a potentially negligible effect to variations in pressurization time. For this project, the conclusion is a potentially increased validity of results.
The group carried out further preconditioning experiments, where small quantities of non-solvent were added to the polymeric solution to reduce solvent strength. Equally, lower $CO_2$ pressures were applied prior to the final precipitation pressure. While the top surfaces were found to display increased pore density, less cellular structure and lower degrees of interconnectivity were observed.

[22] This effect can be supported by lowering the temperature of the supercritical fluid.
[23] Solutions were obtained by dissolving polycaprolactame in 2,2,2-trifluoroethanol.

The work of Matsuyama et al. on the phase separation of polystyrene-toluene solutions evaluated the effect of increasing the process pressure from 7.5 to 15 MPa. They observed that the average pore size increased from 7 to 11 µm, which was explained as consequence of the higher content in the overall system, creating naturally larger pores upon phase separation. As the pores in the top layer equally increase in size, the creation of thicker top layers was observed as a side effect. In addition, it was speculated, that the lower viscosity of the system at high $CO_2$ pressure facilitates mass transport and therefore allows for pores to grow larger [79].

### 3.5.2 $CO_2$ pressure in polymer foaming

Jacobs et al. [151] published their work on foamed Poly(styrene-co-methyl methacrylate), which was carried out using solid polymer samples[24], which were exposed to $scCO_2$ at pressures between 15 and 21 MPa. No information on the duration of exposure was provided. It was found, that the effect of varying the pressure in the studied range influenced the obtained structure less strongly, than process temperature did. Only until a certain threshold temperature, which was considered to be linked to the adsorption isotherms, changes in pressure affected the obtained structure. Results on pore dimensions were exclusively presented qualitatively.
For increased pressure in the range from 10 to 17.5 MPa, a decrease in pore size was observed, together with an increase in pore density. Lower structural uniformity was indicated by a broader pore size distribution.
Further, a two-step pressure reduction, instead of depressurizing the cell at once, was found to result in the generation of a bimodal foam[25]. This advice is considered useful for optimizing the creation of hierarchical networks, comprised by transport and storage pores as discussed earlier.

The study of Reverchon et al. on polystyrene and cellulose acetate foaming reported a decreased average pore size (from 25 to 75 µm) upon increasing $CO_2$ pressure from 10 to 25 MPa [152]. However, pore size distributions were widest for low pressures and narrowest for high pressures, contradicting the results of Jacobs et al. mentioned above.

In another work, Yang et al. prepared microcellular polyurethane foams using $scCO_2$ as blowing agent [153]. Polymer precursors were mixed in the pressurized cell and were subjected to two different process protocols.
Applying a one-step treatment at constant pressure between 10 to 20 MPa, the generation of bimodal structures was observed. For lower pressures, the average populations measured around 3 and 50 µm, while for higher pressures, average dimensions were determined as 2 and 100 µm.
For optimization, the researchers proposed a two-step protocol to favour the generation of a structure with uniform porosity, instead of the bimodal cellular character. In particular, this consisted in a low-pressure phase to saturate the polymer with $scCO_2$ (the optimum saturation pressure was identified as 8 MPa), followed by a high-pressure curing phase. Due to the higher density of $scCO_2$, implying a more liquid-like character, less fluid was dissolved in the polymer. In turn, the nucleation/growth of pores ended at an earlier moment during curing, yielding smaller pore sizes and a higher pore density[26].
A final question addresses the practical realization of depressurization, which reportedly

[24] It is not specified, whether the samples were used in form of powder or pellets.

[25] A bimodal pore distribution presents not one average pore size, but rather a distribution, that peaks for two different pore sizes.

[26] For a curing pressure of 10 MPa, the average pore size was 12 µm, while it was reduced to 2.3 µm for 20 MPa.

varied between 24 and 476 MPa/s[27]. The fast reduction of pressure supported kinetically dominated demixing mechanisms and, according to the study, generated smaller pores (50 to 3 µm).

### 3.5.3 $CO_2$ pressure in combined approaches

Sizov et al. worked on the preparation of porous membranes via supercritical fluid-assisted phase separation (termed "inversion" by the group), based on polybenzimidazole-dimethylacetamide solutions [154]. The parameters of the phase separation process remained constant (30 MPa $CO_2$ pressure at a constant flow of 5 mL/min during 1 h, cell temperature of 40 ℃). Different depressurization rates from to 0.5 to 30 MPa/min were found to not affect membrane morphology, thickness or functional properties.

On the other hand, the study of Salerno et al. on the preparation of polycaprolactone foams, following a combined phase separation and foaming approach, concluded differently [96]. Polymeric solutions with various organic solvents were exposed to supercritical $CO_2$ at 50 ℃ and 20 MPa during 1 to 17 h, followed by a rapid depressurization.
Increased $CO_2$ pressure during the phase separation step was linked to a visually slightly more voluminous and cloudy polymer solution[28]. While this opacity is a sign of solid-liquid polymer precipitation, the volume increase suggests higher exchange/infiltration of $scCO_2$ with the polymer solution during the phase separation. Based on earlier cited references, this could translate to the creation of larger pores.
In the foaming context, higher pressure is considered to assist diffusion of the supercritical fluid into the polymer and to increase plasticity. For example, the melting of polycaprolactone is reportedly taking place at 35 ℃ instead of 60 ℃ for $CO_2$ pressures above 10 MPa [155] [90].

### 3.5.4 Conclusion of the parameter $CO_2$ pressure

The assignment of exact effects of changing pressure on the expected sample morphology or structure requires an individual evaluation for each ternary system, in particular, when additives like conductive particles are added. Still, the publications on fabricating porous polymer membranes allow drawing general conclusions.

During phase separation, increased pressures imply a higher $CO_2$ density, which was linked to faster demixing and to a tendency towards the generation of more cellular structures. In literature, the formation of a more dense membrane-like top layer was observed. Due to its limiting effect on diffusion, maintaining a lower pressure could be a better alternative in this project. In combination with slowly crystallizing polymers, the formation of homogeneously structured surfaces could be favoured.
Reportedly, saturation of the polymer by means of $scCO_2$ is favoured by increased pressure. However, different trends of pore size evolution with increased pressure are reported as well. The mechanism is eventually to be studied for each ternary system in question, particularly when bimodal structures are obtained.

For potential future experiments, the multi-step protocols could present an interest for investigation. Promising results were reported for limited saturation pressures and for two-step depressurization protocols, potentially favouring the generation of structures of hierarchical porosity.

[27] The reported value is considered rather high, but technically not impossible to realize, depending on the particular experimental set-up.

[28] A window allowed to observe the cell interior during the process.

## 3.6 Conclusions of chapter III

The aim of this chapter consisted in the detailed study of structuration parameters on the generation of porosity and on the evolution of electrochemical behaviour. The choice of parameters under investigation was based on the hypothesis, that polymeric solutions and diluted conductive inks behave similarly upon exposure to supercritical $CO_2$.
Structured electrodes were studied by means of a selection of physical and electrochemical characterization techniques of complementary nature. Due to the intrinsic difference of techniques, results were compared carefully. A further comparison against literature values was carried out. The qualitative evaluation of results represents the chapter's main interest. Generally, results were normalized to either the geometric electrode surface or the electrode weight, to eliminate uncertainties arising from the sample preparation.

Digital Microscopy provided a means to visually verify the physical state of electrodes for cracks or delaminated areas. Further, the software tools allowed for the estimation of overall porosity by means of reconstructing height and volume. While the quantitative results provided room for improvement, the technique is principally fast and allows to identify trends relative to changes in the structuration protocol.
The main advantage of Scanning Electron Microscopy consists in the image resolution, which allowed to study the electrode morphology/structuration in detail. The application of an image treatment, aimed at characterizing pore sizes and surface porosity, equally presents the potential for optimization.
Furthermore, imaging the electrode cross-sections was explored. The preparation of samples turned out to be challenging and requires alternative techniques. X-Ray tomography could present a potentially non-destructive method to study bulk porosity. However, the technology is not readily accessible and costly, hence unsuited for characterizing a big set of samples.

Electrochemical techniques allowed to access the bulk of electrodes and comprised capacitive cyclic voltammetry studies in a base electrolyte, as well as faradaic studies, relying on the outer-sphere redox probe ruthenium hexaamine.
The evolution of capacitive currents, correlating with the generation of specific surface area, indicated changes in electrode porosity. Further, it allowed to estimate areal and gravimetric capacitances. Results generally matched literature on porous carbon-based electrodes. The faradaic current evolution, linked primarily to the electrochemically active surface, provided an insight into the charge transfer behaviour. In addition, an idea of mass-transport phenomena were obtained.
Chronoamperometric studies were included as a fast, alternative method for determining the electroactive surface.
Electrochemical Impedance Spectroscopy was considered to allow distinguishing between the capacitive and pseudo-capacitive response of electrodes. While the technique provides a high density of information, the detailed interpretation appeared limited by the uncertainty associated with the fit of equivalent circuits. A potential for improving the extraction of data is seen in identifying equivalent circuits, which may represent the physical electrode structure better.

The ratio of separation and saturation time was studied, maintaining a constant total exposure time. In digital microscopy, estimated height and volume peaked for 10/20 ($t_{sep}/t_{sat}$) deposits.
The comparison of SEM images with works published on phase separation of polymeric solutions highlighted the visual similarity. It suggested, that supercritical fluid-assisted phase separation could be the primary structure-generating mechanism. In particular,

the highly interconnected pore network, i.e. the open porosity, correlated with the presumably low polymer content in the diluted ink. The obtained primary microstructure appeared th be decorated with nanoscale-features, potentially composed by agglomerated polymer and carbon particles. The estimated surface porosity was largest for 20/10 ($t_{sep}/t_{sat}$) deposits and presented a bimodal distribution of pore size with two main pore diameters of different size.
Structured electrodes exhibited a pronounced pseudo-capacitive character, which was linked to the oxygen plasma-treatment. The calculated double layer capacitance was comparable to literature on structured carbon electrodes. Faradaic currents increased by one order, while indicating thin-layer type diffusion, opposed to the linear, semi-infinite diffusion which was exhibited by unstructured electrodes. The generation of porosity following the structuration protocol is clearly indicated. The character of charge transfer was found to be quasi-reversible, which is of practical interest for sensing applications.
Chronoamperometric studies confirmed an altered diffusion behaviour as a result of the porosity. Further, it alowed to estimate an increase in electroactive surface by more than two orders of magnitude.
The determination of capacitance via impedance spectroscopy generally confirmed previous results, with a largest capacitance assigned to the 20/10 ($t_{sep}/t_{sat}$) deposits.

The study of variable separation time at constant saturation time of 30 min aimed to provide a better understanding of the interplay of phase separation and foaming. The choice of saturation time followed the idea of solubilizing a maximum quantity of $scCO_2$ in the polymer, while allowing residual EGDA to diffuse into the $scCO_2$.
Peak values for height and for reconstructed volumes were observed for the 10/30 and 20/30 ($t_{sep}/t_{sat}$) deposits. Results for even longer seperation times indicated a detrimental effect on the structuration, yielded an insight into the time span required for the generation of structure of interest. However, it is not strictly equivalent to the end of the demixing process. The SEM image treatment allowed to assign smallest generated pores to the 20/30 ($t_{sep}/t_{sat}$) deposits, together with the smallest surface porosity.
The gravimetric capacitance increased by a factor of almost 40, exceeding literature values. Largest electroactive surfaces were found for 20/30 ($t_{sep}/t_{sat}$) electrodes.
The electroactive surface determined by chronoamperometry peaked at around 100 $m^2/g$ for the same electrode.
The corresponding normalized double layer capacitance in the impedance study was calculated to 4.9 $mF/cm^2$.
In conclusions, based on the generally improved results, longer saturation times of 30 min (under the experimental circumstances) are considered beneficial.

The interpretation of saturation temperature is based on the assumption, that the major phase separation is still ongoing after 10 to 20 min. This implies a potential overlap with polymer foaming. Both polymer phase separation and foaming are theoretically susceptible to temperature changes due to a different density of $scCO_2$ and the polymer's glass transition temperature.
Thinner deposits were recovered for elevated saturation temperature, particularly for $t_{sep}$ of 0 min, indicating the formation of smaller pores and/or less overall porosity. Together with the general absence of the membrane-like top layer, which suggested slower demixing, the observations align with reduced $CO_2$ density at higher temperatures.
SEM images yielded lower surface pore counts, increased pore size and slightly larger areas covered by pores, compared to lower saturation temperature.
The maximum capacitance was slightly smaller for higher saturation temperature, equally aligning with larger pores and a resulting smaller specific surface area. Literature suggests a reduced viscosity of the polymer to be a factor for pore growth. Faradaic current

studies emphasized thin-layer diffusion, in particular for the electrode 20/30 ($t_{sep}/t_{sat}$). Smaller electroactive surfaces compared to lower $T_{sat}$ were confirmed by chronoamperometry. The impedance studies lead to interesting observations, consisting in an extended low-impedance resistive region at high frequencies and a more ideal character of the capacitance.

A difficulty arose from the unknown ink composition, specifically regarding the content of polymeric binder. Complex diffusion and convection mechanisms reportedly play a role in phase separation. Besides, different compositions of the ternary system can undergo different types of demixing, resulting in the formation of different structures. In this context, the study of ink dilution provided a means to estimate the effect on the phase separation mechanism.
For high ink dilution, deposits were very filigree, but fragile. As expected, the lower overall solid content of the ink lead to reduced interconnectivity of the structure. The visual impression supported the idea of kinetically driven, fast phase separation.
Lower height and volume of deposits was assigned to low ink dilution, in which case thermodynamically driven demixing was suspected to dominate the structural generation. Homogeneous surfaces of uniform structure were obtained.
Highest surface porosity and largest pore diameters were determined for electrodes corresponding to dilutions 3:7 and 4:6 (ink:EGDA).
Aligning with the volume generation, capacitances extracted from cyclic voltammorgams generally increased with ink dilution. Faradaic current studies underlined thin layer-type diffusion to play a role particularly for moderate ink dilution. Electroactive surfaces were estimated to be largest. The trend was confirmed by chronoamperometry, with an increased quantitative estimation up to 122 $m^2/g$ for dilution 4:6 (ink:EGDA). The double layer capacitance determined via impedance spectroscopy peaked for dilutions 3:7 and 4:6 (ink:EGDA), however, the trend was incoherent with the study of capacitive currents.

The influence of process pressure was not experimentally investigated. Literature suggests to study its relevance for each particular ternary system, yet general observations were reported. Reduced pressure[29], allowing for slow demixing, favours the generation of a homogeneous structure without thin membrane-like top layers. Foaming, on the other hand, is thought to potentially benefit from increased $CO_2$ pressure. Literature, however, doesn't provide a clear conclusion on this aspect, as mentioned previously in the introduction.
The rate of depressurization is considered to be a parameter of higher importance. In reference works, faster rates favoured the creation of higher pore densities and smaller pore diameters.

The study of process parameters allowed to identify an optimum structuration protocol for the functionalization of electrodes. In particular, 20 min separation time, 30 min saturation time and a saturation temperature of 40 °C were paired with ink of dilution 4:6 (ink:EGDA). The criteria for decision were surface homogeneity of obtained deposits and the development of specific and electroactive surface, as well as mechanical integrity. It was observed, that the moderate factors of ink dilution allowed to no longer apply the thin layer of undiluted ink, which previously served for promoting adhesion to the diluted ink. For a future continuation of studies, this allows removing one factor of uncertainty from the the interpretation of results.

Some questions remained unanswered, e.g. regarding the optimization of phase separation and foaming processes. Literature suggested to operate at a two-step pressure

[29] 8 MPa in comparison with the references is considered low.

protocol, in addition to the two-step temperature protocol. This modification could allow to precisely create bimodal structures, in which pores could support either diffusion or charge storage.
To further evaluate the structural generation, the study of cross-sections is considered essential and requires adapted techniques.
For precise studies on the structural generation, simulation of thermodynamic and kinetic demixing could compensate for the time-intensive experimental work. However, the detailed knowledge of thermodynamic basics and particular information of the system under investigation, such as diffusion coefficients, solubility parameters and interaction with the conductive particles is not to be underestimated.
To confirm the presence of residual EGDA, an additional chemical analysis technique is to be added to the protocol.

# Chapter IV

# Hydrogen peroxide sensing

After having demonstrated the controlled structuration of carbon ink by means of supercritical $CO_2$, chapter IV investigates the transfer of technology towards practical applications.
Hydrogen peroxide sensing has been of high interest since early sensor development and it is an established application in amperometric sensing. For an exemplary study, different types of hydrogen peroxyde sensors were prepared and evaluated regarding key sensor characteristics which are stability, sensitivity, limit of detection and stabilization time. The outline of this chapter is as follows (see Figure IV.1).

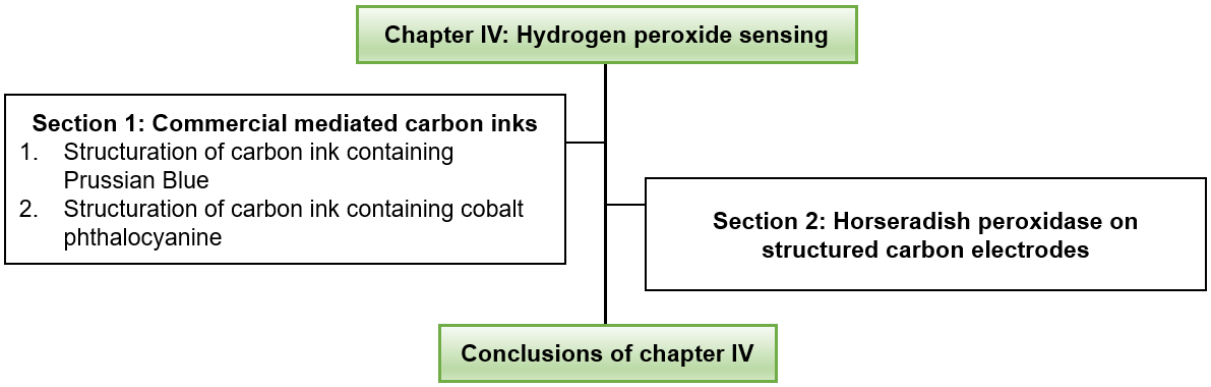


Figure IV.1: The schematic structure of chapter IV on hydrogen peroxide sensors.

A brief introduction to hydrogen peroxide sensors is given in section one, explaining the operational mechanisms and listing some of the relevant work for a comparison.

Section two covers sensors based on a commercial mediated carbon ink, which was subjected to the optimized supercritical $CO_2$ structuration treatment. In particular, the mediator Prussian blue was in focus, which is of common use in the preparation of hydrogen peroxide sensors.

A different approach to hydrogen peroxide sensing was studied in section two, by functionalizing the structured carbon electrodes with the enzyme horseradish peroxidase. The particular class of biosensors is well-reported in literature and allowed for a comparison of the structured electrodes.

The chapter closes with a conclusion on the studies with the aim to determine the utility of the structured carbon electrodes in different types of hydrogen peroxide sensing applications.

## 4.1 Introduction to hydrogen peroxide sensing

Hydrogen peroxide ($H_2O_2$) is a chemical used in high concentration as industrial bleaching [156] and cleaning agent [157] and at lower concentrations as antiseptic [158]. In the human organism, it is known to participate in brain-cell signaling [159] and cell metabolism. However, it can be cytotoxic as a result of the imposed oxidative stress [160] and recent studies link it to the development of insulin-resistance [161].
Classical analytical techniques for determining $H_2O_2$ concentrations in samples comprise e.g. fluorimetry [162] and colorimetry [163], which generally require complex equipment and long analysis times. Electrochemical methods are considered less time consuming, less costly[1] and compatible with portable devices due to the potential of miniaturization. While the overpotentials, required for the oxidation of $H_2O_2$ on unmodified carbon electrodes, are relatively large and thus disadvantageous for amperometric sensing in complex media, the chemical modification of electrodes represents a useful solution.

## 4.2 Commercial, mediated carbon ink containing Prussian blue

Enzymatic biosensors have been the subject of many studies, but require special attention during preparation, use and storage due to lack of enzyme stability. Therefore, enzyme-free $H_2O_2$ sensors have attracted a particular interest due to their long-term stability and relative ease of preparation. The structuration of commercial carbon inks containing redox mediating species was considered a close adaptation of the previous experiments.

### 4.2.1 The reduction of hydrogen peroxide on Prussian blue

Prussian blue (PB), or ferric hexacyanoferrate (II), was discovered to have catalytic properties in the reduction of $H_2O_2$ by Itaya et al. [164] and has since been frequently used for the amperometric detection at potentials around 0 V vs. Ag/AgCl RE. In particular, the reduced form of PB, Prussian white (PW), catalytically reacts with $H_2O_2$ to PB and hydroxide ions. PB is then electrochemically regenerated on the electrode according to the equations below IV.1 [165] and IV.2 [164]. The schematic reduction and regeneration was visualized by Cinti et al. [16], see Figure IV.2.

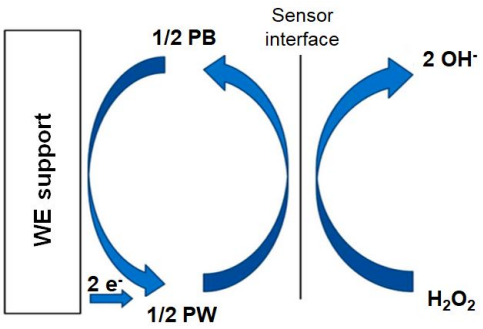


Figure IV.2: The mediated reduction of hydrogen peroxide on prussian blue, which is electrochemically regenerated; Figure adapted from [16].

[1] An exception may be the use of platinum electrodes to reduce $H_2O_2$.

$$Fe_4^{III}\left[Fe^{II}(CN)_6\right]_3 + 4e^- + 4K^+ \leftrightarrow K_4Fe_4^{II}\left[Fe^{II}(CN)_6\right]_3 \quad \text{(IV.1)}$$

$$K_4Fe_4^{II}\left[Fe^{II}(CN)_6\right]_3 + 2H_2O_2 \rightarrow Fe_4^{III}\left[Fe^{II}(CN)_6\right]_3 + 4OH^- + 4K^+ \quad \text{(IV.2)}$$

The electron transfer is accompanied by the intercalation of cations in the crystalline structure of PB [166], which is of potential interest at a later point.

In the past, the mediator has typically been deposited or immobilized on the working electrode via the chemical reaction of precursors, forming PB directly on the surface of WE, or via electrochemical methods. Alternatively, it can be incorporated in the WE material.
Table IV.1 presents a selection of works on carbon-based $H_2O_2$ sensors with incorporated PB in the first section. Regarding the work of McBeth et al., it is pointed out, that the communicated sensitivity does not seem to match the reported results. A revision of the paper (see the description below the table) leads to a value similar to what was reported by Chmayssem et al. and others.

Table IV.1: Hydrogen peroxide sensors prepared based on carbon ink electrodes containing Prussian blue.

| **WE** | **Lin. range (µM)** | **LOD (µM)** | **LOQ (µM)** | **Sensitivity (nA/ µM mm$^2$)** | **Medium (pH)** | **$E^{\star}_{app}$ (V)** | **Ref.** |
|---|---|---|---|---|---|---|---|
| Gwent P2 ink | 0.9-200 | 0.5 | 0.9 | -1.72$^{\dagger}$ | CMEM (7.4) | -0.10 | [165] |
| Gwent P2 ink | 100-400 | 8.0 | - | -1.43 | PBS (7.4) | -0.05 | [167] |
| PB in carbon ink | 0.5-1000 | 0.3 | - | 1.35 | PBS + KCl (6.0) | -0.05 | [168] |
| PB in carbon ink | 0.5-5000 | 0.5 | - | 4.25 | PBS (6.0) | 0.00 | [169] |
| PB in carbon ink | 0.4-100 | 0.4 | - | -1.37 | PBS (7.4) | 0.00 | [170] |

**CMEM**: Serum supplemented Eagle's medium; * Despite the communicated value of 27 µA/µM mm$^2$ the displayed calibration curve displays a drop of 2 µA over 200 µM $H_2O_2$ for an electrode surface of 5.81 mm$^2$, yielding 1.72 nA/µM mm$^2$; **PBS**: Phosphate Buffered Saline; $^{\dagger}$: potentials refered vs. Ag/AgCl, 3 M KCl.

#### 4.2.1.1 Electrode preparation and characterization

Carbon-graphite ink (C2070424P2, Gwent, UK) containing Prussian Blue is in the following referenced as "P2-PB" ink. While the exact ink composition and polymer content are unknown, the technical data sheet reports a solid content (at 130 °C) of 42-43 %, which generally corresponds to the previously studied carbon ink.
In consequence, the optimum structuration protocol detailed previously was applied on 1.3 µL of diluted ink in ratio 4:6 w/w (ink:EGDA). An oxygen plasma treatment (450 sccm, 200 W, 20 s) proceeded the structuration due to displayed hydrophobic behaviour.

The characterization techniques presented in the context of carbon ink were employed and materials or parameters are not specified in again, as long as they remained the same. The basic characterization comprised scanning electron microscopy, cyclic voltammetry and electrochemical impedance spectroscopy.

An exception consists in the electrode/sensor calibration, which was carried out in amperometric mode in a three-electrode cell with a Pt-CE and a Ag/AgCl RE (3 M KCl) at small negative applied potentials[2], generally -44 mV. Electrodes were left for typically

[2]In order to avoid the oxidation of electrochemically interfering compounds in complex organic/physiologic media, the choice of a small working electrode bias is beneficial. The effect of the applied potential was for example studied by Moscone et al. [169].

around 20 min, but up to several hours in some cases, to obtain a stable base-line current. From 30 % hydrogen peroxide (PERDROGEN, Sigma-Aldrich), solutions of 8.821 mM were freshly prepared by diluting with 1 x PBS and added stepwise to 40 mL 1 x PBS base electrolyte (pH 7.3). The waiting time between additions varied between 3 to 10 min depending on the added amount of peroxide solution in order to guarantee for a stable signal. After each addition, the electrolyte was stirred for 10 s to accelerate the diffusion of peroxyde.

X-Ray photoelectron spectroscopy was carried out by Lukasz Borowik from the nanocharacterization platform at CEA-Leti. The instrument (PHI 5000 VersaProbe II) was equipped with a monochromatic Al K$\alpha$ source (h$\nu$=1486.6 eV) with a spot size of 200 µm. The energy resolution of the high-resolution spectra is 0.8 eV. The samples/ ink deposits were prepared in equivalent manner to the SEM samples.

## 4.2.2 Results and Discussion of structured Prussian Blue ink

### 4.2.2.1 Scanning Electron Microscopy

To confirm the effect of the scCO$_2$-treatment, SEM images of dried (3 h, 80 ℃, "R80") and structured ($t_{sep}/t_{sat}$ = 20/30)[3] ink deposits are compared in Figure IV.3 with different factors of magnification in series 1 to 3. Dried, non-structured deposits, series a), are compared to structured deposits, series b). By breaking the deposit and carefully placing a fragment on a suitable support (previously impeded due to the discussed sample fragility), it was possible to prepare a transversal image of the structured deposit, see series c).

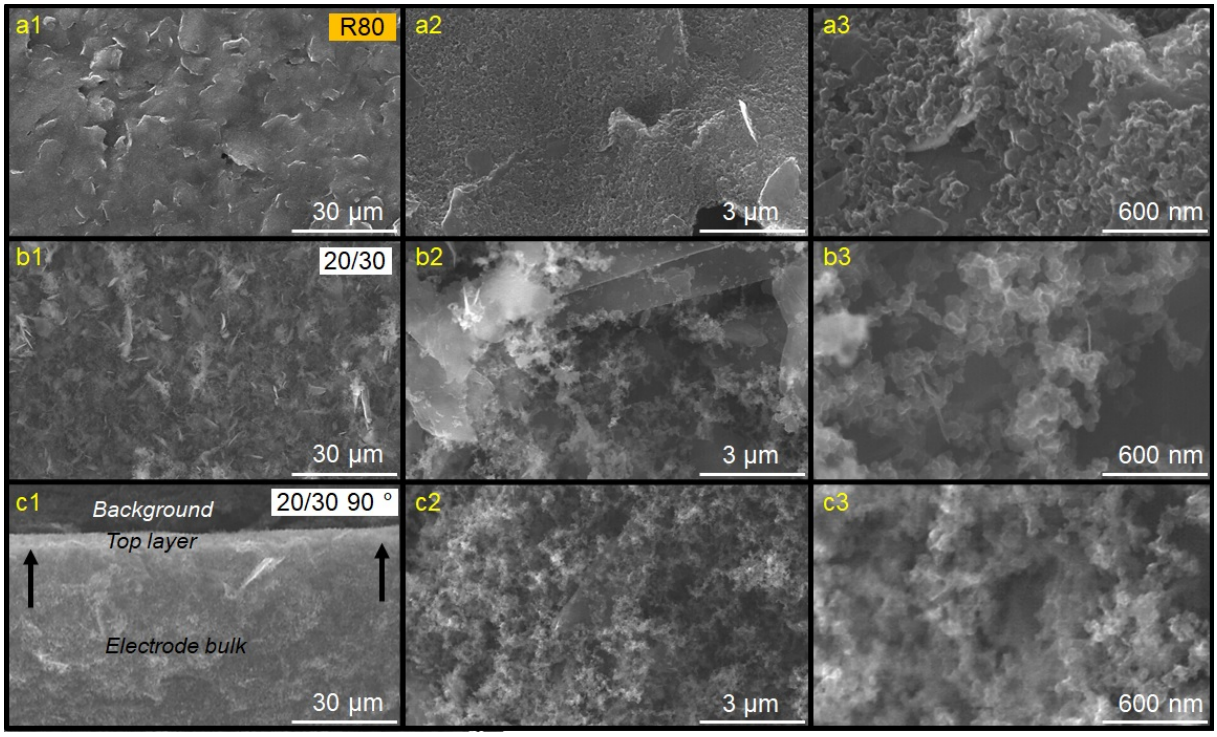


Figure IV.3: SEM images of a) dried (80 ℃, 3 h) and b) structured P2-PB ink deposits ($t_{sep}/t_{sat}$ = 20 min/30 min, $T_{sep}/T_{sat}$ = 23 ℃/40 ℃, ink:EGDA = 4:6 (w/w)); c) a transversal fracture with arrows indicating the location of the membrane-like top layer.

[3]The structuration parameters and ink dilution were set to match the optimized protocol.

Opposed to dried BQ242 ink, the surface of non-structured R80-P2-BQ deposits is structured differently and presents itself flat at comparable magnification. The pronounced features in Figure IV.3 a1) and a2) are thought to correspond to graphite flakes and indicate an approximate size of 10 to 30 µm. Very few pores/cavities in the range of several microns are visible. At high magnification, Figure IV.3 a3), agglomerates of on average 100 µm become observable, covering the flakes. Presumably, these are composed by polymeric binder and smaller carbon particles, such as carbon black. A visual similarity compared to BQ242 ink is noted.
In top-view, the structured deposits display a similar surface structure, as BQ242 carbon ink. Particularly, a higher visual presence of spike-shaped features is observed. Taking images at higher magnification into consideration, these could be explained by differently oriented graphite platelets. The filigree structure decorating the flakes allows distinguishing pores in the sub-micron range.

The transversal images provide an insight into the generation of bulk structure. A membrane-like surface layer is indicated in Figure IV.3 c1). In comparison to the electrode bulk, the higher image contrast suggests a different composition of the material, which may be in agreement to literature, discussed previously in the context of phase separation. In this case, it is of approximately 10 µm in thickness. Visually, a good connection with the underlying bulk material is noted. The magnification of the bulk provides a comparable porosity as encountered on the deposit surface, but with a higher degree of homogeneity. The SEM images suggest a structural generation by phase separation and foaming as observed before, although further studies are required to validate the effect of changing process parameters.

#### 4.2.2.2 Cyclic voltammetry

Cyclic voltammetry was performed on an unstructured R80-P2 electrode at 50 mV/s scan rate in 1x PBS. The $5^{th}$ cycles of an electrode without and with plasma-treatment (450 sccm, 200 W, 20 s) are displayed in Figure IV.4. It is pointed out, that CV of Prussian Blue generally display a different shape, depending on the electrolyte. The recorded curves match what is referenced for phosphate buffers [171] [165]. A particular resemblance to the CV of screen-printed P2 ink in PBS, published by Chmayssem et al., is pointed out [167].
Further, the choice of the potential window scanned during the measurement limits the observed response of the system to the oxidation of Prussian White to Prussian Blue, explaining the observation of only one redox reaction in the chosen potential window[4].
The presence of two sets of oxidation/reduction peaks in phosphate buffer may originate from the different complexation of hexacyanoferrate in electrolytes with varying potassium concentrations or potentially the presence of NaCl [172].

A qualitative comparison of the curves allows distinguishing an increased pseudocapacitive character for the plasma-treated electrode. The increase in peak current for plasma-treated electrodes is around 4. The trend generally matches observations made for plasma-treated carbon ink. In addition, the Faradaic currents, i.e. peak currents, are of increased height, suggesting a larger electroactive surface area.

[4] A third state of the system is reached via the oxidation of Prussian Blue to Berlin Green at higher anodic potentials

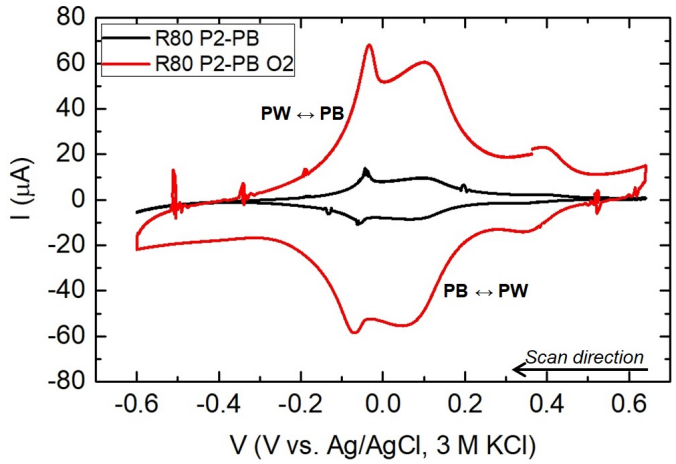


Figure IV.4: Cyclovoltammetric responses ($5^{th}$ cycles) of a non-structured P2-PB electrode, cycled at 50 mV/s in PBS (1x, pH 7.0) before and after oxygen-plasma treatment. Onset at 0.4 V.

Cyclic voltammetry of non-structured R80 and structured 20/30 ($t_{sep}/t_{sat}$) electrodes was repeated in 1 x PBS for comparison.
The response of the non-structured electrode is diplayed in Figure IV.5 a) before, after one and after two protocols of $H_2O_2$ additions ("post CA"). A relatively small capacitive component is distinguishable next to the response of the PB system, which displays the two pairs of redox transitions. The potential scan range was kept rather small, as larger potentials are known to decompose the mediator.
The peaks attributed to the PB/PW transition are increased after the first and again after the second protocol of $H_2O_2$ additions. Interestingly, the inverse was expected due to the degradation of PB in presence of elevated $H_2O_2$ concentrations. Therefore, the observation is associated with an increased specific surface, possibly due to mild surface etching. The removal of polymer and residual contamination from the electroactive sites was proposed by McBeth et al. [165], explaining the higher currents.

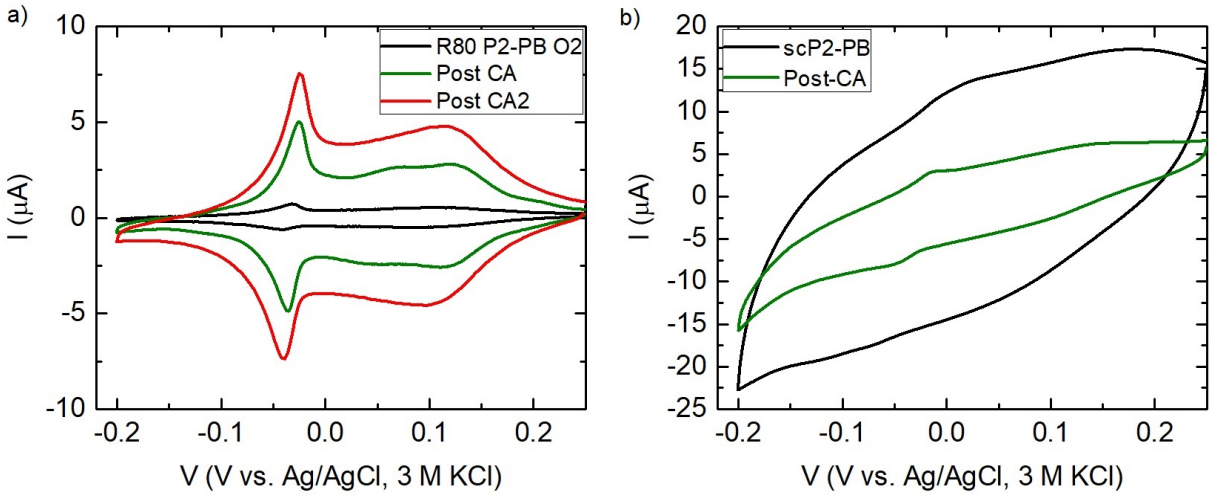


Figure IV.5: Cyclic voltammetry in 1 x PBS (pH 7.4) on a) non-structured R80-PB and b) structured P2 ink (20/30 protocol) before and after carrying out hydrogen peroxide additions to characterize the electrodes. $5^{th}$ cycles are displayed. Onset at -0.2 V.

In Figure IV.5 b), the response of a structured electrode is shown. The initial state is compared to one protocol of $H_2O_2$ additions.
For the fresh electrode, the increased (pseudo-)capacitive response is noticed and linked to the structuration, as earlier. Relative to the non-structured electrode, the peaks of the PB/PW transitions appear to some extent smaller, wider and shifted by around 0.04 V. The larger overpotentials, required for oxidation and reduction to occur, are again explained by the potentially increased inter-particle resistance of the carbon species.
After one protocol of $H_2O_2$ additions, the recorded CV is altered and in particular suggests a less pseudo-capacitive character. As before, mild surface etching is proposed as explanation.

#### 4.2.2.3 Electrochemical impedance studies

Impedance spectra were recorded in 2 mM ruthenium hexaamine (II) at the half-wave potential of the redox probe. Figure IV.6 shows the a) Nyquist and b) Bode plots of electrodes in initial state and after one and two protocols of $H_2O_2$ additions.

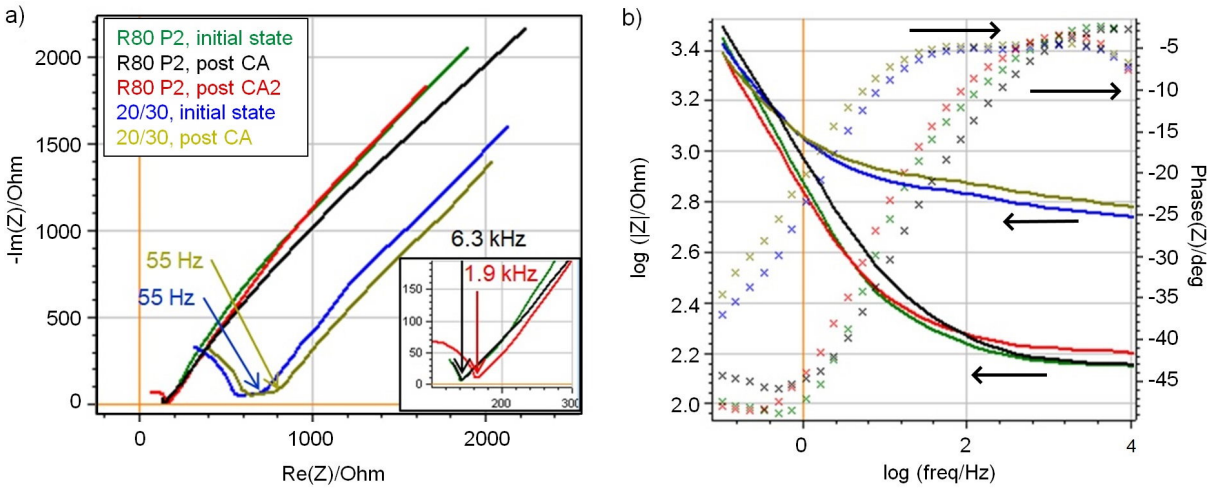


Figure IV.6: Impedance spectra of non-structured (R80) and structured (20/30) P2-PB ink electrodes in 1 M KCl, 2 mM ruthenium hexaamine (II) at $E_{1/2,RHT}$ of -180 mV; a) Nyquist and b) Bode plots. The data correponds to electrodes before and after protocols of $H_2O_2$ additions (post CA).

The Nyquist plots display partial semi-circles, which cross the y-axis, when extending the data points, which is supposedly due to the response of the electrical connections.
Unstructured electrodes present no distinguishable R/C semi-circle at high-frequencies, which confirms observations for carbon BQ242 ink. In consequence, low charge transfer resistance and low series resistance are assigned. In the Bode plots, the high-frequency region from 10 kHz to 1 kHz correspondingly shows a plateau at relatively low impedance with a phase angle smaller than 10 °. The cut-off frequency associated with the double layer capacitance is located at around 100 Hz. For lower frequencies, a Warburg-type contribution to the impedance is indicated by a phase angle of 45 ° and is seen as a sign of linear, semi-infinite diffusion. The interpretation matches the impression obtained from SEM images, which present a macroscopically flat surface.

The structured electrodes distinguish themselves by a different behaviour. In particular, an increased series resistance and charge transfer resistances is noted, matching the interpretations of CV. In the Bode plots, a corresponding high-frequency plateau

is present at higher impedance. According to earlier observations on structured BQ242 carbon ink, the plateau is extended over a larger range of frequencies. The phase angle remains smaller, than 10 ° from approximately 10 to 1 kHz and is rather constant over two orders of frequency. It is mentioned, however, that the plateau is less flat, than for unstructured electrodes. This may arise from the suspected pseudo-capacitive character and matches the slightly higher phase angle, associated with the plateau.
The cut-off frequency of the double layer capacitance is located at approximately 10 Hz. For lower frequencies, the electrodes display a slope of around 45 ° in the Nyquist plot, however the Bode plots suggest some deviation from Warburg-type impedance, as the phase angles remain smaller than 45 °.
Overall, a characteristic response was observed for both non-structured and structured P2 ink, with matching tendencies compared to BQ242 carbon ink. The presence of the redox mediator potentially contributes to the overall less capacitive and more resistive behaviour of electrodes.

After the addition of $H_2O_2$, the spectra in Nyquist plots for both unstructured and structured electrodes are slightly shifted towards higher series resistance. Together with the small changes in the Bode plots, this may express the decomposition of PB.

#### 4.2.2.4 Protocols of hydrogen peroxide addition

Figure IV.7 displays current responses for selected electrodes during the stepwise addition of $H_2O_2$ for a small negative WE bias. The current spikes are a consequence of the agitation following the additions and may be linked to the disturbance of the local charge equilibrium at the electrode interface.

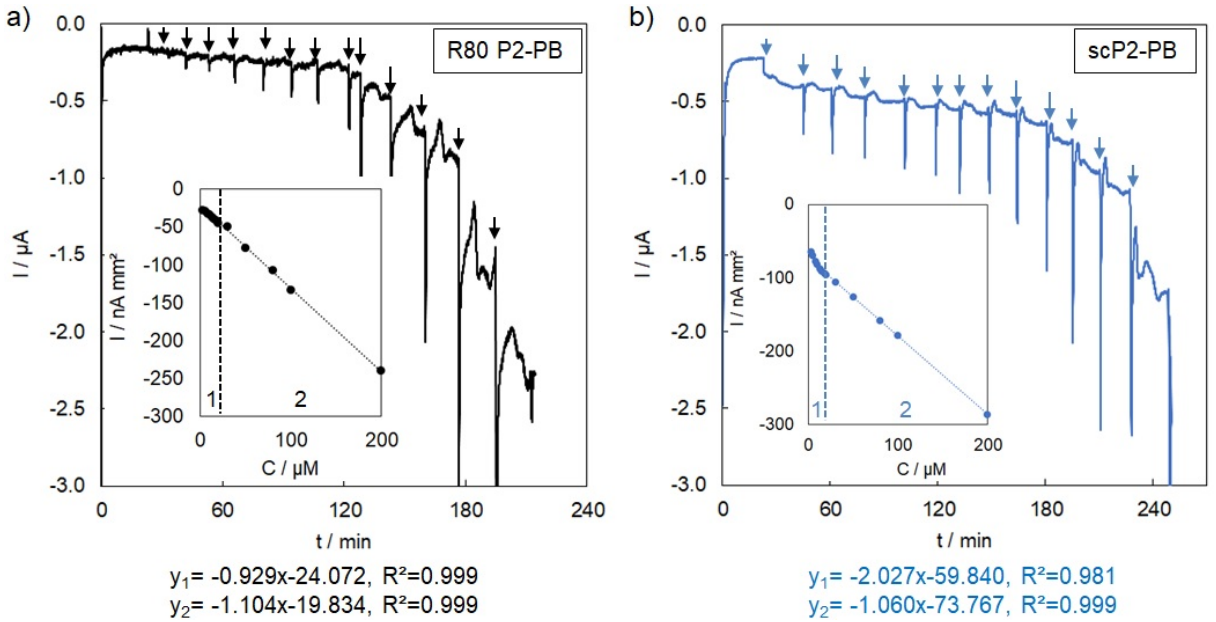


Figure IV.7: Characterization of a) non-structured and b) structured P2-PB ink electrodes during stepwise addition of hydrogen peroxide at -44 mV WE bias. The arrows indicate the additions to concentrations of 5, 8, 10, 13, 15, 18, 20, 30, 50, 80, 100, 200 µM $H_2O_2$. Calibration curves are added to the plot, with two regions of different slope.

For structured electrodes, a longer current stabilization time was generally observed, suggesting a link to diffusion and migration of analytes and ions into the porous bulk structure. The wave-like stabilization pattern is thought to originate from the agitation

of the solution after each addition. Eventually, diffusion and migration may play a role, as well as the temporal disbalance of the local charge equilibrium at the interface.
The corresponding calibration curves are presented in the plots, normalized to the geometric electrode surfaces. The sensitivity of the electrodes is extracted from the slopes, which were subjectively divided into two concentration ranges in order to assure a more linear fit (smaller and larger than 20 µM $H_2O_2$).

The results of electrode characterization are listed in Table IV.2 for different P2-PB ink-based electrodes. Extracted results include the background noise, $E_{appl.}$, the limit of detection (LOD) based on a signal-to-noise ratio[5] of 3 and the sensitivity to $H_2O_2$.
Besides for the initially indicated structuration and characterization protocols, several different electrodes were prepared for studying the effects of ink dilution and applied potential $E_{appl.}$. No particular difference was observed, in comparison with the optimum protocol[6] and in consequence, corresponding electrodes are not further discussed.

Table IV.2: Selected results of the characterization of P2-PB electrodes with values for non-structured electrodes in the upper section and for structured electrodes in the lower section. The optimum protocol was applied for two similar ink dilutions 3:7 and 4:6.

| **Electrode** | **PTS** | **WE bias (mV)** | **Noise (nA)** | **LOD (µM)** | **Sensitivity < 20 µM (nA/µM mm$^2$)** | **$R^2$** | **Sensitivity > 20 µM (nA/µM mm$^2$)** | **$R^2$** |
|---|---|---|---|---|---|---|---|---|
| R80 | VMP-300 | -44 | 15 | < 13 | -0.814 | 1.000 | -0.867 | 0.984 |
| R80 | VMP-300 | -44 | 30 | 20 | -1.230 | 0.999 | -0.945 | 0.669 |
| R80 | VMP-300 | -44 | 15 | 8 | -1.095 | 1.000 | -0.984 | 0.993 |
| R80 | PS-4 | -44 | 3.5 | < 5 | -0.672 | 0.998 | -1.040 | 1.000 |
| $scCO_2$, 3:7 | VMP-300 | -44 | 3 | < 5 | -0.849 | 0.970 | -0.900 | 0.829 |
| $scCO_2$, 3:7 | VMP-300 | -44 | 3 | 15 | -0.214 | 0.956 | -0.235 | 0.962 |
| $scCO_2$, 4:6 | VMP-300 | -44 | 8 | 3 | -1.089 | 0.996 | -1.884 | 0.973 |
| $scCO_2$, 4:6 | PS-4 | -44 | 0.1 | < 5 | - | - | -0.152 | 0.905 |

Potentiostats (PTS): BioLogic VMP-300 and PalmSens-4 (PS-4)

Noise levels for non-structured electrodes were in the range of 10 to 30 nA (average of 14.7 nA), compared to 0.5 to 8 nA (average of 2.4 nA) for structured electrodes. The structuration appeared to have a beneficial effect on the reduction of noise, eventually due to the capacitive electrode nature acting as "dampener" for interfering signals. Alternatively, the orientation of graphite flakes could play a role, as a work of Lee et al. on carbon nanotube networks suggests [173]. However, further investigation is required to verify, which mechanism applies in this case.
The limit of detection was between 5 to 20 µM for non-structured electrodes (average of 10.6 µM) and reduced to 2 to 15 µM for structured electrodes (average of 7 µM). A potential explanation is the reduced noise level, besides the potential creation of more electroactive sites, leading to increased signals.
The sensitivity of non-structured electrodes is estimated as -99 nA/µM cm$^2$ over the entire concentration range up to 400 µM and to -94.6 nA/µM cm$^2$ below 20 µM of hydrogen peroxide. In contrast, -55.6 nA/µM cm$^2$ were determined over the entire concentration range for structured electrodes and -58.6 nA/µM cm$^2$ for lower concentrations below 20 µM.
In conclusion, the sensitivity of structured electrodes was surprisingly reduced, in combination with generally longer stabilization times. Possible explanations include a reduced accessibility of electroactive sites, an insufficient charge transfer between PB and the

[5] A misconception found in literature was adopted, instead of determining the LOD via 3.3 sigma/slope.

[6] The optimum structuration protocol was based on ink dilution in ratio 4:6 w/w (ink:EGDA), $t_{sep}/t_{sat}$=20/30 (min/min) and -44 mV bias

carbon particles and the initial low presence of mediator. As Prussian Blue is soluble in aqueous solutions, some degree of dissolution in EGDA is possible[7]. Another potential interaction arises from the quadrupole moment of $CO_2$. In conclusion, the partial dissolution and extraction of Prussian blue during the structuration cannot be excluded.

#### 4.2.2.5 Mediator loss investigated by X-Ray photoelectron spectroscopy

In the following, X-Ray photoelectron spectroscopy was carried out. As Prussian Blue contains both nitrogen and iron, these elements were considered to be characteristic and their relative presence was seen as a means to confirm the mediator loss. Referenced binding energies were looked up in literature to interpret the provided results [174].
Survey scans are displayed in Figure IV.8 for a) the unstructured and b) the structured deposit. High-intensity signals are the O1s (≈ 530 eV) and the C1s (≈ 285 eV) core level peaks, which are accompanied by Auger peaks at higher binding energies. It is interesting to note, that the signal of highest intensity for the non-structured sample corresponds to C1s, while the O1s peak is second highest. The structured sample displays an inverse order. One hypothesis consists in the assumed higher quantity of polymer near the top layers, eventually contributing to more oxygenated surface functionalities.
A general observation is the larger intensity, increased by a factor of three, linked to the unstructured sample. The difference suggests changed material characteristics and similar observations were in the past observed for porous samples [175].
Surprisingly, both spectra display characteristic chlorine peaks (Cl2s ≈ 271 eV, Cl2p ≈ 200 eV) of low intensity, which is regarded as potential contamination. The samples were never in contact with PBS, however. Furthermore, low-intensity silicon-related peaks (Si2s ≈ 151 eV, Si2p ≈ 99 eV) are equally attributed to contamination, eventually originating from the sample supports, which consisted in pieces of gold-sputtered silicon wafer.

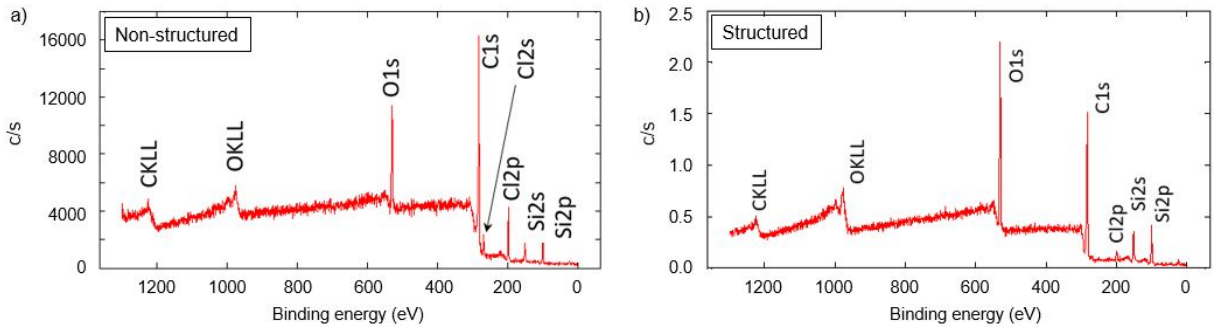


Figure IV.8: XPS survey scans of a) non-structured and b) structured P2-PB ink deposits. Results were provided by Dr. Lukasz Borowik (LEA-Leti/PFNC). An AlK$\alpha$ source with a spot size of 200 µm was used.

High resolution spectra of O1s, Fe2p3/2, C1s and N1s are depicted in Figure IV.9, despite the visual absence of iron and nitrogen-related peaks in the survey scans.
The shape of the O1s core-level peaks is identical for both samples and its location at a binding energy 530 eV shifted by 1 eV according to literature (531 mV in [174]). However, no characteristic compound type is referenced for this value.
The Fe2p3/2 spectra indicate a low intensity peak arond 706 mV, which is equally shifted by 1 eV, compared with literature (707 eV [174]). The 1 eV difference is potentially arising from the equipment or an erroneous calibration, respectively. The intensity of iron,

[7]The polar and hydrogen Hansen solubility parameters of water and EGDA are rather different, however the dipolar component is similar, see [20]

based on comparing the intensities of high-resolution scans, was estimated to correspond to a concentration inferior than 1 % on the sample surface. For the structured sample, barely any peak is distinguishable against the background, which is a sign of the absence of the mediator on the surface.
The C1s peak suggests a different deconvolution for non-structured and structured samples with at least three main contributions. An estimative assignment is presented here. According to the binding energies, the main contribution (1) originates from carbides. This is unexpected, since the carbon ink should rather present a main contribution from C-C bonds. Specifically as a miscalibration of the equipment was already mentioned, the main response is therefore linked to C-C bonds ($\approx$ 284.5 eV, shifted by +2 eV) and the other peaks are assigned correspondingly. Peak (2) then indicates C-O bonds ($\approx$ 286.5 eV, +2 eV) and peak (3) is based on C=O bonds ($\approx$ 288.2 eV, +2 eV).
The N1s core level scans are of relatively low intensities and, after shifting the spectrum of the non-structured electrode by 2 eV to higher binding energies (not displayed), show a corresponding position of the principal peak for both samples. For the non-structured sample, a broad peak from approximately 395 to 400 eV is expressed, which, after correction for the suspected shift, matches relatively well to the binding energy of cyanides which is referenced between 397.5 and 400.5 eV and in accordance with the chemical nature of Prussian Blue (ferric hexacyanoferrate (II)) [174]. No explanation is found for the distinct peak around 395 eV. In comparison, the structured sample presents only traces of the compound assigned to cyanides, which matches the lower intensity of Fe2p3/2.

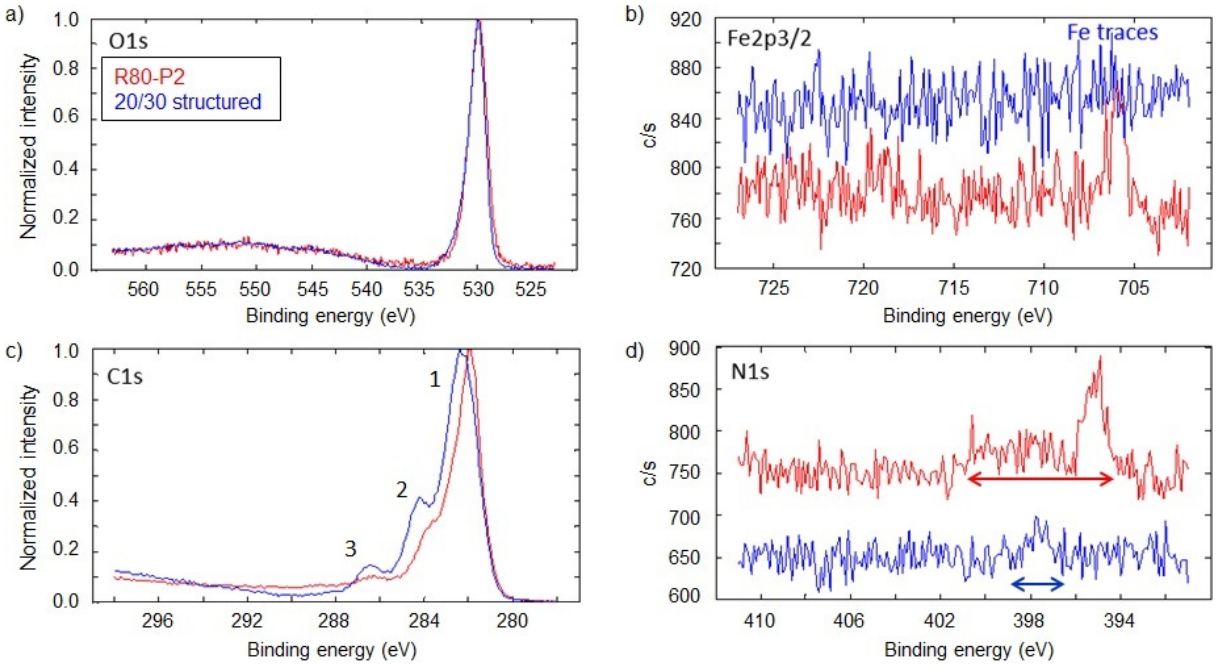


Figure IV.9: High resolution scans of a) O1s, b) Fe2p3/2, c) C1s and d) N1s on non-structured (red) and structured (blue) ink deposits. Results were provided by Dr. Lukasz Borowik (CEA-Leti/PFNC). An AlK$\alpha$ source with 0.8 eV energy resolution was used.

The different intensities of Fe2p3/2 and N1s in the spectra of the structured sample can be explained by either the preferential incorporation of Prussian Blue in the bulk, instead of the surface, the coverage by polymer with a resulting inaccessibility or the partial dissolution during structuration as explained before.

## 4.3 Enzymatic reduction of hydrogen peroxide

The mediatorless reduction of $H_2O_2$ on carbon electrodes has been realized by means of enzymes which can catalyse the reduction or oxidation. Otherwise, which rather large overpotentials would be required, as was stated before. Peroxidase enzymes in particular have attracted interest due to their selectivity, i.e. their specific reaction with substrates and the general possibility for undergoing a direct electron transfer with the transducer material [176]. One commonly reported drawback, however, linked to enzymatic biosensors in general, is the high mobility of enzymes which cause signal instability[8] [177].

The use of carbon-based transducers in enzymatic biosensors has in the past been studied for carbon black, carbon, graphite and carbon nanotubes, as specified in a review by Razulas et al. [178]. A specific benefit was associated with the possibility of electrode bulk modification [179]. In particular, the incorporation of enzymes into the carbon matrix was proposed, resulting in small distances between enzymes and the transducer. Principally, this step favours electron transfer between the two and, as a result of the enzymes' physical protection, increased stabilities were observed.
Here, the motivation of depositing a peroxidase is based on the idea to increase enzyme stability via its physical entrapment in the porous electrode structure. Further, the increased number of electroactive sites were thought to promote the electrochemical sensing properties, e.g. sensitivity. The enzyme horseradish peroxidase (HRP) was chosen due to its prominence in electrochemical application, implying a thorough base of literature for understanding the reaction mechanisms.

### 4.3.1 Introduction to horseradish peroxidase

Horseradish peroxidase has three metal centers, see Figure IV.10 a), two of which are calcium atoms and the third is an iron-heme group, whose chemical structure is displayed in b) [17] [18]. The iron center is considered available for the attachment of hydrogen peroxide and thus in central focus of the electrocatalytic activity.

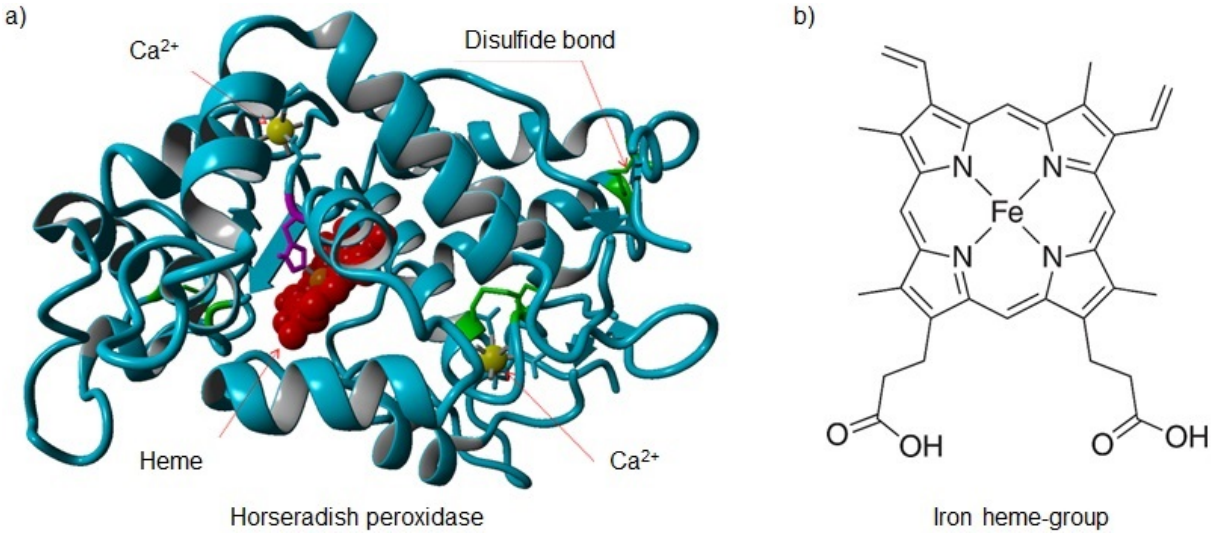


Figure IV.10: a) A visual representation of horseradish peroxidase, reproduced from [17] and b) the chemical structure of the iron heme-group, reproduced from [18].

[8]While this aspect initially motivated the research on enzymeless sensors, based e.g. on Prussian blue, recent advances in enzyme immobilization highlight the potential of biosensors.

While in literature, HRP has mainly been considered to be used for the electrocatalytic oxidation of phenolic substrates [180], the reduction of $H_2O_2$ is equally proposed. The mechanism is depicted in Figure IV.11 and involves a two-step reduction of the heme-group (compound-I, then compound-II), yielding ferriperoxidase. This reduced form is then oxidized by $H_2O_2$, which generates a water molecule, two protons and transforms the iron-heme group back to its initial state. The electrocatalytic cycle is closed by the transformation of ferriperoxidase back to HRP.

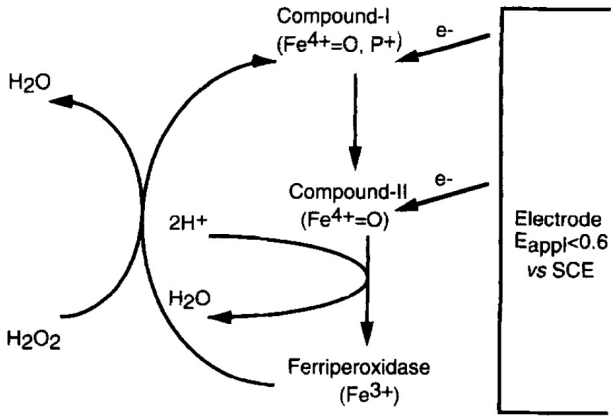


Figure IV.11: The mechanism of direct electrocatalytic reduction of $H_2O_2$ on an electrode modified with horseradish peroxidase. Figure reproduced from [19].

It is mentioned, that some of the reported electrode modifications by HRP rely on more complex mechanisms. For example, the use of coenzymes, e.g. phenolic compounds have been reported to accellerate the charge transfer coefficient [19]. Therefore, the discussed model presents only a very specific case.

### 4.3.2 Horseradish peroxidase on structured carbon electrodes

Generally, the catalytic activity of HRP can be transformed into an electrochemical signal by means of a mediator, e.g. hexacyanoferrate (II) [181], or via a direct electron transfer presented by Ruzgas et al. [19]. Specifically carbon electrodes have been studied as transducer material for peroxidase-modified electrodes.
Increased heterogeneous electron transfer rate constants have been associated with carbons exhibiting a high number of carboxylic groups. The beneficial influence on sensing performance was studied by Ruzgas et al. for edge-oriented pyrolytic graphite. It was suggested, that high sensitivity correlated with increasing fractions of carboxylic groups, which again is linked to the specific surface area (SSA). In some cases, sensitivity was only limited by the mass transport of peroxide and not the quality of charge transfer [19]. The idea of using high-SSA electrode materials was confirmed by Munge et al., who proposed using a structured CNT electrode as support for HRP deposition. The increased bioelectrocatalytic current of $H_2O_2$ reduction verified the interest in using structured or porous carbon materials [182].

A further advantage of structured biosensor electrodes is the enzymes' physical protection, which was in the past realized by immobilizing enzymes in polymer matrices. However, results revealed low sensitivities, which were explained by the diffusion-limit of the polymer membranes imposed on $H_2O_2$. Popescu et al. proposed to physically entrap the enzymes in microporous carbon, which lead to enhanced behaviour [183]. Eventually, the improvement was promoted in addition by the closer proximity of enzymes and

transducer in a confined space. Overall, the interest for structured, enzyme-functionalized carbon electrodes has been demonstrated.

The literature on porous carbon electrodes for non-mediated $H_2O_2$ sensing by means of physisorbed HRP presents itself rather scarce due to the high number of process variables. These include electrode material, the type of enzyme deposition/bonding and the type of electron transfer (mediated/non-mediated). Table IV.3 lists a selection of comparable works, including non-structured, functionalized carbon electrodes.

Table IV.3: Hydrogen peroxide sensors prepared based on carbon ink electrodes functionalized with horseradish peroxidase (HRP). Enzymes were adsorbed except when indicated else.

| **WE** | **Lin. range (µM)** | **LOD (µM)** | **Sensitivity (nA/ µM cm$^2$)** | **Medium (pH)** | **$E^{\star}_{app}$ (V)** | **Ref.** |
|---|---|---|---|---|---|---|
| HRP/CPE | 6.0-35.4 | 0.48 | 143 | PBS (5x, 7.0) | -0.35 | [184] |
| HRP/CPE | 10-11300 | 0.65 | 2.5[b] | 0.1 M CB (6.5) | -0.40 | [185] |
| HRP/porous CPE | 44-310 | 2.9 | 12.5[b], FI | 0.01 M KPB (5.0) | 0.00 | [186] |
| HRP-CPE | - | 0.1 | 78, FI | 0.1 M KCl (8.0) | -0.05 | [183] |
| HRP/CPE | 0.5-20 | low µM | 4, batch | PBS (5x,7.4) | -0.03 | [187] |
| HRP/porous graphene | 0.08-664 | 0.00003 | 74.3 | PBS (20x, 7.0) | -0.93 | [188] |
| HRP/CFT[f] | 0.1-3.0 | 0.08 | 392 | PBS (10x, 7.0) | 0.00 | [189] |
| HRP/nano-AU/CCPE | 12.2-2430 | 6.3 | 13 | PBS (6.7x, 7.0) | -0.90 | [190] |
| HRP/CMF-CNT/graphite[k] | $< 1000^b$ | - | 4500[b] | PBS (7.0) | -0.30 | [191] |

$^{\star}$ Potentials are referenced against Ag/AgCl, 3 M KCl; CPE: Carbon paste electrode; [a] HRP incorporated in carbon paste; [b] our (calculated) estimation; CB:citrate buffer; KPB: potassium phthalate buffer; FI: flow-injection mode; GN: graphene; CFT: carbon felt, chemisorbed enzyme; [f] mediated with 0.25 mM hydroquinone; CCPE: chitosan-entrapped carbon paste electrode; [k] CMF-CNT: carbon microfibers on carbon nanotubes; [l] covalently bound enzymes

### 4.3.3 Experimental approach

Non-structured carbon electrodes were prepared by drying DuPont BQ242 carbon ink (80 ℃, 3 h). The structured carbon electrodes were prepared according to the optimized preparation protocol[9], before undergoing a step of oxygen-plasma treatment (450 sccm, 200 W, 20 s). While this step was simply necessary to allow the aqueous enzyme solution to penetrate the structure, previous studies suggested the beneficial effect of creating oxidized surface functionalities. These were thought to promote specifically electrostatic interaction between graphite edge-planes and enzymes, thus enhancing heterogeneous electron transfer rate constants [192].
HRP solutions (10 mg/mL) were freshly prepared by dissolving the enzyme (Sigma, CAS 9003-990, 150-250 u/mg) in PBS (10x) and waiting for several minutes for homogenization. Then, electrodes were functionalized by drop-casting 4 µL of HRP solution on each structured carbon electrode of the PCB, statistically corresponding to 6-10 units per electrode[10]. The electrodes were covered and left overnight at 4 ℃ for the enzymes to adsorb, as carried out in other works [183]. The characterization was carried out using the three-electrode setup used previously. The OCP of as-prepared electrodes were measured during 15 min in PBS (1x, pH 7.4). This step equally served to rinse any excess enzymatic solution off the electrodes. CV were recorded in fresh PBS (10 mV/s, -0.2 to 0.6 V vs. Ag/AgCl, 3 M KCl, 3 cycles).

[9] Ink:EGDA = 4:6 (w/w), $t_{sep}$=20 min, $t_{sat}$=30 min
[10] In hindsight, this enzyme loading appears rather low.

Amperometric hydrogen peroxide sensing was carried out at an applied potential of -100 mV. For solutions of neutral pH-value, this is reportedly located in the range of electrocatalytical reduction [193]. PBS (1x, pH 7.4) served as electrolyte and was kept at 26 ℃. After applying the working potential, the sensors were left for 10 min under stirred conditions (magnetic stirring, 250 rpm) for the signal to stabilize. Afterwards, the $H_2O_2$ additions of different concentration ranges were started, beginning with 20 µM. All 4 electrodes per PCB were characterized at once.
Calibration curves were prepared by averaging the currents prior to each subsequent addition and plotting the values against the $H_2O_2$ concentration.

## 4.3.4 Results and discussion

### 4.3.4.1 Basic electrochemical response

Figure IV.12 a) displays the OCP recorded on fresh, functionalized electrodes upon their first immersion in the electrolyte. A general observation was the different stabilization behaviour of the OCP, i.e. the increasing potential of structured electrodes opposed to the decreasing potentials of unstructured electrodes. Potentially, this is linked to different hydration or diffusion behaviour in the bulk of structured electrodes. Eventually, the aforementioned surface activation of structured electrodes, which is thought to primarily occur in the outside region of the electrode, may have played a role.
The OCP of structured electrodes, on average, is slightly increased (40±23 mV for structured and 13±10 for non-structured electrodes), potentially indicating a higher enzyme load. In particular the presence of $Ca^{2+}$ could lead to a positive shift in OCP.
The OCPs displayed the tendency to reach plateau values, which took a longer time for the structured electrodes. This stability was interpreted as electrode functionality, i.e. no apparent enzyme degradation over the course of 15 minutes occurred.

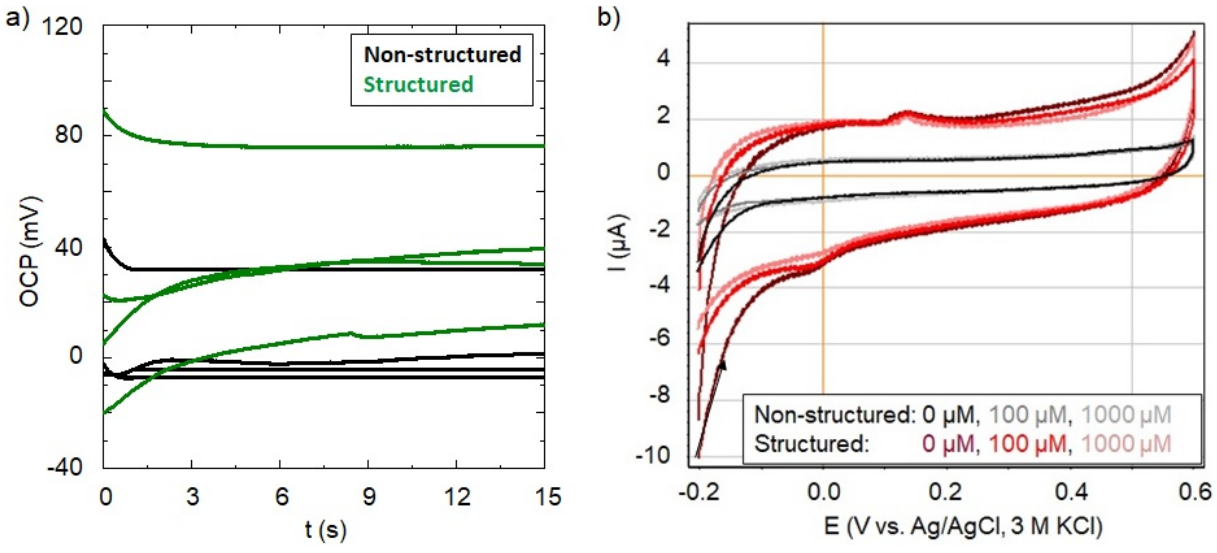


Figure IV.12: a) OCP recorded in PBS (1x, pH 7.4) during 15 min with fresh electrodes, directly after the enzyme adsorption. The responses correspond to two PCB with four electrodes each. b) CV of the same electrodes recorded in fresh PBS (1x, pH 7.4) at 10 mV/s starting at -0.2 V. The third cycles are displayed.

Figure IV.12 b) shows the third cycles of CV in fresh electrolyte for the same set of electrodes at different concentrations of $H_2O_2$. In particular, the capacitive/ pseudo-capacitive

character after structuration becomes apparent. Impedance spectra, not displayed here, aligned with the earlier observed tendency of higher series resistance for structured electrodes. These were in particular an extended high-frequency, low-impedance region and a capacitive character for low frequencies (phase angle of -80 °). Furthermore, the small additional redox peaks, considered as contamination, is present.
In absence of $H_2O_2$, no further faradaic responses were observed, besides for the eventual increased reduction of oxygen in the electrolyte at anodic potentials smaller than -150 mV. Interestingly, in presence of up to 1 mM $H_2O_2$, successively smaller anodic currents were recorded for negative applied potentials[11]. According to literature, the electrocatalytic response of HRP in presence of $H_2O_2$ was expected to result in increasingly higher anodic currents in this potential range. As a consequence of this contradictory observation, complementary studies were necessary to confirm the electrode responses.

#### 4.3.4.2 $H_2O_2$ additions

The subsequent characterization of electrodes in chronoamperometric mode was carried out to realize $H_2O_2$ additions. Figure IV.13 a) displays the current responses of electrodes on two PCB. One PCB comprised 4 non-structured electrodes, modified with HRP (black curves), while the other 4 electrodes were structured prior to functionalization. While the number and concentrations of additions was equivalent in all cases, the stabilization of current responses, linked to structured electrodes, was longer, resulting in different total durations.

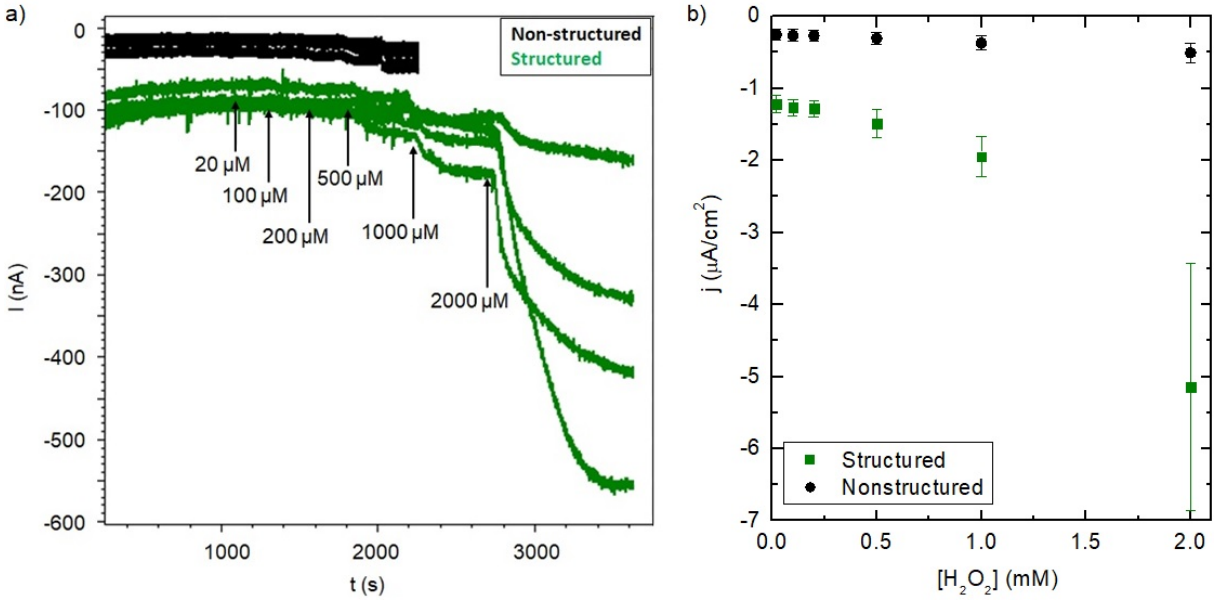


Figure IV.13: a) Amperometric detection of $H_2O_2$ at -100 mV in PBS (1x, pH 7.4) at 26 °C. The responses correspond to two PCB with four electrodes in the same concentration range up to 2 mM; b) Averaged calibration curves for each PCB, from which sensitivities were extracted.

The extracted calibration curves are not separately displayed for every electrode. Instead, averages for each PCB were calculated, as shown in Figure IV.13 b). The responses of electrodes were considered to be not ideally linear over the entire concentration range.

[11]Of the tested concentration range, only the CV for 100 and 1000 µM are depicted. However, all obtained results followed this tendency.

Thus, the range was reduced for the calculation of trend lines for structured electrodes. The increasing slope for the structured electrodes around 2 mM, however, is curious and requires verification (see below).
Besides, the applied trend lines are reasonably linear. For structured electrodes, sensitivities increased by a factor 6, which principally corresponds to the order of increase in specific and electroactive surface, which was determined in the last chapter for structured carbon electrodes.
In comparison to literature, the sensitivity for the unstructured electrodes fits relatively well (a match of 89.5 %) to what was published in the work of Teng et al. [184]. The group studied carbon paste electrodes, which were modified by using a similar enzyme deposition protocol. The publication is further the only one to work with a similar electrode material, functionalization method, electrolyte and WE bias. This, in turn, suggests validity of the results obtained in this project and highlights the improved sensitivity of the structured electrodes.

Following the previous observation, additions were repeated with fresh electrodes in a wider concentration range up to 12 and 30 mM depending on the electrode response, see Figure IV.14 a). Of the several electrodes tested, only one electrode response is displayed for each case. All measurements were affected by relatively high noise levels, which was found to be a consequence of the magnetic stir bar. However, further unexplained factors caused additional electronic noise. This is visible e.g. for the structured electrodes at the sudden noise drop between 500 µM and 4 mM.
The stabilization time, prior to starting the additions, was chosen as 30 minutes. In retrospective, this appears insufficient and limits the validity of interpreting the first additions, during which the electrodes were still stabilizing. In a potential future of the project, for exact quantitative measurements, it is proposed to extend stabilization times.

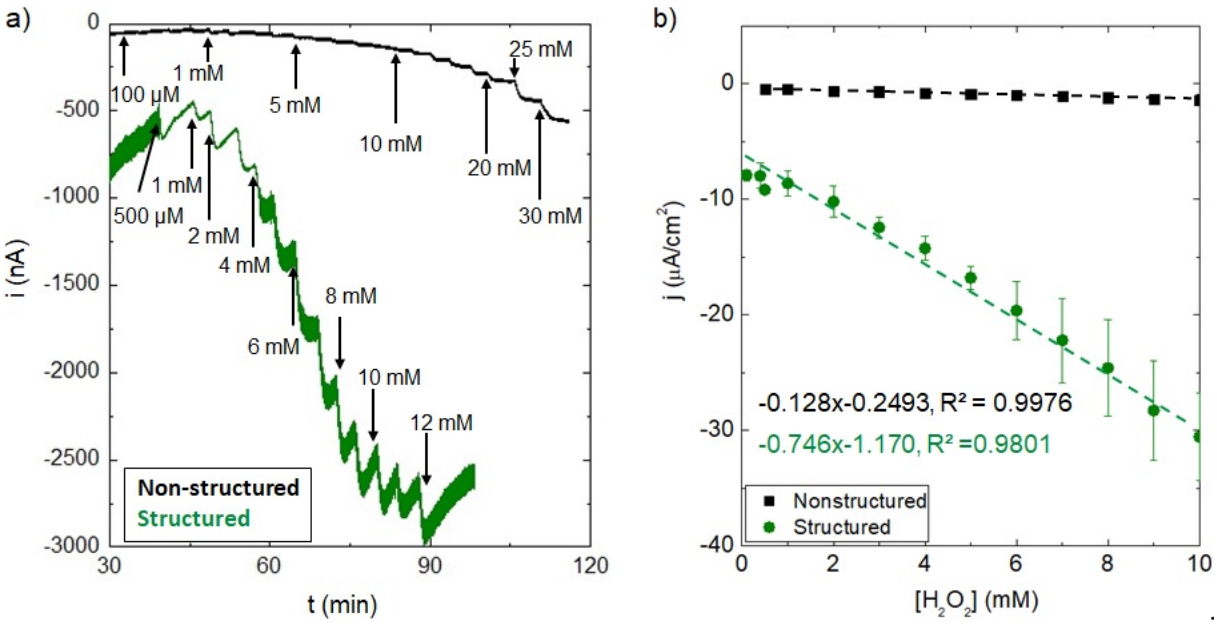


Figure IV.14: Amperometric detection of $H_2O_2$ at -100 mV in PBS (1x, pH 7.4) at 26 ℃ with a) stepwise $H_2O_2$ additions; b) the extracted characterization curves limited to the linear, dynamic ranges, see dotted trend lines. The results for all electrodes per PCB were averaged.

It was observed, that structured electrodes attained a current plateau from around 10 mM on, while the response for unstructured electrodes remained linear up to 30 mM.

Eventually, the porous electrodes were subject to diffusion limits. Particularly, $H_2O_2$ may have been hindered from quickly entering the porous bulk, thus representing a rate-limiting step. As in that case, a constant linear slope would be expected, it is suspected, that longer stabilization times between the additions are better adapted for further measurements.
Equally, the accumulation of reaction products may have played an additional role. In particular, a locally altering pH value is suspected. Past research confirmed the effect of electrolyte acidity on a reduction in enzyme activity of HRP [184] [194].
In consequence, the determination of trend lines was adapted, as can be seen by the dotted lines in Figure IV.14 b). The responses of all electrodes for each PCB were averaged to prepare this plot.
For unstructured electrodes, the determined sensitivity aligns well with the first results, indicating a linear response over a wide concentration range. This specifically underlines the similarity to the work of Teng et al. [184].
For structured electrodes, the increase in sensitivity appears more pronounced than before, yielding on average 2480 nA/µM $cm^2$, with peak values of 4245 nA/µM $cm^2$. This very remarkable value corresponds to an improvement by a factor of 35 and is in the range of studies published on HRP deposited on composites of carbon nanotubes and carbon microfibers [191]. At the same time, resulting from slight variations in the structural generation of electrodes per PCB, structured electrodes are linked to a larger variability of results.

## 4.4 Conclusions of chapter IV

The functionalization of porous carbon electrodes, prepared by means of supercritical $CO_2$-assisted structuration, followed the previously determined optimum protocol. The step was motivated by the interest to explore the electrode's practical application. The electrochemical detection of $H_2O_2$, a molecule of high medical and industrial interest, was chosen due to the broad range of available literature and possibilities of detection.

In a first attempt, the structuration protocol was transferred to a mediated, commercial carbon ink containing the electrochemically active, iron-based compound Prussian blue (PB), which has been employed in non-enzymatic $H_2O_2$ sensing since long-time. The recovery of porous electrodes was confirmed by SEM, suggesting the successful structuration of this second ink, despite its unknown exact composition. It was possible to improve the sample preparation technique for cross-section SEM imaging.
The electrochemical characterization by means of CV allowed recording the characteristic response of the redox mediator in case of the non-structured electrodes. The capacitive or pseudo-capacitive character, respectively, of structured electrodes was highlighted, confirming EIS measurements. However, the signature of PB was only poorly expressed after structuration, which was interpreted as a sign of mediator loss. This hypothesis was later confirmed by means of XPS measurements which were carried out by Dr. Lukasz Borowik of the PFNC at CEA Grenoble. The high-resolution spectra corresponding to iron and nitrogen core levels, characteristic for the mediator, did not display any significant peaks. The potential, partial solubility of the mediator in $scCO_2$ was assumed, implying its extracted from the ink and specifically in surface-near regions.
The electrode responses to $H_2O_2$ were investigated in chronoamperometric mode at small negative WE potentials. Measurements yielded lower sensibilities for structured electrodes, conformal with the loss of mediator. Furthermore it was noted, that the increased specific surface resulted in reduced noise levels and, in consequence, improvements in the detection limit.

To circumvent the problem of losing electroactive material during the structuration process, the adsorption of horseradish peroxidase (HRP) on structured carbon electrodes was studied. Part of the interest for preparing enzymatic biosensors was to profit from the developed specific and electroactive surface in the electrode bulk, providing physical protection for the generally fragile, enzymatic structure.
A basic general electrochemical characterization of as-obtained electrodes was carried. It mainly indicated the capacitive nature, as a result of the structuration, via cyclic voltammetry and impedance spectroscopy (results not displayed).
The sensing performance was verified by carrying out $H_2O_2$ additions in amperometric mode at negative WE potential. Primarily, the increased sensibility of structured electrodes by a factor between 6 and 35 was revealed, depending on the concentration range. In comparison with literature, this value is considered comparable with respect to other approaches, which rely on more complex materials and more sophisticated electrode preparation.
The observations are of high interest for preparing multi-enzymatic sensors, where HRP is e.g. coupled with glucose oxidase or lactase, which generate $H_2O_2$ as a by-product. These so-called enzymatic cascades are commonly used for the preparation of a variety of sensors of high medical interest, e.g. in glucose sensing.

The studies on HRP present a further potential for improving the adsorption protocol, e.g. by depositing HRP on electrodes under acidic conditions, which was in the past linked to higher sensor performance [183]. With the same objective, other groups added sugar

to the enzymatic solutions to maintain a compact conformation of the enzyme during the adsorption step [195].
In some cases, HRP was solubilized in $scCO_2$ and deposited on pre-structured materials, to support the infiltration by the enzyme [196]. This, in particular, is considered highly promising for a further adaptation of the $scCO_2$ process, which principally allows to add a dynamic step of fluid flow. This step could be located after the phase separation, prior to the saturation phase and thus allow to prepare enzymatic, porous biosensors in one single, rapid and technologically uncomplicated treatment.

During the project, several additional studies were carried out in the context of $H_2O_2$ sensing, but could not be included in the manuscript. In particular, a second mediated carbon ink was structured, containing the mediator cobalt phthalocyanine. Respective electrodes were tested in amperometric mode at a WE bias of 0.7 V. The results were more promising, than in the case of PB and consisted in slight improvements of sensitivity, noise and detection limit.
In order to profit from the generated structure of the carbon electrodes, the electrodepositions of PB, of PB in a PEDOT matrix and of Pt were realized in separate studies. Results revealed a mixed interest. In particular, PB-PEDOT appeared promising for a further optimization of the deposition protocol. In parallel, some intrinsic difficulties of combining an electrodeposition process with porous electrodes became apparent.
The biosensing application of structured carbon electrodes was further investigated by adsorbing the enzyme tyrosinase to prepare dopamine sensors. The results pointed out the enhanced sensing performance of structured electrodes, which is considered an important factor for evaluating the perspectives of the project.

# General conclusions and perspectives

## General conclusions

The studies performed during this PhD project are situated in the context of developping structured and porous carbon materials for electrochemical application. Electrodes in sensing technology in the medical, environmental and the industrial field, as well as in energy storage application, have in past research been improved by increasing the electrode/ electrolyte interface. As the vast majority of presented methods presents drawbacks, such as long preparation times arising from complex multi-step approaches, as well as the safety and environmental hazard linked to the use of aggressive reagents, an alternative structuration method was tested.

The industrialized electrode fabrication method, based on the deposition of a conductive ink, was combined with an **innovative one-step structuration** treatment based on supercritical $CO_2$. The process protocol was chosen with the intention to unify two pore-generating mechanisms, **supercritical fluid-assisted phase separation** and **supercritical $CO_2$-foaming** with **extraction of the solvent** phase. The as-obtained electrodes did not require an additional curing or drying step during fabrication.
Comparability of the results was assured by applying a common set of complementary physical and electrochemical characterization techniques throughout the entire study. Thus, information related to electrode surface and bulk could be studied and linked to the change of structuration parameters. The latter were systematically modified in separate studies. Their effect on the formation of pores and the generation of surface was principally evaluated in qualitative manner, with the aim to identify an optimum process protocol. The quantitative evaluation was potentially limited, but results generally fall into ranges, which are compatible with literature on porous electrodes.

The **ratio of phase separation time to polymer saturation time ($t_{sep}/t_{sat}$)** was introduced, to confirm both the occurrence of phase separation and polymer foaming. Indeed, the results generally suggest a combined mechanism for the diluted ink in study. A multi-modal generation of pore sizes was identified, with the largest pores measuring around 10 µm, a major population of pores measuring several 100 nm in diameter and the smallest structures measuring less than 100 nm. Highest values of specific capacitance were determined for a ratio $t_{sep}/t_{sat}$ of 20/10. The same electrodes yielded largest specific and electroactive surfaces, corresponding to an increase of approximately 7 relative to the geometric electrode surface ($A_{geo}$).

In the **study of variable separation time at constant saturation time**, $t_{sat}$ was set to a long time to favour solvent extraction and polymer foaming, while the rest of the protocol was maintained as before. For separation times in the range of 10 to 20 min, electrodes displayed the smallest surface pore diameter. This correlated with highest capacitance values, largest faradaic currents and the largest developed volume. The electrodes were thus associated with the largest specific and electroactive surface, which increased by factors 12 and 14 relative to $A_{geo}$.

In the study of **process temperature**, higher $T_{sat}$ were investigated upon their effect on polymer foaming. The rest of process parameters varied as before. Imaging techniques suggested a high visual coherence amongst electrodes and potentially the loss of a membrane-like surface layer which is commonly formed in phase separation processes. The pore sizes and total pore volume were largest for $t_{sep}$ between 10 and 20 $t_{sep}$, correlating with a lower pore count. While capacitive currents seemed unchanged, faradaic currents were reduced to some extent. It was concluded, that the increased process temperature in the studied range had a slightly detrimental effect on the generation of surface. On the other hand, the results again confirmed the trend of maximum values for separation times around 20 min, which allowed to propose an optimized structuration protocol.

The modification of **ink dilution** represented a highly interesting subject of investigation and was studied on electrodes, prepared using the identified optimum protocol. Besides for the mechanical characteristics, pore generation and electrochemical behaviour could be modified. Largest specific surface areas were associated with highly diluted ink of ratio 3:17 (ink:EGDA, w/w). The maximum development of faradaic surface, however, was found for inks of relatively low dilution (4:6, 3:7 and 2:8).

A general observation made for structured electrodes consisted in the effect on diffusion and migration, respectively, of analytes. The electrochemical behaviour indicated **thin-layer type diffusion**, characteristic for confined redox species in a porous electrode, which distinguished the electrodes from their non-structured equivalents. For electrode functionalization, it was considered of high practical potential.

The **transfer of the structuration technique** to other commercial inks containing redox mediators for the preparation of electrocatalytic sensors, sensitive to hydrogen peroxide, was investigated. The structuration protocol was primarily considered successful, however there is room for further detailed studies. While results of structured electrodes suggested reduced noise, the potential loss of mediator in supercritical $CO_2$ was suspected. The adsorption of the enzyme horseradish peroxidase (HRP) in prestructured electrodes, on the other hand, lead to clearly improved biosensor performance in the detection of hydrogen peroxide. The sensitivity to hydrogen peroxide increased by one order, which is in general correlation with the increase in specific and electroactive surface studied earlier.

**Complementary studies** are partially still under investigation and therefore not included in the manuscript:

- Structured electrodes have been investigated for the preparation of **ion-sensitive electrodes** (ISE) [197]. In this project, structured carbon electrodes were functionalized by depositing a polymeric membrane, containing ionophores. The as-obtained potassium-sensitive ISE were operational, however no signal-enhancement or noise-reduction was achieved. Particularly the viscosity of the membrane solution was suspected to present the potential for further optimization, as to allow infiltration of the filigree network. Additionally, the choice of a less aggressive solvent, i.e. not leading to the dissolution of the polymeric binder, is required to preserve the structure. Further, the hydrophobic character of as-structured carbon electrodes is potentially beneficial for suppressing the formation of an aqueous layer at the transducer/collector interface. This problematic has been pointed out in past work [198]. The use of an intrinsically hydrophobic material is potentially beneficial to promote longevity of the ISE.

- The additional incorporation of $TiO_2$ anatase particles in commercial carbon ink was investigated for an application in e.g. glucose or cholesterol sensing. Salerno et al. described the addition of $TiO_2$ in polycaprolactone solutions prior to a supercritical

$CO_2$-assisted structuration[12]. Interestingly, though, the particles acted as filler and were not investigated for their catalytic properties [96]. In this project, CV and EIS studies confirmed the generation of porous composite electrodes which generally presented results, comparable to pure structured carbon ink. Thus, the specific and electroactive surfaces were successfully increased. The effect of the particles on catalytic properties is still under investigation.

- In the context of $H_2O_2$ sensing, the **electrodeposition of Prussian blue (PB)** on structured carbon electrodes was carried out, leading to a reduction of noise and, in consequence, lower detection limits. While the sensitivity to $H_2O_2$ was increased by over one order, PB dissolved in aqueous media. In an attempt to immobilize PB, it was co-electrodeposited in a PEDOT matrix. Results confirmed an improvement of the detection limit and sensitivity, as well as the successful retention of the mediator. The noise level, on the other hand, increased.

- In consequence of the promising results with HRP, **tyrosinase-based biosensors** were prepared for dopamine sensing. The results confirmed an increased sensor sensitivity for structured electrodes.

**In conclusion, an innovative method for the (nano-)structuration of carbon electrodes, based on the supercritical $CO_2$-assisted structuration of carbon ink, was studied. The obtained results on both electrode characterization, as well as functionalized electrodes, are considered very promising and highly suggest to continue the work in the field.**

# Perspectives

During the project, a focus was placed on understanding the structuration mechanisms from a physical point of view, in order to obtain control over the generated structure. However, as the evaluation of practical utility was the second main interest, several questions remained unanswered due to the limited, available time frame and thus require further detailed study.

The **manipulation of phase separation mechanisms** requires the knowledge of the exact composition of the system and of thermodynamic information on the interaction between solvent and non-solvent. For polymer foaming, the location of the glass transition temperature is required for the correct choice of process temperature. The exact composition of the commercial DuPont BQ242 carbon ink, however, was unknown. While the type of carbon particles in conductive inks generally falls into a small group of potential candidates, the type and content of polymeric binder are more difficult to estimate. Further, classical phase separation theory does not take the additives (here carbon particles) into consideration, which certainly need to be addressed as well. Reasons may be the potential agglomeration, changed viscosity or interaction with one of the liquid phases.

The work on **ink formulations** is regarded essential in a potential continuation of the subject, to guarantee more precise control over the process parameters. The incorporation of different types of conductive (carbon) particles, for example graphite platelets of different size, could allow to bridge pores and increase electrode conductivity.
In this context, it is equally possible to investigate the potential of incorporating hard-templates, soluble after a certain exposure to supercritical $CO_2$.

[12]While described as foaming, a phase separation process is presumed based on the reported process parameters, particularly due to the rather slow depressurization conditions.

Further, the structuration of conductive polymers is considered to be of potential interest. Studies on the polymerization of polypyrrole in presence of supercritical $CO_2$ were carried out [199] [200], suggesting the potential to adapt the process to generate porous electrodes.

The potential for **improving the characterization techniques**, particularly sample preparation for cross-section imaging, is pointed out. Additionally, non-destructive methods for obtaining complementary information on the generated porosity and on (specific) surface are of high interest. While it seems unrealistic, to perform X-Ray tomography for a large set of electrodes, the realization of $Kr_2$ adsorption-desorption isotherms could allow reducing the required sample mass. Respective measurements could not be performed during the thesis due to technical difficulties with the equipment.
Alternatively, techniques such as Small-Angle X-ray Scattering (SAXS) could provide further insight into the fundamental mechanisms of polymer foaming, particularly when studying composites of polymers and carbon particles. A study on the crystallization behaviour of polycaprolactone/MWCNT composites by means of SAXS was published by Wurm et al. [201]. Initial tests in relation with cellulose acetate samples were carried out in this project[13]. The characterization of composite materials was limited due technical problems with the equipment.

In the context of optimizing the structuration protocol, the potential interest for carrying out **simulation of the combined structuration** is highlighted. The prediction of optimum process parameters for different systems could potentially save considerable experimentation time. However, a such task is rather complex and based on the profound knowledge of thermodynamic principles, diffusion mechanisms and the availability of related data for all components in question.

The structured electrodes prepared in this project were found very promising for a functionalization with enzymes. It could be of interest to employ the $scCO_2$-assisted structuration of conductive inks in the fabrication of low-cost amperometric biosensors or of multi-enzymatic platforms, e.g. for glucose sensing.
Furthermore, the observation of the extended low-impedance region in EIS studies is potentially a suited property for other application. Examples are electrodes used in deep brain stimulation, i.e. the treatment of neurological disorders such as epilepsy or Parkinson's.

[13]The work of Dr. Arnaud de Geyer is highly appreciated for characterizing the samples.

# A

## A.1 Effect of oxygen plasma exposure time

The duration of plasma exposure time was varied, to study the effect on hydrophobicity of the ink deposits. Contact angle measurements (Digidrop CME 204, GBX Scientific LTD, Ireland) were carried out, following the sessile drop technique.
Structured ink deposits were prepared and initial contact angles were measured. 1.5 µL of deionized water were deposited in the center of each deposit and pictures taken in side-view. After identifying a base line, separating the sample support from each deposit, results were provided by the software. For each deposit, ten successive measurements [14] were carried out. As deposits were found to soak, the measurements were grouped into "measurement 1-5" and "measurement 6-10", averaging data sets in groups of five measurements. After allowing the deposits to thoroughly dry, an oxygen plasma of between 10 and 30 s duration was applied and contact angles were remeasured.

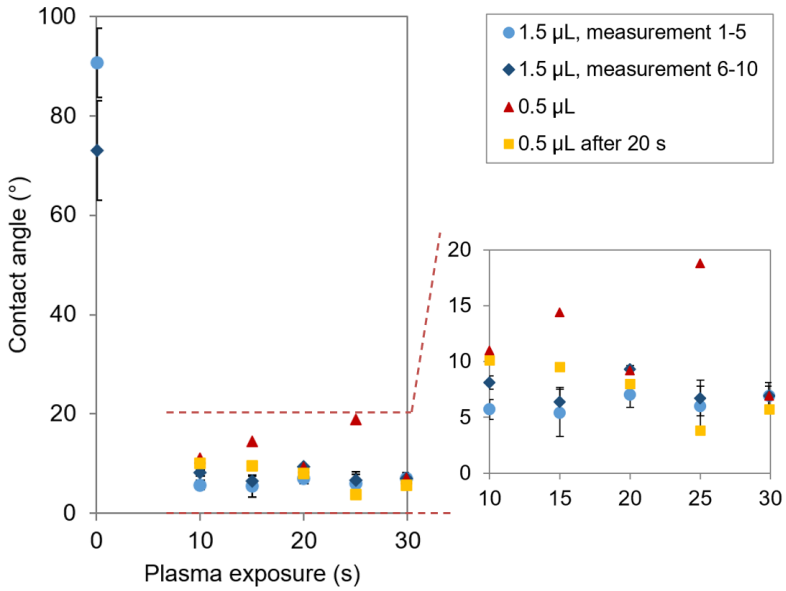


Figure IV.15: Effect of the duration of oxygen plasma treatment and wetting time on the contact angle, measured on structured ink deposits. For 1.5 µL water, five data points were averaged. For 0.5 µL water, only single measurements were carried out.

Figure IV.15 displays the averaged contact angles for structured deposits before any plasma-treatment (0 s) and after plasma-exposure.
Before plasma treatment, the first five averaged droplets yielded contact angles of around

[14] Measurements consisted in the deposition of water, measuring the contact angle and careful removal of water by soaking it up with the edge of a tissue.

90 °, indicating a neutral to slightly hydrophobic surface[15]. Repeating the measurement, contact angles were slightly reduced to around 73 °. A relatively large deviation in contact angles was observed.
After plasma treatment, contact angles averaged to 6 °, which relates to a highly hydrophilic surface. Interestingly, measurements 6-10 yielded slightly increased contact angles. Potentially, the drying of deposits by means of a tissue did not remove all water. In consequence, the porous structures were eventually saturated, which is the reason for the observations. No particular correlation between plasma exposure time and contact angle was observed.

Due to the suspected saturation of structured deposits, the deposits were dried overnight. Measurements were then repeated with a reduced volume of water (0.5 µL). To confirm the effect of soaking, another series of measurements was added after a waiting time of 20 s. Only one measurement per deposit was performed.
Interestingly, no clear correlation of plasma exposure time and contact angle was observed initially. Values were even found to slightly increase, compared to the previous measurements. After leaving the droplets to sit on the surface, however, an almost linear tendency was discernible towards smaller contact angles. After 10 s, a contact angle of 10 ° was measured which reduced to 6 ° after 30 s. For the later project, the interest to add a saturation step to the protocol, was noted. In particular, electrochemical characterization should not be started immediately, after immersing the electrodes in the electrolyte.
It is thought, that prolonged plasma treatment times may have allowed the plasma to enter further in the bulk of structured deposits. The oxidation of a larger total surface area may have promoted wetting.

## A.2 Sample preparation for nitrogen adsorption desorption isotherms

One characteristic of nitrogen adsorption experiments is the requirement of carrying out experiments with a certain threshold total surface of samples in the range of 5 to 10 $m^2$. For materials with a comparably low SSA, this implies to prepare a sufficiently large quantity of sample material. In this case, a relatively large quantity of structured ink deposits was prepared, as presented in the following (protocol outlined in Figure IV.16 b)).

1. 20 mL of diluted ink were poured into a glass dish of around 15 cm in diameter and spread out, before applying the $scCO_2$-structuration as detailed earlier. The structuration was not successful and residual solvent was visible in the dish.

2. In order to maintain the same structuration parameters as before, further nitrogen adsorption samples were prepared in equivalent manner to the ink deposits. In particular, masks were applied on suitable supports and ink was deposited for each deposit separately.
   The beneficial effect of allowing a certain flow of supercriticial fluid in the cell (from the fluid inlets to the outlet) was observed. Potentially, solvent extraction is hindered otherwise and in consequence, sample placement is important. To meet the criteria, supports had to resemble a raised platform and required the presence of holes, as displayed in FigureIV.16 a).

[15] A contact angle of 90 ° is defined as the transition between hydrophilic and hydrophobic character.

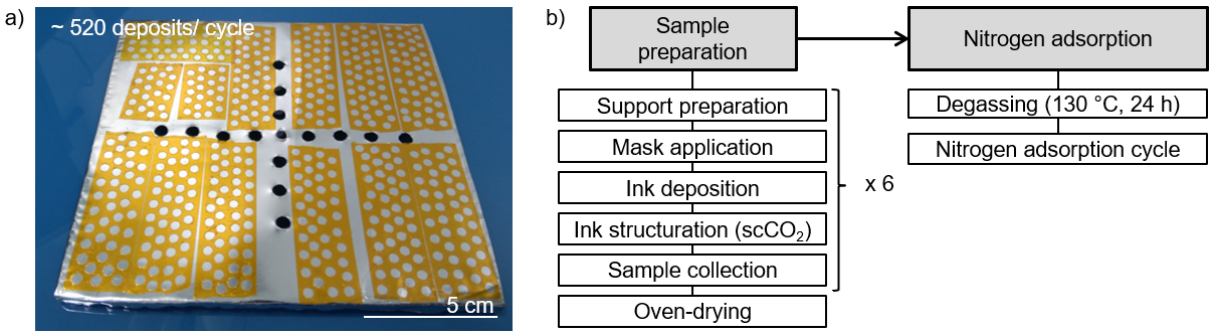


Figure IV.16: a) Support for the ink deposits for the preparation of nitrogen adsorption studies. b) Sample preparation and experimental protocol.

The total duration of ink deposition took approximately thirty minutes. Compared to the sample "transfer time" mentioned earlier, this varies significantly. However, the dilution with EGDA prevented noticeable drying effects. During the recovery of structured deposits, care had to be taken to use tools that would not electrostatically charge. Specifically, the loss of sample material was encountered in earlier attempts, as it kept adhering to tools and equipment. In total, six structuration cycles were carried out, resulting in around 3100 structured deposits with a total mass of 314 mg. In order to assure the complete removal of any residual solvent and volatile phases, the sample material was dried overnight in an oven at 80 °C.

## A.3 Determination of SEM image treatment

The following section outlines the process of determining a SEM image treatment. The results of the parameter studies are qualitatively presented. A quantitative evaluation was based on particle count (i.e. pore number), average particle size (i.e. average pore size) and % area (i.e. fraction of the surface area consisting of pores).
Figure IV.17 displays the influence of image contrast, while maintaining constant image blurr and threshold.

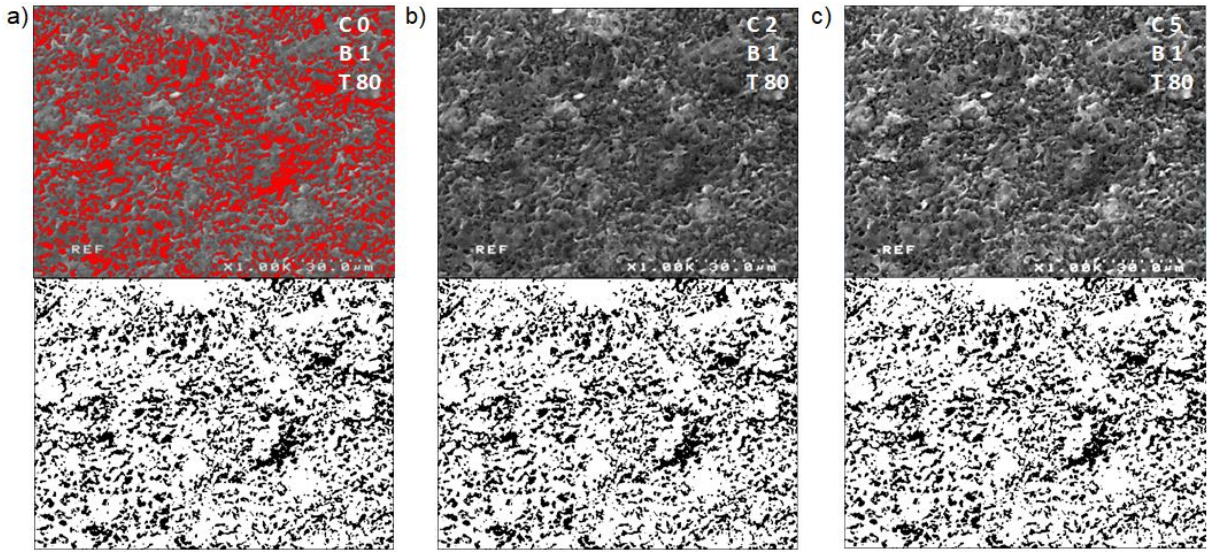


Figure IV.17: Refinement of the SEM image treatment protocol with the parameter contrast in focus.

The influence of image threshold at constant contrast and blurr was further evaluated by comparing four different settings (Figure IV.18). Three different values for the parameter image blurr were investigated, while image contrast and threshold were maintained constant (Figure IV.19).

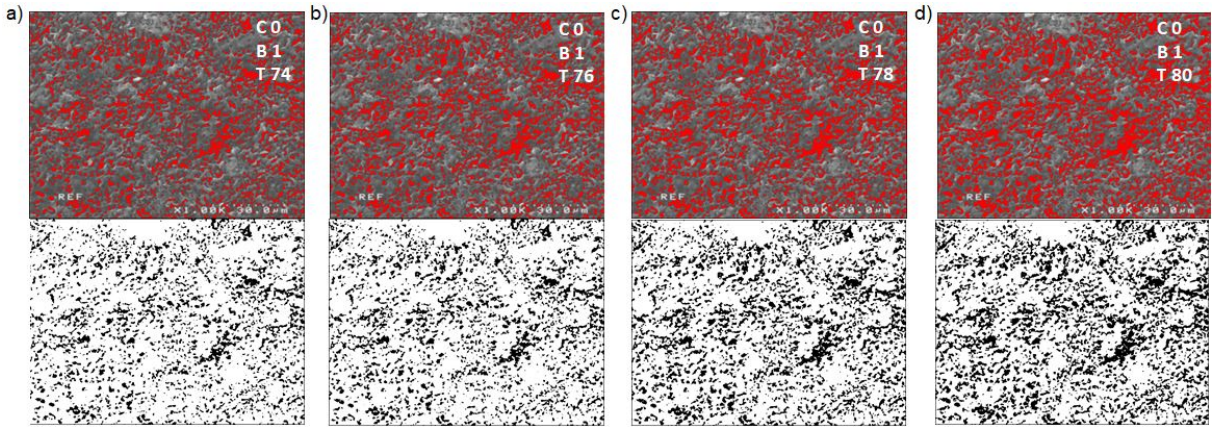


Figure IV.18: Refinement of the SEM image treatment protocol with the parameter threshold in focus.

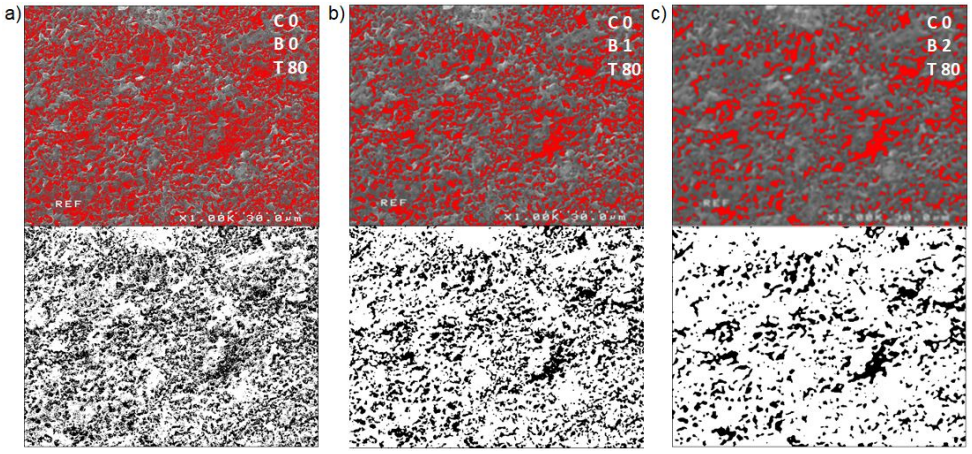


Figure IV.19: Refinement of the SEM image treatment protocol with the parameter image blurr in focus.

Table IV.4: Results of the parameter study for SEM image-treatment.

| | **Particle count** | **Average particle size (µm)** | **Covered area (%)** |
|---|---|---|---|
| Contrast 0 | 1278 | 2.0 | 22.7 |
| Contrast 2 | 1278 | 2.0 | 22.7 |
| Contrast 5 | 1278 | 2.0 | 22.7 |
| Blurr 0 | 4700 | 0.7 | 28.7 |
| Blurr 1 | 1278 | 2.0 | 22.7 |
| Blurr 2 | 561 | 3.0 | 12.5 |
| Threshold 74 | 1625 | 1.0 | 15.8 |
| Threshold 76 | 1600 | 1.0 | 16.8 |
| Threshold 78 | 1427 | 2.0 | 20.6 |
| Threshold 80 | 1278 | 2.0 | 22.7 |

## A.4 Python script for CV peak data extraction

```
import numpy as np
import matplotlib.pyplot as plt
from sklearn.linear_model import LinearRegression
#-----------------------------------------------------------------


#Import data-----------------------------------------------------------

file = np.loadtxt('helper_2.txt',delimiter='\t')

potential_arr=file[:,0]
current_arr=file[:,1]

current_list=current_arr.tolist()
potential_list=potential_arr.tolist()


#Find I_max and I_min-------------------------------------------------

maxVal=file[1]
maxVal=max(current_list)

minVal=file[1]
minVal=min(current_list)

print("I_max = " + str(maxVal) + " mA")
print("I_min = " + str(minVal) + " mA")


#Find P(I_max) and P(I_min)--------------------------------------
c_max_index=current_list.index(max(current_list))
c_min_index=current_list.index(min(current_list))
#print("Indcx for I_max:" + str(c_max_indcx))
#print("Index for I_min:" + str(c_min_index))

P_ox = potential_list[(c_max_index)]
P_red =potential_list[(c_min_index)]
print("P_ox = " + str(P_ox) + " V")
print("P_red = " + str(P_red) + " V")

print("REPLACE ABSOLUTE MAX/MIN")
#Create trends---------------------------------------------------

Ox_trend_start= potential_list[(c_max_index)-75]
Ox_trend_end= potential_list[(c_max_index)-60]
print("Ox_trend_start = " + str(Ox_trend_start) + " V")
print("Ox_trend_end = " + str(Ox_trend_end) + " V")

x_total=np.potential_arr=file[:,0].reshape((-1,1))

x_ox=np.potential_arr=file[(c_max_index-75):(c_max_index-60),0].reshape(-1,1)
y_ox=np.current_arr=file[(c_max_index-75):(c_max_index-60),1]

model_ox=LinearRegression().fit(x_ox,y_ox)
model_ox_pred=model_ox.predict(x_total)
r_sq_ox=model_ox.score(x_ox, y_ox)
print("R_ox^2 = "+ str(r_sq_ox))
print("Intercept_ox = "+ str(model_ox.intercept_) + " mA")
print("Slope_ox = "+ str(model_ox.coef_) + " mA/V")
```

Figure IV.20: The Python script (part 1/3) for data extraction based on .txt CV files.

```
Red_trend_start= potential_list[(c_min_index)-75]
Red_trend_end= potential_list[(c_min_index)-60]
print("Red_trend_start = " + str(Red_trend_start) + " V")
print("Red_trend_end = " + str(Red_trend_end) + " V")

x_red=np.potential_arr=file[(c_min_index-75):(c_min_index-60),0].reshape(-1,1)
y_red=np.current_arr=file[(c_min_index-75):(c_min_index-60),1]

model_red=LinearRegression().fit(x_red,y_red)
model_red_pred=model_red.predict(x_total)
r_sq_red=model_red.score(x_red, y_red)
print("R_red^2 = "+ str(r_sq_red))
print("Intercept_red = "+ str(model_red.intercept_) + " mA")
print("Slope_red = "+ str(model_red.coef_) + " mA/V")


#Peak heights-----------------------------------------------------

Base_P_ox=model_ox.coef_*P_ox+model_ox.intercept_
Base_P_red=model_red.coef_*P_red+model_red.intercept_
I_pc=max(current_list)-Base_P_ox
I_pa=min(current_list)-Base_P_red
print("I_pc = "+ str(I_pc) + " mA")
print("I_pa = "+ str(I_pa) + " mA")


#Peak fitting with parabolas-------------------------------------
N=15

x_peakfit_ox=np.potential_arr=file[(c_max_index-50):(c_max_index+50),0]
y_peakfit_ox=np.current_array=file[(c_max_index-50):(c_max_index+50),1]

a_ox=np.polyfit(x_peakfit_ox, y_peakfit_ox, N)
b_ox=np.poly1d(a_ox)

plt.plot(x_peakfit_ox, b_ox(x_peakfit_ox), 'bo')

x_peakfit_red=np.potential_arr=file[(c_min_index-30):(c_min_index+50),0]
y_peakfit_red=np.current_arr=file[(c_min_index-30):(c_min_index+50),1]

a_red=np.polyfit(x_peakfit_red, y_peakfit_red, N)
b_red=np.poly1d(a_red)

plt.plot(x_peakfit_red, b_red(x_peakfit_red), 'bo')


#Create plot-----------------------------------------------------

plt.figure(1,figsize=(5,4))

plt.plot(potential_list,current_list,'r+', x_total, model_ox_pred, 'g.', x_total
plt.legend(['sample xy'],loc='best')
plt.ylabel('Current / mA')
plt.xlabel('Potential / V')
plt.show()
```

Figure IV.21: The Python script (part 2/3) for data extraction based on .txt CV files.

```
#Surface calculation-----------------------------------------------

Ox_p_st=potential_list[(c_max_index)-50]
Ox_p_e=potential_list[(c_max_index)+50]
N1=len(potential_list[(c_max_index)-50:(c_max_index)+50])

#Red_p_st=potential_list[(c_min_index)-30]
#Red_p_e=potential_list[(c_min_index)+30]
#N2=str(len(potential_list[(c_min_index)-30:(c_min_index)+30]))

print("Ox_Peakfit from " + str(Ox_p_st) + " to " + str(Ox_p_e))
#print("Red_Peakfit from " + str(Red_p_st) + " to " + str(Red_p_e))



f=b_ox
f2=model_ox_pred.linspace(Ox_p_st, Ox_p_e, 100)


#WORKING 1--------
#x_pfit_ox=np.linspace(Ox_p_st, Ox_p_e, N1)
#f=f(x_pfit_ox)
#F=f[0] + 0.5 *x_pfit_ox**2
#area=integrate.cumtrapz(F, x_pfit_ox, initial=0)
#plt.plot(x_pfit_ox, f, 'bo', x_pfit_ox, f[0] + 0.5 *x_pfit_ox**2, 'b-')
#plt.show()
#print(str(area/0.005)+ " mC")


from scipy import integrate
x_pfit_ox=np.linspace(Ox_p_st, Ox_p_e, N1)
f=f(x_pfit_ox)
F=integrate.cumtrapz(f, x_pfit_ox, initial=0)
area_ox_data=np.sum(F)

f2=f2(x_pfit_ox)
F2=integrate.cumtrapz(f2, x_pfit_ox, initial=0)
area_ox_trend=np.sum(F2)

print(str((area_ox_data)/0.005)+ " mC")

#plt.plot(x_pfit_ox, F, 'bo', x_pfit_ox, f[0] + 0.5 *x_pfit_ox**2, 'b-')
#plt.show()

#def integrate_ox (f, Ox_p_st, Ox_p_e, N1):
#    x_peakfit_ox=np.linspace(Ox_p_st, Ox_p_e, N1)
#    f=f(x_peakfit_ox)
#    F=integrate_ox.cumtrapz(f, x_peakfit_ox, initial=0)
#    area_ox=np.sum(F)
#    return area_ox
#print(area_ox)

#def integrate_red (g, red_peak_start, red_peak_end, N):
#    x_trend_red=np.linspace(red_peak_start, red_peak_end, N)
#    gx_trend_red=g(x_trend_red)
#    area_red=np.sum((gx_trend_red)*(red_peak_end-red_peak_start)/N)
#    return area_red
```

Figure IV.22: The Python script (part 3/3) for data extraction based on .txt CV files.

## A.5 Sample preparation for digital microscopy

Table IV.5: Parameters for the preparation of digital microscopy samples on glass supports. Ink volumes were 1.0 and 1.5 µL.

| **Study** | **Dilution (ink:EGDA, w/w)** | **$t_{sep}$/$t_{sat}$ (min/min)** | **$T_{sep}$/$T_{sat}$ (°C/°C)** |
|---|---|---|---|
| Parameter $t_{sep}$/$t_{sat}$ | 2:8 | 0/30 | 30/40 |
| | 2:8 | 10/30 | 20/40 |
| | 2:8 | 20/30 | 20/40 |
| | 2:8 | 30/30 | 20/40 |
| Parameter $t_{sep}$ at $t_{sat}$ cst. | 2:8 | 0/30 | 20/60 |
| | 2:8 | 10/30 | 20/60 |
| | 2:8 | 20/30 | 20/60 |
| | 2:8 | 30/30 | 30/60 |
| Parameter BQ:EGDA | 1:10 | 20/30 | 20/40 |
| | 3:17 | 20/30 | 20/40 |
| | 2:8 | 20/30 | 20/40 |
| | 3:7 | 20/30 | 20/40 |
| | 4:6 | 20/30 | 20/40 |
| | 5:5 | 20/30 | 20/40 |
| | 1:0 | 20/30 | 20/40 |

# B

## Introduction

Dans la recherche actuelle sur les électrodes, « nano » est un terme sur lequel on peut souvent trébucher, principalement dans le contexte des nanomatériaux ou de la nanostructure. La définition des terminologies est assez claire, les nanomatériaux se référant à des objets et les nanostructures se référant à des agglomérations de molécules ou d'atomes mesurant entre 0.1 et 100 nm dans au moins une dimension. La nano-structuration peut donc être comprise comme un processus de création d'une surface comprenant des caractéristiques avec des dimensions à ladite échelle. L'incorporation ou le dépôt de nanomatériaux réels sur une surface est possible pour atteindre cet objectif, mais pas strictement requis car une grande variété de matériaux peut être synthétisée et adaptée pour répondre aux spécifications souhaitées.

Il est largement reconnu que les nanomatériaux présentent des propriétés intrinsèques intéressantes qui diffèrent souvent considérablement des caractéristiques des matériaux en vrac. Un exemple est leur surface spécifique généralement grande, respectivement le rapport entre surface et volume. Dans les applications électrochimiques, la surface impliquée dans une réaction reçoit une attention particulière, car l'interface d'une électrode et de son électrolyte environnant représente le centre de transfert de charge. La surface de l'électrode est donc un paramètre essentiel pour discuter et évaluer ses performances électrochimiques.
Dans une application de capteur, cela peut se traduire par les paramètres de stabilité, de sensibilité, de rapport signal-bruit et de limite de détection. Ainsi, en nano-structurant l'électrode, il faut s'attendre à une augmentation des performances électrochimiques, car des courants plus élevés et des charges plus élevées peuvent être échangés. De nombreux travaux ont confirmé l'intérêt de l'application d'électrodes nanostructurées dans les domaines de la chimie analytique à usage médical, environnemental et industriel, ainsi que dans les applications de stockage d'énergie.

Un aspect controverse qui est partagé par les publications est la complexité de l'approche de structuration. Bien que des électrodes très performantes puissent être obtenues et que des propriétés électrochimiques intéressantes aient été observées, la préparation des électrodes est généralement de nature élaborée en raison du nombre d'étapes impliquées, ce qui implique des protocoles de préparation fastidieux. En outre, l'utilisation de matériaux exotiques est fréquemment signalée, ce qui limite l'intérêt pour une fabrication à l'échelle industrielle. En conséquence, la question principale et l'objectif de ce projet de thèse étaient d'identifier une méthode de nano-structuration alternative de coût relativement faible, de faible complexité de fabrication et de temps de production court par rapport aux approches rapportées.

En se focalisant sur les techniques établies pour la préparation des électrodes, par exemple le dépôt d'encres conductrices, une méthode supercritique à base de $CO_2$ a été identifiée, qui est considérée comme compatible avec un processus de production additive. Sur

la base des mécanismes bien étudiés de séparation de phase des systèmes multicomposants et de moussage polymère assisté par fluide supercritique, un traitement combiné a été appliqué aux encres conductrices de structure et optimisé en étudiant séparément l'influence de différents paramètres de structuration. Dans une étape ultérieure, l'application pratique des électrodes obtenues a été étudiée dans l'intention d'une application potentielle dans le domaine médical.

# Résumé du chapitre I: Les électrodes carbones structurées

Un choix minutieux de supports d'électrodes a présenté une base pour ce travail, principalement dirigé par la compatibilité des matériaux avec le $CO_2$ supercritique et la conception de l'équipement de fluide supercritique. Les PCB avec collecteurs Au ont été identifiés comme idéaux à condition d'une couverture complète avec de l'encre afin de ne pas exposer d'Au sous-jacent. Dans la pratique, les PCB étaient avantageux en raison de leur conception plate, robuste mais polyvalents, permettant de préparer quatre électrodes selon le même protocole.
Néanmoins, le PCB a présenté un compromis dans l'adhérence mécanique et le contact électrique entre Au et les dépôts d'encre structurés spécifiquement dans les premières étapes du projet. De plus, lors du recyclage du PCB, il a été constaté que l'encre de carbone avait un effet plutôt corrosif. Une décoloration sous forme de taches et sur le bord extérieur a été observée. Les explications possibles incluent les défauts mécaniques introduits lors de la manipulation et de l'exposition du Ni ou du Cu, les défauts cristallographiques initiaux et une dégradation éventuelle du revêtement supérieur diélectrique après un contact répété avec des solvants agressifs. Il est important de tenir compte de l'influence éventuelle sur les résultats. Le contact possible des matériaux sous-jacents avec les environnements aqueux peut avoir conduit à l'oxydation ou à la formation d'une variété de sels ou de sous-produits.

Dans la suite, un protocole de préparation d'électrodes a été identifié comprenant une étape de nettoyage, le dépôt de masque et le dépôt d'encre carbone commerciale diluée DuPont BQ242 avant le séchage ou la structuration de l'électrode. L'identification d'un protocole de structuration particulier était un résultat empirique et des difficultés ont été rencontrées en raison de la variété des différents paramètres du processus. La prise en compte, par exemple, d'une étape de la température du procédé n'a été jugée importante que dans la mesure où sa modification fortuite a affecté les résultats. Pour la suite du projet, il était important de maintenir un équilibre entre des études détaillées des paramètres et une évaluation de l'intérêt pratique de la technique.
Un facteur d'incertitude a été introduit par la diminution de la fiabilité de l'équipement des fluides supercritiques pendant la saison froide de l'année, ce qui a entraîné des temps de pressurisation légèrement plus longs de la cellule et un nombre considérable de tentatives infructueuses. Des adaptations techniques peuvent résoudre ce problème dans un avenir potentiel.

# Résumé du chapitre II: La structuration d'une encre carbone et caractérisation

Le protocole de caractérisation des électrodes visait principalement à trouver des moyens d'étudier le degré de structuration et de porosité. En raison de la nature des tech-

niques physiques et électrochimiques, les résultats donnent un aperçu de différents types d'informations structurelles qui peuvent être liées à la surface, aborder la surface et le volume en parallèle ou se rapporter aux sites électrochimiquement actifs / accessibles. Ainsi, il a été jugé essentiel de comparer une variété de techniques pour évaluer si les résultats présentaient des tendances similaires. En outre, la faisabilité technique, la réalisabilité et la facilité d'exécution des mesures étaient intéressantes.
La microscopie optique et numérique s'est avérée idéale pour une vérification visuelle rapide de la structuration générale du succès. Cependant, l'estimation de la taille des pores nécessite un équipement très avancé et augmente considérablement le temps de mesure. Les techniques physiques comme le SEM imposent une préparation d'échantillons et des connaissances techniques particulières, mais représentent l'étalon-or afin de descendre visuellement à des résolutions spatiales dans la gamme nanométrique. Toutes les techniques de génération d'images exigent un traitement d'images pour obtenir des informations quantitatives. Les limites résident dans la mise au point sur la surface, car la rupture des électrodes impliquait une perte de structure. Les mesures d'adsorption d'azote ont été considérées comme difficiles à réaliser en raison de la grande quantité requise de matériau d'échantillonnage. Bien que cela dépende de l'ASS de l'échantillon et puisse être amélioré, la technique reste chronophage.
La surface spécifique$_{BET}$ a été estimé à 10 $m^2$ et suggérait un faible degré de développement structurel. Une corrélation avec les images SEM consistait en l'identification d'un léger degré de structure dans la dimension de 50-100 nm, expliquant potentiellement l'hystérésis indiquée dans l'isotherme adsorption-désorption. Bien que la technique n'ait pas été utilisée dans le projet, elle a fourni un aperçu important et est d'un intérêt possible pour la répétition avec un adsorbant de pression de vapeur plus faible comme krypton. Une technique alternative, exigeant des niveaux plus élevés de réglementations de sécurité, pourrait être la porosimétrie au mercure.

Les techniques de caractérisation électrochimiques représentent des moyens polyvalents et bien adaptés pour étudier le comportement des électrodes, en particulier lorsque les méthodes physiques atteignent leurs limites. La variété des techniques permet de conclure non seulement sur l'ESS, la nature du transfert de charge, mais aussi d'interpréter indirectement le degré de structuration via les caractéristiques liées à la diffusion. Cependant, de petits changements dans le traitement des échantillons peuvent affecter de manière significative les résultats et une attention particulière est nécessaire pour garantir la comparabilité des données.
À titre d'exemple, le caractère hydrophile des électrodes structurées nécessitait une amélioration pour permettre le mouillage et un traitement au plasma à l'oxygène a été effectué. En conséquence, les effets du traitement au plasma et de la structuration ont été techniquement superposés et des études comparatives sur des électrodes non structurées ont été nécessaires pour interpréter les résultats, comme détaillé dans le chapitre III. L'écriture du script Python a été jugée nécessaire pour extraire des données quantitatives des données CV et on ne sait pas pourquoi l'outil logiciel fourni par le fabricant du potentiostat imposait des limitations. Le niveau d'incertitude discuté concernant les frais calculés doit être gardé à l'esprit pour une discussion quantitative plus approfondie.
La chronoampérométrie et l'EIS présentent d'autres méthodes établies pour la caractérisation des électrodes. Afin de fournir des résultats significatifs sur les électrodes structurées, il a été constaté qu'un bon mouillage des électrodes structurées était nécessaire, expliquant l'inclusion d'un certain temps de mouillage dans les protocoles de caractérisation. Directement liée est la théorie différente qui différencie l'électrochimie sur les électrodes non poreuses et poreuses, d'une importance particulière pour l'interprétation et l'évaluation des données dans les chapitres suivants.

# Résumé du chapitre III: Les études des paramètres de procès

L'objectif de ce chapitre était l'étude détaillée des paramètres du processus de structuration sur la génération de porosité et sur l'évolution du comportement électrochimique. Le choix des paramètres étudiés était basé sur l'hypothèse que les solutions polymères et les encres conductrices diluées se comportent de manière similaire lors de l'exposition au $CO_2$ supercritique.
Les électrodes structurées ont été étudiées par une sélection de techniques de caractérisation physique et électrochimique de nature complémentaire. En raison de la différence intrinsèque des techniques, les résultats ont été comparés avec soin, en particulier lors de la comparaison avec les valeurs de la littérature. L'évaluation qualitative des résultats représente le principal intérêt du chapitre. En général, les résultats ont été normalisés à la surface géométrique de l'électrode ou au poids de l'électrode pour éliminer l'incertitude découlant de la préparation de l'échantillon.

La microscopie numérique a fourni un moyen de vérifier visuellement l'état physique des électrodes pour les fissures ou les zones délaminées. De plus, les outils logiciels ont permis d'estimer la porosité globale par reconstruction de la hauteur et du volume. Bien que les résultats quantitatifs soient controversés, la technique est principalement rapide et permet d'identifier les tendances par rapport aux changements dans le protocole de structuration.
Le principal avantage de la microscopie électronique secondaire réside dans la résolution de l'image, qui a permis d'étudier en détail la morpholgie et lastructuration de l'électrode. L'application d'un traitement d'images était nécessaire pour caractériser la taille des pores et la porosité de surface, présentant un potentiel d'amélioration supplémentaire.
En outre, une imagerie exploratoire des sections transversales des électrodes a été réalisée. La préparation des échantillons s'est avérée difficile et offre toujours une marge d'optimisation. La tomographie aux rayons X pourrait représenter une alternative non destructive potentielle pour étudier la porosité en vrac, mais la technique n'est pas facilement accessible et coûteuse.

Les techniques électrochimiques permettaient d'accéder à la majeure partie des électrodes et comprenaient des études de voltampérométrie cyclique capacitive et faradique dans un électrolyte de base et utilisant la sonde redox de la sphère externe ruthénium hexamine. L'évolution du courant capacitif, corrélée à la génération d'une surface spécifique, a représenté des changements dans la porosité des électrodes et a permis d'estimer les capacités aérales et gravimétriques. Les résultats correspondaient généralement à la littérature sur les électrodes poreuses à base de carbone. L'évolution du courant faradaique, liée à la surface électrochimiquement active, a donné un aperçu du transfert de charge et du transfert de masse. Les études chronoampérométriques ont été incluses comme méthode alternative rapide pour déterminer la surface électroactive.
La spectroscopie d'impédance électrochimique a été considérée comme permettant de distinguer la réponse capacitive et pseudo-capacitive des électrodes. Bien que la technique fournisse une forte densité d'informations, l'interprétation détaillée semblait limitée par l'incertitude associée à l'ajustement de circuits équivalents.

Le rapport entre le temps de séparation et le temps de saturation a été étudié, en maintenant un temps d'exposition total constant. En microscopie numérique, la hauteur et le volume estimés ont culminé pour les dépôts de 10/20 ($t_{sep}/t_{sat}$). La comparaison des images SEM avec les travaux publiés sur la séparation de phase des solutions polymères a mis en évidence la similitude visuelle et a suggéré une séparation de phase assistée par

fluide supercritique comme mécanisme principal de génération de structure. Le caractère hautement interconnecté et la porosité ouverte étaient corrélés avec la teneur en polymère probablement faible de l'encre diluée. La structure semblait décorée de caractéristiques à l'échelle nanométrique, potentiellement composées de polymères agglomérés et de particules de carbone. La porosité de surface estimée était la plus importante pour les dépôts de 20/10 ($t_{sep}/t_{sat}$) et présentait une distribution bimodale de la taille des pores.
Les électrodes structurées présentaient un caractère pseudo-capacitif prononcé, lié au traitement au plasma à l'oxygène. La capacité de double couche calculée était comparable à la littérature sur les électrodes de carbone structurées. Les courants faradiques ont augmenté d'un ordre de grandeur, tout en indiquant une diffusion de type couche mince au lieu de la diffusion linéaire semi-infinie qui s'applique aux électrodes non structurées. Les résultats soutiennent la création de porosité, tout en confirmant le transfert de charge quasi réversible.
L'altération du comportement de diffusion a été confirmée par chronoampérométrie, ce qui a conduit à une estimation de l'augmentation de la surface électroactive de plus de deux ordres de grandeur. La détermination de la capacité par spectroscopie d'impédance a généralement confirmé les résultats précédents, avec la plus grande capacité attribuée aux dépôts 20/10 ($t_{sep}/t_{sat}$).

L'étude du temps de séparation variable à un temps de saturation constant de 30 min visait à fournir une meilleure compréhension de la séparation de phase et de la mousse. Le choix du temps de saturation a suivi l'idée de solubiliser une quantité maximale de $CO_2$ dans le polymère, tout en permettant à l'EGDA résiduel de diffuser dans le $CO_2$.
La hauteur et les volumes reconstruits ont culminé pour les dépôts 10/30 et 20/30 ($t_{sep}/t_{sat}$). Les résultats pour des temps de séparation plus longs ont indiqué un effet néfaste concernant la structuration. Bien que cela ait donné un aperçu important de la période de temps nécessaire pour que la génération structurelle d'intérêt se produise, cela n'équivaut pas automatiquement à la fin du processus de démélange. Le traitement d'images SEM a permis d'attribuer les plus petits pores générés aux dépôts 20/30 ($t_{sep}/t_{sat}$), ainsi que la plus petite porosité de surface.
La capacité gravimétrique a augmenté d'un facteur de près de 40, dépassant la littérature. Les plus grandes surfaces électroactives ont été trouvées pour les électrodes 20/30 ($t_{sep}/t_{sat}$). La surface électroactive déterminée par chronoampérométrie a culminé à environ 100 m $^2$ / g pour la même électrode. La capacité normalisée correspondante à double couche dans l'étude d'impédance a été calculée à 4,9 mF / cm $^2$. Sur la base des résultats généralement plus importants, une influence bénéfique du temps de saturation plus long de 30 min est conclue dans les circonstances expérimentales.

L'interprétation de la température de saturation est basée sur l'hypothèse que la séparation de phase majeure n'est pas terminée pour des temps de séparation inférieures à 10 ou 20 min, ce qui met en œuvre un chevauchement potentiel de mécanismes. La séparation de phase polymère et la mousse sont théoriquement sensibles aux changements de température dus à la densité de $CO_2$ modifiée et à la température de transition vitreuse du polymère. Des dépôts plus minces ont été récupérés pour une température de saturation élevée, en particulier pour $t_{sep}$ de 0 min, indiquant la formation de pores plus petits et/ou d'une porosité globale moindre. Avec l'absence générale de la couche supérieure en forme de membrane, suggérant un démélange plus lent, les observations s'alignent sur une densité réduite de $CO_2$ à des températures plus élevées.
Les images SEM ont donné un nombre de pores de surface plus faible, une taille de pores accrue et des zones couvertes légèrement plus grandes, par rapport à une température de saturation plus basse. Les capacités maximales étaient légèrement plus faibles pour

une température de saturation plus élevée, s'alignant également sur des pores plus grands et une surface spécifique plus petite. La littérature suggère une viscosité réduite des polymères comme facteur de croissance des pores. Les études de courant faradique ont mis l'accent sur la diffusion en couche mince en particulier pour l'électrode 20/30 ($t_{sep}/t_{sat}$). Des surfaces électroactives plus petites par rapport à des $T_{sat}$ plus faibles ont été confirmées par chronoampérométrie. Les études d'impédance conduisent à des observations intéressantes consistant en une région résistive étendue à basse impédance à hautes fréquences et un caractère plus idéal de la capacité.

Une difficulté est née de la composition inconnue de l'encre, en particulier en ce qui concerne la teneur en liant polymère. Les mécanismes complexes de diffusion et de convection jouent un rôle dans la séparation des phases, et différentes compositions du système ternaire peuvent subir différents types de démélange, générant différentes structures. Dans ce contexte, l'étude de la dilution de l'encre a fourni un moyen d'estimer l'effet sur le mécanisme de séparation de phase.
Pour une dilution élevée de l'encre, les dépôts étaient très filigranes, mais fragiles. La teneur globale en solides plus faible a réduit l'interconnectivité de la structure, comme prévu. L'impression visuelle soutenait l'idée d'une séparation de phase rapide et cinétique. Une hauteur/un volume de dépôt plus faible a été attribué à une faible dilution de l'encre, auquel cas le démélange thermodynamique a été soupçonné de dominer la génération de structure. Des surfaces homogènes à structure uniforme ont été obtenues pour les encres de faible dilution. La porosité de surface la plus élevée et les diamètres de pores les plus grands ont été déterminés pour les électrodes correspondant aux dilutions 3:7 et 4:6 (encre:EGDA).
En fonction de la génération de volume, les capacités extraites des voltammogrames cycliques augmentaient généralement avec la dilution de l'encre. Les études faradiques actuelles ont mis en avant la diffusion de type couche mince, en particulier pour une dilution modérée de l'encre, ainsi que les plus grandes surfaces électroactives. La tendance a été confirmée par la chronoampérométrie, avec une estimation quantitative accrue jusqu'à 122 $m^2$ / g pour la dilution 4: 6 (encre: EGDA). La capacité à double couche déterminée par spectroscopie d'impédance a culminé pour les dilutions 3:7 et 4:6 (encre:EGDA) et la tendance était incohérente avec l'étude du courant capacitif.

L'influence de la pression du procédé n'a pas été étudiée expérimentalement. La littérature suggère d'étudier son influence pour chaque système ternaire particulier, mais des observations générales ont été rapportées. Le démélange lent favorise la génération d'une structure homogène sans couches supérieures minces en forme de membrane, ce qui implique que le choix d'une pression réduite[16]. D'autre part, on pense que la mousse bénéficie d'une pression accrue de $CO_2$, mais ce sujet est couvert de manière controversée dans la littérature. Le taux de dépressurisation est considéré comme un paramètre plus important. Des taux plus rapides ont favorisé des densités de pores plus élevées, c'est-à-dire des diamètres de pores plus petits dans les références.

L'étude des paramètres du procédé a permis d'identifier un protocole de structuration optimale pour la fonctionnalisation des électrodes. En particulier, un temps de séparation de 20 min, un temps de saturation de 30 min et une température de saturation de 40 textcelsius ont été choisis pour une dilution 4: 6 (encre: EGDA). Les critères de décision étaient l'homogénéité de la surface et le développement de surfaces spécifique et électroactive. Un avantage de la dilution modérée de l'encre était la suppression de la fine couche d'adhérence favorisant l'encre non diluée, directement avant le dépôt de l'encre de dilution. L'interprétation des résultats a été jugée facilitée par la suppression d'une

[16] 8 MPa dans ce contexte est considéré comme faible

variable.

Les questions ouvertes concernent l'optimisation du processus de séparation de phase et de moussage, pour lequel la littérature a suggéré de fonctionner à un protocole de pression en deux étapes, en plus du protocole de température en deux étapes. Cette modification pourrait permettre de créer avec précision des structures bimodales, dans lesquelles les pores pourraient supporter soit la diffusion, soit le stockage de charge. Pour étudier plus avant la génération structurelle, l'étude des coupes transversales est considérée comme essentielle et nécessite des techniques adaptées.
Pour des études précises sur la génération structurelle, la simulation du démélange thermodynamique et cinétique pourrait compenser le travail expérimental fastidieux. Cependant, la connaissance détaillée des bases thermodynamiques et des informations particulières du système étudié, telles que les coefficients de diffusion, les paramètres de solubilité et l'interaction avec les particules conductrices, ne doit pas être sous-estimée. Pour confirmer la présence d'EGDA résiduel, une technique d'analyse chimique supplémentaire doit être ajoutée au protocole.

# Résumé du chapitre IV: Capteurs sensibles au peroxide d'hydrogène

La fonctionnalisation des électrodes de carbone poreux, préparées au moyen d'une structuration assistée par $CO_2$ supercritique, a suivi le protocole optimal déterminé précédemment. Cette étape a été motivée par l'intérêt d'explorer l'application pratique de l'électrode. La détection électrochimique de $H_2O_2$, une molécule de grand intérêt médical et industriel, a été choisie en raison du large éventail de la littérature disponible et des possibilités de détection.

Dans une première tentative, le protocole de structuration a été transféré à une encre de carbone commerciale contenant un composé électrochimique à base de fer, le bleu de Prusse (PB), qui est utilisé depuis longtemps pour la détection non-enzymatique de $H_2O_2$. La récupération d'électrodes poreuses a été confirmée par SEM, suggérant la structuration réussie de cette seconde encre, malgré sa composition exacte inconnue. Il a été possible d'améliorer la technique de préparation de l'échantillon pour l'imagerie SEM en coupe transversale.
La caractérisation électrochimique au moyen de CV a permis d'enregistrer la réponse caractéristique du médiateur redox dans le cas des électrodes non structurées. Le caractère capacitif ou pseudo-capacitif, respectivement, des électrodes structurées a été mis en évidence, confirmant les mesures EIS. Cependant, la signature du PB n'était que faiblement exprimée après la structuration, ce qui a été interprété comme un signe de perte de médiateur. Cette hypothèse a été confirmée par la suite au moyen de mesures XPS qui ont été effectuées par le Dr. Lukasz Borowik du PFNC au CEA Grenoble. Les spectres à haute résolution correspondant aux niveaux du noyau de fer et d'azote, caractéristiques du médiateur, ne présentaient pas de pics significatifs. La solubilité potentielle et partielle du médiateur dans le $scCO_2$ a été supposée, ce qui implique son extraction de l'encre et spécifiquement dans les régions proches de la surface.
Les réponses des électrodes à $H_2O_2$ ont été étudiées en mode chronoampérométrique à de petits potentiels négatifs de WE. Les mesures ont donné des sensibilités plus faibles pour les électrodes structurées, conformément à la perte de médiateur. En outre, il a été noté que l'augmentation de la surface spécifique a entraîné une réduction des niveaux de bruit et, par conséquent, une amélioration de la limite de détection.

Pour contourner le problème de la perte de matériau électroactif pendant le processus

de structuration, l'adsorption de la peroxydase de raifort (HRP) sur des électrodes de carbone structurées a été étudiée. Une partie de l'intérêt pour la préparation de biocapteurs enzymatiques était de profiter de la surface spécifique et électroactive développée dans la masse de l'électrode, fournissant une protection physique pour la structure enzymatique généralement fragile.
Une caractérisation électrochimique générale de base des électrodes telles qu'obtenues a été effectuée. Elle a principalement indiqué la nature capacitive, comme résultat de la structuration, via la voltammétrie cyclique et la spectroscopie d'impédance.
La performance de détection a été vérifiée en effectuant des additions de $H_2O_2$ en mode ampérométrique à un potentiel WE négatif. Principalement, l'augmentation de la sensibilité des électrodes structurées par un facteur compris entre 6 et 35 a été révélée, en fonction de la gamme de concentration. En comparaison avec la littérature, cette valeur est considérée comme comparable par rapport à d'autres approches, qui reposent sur des matériaux plus complexes et une préparation plus sophistiquée des électrodes.
Ces observations sont d'un grand intérêt pour la préparation de capteurs multi-enzymatiques, où la HRP est par exemple couplée à la glucose-oxydase ou à la lactase, qui génèrent $H_2O_2$ comme sous-produit. Ces cascades enzymatiques sont couramment utilisées pour la préparation d'une variété de capteurs de grand intérêt médical, par exemple pour la détection du glucose.

Les études sur la HRP présentent un autre potentiel d'amélioration du protocole d'adsorption, par exemple en déposant la HRP sur les électrodes dans des conditions acides, ce qui était dans le passé lié à une meilleure performance du capteur [183]. Avec le même objectif, d'autres groupes ont ajouté du sucre aux solutions enzymatiques pour maintenir une conformation compacte de l'enzyme pendant l'étape d'adsorption [**?**].
Dans certains cas, la HRP a été solubilisée dans du $scCO_2$ et déposée sur des matériaux préstructurés, pour favoriser l'infiltration par l'enzyme [196]. Ceci, en particulier, est considéré comme très prometteur pour une adaptation ultérieure du procédé $scCO_2$, qui permet principalement d'ajouter une étape dynamique d'écoulement fluide. Cette étape pourrait être située après la séparation de phases, avant la phase de saturation, et permettrait ainsi de préparer des biocapteurs poreux enzymatiques en un seul traitement, rapide et technologiquement simple.

Au cours du projet, plusieurs études supplémentaires ont été réalisées dans le contexte de la détection de $H_2O_2$, mais n'ont pas pu être incluses dans le manuscrit. En particulier, une deuxième encre de carbone médiée a été structurée, contenant le médiateur phtalocyanine de cobalt. Les électrodes respectives ont été testées en mode ampérométrique à une polarisation WE de 0,7 V. Les résultats ont été plus prometteurs que dans le cas du PB et ont consisté en de légères améliorations de la sensibilité, du bruit et de la limite de détection.
Afin de profiter de la structure générée des électrodes de carbone, les électrodépositions de PB, de PB dans une matrice PEDOT et de Pt ont été réalisées dans des études séparées. Les résultats ont révélé un intérêt mitigé. En particulier, le PB-PEDOT est apparu prometteur pour une optimisation du protocole de déposition. En parallèle, certaines difficultés intrinsèques à la combinaison d'un processus d'électrodéposition avec des électrodes poreuses sont apparues.
L'application des électrodes de carbone structurées pour le biosensing a été étudiée plus avant en adsorbant l'enzyme tyrosinase pour préparer des capteurs de dopamine. Les résultats ont mis en évidence l'amélioration des performances de détection des électrodes structurées, ce qui est considéré comme un facteur important pour évaluer les perspectives

du projet.

# Conclusions générales

Les études réalisées dans le cadre de ce projet de doctorat s'inscrivent dans le contexte du développement de matériaux en carbone structurés et poreux pour des applications électrochimiques. Les électrodes dans les technologies de détection dans le domaine médical, environnemental et industriel, ainsi que dans les applications de stockage d'énergie, ont été améliorées dans les recherches passées en augmentant l'interface électrode/électrolyte. Comme la grande majorité des méthodes présentées présentent des inconvénients, tels que de longs temps de préparation dus à des approches complexes en plusieurs étapes, ainsi que les risques pour la sécurité et l'environnement liés à l'utilisation de réactifs agressifs, une méthode de structuration alternative a été testée.

La méthode industrialisée de fabrication des électrodes, basée sur le dépôt d'une encre conductrice, a été combinée à un traitement **innovant de structuration en une étape** basé sur le $CO_2$ supercritique. Le protocole de traitement a été choisi dans l'intention d'unifier deux mécanismes de génération de pores, la **séparation de phase assistée par fluide supercritique** et la **moussage par $CO_2$ supercritique** avec la **extraction du solvant**. Les électrodes telles qu'elles ont été obtenues n'ont pas nécessité d'étape supplémentaire de durcissement ou de séchage pendant la fabrication.
La comparabilité des résultats a été assurée par l'application d'un ensemble commun de techniques complémentaires de caractérisation physique et électrochimique tout au long de l'étude. Ainsi, les informations relatives à la surface et au volume de l'électrode ont pu être étudiées et liées à la modification des paramètres de structuration. Ces derniers ont été systématiquement modifiés dans des études séparées. Leur effet sur la formation de pores et la génération de surface a été principalement évalué de manière qualitative, dans le but d'identifier un protocole de traitement optimal. L'évaluation quantitative était potentiellement limitée, mais les résultats se situent généralement dans des fourchettes compatibles avec la littérature sur les électrodes poreuses.

Le **rapport du temps de séparation de phase au temps de saturation du polymère ($\mathbf{t}_{sep}/\mathbf{t}_{sat}$)** a été introduit, afin de confirmer à la fois l'occurrence de la séparation de phase et du moussage du polymère. En effet, les résultats suggèrent généralement un mécanisme combiné pour l'encre diluée à l'étude. Une génération multimodale de tailles de pores a été identifiée, avec les plus grands pores mesurant environ 10 µm, une population majeure de pores mesurant plusieurs 100 nm de diamètre et les plus petites structures mesurant moins de 100 nm. Les valeurs les plus élevées de capacité spécifique ont été déterminées pour un rapport $t_{sep}/t_{sat}$ de 20/10. Les mêmes électrodes ont donné les plus grandes surfaces spécifiques et électroactives, correspondant à une augmentation d'environ 7 par rapport à la surface géométrique de l'électrode ($A_{geo}$).

Dans la **étude du temps de séparation variable à temps de saturation constant**, $t_{sat}$ a été fixé à un temps long pour favoriser l'extraction du solvant et le moussage du polymère, tandis que le reste du protocole a été maintenu comme précédemment. Pour des temps de séparation de l'ordre de 10 à 20 min, les électrodes présentaient le plus petit diamètre de pore de surface. Ceci était en corrélation avec les valeurs de capacité les plus élevées, les courants faradiques les plus importants et le plus grand volume développé. Les électrodes étaient donc associées à la plus grande surface spécifique et électroactive, qui augmentait par des facteurs 12 et 14 par rapport à $A_{geo}$.

Dans l'étude de la **température du procédé**, les $T_{sat}$ plus élevées ont été étudiées en

fonction de leur effet sur le moussage du polymère. Les autres paramètres du processus ont été modifiés comme précédemment. Les techniques d'imagerie ont suggéré une cohérence visuelle élevée entre les électrodes et potentiellement la perte d'une couche superficielle semblable à une membrane qui est généralement formée dans les processus de séparation de phase. La taille des pores et le volume total des pores étaient les plus grands pour des $t_{sep}$ entre 10 et 20 $t_{sep}$, en corrélation avec un nombre de pores plus faible. Alors que les courants capacitifs semblent inchangés, les courants faradiques ont été réduits dans une certaine mesure. Il a été conclu que l'augmentation de la température du processus dans la gamme étudiée a eu un effet légèrement préjudiciable sur la génération de la surface. D'autre part, les résultats ont à nouveau confirmé la tendance des valeurs maximales pour les temps de séparation autour de 20 min, ce qui a permis de proposer un protocole de structuration optimisé.

La modification de la dilution de l'encre représente un sujet d'investigation très intéressant et a été étudiée sur des électrodes, préparées en utilisant le protocole optimal identifié. Outre les caractéristiques mécaniques, la génération de pores et le comportement électrochimique ont pu être modifiés. Les plus grandes surfaces spécifiques ont été associées à l'encre hautement diluée du ratio 3:17 (encre:EGDA, w/w). Le développement maximal de la surface faradique, cependant, a été trouvé pour les encres de dilution relativement faible (4:6, 3:7 et 2:8).
Une observation générale faite pour les électrodes structurées consistait en l'effet sur la diffusion et la migration, respectivement, des analytes. Le comportement électrochimique indiquait une diffusion de type " couche mince ", caractéristique des espèces redox confinées dans une électrode poreuse, ce qui distinguait les électrodes de leurs équivalents non structurés. Pour la fonctionnalisation de l'électrode, elle a été considérée comme ayant un potentiel pratique élevé.

Le transfert de la technique de structuration à d'autres encres commerciales contenant des médiateurs redox pour la préparation de capteurs électrocatalytiques, sensibles au peroxyde d'hydrogène, a été étudié. Le protocole de structuration a d'abord été considéré comme un succès, mais des études plus détaillées sont possibles. Bien que les résultats des électrodes structurées suggèrent une réduction du bruit, la perte potentielle de médiateur dans le $CO_2$ supercritique a été suspectée.
D'autre part, l'adsorption de l'enzyme peroxydase de raifort (HRP) dans les électrodes préstructurées a conduit à une nette amélioration des performances du biocapteur dans la détection du peroxyde d'hydrogène. La sensibilité au peroxyde d'hydrogène a augmenté d'un ordre, ce qui est en corrélation générale avec l'augmentation de la surface spécifique et électroactive étudiée précédemment.

**Des études complémentaires** sont en partie encore en cours d'investigation et ne sont donc pas incluses dans le manuscrit:

- Les électrodes structurées ont été étudiées pour la préparation des **électrodes sensibles aux ions** (ISE) [197]. Dans ce projet, les électrodes de carbone structurées ont été fonctionnalisées par le dépôt d'une membrane polymère contenant des ionophores. Les ISE sensibles au potassium ainsi obtenues étaient opérationnelles, mais aucune amélioration du signal ou réduction du bruit n'a été obtenue. En particulier, la viscosité de la solution de la membrane a été suspectée de présenter un potentiel d'optimisation supplémentaire, afin de permettre l'infiltration du réseau filigrane. En outre, le choix d'un solvant moins agressif, c'est-à-dire n'entraînant pas la dissolution du liant polymère, est nécessaire pour préserver la structure. En outre, le caractère hydrophobe des électrodes de carbone astructurées est potentiellement bénéfique pour supprimer la formation d'une couche aqueuse à l'interface

transducteur/collecteur. Cette problématique a été soulignée dans des travaux antérieurs [198]. L'utilisation d'un matériau intrinsèquement hydrophobe est potentiellement bénéfique pour favoriser la longévité de l'ISE.

- L'incorporation de particules $TiO_2$ anatase dans une encre de carbone commerciale a été étudiée pour une application dans la détection du glucose ou du cholestérol, par exemple. Salerno et al. ont décrit l'ajout de $TiO_2$ dans des solutions de polycaprolactone avant une structuration assistée par $CO_2$ supercritique[17]. Il est toutefois intéressant de noter que les particules ont servi de charge et que leurs propriétés catalytiques n'ont pas été étudiées. Dans ce projet, les études CV et EIS ont confirmé la génération d'électrodes composites poreuses qui ont généralement présenté des résultats comparables à l'encre de carbone structurée pure. Ainsi, les surfaces spécifiques et électroactives ont été augmentées avec succès. L'effet des particules sur les propriétés catalytiques est encore à l'étude.

- Dans le cadre de la détection de $H_2O_2$, le **électrodéposition de bleu de Prusse (PB)** sur des électrodes de carbone structurées a été réalisée, conduisant à une réduction du bruit et, par conséquent, à des limites de détection plus basses. Alors que la sensibilité à $H_2O_2$ a été augmentée de plus d'un ordre, le PB s'est dissous en milieu aqueux. Afin d'immobiliser le PB, il a été co-électrodéposé dans une matrice PEDOT. Les résultats ont confirmé une amélioration de la limite de détection et de la sensibilité, ainsi qu'une rétention réussie du médiateur. En revanche, le niveau de bruit a augmenté.

- En conséquence des résultats prometteurs obtenus avec la HRP, des biocapteurs à base de tyrosinase ont été préparés pour la détection de la dopamine. Les résultats ont confirmé une sensibilité accrue du capteur pour les électrodes structurées.

**En conclusion, une méthode innovante pour la structuration/ nano-structuration d'électrodes en carbone, basée sur la structuration assistée par le $CO_2$ supercritique d'encre carbone, a été étudiée. Les résultats obtenus tant sur la caractérisation des électrodes, que sur les électrodes fonctionnalisées, sont considérés comme très prometteurs et suggèrent fortement de poursuivre les travaux dans ce domaine.**

# Perspectives

Au cours du projet, l'accent a été mis sur la compréhension des mécanismes de structuration d'un point de vue physique, afin d'obtenir un contrôle sur la structure générée. Cependant, comme l'évaluation de l'utilité pratique était le deuxième intérêt principal, plusieurs questions sont restées sans réponse en raison du temps limité disponible et nécessitent donc une étude plus détaillée.

La **manipulation des mécanismes de séparation de phases** nécessite la connaissance de la composition exacte du système et des informations thermodynamiques sur l'interaction entre solvant et non-solvant. Pour le moussage des polymères, la localisation de la température de transition vitreuse est nécessaire pour le choix correct de la

[17] Bien que décrit comme moussant, un processus de séparation de phase est présumé sur la base des paramètres du processus rapportés, en particulier en raison des conditions de dépressurisation plutôt lentes.

température du procédé. La composition exacte de l'encre carbone commerciale DuPont BQ242 était cependant inconnue. Si le type de particules de carbone dans les encres conductrices appartient généralement à un petit groupe de candidats potentiels, le type et le contenu du liant polymère sont plus difficiles à estimer. De plus, la théorie classique de la séparation des phases ne prend pas en considération les additifs (ici les particules de carbone), qui doivent certainement être pris en compte également. Les raisons peuvent être l'agglomération potentielle, la modification de la viscosité ou l'interaction avec l'une des phases liquides.

Les travaux sur les **formulations d'encre** sont considérés comme essentiels dans une éventuelle poursuite du sujet, pour garantir un contrôle plus précis des paramètres du processus. L'incorporation de différents types de particules conductrices (carbone), par exemple des plaquettes de graphite de différentes tailles, pourrait permettre de ponter les pores et d'augmenter la conductivité des électrodes.
Dans ce contexte, il est également possible d'étudier le potentiel d'incorporation de modèles durs, solubles après une certaine exposition au $CO_2$ supercritique. En outre, la structuration de polymères conducteurs est considérée comme potentiellement intéressante. Des études sur la polymérisation du polypyrrole en présence de $CO_2$ supercritique ont été réalisées [199] [200], suggérant la possibilité d'adapter le processus pour générer des électrodes poreuses.

Le potentiel d'amélioration des techniques de caractérisation, en particulier la préparation des échantillons pour l'imagerie en coupe transversale, est souligné. En outre, les méthodes non destructives permettant d'obtenir des informations complémentaires sur la porosité générée et sur la surface (spécifique) présentent un grand intérêt. Bien qu'il semble irréaliste de réaliser une tomographie aux rayons X pour un grand nombre d'électrodes, la réalisation d'isothermes d'adsorption-désorption de $Kr_2$ pourrait permettre de réduire la masse d'échantillon requise. Les mesures respectives n'ont pas pu être réalisées au cours de la thèse en raison de difficultés techniques avec l'équipement.
Par ailleurs, des techniques telles que la diffusion des rayons X aux petits angles (SAXS) pourraient permettre de mieux comprendre les mécanismes fondamentaux du moussage des polymères, notamment lors de l'étude des composites de polymères et de particules de carbone. Une étude sur le comportement de cristallisation des composites polycaprolactone/MWCNT au moyen de la SAXS a été publiée par Wurm et al. [201]. Des tests initiaux en relation avec des échantillons d'acétate de cellulose ont été réalisés dans le cadre de ce projet[18]. La caractérisation des matériaux composites a été limitée en raison de problèmes techniques avec l'équipement.

Dans le cadre de l'optimisation du protocole de structuration, l'intérêt potentiel de réaliser une **simulation de la structuration combinée** est mis en évidence. La prédiction des paramètres optimaux du processus pour différents systèmes pourrait potentiellement économiser un temps considérable d'expérimentation. Cependant, une telle tâche est assez complexe et repose sur la connaissance approfondie des principes thermodynamiques, des mécanismes de diffusion et la disponibilité de données connexes pour tous les composants en question.

Les électrodes structurées préparées dans ce projet se sont avérées très prometteuses pour une fonctionnalisation avec des enzymes. Il pourrait être intéressant d'utiliser la structuration d'encres conductrices assistée par $scCO_2$ pour la fabrication de biocapteurs ampérométriques à faible coût ou de plateformes multi-enzymatiques, par exemple pour la détection du glucose.

[18]Le travail du Dr. Arnaud de Geyer est hautement apprécié pour la caractérisation des échantillons

En outre, l'observation de la région étendue de basse impédance dans les études SIE est une propriété potentiellement adaptée à d'autres applications. Par exemple, les électrodes utilisées dans la stimulation cérébrale profonde, c'est-à-dire le traitement de troubles neurologiques tels que l'épilepsie ou la maladie de Parkinson.

# Bibliography


[1] Zaheen Ullah Khan, Ayesha Kausar, and Hidayat Ullah. A review on composite papers of graphene oxide, carbon nanotube, polymer/go, and polymer/cnt: Processing strategies, properties, and relevance. *Polymer-Plastics Technology and Engineering*, 55(6):559–581, 2016.

[2] Alain Walcarius. Recent trends on electrochemical sensors based on ordered mesoporous carbon. *Sensors*, 17(8):1863, 2017.

[3] Jimena Castro-Gutiérrez, Alain Celzard, and Vanessa Fierro. Energy storage in supercapacitors: Focus on tannin-derived carbon electrodes. *Frontiers in Materials*, 7:217, 2020.

[4] Theodore F Baumann, Marcus A Worsley, T Yong-Jin Han, and Joe H Satcher Jr. High surface area carbon aerogel monoliths with hierarchical porosity. *Journal of Non-Crystalline Solids*, 354(29):3513–3515, 2008.

[5] S Angus, B Armstrong, KM De Reuck, et al. Carbon dioxide: International thermodynamic tables of the fluid state-3. *Pergamon Press, New York*, 3:266, 1976.

[6] Li Zhang. *The study of phase separation in the miscibility gap and ion specific effects on the aggregation of soft matter system*. PhD thesis, Université Paris Saclay (COmUE); Northwestern Polytechnical University (Chine), 2016.

[7] Konstantin V Pochivalov, Andrey V Basko, Tatiana N Lebedeva, Anna N Ilyasova, Mikhail Yu Yurov, Roman Yu Golovanov, Vladimir V Artemov, Vladimir V Volkov, Alexander A Ezhov, Alexey V Volkov, et al. Thermally induced phase separation in semicrystalline polymer solutions: How does the porous structure actually arise? *Materials Today Communications*, page 102558, 2021.

[8] Yeh Wei Kho, Douglass S Kalika, and Barbara L Knutson. Precipitation of nylon 6 membranes using compressed carbon dioxide. *Polymer*, 42(14):6119–6127, 2001.

[9] Albertus Johannes Reuvers. Membrane formation: diffusion induced demixing processes in ternary polymeric systems. *Enschede, The Netherlands: Twente University*, 1987.

[10] Chia-wen Carmen Hsieh. *Effect of molecular structure on the viscoelastic properties of cellulose acetate in a ternary system*. PhD thesis, University of British Columbia, 2010.

[11] P Van de Witte, PJ Dijkstra, JWA Van den Berg, and J Feijen. Phase separation processes in polymer solutions in relation to membrane formation. *Journal of membrane science*, 117(1-2):1–31, 1996.

[12] Charles A Jones, Amy Zweber, James P DeYoung, James B McClain, Ruben Carbonell, and Joseph M DeSimone. Applications of "dry" processing in the microelectronics industry using carbon dioxide. *Critical Reviews in Solid State and Materials Sciences*, 29(3-4):97–109, 2004.

[13] D Sanli, SE Bozbag, and C Erkey. Synthesis of nanostructured materials using supercritical co 2: Part i. physical transformations. *Journal of Materials Science*, 47(7):2995–3025, 2012.

[14] A Hamelin. Cyclic voltammetry at gold single-crystal surfaces. part 1. behaviour at low-index faces. *Journal of Electroanalytical Chemistry*, 407(1-2):1–11, 1996.

[15] E Reverchon and S Cardea. Formation of cellulose acetate membranes using a supercritical fluid assisted process. *Journal of Membrane Science*, 240(1-2):187–195, 2004.

[16] Stefano Cinti, Fabiana Arduini, Danila Moscone, Giuseppe Palleschi, and Anthony J Killard. Development of a hydrogen peroxide sensor based on screen-printed electrodes modified with inkjet-printed prussian blue nanoparticles. *Sensors*, 14(8): 14222–14234, 2014.

[17] Bo Zhu, Takuro Mizoguchi, Takaaki Kojima, and Hideo Nakano. Ultra-high-throughput screening of an in vitro-synthesized horseradish peroxidase displayed on microbeads using cell sorter. *PloS one*, 10(5):e0127479, 2015.

[18] Shirley Nakagaki, Kelly ADF Castro, Maria da Graça PMS Neves, Maria do Amparo Faustino, and Yassuko Iamamoto. The research on porphyrins and analogues in brazil: A small review covering catalytic and other applications since the beginning at universidade de são paulo in ribeirão preto until the joint venture between brazilian researchers and colleagues from universidade de aveiro, portugal. *Journal of the Brazilian Chemical Society*, 30(12):2501–2535, 2019.

[19] Tautgirdas Ruzgas, Elisabeth Csöregi, Jenny Emnéus, Lo Gorton, and György Marko-Varga. Peroxidase-modified electrodes: fundamentals and application. *Analytica Chimica Acta*, 330(2-3):123–138, 1996.

[20] Charles M Hansen. *Hansen solubility parameters: a user's handbook*. CRC press, 2007.

[21] Martin JD Clift, Kirsten Dobson, Geoffrey Hunt, Peter Gehr, Barbara Rothen-Rutishauser, Iseult Lynch, and Flemming Cassee. Nanoimpactnet nomenclature, 2010.

[22] Dieter Neuschutz. State and trends of the electric arc furnace technology. *High Temperature Material Processes: An International Quarterly of High-Technology Plasma Processes*, 4(1), 2000.

[23] Wenjing Yuan, Yu Zhou, Yingru Li, Chun Li, Hailin Peng, Jin Zhang, Zhongfan Liu, Liming Dai, and Gaoquan Shi. The edge-and basal-plane-specific electrochemistry of a single-layer graphene sheet. *Scientific reports*, 3(1):1–7, 2013.

[24] M Kavitha and AM Kalpana. Carbon nanotubes: Properties and applications-a brief review. *i-manager's Journal on Electronics Engineering*, 7(3):1, 2017.

[25] ON Shornikova, EV Kogan, NE Sorokina, and VV Avdeev. The specific surface area and porous structure of graphite materials. *Russian Journal of Physical Chemistry A*, 83(6):1022–1025, 2009.

[26] Jay Janzen and Gerard Kraus. Specific surface area measurements on carbon black. *Rubber Chemistry and Technology*, 44(5):1287–1296, 1971.

[27] Patrice Simon and Andrew Burke. Nanostructured carbons: double-layer capacitance and more. *The electrochemical society interface*, 17(1):38, 2008.

[28] Songtao Zhang, Mingbo Zheng, Zixia Lin, Nianwu Li, Yijie Liu, Bin Zhao, Huan Pang, Jieming Cao, Ping He, and Yi Shi. Activated carbon with ultrahigh specific surface area synthesized from natural plant material for lithium–sulfur batteries. *Journal of Materials Chemistry A*, 2(38):15889–15896, 2014.

[29] Andreas Stein, Zhiyong Wang, and Melissa A Fierke. Functionalization of porous carbon materials with designed pore architecture. *Advanced Materials*, 21(3):265–293, 2009.

[30] Mehulkumar A Patel, Feixiang Luo, Keerthi Savaram, Pavel Kucheryavy, Qiaoqiao Xie, Carol Flach, Richard Mendelsohn, Eric Garfunkel, Jenny V Lockard, and Huixin He. P and s dual-doped graphitic porous carbon for aerobic oxidation reactions: enhanced catalytic activity and catalytic sites. *Carbon*, 114:383–392, 2017.

[31] Yimin Sun, Shaohong Luo, Helei Sun, Wei Zeng, Chenxi Ling, Dugang Chen, Vincent Chan, and Kin Liao. Engineering closed-cell structure in lightweight and flexible carbon foam composite for high-efficient electromagnetic interference shielding. *Carbon*, 136:299–308, 2018.

[32] RI Baxter, RD Rawlings, N Iwashita, and Y Sawada. Effect of chemical vapor infiltration on erosion and thermal properties of porous carbon/carbon composite thermal insulation. *Carbon*, 38(3):441–449, 2000.

[33] Hem Prakash Karki, Laxmi Kafle, Devi Prasad Ojha, Jun Hee Song, and Han Joo Kim. Three-dimensional nanoporous polyacrylonitrile-based carbon scaffold for effective separation of oil from oil/water emulsion. *Polymer*, 153:597–606, 2018.

[34] Jie Gong, Guoqun Zhao, Guilong Wang, Lei Zhang, and Bo Li. Fabrication of macroporous carbon monoliths with controllable structure via supercritical co2 foaming of polyacrylonitrile. *Journal of CO2 Utilization*, 33:330–340, 2019.

[35] Yadian Xie, Duygu Kocaefe, Chunying Chen, and Yasar Kocaefe. Review of research on template methods in preparation of nanomaterials. *Journal of Nanomaterials*, 2016, 2016.

[36] Dayoung Lee, Jin-Young Jung, Min-Jung Jung, and Young-Seak Lee. Hierarchical porous carbon fibers prepared using a sio2 template for high-performance edlcs. *Chemical Engineering Journal*, 263:62–70, 2015.

[37] Sining Zheng, Dan Wu, Limei Huang, Mengxin Zhang, Xiuling Ma, Zhangjing Zhang, and Shengchang Xiang. Isomorphic mof-derived porous carbon materials as electrochemical sensor for simultaneous determination of hydroquinone and catechol. *Journal of Applied Electrochemistry*, 49(6):563–574, 2019.

[38] Pei-Xi Wang, Vitor M Zamarion, Wadood Y Hamad, and Mark J MacLachlan. Hard-templating of prussian blue analogues in mesoporous silica and organosilica. *Dalton Transactions*, 44(33):14724–14731, 2015.

[39] Yating Hu, Huajun Liu, Qingqing Ke, and John Wang. Effects of nitrogen doping on supercapacitor performance of a mesoporous carbon electrode produced by a hydrothermal soft-templating process. *Journal of Materials Chemistry A*, 2(30): 11753–11758, 2014.

[40] Nannan Lu, Tingting Zhang, Xiaoyi Yan, Yue Gu, He Liu, Zhiqian Xu, Haixin Xu, Xuwen Li, Zhiquan Zhang, and Ming Yang. Facile synthesis of 3d n-doped porous carbon nanosheets as highly active electrocatalysts toward the reduction of hydrogen peroxide. *Nanoscale*, 10(31):14923–14930, 2018.

[41] Farshad Barzegar, Abubakar A Khaleed, Faith U Ugbo, Kabir O Oyeniran, Damilola Y Momodu, Abdulhakeem Bello, Julien K Dangbegnon, and Ncholu Manyala. Cycling and floating performance of symmetric supercapacitor derived from coconut shell biomass. *AIP Advances*, 6(11):115306, 2016.

[42] Diana Jiménez-Cordero, Francisco Heras, Miguel A Gilarranz, and Encarnación Raymundo-Piñero. Grape seed carbons for studying the influence of texture on supercapacitor behaviour in aqueous electrolytes. *Carbon*, 71:127–138, 2014.

[43] V Thirumal, K Dhamodharan, R Yuvakkumar, G Ravi, B Saravanakumar, M Thambidurai, Cuong Dang, and Dhayalan Velauthapillai. Cleaner production of tamarind fruit shell into bio-mass derived porous 3d-activated carbon nanosheets by cvd technique for supercapacitor applications. *Chemosphere*, page 131033, 2021.

[44] Stephen Fletcher. Screen-printed carbon electrodes. *Electrochemistry of Carbon Electrodes*, pages 425–444, 2015.

[45] Xiao-Li Su, Ming-Yu Cheng, Lin Fu, Jing-He Yang, Xiu-Cheng Zheng, and Xin-Xin Guan. Superior supercapacitive performance of hollow activated carbon nanomesh with hierarchical structure derived from poplar catkins. *Journal of Power Sources*, 362:27–38, 2017.

[46] Santhana Sivabalan Jayaseelan, Sivaprakasam Radhakrishnan, Balasubramaniam Saravanakumar, Min-Kang Seo, Myung-Seob Khil, Hak-Yong Kim, and Byoung-Suhk Kim. Mesoporous 3d nico2o4/mwcnt nanocomposite aerogels prepared by a supercritical co2 drying method for high performance hybrid supercapacitor electrodes. *Colloids and Surfaces A: Physicochemical and Engineering Aspects*, 538: 451–459, 2018.

[47] Yue Li, Qinglei Liu, Danmiao Kang, Jiajun Gu, Wang Zhang, and Di Zhang. Freeze-drying assisted synthesis of hierarchical porous carbons for high-performance supercapacitors. *Journal of Materials Chemistry A*, 3(42):21016–21022, 2015.

[48] Qing-Yun Wu, Ling-Shu Wan, and Zhi-Kang Xu. Crystallizable diluent-templated polyacrylonitrile foams for macroporous carbon monoliths. *Polymer*, 54(1):284–291, 2013.

[49] Adavan Kiliyankil Vipin, Bunshi Fugetsu, Ichiro Sakata, Hideki Tanaka, Ling Sun, Shunitz Tanaka, Mauricio Terrones, Morinobu Endo, and Mildred Dresselhaus. Three dimensional porous monoliths from multi-walled carbon nanotubes and polyacrylonitrile. *Carbon*, 101:377–381, 2016.

[50] Shimon Reich and I Michaeli. Electrical conductivity of small ions in polyacrylonitrile in the glass–transition region. *Journal of Polymer Science: Polymer Physics Edition*, 13(1):9–18, 1975.

[51] Ya-Qiong Wang, Han-Xiong Huang, Bin Li, and Wei-Shan Li. Novelly developed three-dimensional carbon scaffold anodes from polyacrylonitrile for microbial fuel cells. *Journal of Materials Chemistry A*, 3(9):5110–5118, 2015.

[52] A Barroso-Bogeat, M Alexandre-Franco, C Fernández-González, J Sánchez-González, and V Gómez-Serrano. Electrical conductivity of metal (hydr) oxide–activated carbon composites under compression. a comparison study. *Materials Chemistry and Physics*, 152:113–122, 2015.

[53] Lijian Xu, Nongyue He, Jingjing Du, and Yan Deng. Determination of tannic acid by adsorptive anodic stripping voltammetry at porous pseudo-carbon paste electrode. *Electrochemistry communications*, 10(11):1657–1660, 2008.

[54] Ali Babaei, Mohammad Moradi, Masoud Sohrabi, Samira Feshki, and Maziar Marandi. Fabrication of tio2 hollow spheres and its application in modification of carbon paste electrode for simultaneous determination of dopamine and piroxicam in the presence of ascorbic acid. *Journal of Nanostructures*, 8(2):119–130, 2018.

[55] Rajdip Bandyopadhyaya, Einat Nativ-Roth, Oren Regev, and Rachel Yerushalmi-Rozen. Stabilization of individual carbon nanotubes in aqueous solutions. *Nano letters*, 2(1):25–28, 2002.

[56] Ehsan Danesh, Seyed Reza Ghaffarian, and Payam Molla-Abbasi. Non-solvent induced phase separation as a method for making high-performance chemiresistors based on conductive polymer nanocomposites. *Sensors and Actuators B: Chemical*, 155(2):562–567, 2011.

[57] JS Colton and NP_ Suh. The nucleation of microcellular thermoplastic foam with additives: Part i: Theoretical considerations. *Polymer Engineering & Science*, 27 (7):485–492, 1987.

[58] SM Hitchen and JR Dean. Properties of supercritical fluids. pages 1–11. Springer, 1993.

[59] Maartje F Kemmere. Supercritical carbon dioxide for sustainable polymer processes. *Supercritical carbon dioxide: In polymer reaction engineering*, pages 1–14, 2005.

[60] Erdogan Kiran and Joan F Brennecke. Current state of supercritical fluid science and technology. 1993.

[61] Hulya Peker, MP Srinivasan, JM Smith, and Ben J McCoy. Caffeine extraction rates from coffee beans with supercritical carbon dioxide. *AIChE Journal*, 38(5): 761–770, 1992.

[62] E Reverchon, G Della Porta, and F Senatore. Supercritical co2 extraction and fractionation of lavender essential oil and waxes. *Journal of Agricultural and Food Chemistry*, 43(6):1654–1658, 1995.

[63] Leon JM Jacobs, Maartje F Kemmere, and Jos TF Keurentjes. Sustainable polymer foaming using high pressure carbon dioxide: a review on fundamentals, processes and applications. *Green Chemistry*, 10(7):731–738, 2008.

[64] Sidney Loeb and Srinivasa Sourirajan. Sea water demineralization by means of an osmotic membrane. ACS Publications, 1962.

[65] Heru Susanto and Mathias Ulbricht. Characteristics, performance and stability of polyethersulfone ultrafiltration membranes prepared by phase separation method using different macromolecular additives. *Journal of Membrane Science*, 327(1-2): 125–135, 2009.

[66] Nafiu Umar Barambu, Muhammad Roil Bilad, Mohamad Azmi Bustam, Nurul Huda, Juhana Jaafar, Thanitporn Narkkun, and Kajornsak Faungnawakij. Development of polysulfone membrane via vapor-induced phase separation for oil/water emulsion filtration. *Polymers*, 12(11):2519, 2020.

[67] Dong Hwee Kim, Jisu Choi, Young Taik Hong, and Sung Chul Kim. Phase separation and morphology control of polymer blend membranes of sulfonated and nonsulfonated polysulfones for direct methanol fuel cell application. *Journal of membrane science*, 299(1-2):19–27, 2007.

[68] Junyoung Han, Wonseok Lee, Jae Min Choi, Rajkumar Patel, and Byoung-Ryul Min. Characterization of polyethersulfone/polyimide blend membranes prepared by a dry/wet phase inversion: Precipitation kinetics, morphology and gas separation. *Journal of membrane science*, 351(1-2):141–148, 2010.

[69] Marcel Mulder and J Mulder. *Basic principles of membrane technology*. Springer Science & Business Media, 1996.

[70] Joel Henry Hildebrand and Robert Lane Scott. *The solubility of nonelectrolytes*. Reinhold publishing company New York, 1950.

[71] Chien P Hsu, Rong H Guo, Chi C Hua, Cheng-L Shih, Wei-T Chen, and Tien-I Chang. Effect of polymer binders in screen printing technique of silver pastes. *Journal of polymer research*, 20(10):1–8, 2013.

[72] Evan Andrews, Sai Katla, Challa Kumar, Matthew Patterson, Phillip Sprunger, and John Flake. Electrocatalytic reduction of co2 at au nanoparticle electrodes: effects of interfacial chemistry on reduction behavior. *Journal of The Electrochemical Society*, 162(12):F1373, 2015.

[73] Anwar Mohammed and Michael Pecht. A stretchable and screen-printable conductive ink for stretchable electronics. *Applied Physics Letters*, 109(18):184101, 2016.

[74] Marcel Mulder. Preparation of synthetic membranes. In *Basic principles of membrane technology*, pages 71–156. Springer, 1996.

[75] Klaus Kimmerle and Heiner Strathmann. Analysis of the structure-determining process of phase inversion membranes. *Desalination*, 79(2-3):283–302, 1990.

[76] Jung-Ae Lim, Nam-Soo Park, Jin-Soo Park, and Jae-Hwan Choi. Fabrication and characterization of a porous carbon electrode for desalination of brackish water. *Desalination*, 238(1-3):37–42, 2009.

[77] Ethan B Secor, Manuel H Dos Santos, Shay G Wallace, Nathan P Bradshaw, and Mark C Hersam. Tailoring the porosity and microstructure of printed graphene electrodes via polymer phase inversion. *The Journal of Physical Chemistry C*, 122 (25):13745–13750, 2018.

[78] Qian Yang, Xiaqing Wu, Hailong Peng, Longwen Fu, Xingliang Song, Jinhua Li, Hua Xiong, and Lingxin Chen. Simultaneous phase-inversion and imprinting based sensor for highly sensitive and selective detection of bisphenol a. *Talanta*, 176: 595–603, 2018.

[79] Hideto Matsuyama, Hideaki Yano, Taisuke Maki, Masaaki Teramoto, Kenji Mishima, and Kiyoshi Matsuyama. Formation of porous flat membrane by phase separation with supercritical co2. *Journal of Membrane Science*, 194(2):157–163, 2001.

[80] Hideto Matsuyama, Atsushi Yamamoto, Hideaki Yano, Taisuke Maki, Masaaki Teramoto, Kenji Mishima, and Kiyoshi Matsuyama. Effect of organic solvents on membrane formation by phase separation with supercritical co2. *Journal of Membrane Science*, 204(1-2):81–87, 2002.

[81] Hao Zhang, ZG Wang, ZN Zhang, Jin Wu, Jun Zhang, and JS He. Regenerated-cellulose/multiwalled-carbon-nanotube composite fibers with enhanced mechanical properties prepared with the ionic liquid 1-allyl-3-methylimidazolium chloride. *Advanced Materials*, 19(5):698–704, 2007.

[82] Victor Chabot, Drew Higgins, Aiping Yu, Xingcheng Xiao, Zhongwei Chen, and Jiujun Zhang. A review of graphene and graphene oxide sponge: material synthesis and applications to energy and the environment. *Energy & Environmental Science*, 7(5):1564–1596, 2014.

[83] Maria Sarno, Lucia Baldino, Carmela Scudieri, Stefano Cardea, Paolo Ciambelli, and Ernesto Reverchon. Sc-co2-assisted process for a high energy density aerogel supercapacitor: The effect of go loading. *Nanotechnology*, 28(20):204001, 2017.

[84] Maria Sarno, Lucia Baldino, Carmela Scudieri, Stefano Cardea, and Ernesto Reverchon. A one-step sc-co2 assisted technique to produce compact pvdf-hfp mos2 supercapacitor device. *Journal of Physics and Chemistry of Solids*, 136:109132, 2020.

[85] Paolo Alessi, Angelo Cortesi, Ireneo Kikic, and Febe Vecchione. Plasticization of polymers with supercritical carbon dioxide: experimental determination of glass-transition temperatures. *Journal of Applied Polymer Science*, 88(9):2189–2193, 2003.

[86] SG Kazarian. Polymer processing with supercritical fluids. *Polymer science series CC/C of vysokomolekuliarnye soedineniia*, 42(1):78–101, 2000.

[87] Satish K Goel and Eric J Beckman. Generation of microcellular polymeric foams using supercritical carbon dioxide. i: Effect of pressure and temperature on nucleation. *Polymer Engineering & Science*, 34(14):1137–1147, 1994.

[88] Malcolm P Stevens. *Polymer chemistry*, volume 2. Oxford university press New York, 1990.

[89] D Gourgouillon, HMNT Avelino, JMNA Fareleira, and M Nunes Da Ponte. Simultaneous viscosity and density measurement of supercritical co2-saturated peg 400. *The Journal of supercritical fluids*, 13(1-3):177–185, 1998.

[90] Yeong-Tarng Shieh and Huang-Shung Yang. Morphological changes of polycaprolactone with high-pressure co2 treatment. *The Journal of supercritical fluids*, 33(2): 183–192, 2005.

[91] Shutaro Kurosawa, Amyn S Teja, Janusz Kowalik, and Laren Tolbert. Supercritical carbon dioxide processing of conducting composites of polypyrrole and porous crosslinked polystyrene. *Polymer*, 47(9):2997–3004, 2006.

[92] Clémence Nikitine, Elisabeth Rodier, Martial Sauceau, Jean-Jacques Letourneau, and Jacques Fages. Controlling the structure of a porous polymer by coupling supercritical co2 and single screw extrusion process. *Journal of Applied Polymer Science*, 115(2):981–990, 2010.

[93] Natthapong Chuaponpat and Surat Areerat. The effects of foaming conditions on plasticized polyvinyl chloride foam morphology by using supercritical carbon dioxide. *Materials Today: Proceedings*, 5(11):23526–23533, 2018.

[94] Tetsuo Otsuka, Kentaro Taki, and Masahiro Ohshima. Nanocellular foams of ps/pmma polymer blends. *Macromolecular Materials and Engineering*, 293(1):78–82, 2008.

[95] Kelyn A Arora, Alan J Lesser, and Thomas J McCarthy. Preparation and characterization of microcellular polystyrene foams processed in supercritical carbon dioxide. *Macromolecules*, 31(14):4614–4620, 1998.

[96] Aurelio Salerno and Concepción Domingo. Polycaprolactone foams prepared by supercritical co2 batch foaming of polymer/organic solvent solutions. *The Journal of Supercritical Fluids*, 143:146–156, 2019.

[97] D-liver: Eu project designs home care system for liver patients.

[98] M Robert Pinnel and James E Bennett. Qualitative observations on the diffusion of copper and gold through a nickel barrier. *Metallurgical Transactions A*, 7(5): 629–635, 1976.

[99] Lee M Fischer, Maria Tenje, Arto R Heiskanen, Noriyuki Masuda, Jaime Castillo, Anders Bentien, Jenny Émneus, Mogens H Jakobsen, and Anja Boisen. Gold cleaning methods for electrochemical detection applications. *Microelectronic engineering*, 86(4-6):1282–1285, 2009.

[100] Christer Spégel, Arto Heiskanen, Jenny Acklid, Anders Wolff, Rafael Taboryski, Jenny Emnéus, and Tautgirdas Ruzgas. On-chip determination of dopamine exocytosis using mercaptopropionic acid modified microelectrodes. *Electroanalysis: An International Journal Devoted to Fundamental and Practical Aspects of Electroanalysis*, 19(2-3):263–271, 2007.

[101] FG Will and CA Knorr. Untersuchung von adsorptionserscheinungen an rhodium, iridium, palladium und gold mit der potentiostatischen dreieckmethode. *Zeitschrift für Elektrochemie, Berichte der Bunsengesellschaft für physikalische Chemie*, 64(2): 270–275, 1960.

[102] James P Hoare. A cyclic voltammetric study of the gold-oxygen system. *Journal of the Electrochemical Society*, 131(8):1808, 1984.

[103] SES El Wakkad and AM Shams El Din. The anodic oxidation of metals at very low current density. part v. gold. *Journal of the Chemical Society (Resumed)*, pages 3098–3102, 1954.

[104] Dorothy Lozowski. Supercritical co2: A green solvent. *Chemical Engineering*, 117 (2):15, 2010.

[105] Kenneth SW Sing. Reporting physisorption data for gas/solid systems with special reference to the determination of surface area and porosity (recommendations 1984). *Pure and applied chemistry*, 57(4):603–619, 1985.

[106] Arlavinda Rezqita, Raad Hamid, Sabine Schwarz, Hermann Kronberger, and Atanaska Trifonova. Conductive additive for si/mesoporous carbon anode for li-ion batteries: Commercial graphite vs carbon black c65. *ECS Transactions*, 66(9): 17, 2015.

[107] Rongzhong Jiang, Dat T Tran, Joshua P McClure, and Deryn Chu. Increasing the electrochemically available active sites for heat-treated hemin catalysts supported on carbon black. *Electrochimica acta*, 75:185–190, 2012.

[108] Karen Monsalve, Ievgen Mazurenko, N Lalaoui, A Le Goff, M Holzinger, Pascale Infossi, S Nitsche, Jean-Yves Lojou, Marie-Thérèse Giudici-Orticoni, S Cosnier, et al. A h2/o2 enzymatic fuel cell as a sustainable power for a wireless device. *Electrochemistry Communications*, 60:216–220, 2015.

[109] Octavio Garate, Lionel Veiga, Anahí V Medrano, Gloria Longinotti, Gabriel Ybarra, and Leandro N Monsalve. Waterborne carbon nanotube ink for the preparation of electrodes with applications in electrocatalysis and enzymatic biosensing. *Materials Research Bulletin*, 106:137–143, 2018.

[110] Marek Kosmulski. Areal capacitance deserves its own name and symbol, also in colloid chemistry. *Colloids and Surfaces A: Physicochemical and Engineering Aspects*, 623:126652, 2021.

[111] EA Cummings, P Mailley, S Linquette-Mailley, BR Eggins, ET McAdams, and S McFadden. Amperometric carbon paste biosensor based on plant tissue for the determination of total flavanol content in beers. *Analyst*, 123(10):1975–1980, 1998.

[112] AJ Bard and LR Faulkner. *Electrochemical Methods, Fundamentals and Applications*. Wiley Interscience, 1980. 143 pp.

[113] Ralph N Adams. Electrochemistry at solid electrodes. Technical report, M. Dekker,, 1969.

[114] Introducing ec-lab®eis quality indicators: Thd, nsd and nsr. , Bio-Logic Science Instruments, Seyssinet, France, Application note #64, 2018.

[115] Matthew E Suss, Theodore F Baumann, Marcus A Worsley, Klint A Rose, Thomas F Jaramillo, Michael Stadermann, and Juan G Santiago. Impedance-based study of capacitive porous carbon electrodes with hierarchical and bimodal porosity. *Journal of power sources*, 241:266–273, 2013.

[116] Oumaïma Gharbi, Mai TT Tran, Bernard Tribollet, Mireille Turmine, and Vincent Vivier. Revisiting cyclic voltammetry and electrochemical impedance spectroscopy analysis for capacitance measurements. *Electrochimica Acta*, 343:136109, 2020.

[117] Gomaa AM Ali, Osama A Fouad, Salah A Makhlouf, Mashitah M Yusoff, and Kwok Feng Chong. Co 3 o 4/sio 2 nanocomposites for supercapacitor application. *Journal of Solid State Electrochemistry*, 18(9):2505–2512, 2014.

[118] Keiichi Okajima, Keigo Ohta, and Masao Sudoh. Capacitance behavior of activated carbon fibers with oxygen-plasma treatment. *Electrochimica Acta*, 50(11):2227–2231, 2005.

[119] Soshi Shiraishi, Hideyuki Kurihara, Keiji Okabe, Denisa Hulicova, and Asao Oya. Electric double layer capacitance of highly pure single-walled carbon nanotubes (hipco™ buckytubes™) in propylene carbonate electrolytes. *Electrochemistry Communications*, 4(7):593–598, 2002.

[120] Ronald J Rice and Richard L McCreery. Quantitative relationship between electron transfer rate and surface microstructure of laser-modified graphite electrodes. *Analytical Chemistry*, 61(15):1637–1641, 1989.

[121] Longhua Tang, Ying Wang, Yueming Li, Hongbing Feng, Jin Lu, and Jinghong Li. Preparation, structure, and electrochemical properties of reduced graphene sheet films. *Advanced Functional Materials*, 19(17):2782–2789, 2009.

[122] Alexander R Harris, Jie Zhang, Anastassija Konash, Darrell Elton, Mark Hyland, and Alan M Bond. Efficient strategy for quality control of screen-printed carbon ink disposable sensor electrodes based on simultaneous evaluation of resistance, capacitance and faradaic current by fourier transform ac voltammetry. *Journal of Solid State Electrochemistry*, 12(10):1301–1315, 2008.

[123] David Salinas-Torres, Francisco Huerta, Francisco Montilla, and Emilia Morallón. Study on electroactive and electrocatalytic surfaces of single walled carbon nanotube-modified electrodes. *Electrochimica Acta*, 56(5):2464–2470, 2011.

[124] He Wang, Haitao Niu, Hongjie Wang, Wenyu Wang, Xin Jin, Hongxia Wang, Hua Zhou, and Tong Lin. Micro-meso porous structured carbon nanofibers with ultrahigh surface area and large supercapacitor electrode capacitance. *Journal of Power Sources*, 482:228986, 2021.

[125] K Kierzek, E Frackowiak, G Lota, G Gryglewicz, and J Machnikowski. Electrochemical capacitors based on highly porous carbons prepared by koh activation. *Electrochimica Acta*, 49(4):515–523, 2004.

[126] PL Taberna, Patrice Simon, and Jean-François Fauvarque. Electrochemical characteristics and impedance spectroscopy studies of carbon-carbon supercapacitors. *Journal of the Electrochemical Society*, 150(3):A292, 2003.

[127] David Pech, Magali Brunet, Pierre-Louis Taberna, Patrice Simon, Norbert Fabre, Fabien Mesnilgrente, Véronique Conédéra, and Hugo Durou. Elaboration of a microstructured inkjet-printed carbon electrochemical capacitor. *Journal of Power Sources*, 195(4):1266–1269, 2010.

[128] Richard Guy Compton and Craig E Banks. *Understanding voltammetry*. World Scientific, 2018.

[129] SC Wang, KS Chang, and Chiun-Jye Yuan. Enhancement of electrochemical properties of screen-printed carbon electrodes by oxygen plasma treatment. *Electrochimica Acta*, 54(21):4937–4943, 2009.

[130] AJ Bard and LR Faulkner. *Electrochemical Methods, Fundamentals and Applications*. John Wiley Sons, 2001. 237 pp.

[131] Gareth P Keeley and Michael EG Lyons. The effects of thin layer diffusion at glassy carbon electrodes modified with porous films of single-walled carbon nanotubes. *Int. J. Electrochem. Sci*, 4:794–809, 2009.

[132] Noémie Elgrishi, Kelley J Rountree, Brian D McCarthy, Eric S Rountree, Thomas T Eisenhart, and Jillian L Dempsey. A practical beginner's guide to cyclic voltammetry. *Journal of chemical education*, 95(2):197–206, 2018.

[133] Yijun Wang, Juan G Limon-Petersen, and Richard G Compton. Measurement of the diffusion coefficients of [ru (nh3) 6] 3+ and [ru (nh3) 6] 2+ in aqueous solution using microelectrode double potential step chronoamperometry. *Journal of Electroanalytical Chemistry*, 652(1-2):13–17, 2011.

[134] Keith B Oldham. Ultimate cyclic voltammetry: an analytical examination of the reversible case. *Journal of Solid State Electrochemistry*, 17(11):2749–2756, 2013.

[135] Pengcheng Zhu and Yuyuan Zhao. Cyclic voltammetry measurements of electroactive surface area of porous nickel: Peak current and peak charge methods and diffusion layer effect. *Materials Chemistry and Physics*, 233:60–67, 2019.

[136] Henry TH Chan, Enno Kätelhön, and Richard G Compton. Voltammetry using multiple cycles: Porous electrodes. *Journal of Electroanalytical Chemistry*, 799: 126–133, 2017.

[137] Christian Amatore, Sabine Szunerits, Laurent Thouin, and Jean-Stéphane Warkocz. The real meaning of nernst's steady diffusion layer concept under non-forced hydrodynamic conditions. a simple model based on levich's seminal view of convection. *Journal of electroanalytical chemistry*, 500(1-2):62–70, 2001.

[138] E Warburg. Ueber das verhalten sogenannter unpolarisirbarer elektroden gegen wechselstrom. *Annalen der Physik*, 303(3):493–499, 1899.

[139] Samuel J Cooper, Antonio Bertei, Donal P Finegan, and Nigel P Brandon. Simulated impedance of diffusion in porous media. *Electrochimica Acta*, 251:681–689, 2017.

[140] Juan Bisquert and Albert Compte. Theory of the electrochemical impedance of anomalous diffusion. *Journal of Electroanalytical Chemistry*, 499(1):112–120, 2001.

[141] Electrochemimcal impedance spectroscopy primer. , Gamry Instruments, PA, US, Application note, -.

[142] Anis Allagui, Todd J Freeborn, Ahmed S Elwakil, and Brent J Maundy. Reevaluation of performance of electric double-layer capacitors from constant-current charge/discharge and cyclic voltammetry. *Scientific reports*, 6(1):1–8, 2016.

[143] CH Hsu and Florian Mansfeld. Concerning the conversion of the constant phase element parameter y0 into a capacitance. *Corrosion*, 57(09), 2001.

[144] Victor Q Pham, Nagesh Rao, and Christopher K Ober. Swelling and dissolution rate measurements of polymer thin films in supercritical carbon dioxide. *The Journal of supercritical fluids*, 31(3):323–328, 2004.

[145] Hyun-Kon Song, Yong-Ho Jung, Kun-Hong Lee, and Le H Dao. Electrochemical impedance spectroscopy of porous electrodes: the effect of pore size distribution. *Electrochimica Acta*, 44(20):3513–3519, 1999.

[146] Frank Rindfleisch, Todd P DiNoia, and Mark A McHugh. Solubility of polymers and copolymers in supercritical co2. *The Journal of Physical Chemistry*, 100(38): 15581–15587, 1996.

[147] Vannessa Goodship and Erich Okoth Ogur. *Polymer processing with supercritical fluids*, volume 15. iSmithers Rapra Publishing, 2005.

[148] Xia Liao, Haichen Zhang, and Ting He. Preparation of porous biodegradable polymer and its nanocomposites by supercritical co2 foaming for tissue engineering. *Journal of Nanomaterials*, 2012, 2012.

[149] Kirill Arapov, Eric Rubingh, Robert Abbel, Jozua Laven, Gijsbertus de With, and Heiner Friedrich. Conductive screen printing inks by gelation of graphene dispersions. *Advanced Functional Materials*, 26(4):586–593, 2016.

[150] JG Wijmans and CA Smolders. Preparation of asymmetric membranes by the phase inversion process. In *Synthetic Membranes: Science, Engineering and Applications*, pages 39–56. Springer, 1986.

[151] LJM Jacobs, KCH Danen, MF Kemmere, and JTF Keurentjes. A parametric study into the morphology of polystyrene-co-methyl methacrylate foams using supercritical carbon dioxide as a blowing agent. *Polymer*, 48(13):3771–3780, 2007.

[152] E Reverchon and S Cardea. Production of controlled polymeric foams by supercritical co2. *The Journal of Supercritical Fluids*, 40(1):144–152, 2007.

[153] Ze Yang, Dongdong Hu, Tao Liu, Zhimei Xu, and Ling Zhao. Strategy for preparation of microcellular rigid polyurethane foams with uniform fine cells and high expansion ratio using supercritical co2 as blowing agent. *The Journal of Supercritical Fluids*, 153:104601, 2019.

[154] Victor E Sizov, Mikhail S Kondratenko, Marat O Gallyamov, and Keith J Stevenson. Advanced porous polybenzimidazole membranes for vanadium redox batteries synthesized via a supercritical phase-inversion method. *The Journal of Supercritical Fluids*, 137:111–117, 2018.

[155] Ioannis Tsivintzelis, Eleni Pavlidou, and Costas Panayiotou. Biodegradable polymer foams prepared with supercritical co2–ethanol mixtures as blowing agents. *The Journal of Supercritical Fluids*, 42(2):265–272, 2007.

[156] Claustre Prat, Manuel Vicente, and Santiago Esplugas. Treatment of bleaching waters in the paper industry by hydrogen peroxide and ultraviolet radiation. *Water Research*, 22(6):663–668, 1988.

[157] Apha. *Standard Methods for the Examination of Water and Wastewater 14ed.* APHA American Public Health Association, 1976.

[158] Joseph Wang, Yuehe Lin, and Liang Chen. Organic-phase biosensors for monitoring phenol and hydrogen peroxide in pharmaceutical antibacterial products. *Analyst*, 118(3):277–280, 1993.

[159] Li Bao, Marat V Avshalumov, Jyoti C Patel, Christian R Lee, Evan W Miller, Christopher J Chang, and Margaret E Rice. Mitochondria are the source of hydrogen peroxide for dynamic brain-cell signaling. *Journal of Neuroscience*, 29(28):9002–9010, 2009.

[160] Mark B Hampton and Sten Orrenius. Dual regulation of caspase activity by hydrogen peroxide: implications for apoptosis. *FEBS letters*, 414(3):552–556, 1997.

[161] Anita Ayer, Daniel J Fazakerley, David E James, and Roland Stocker. The role of mitochondrial reactive oxygen species in insulin resistance. *Free Radical Biology and Medicine*, 2021.

[162] Albert S Keston and Richard Brandt. The fluorometric analysis of ultramicro quantities of hydrogen peroxide. *Analytical biochemistry*, 11(1):1–5, 1965.

[163] Edgar Pick and Yona Keisari. A simple colorimetric method for the measurement of hydrogen peroxide produced by cells in culture. *Journal of immunological methods*, 38(1-2):161–170, 1980.

[164] Kingo Itaya, Nobuyoshi Shoji, and Isamu Uchida. Catalysis of the reduction of molecular oxygen to water at prussian blue modified electrodes. *Journal of the American Chemical Society*, 106(12):3423–3429, 1984.

[165] Craig McBeth, Andrew Paterson, and Duncan Sharp. Pad-printed prussian blue doped carbon ink for real-time peroxide sensing in cell culture. *Journal of Electroanalytical Chemistry*, 878:114537, 2020.

[166] Arkady A Karyakin. Prussian blue and its analogues: electrochemistry and analytical applications. *Electroanalysis*, 13(10):813–819, 2001.

[167] Ayman Chmayssem, Nicolas Verplanck, Constantin Edi Tanase, Guillaume Costa, Karen Monsalve-Grijalba, Simon Amigues, Mélanie Alias, Maxime Gougis, Véronique Mourier, Séverine Vignoud, et al. Development of a multiparametric (bio) sensing platform for continuous monitoring of stress metabolites. *Talanta*, 229:122275, 2021.

[168] Francesco Ricci, Aziz Amine, Catalin S Tuta, Anton A Ciucu, Fausto Lucarelli, Giuseppe Palleschi, and Danila Moscone. Prussian blue and enzyme bulk-modified screen-printed electrodes for hydrogen peroxide and glucose determination with improved storage and operational stability. *Analytica Chimica Acta*, 485(1):111–120, 2003.

[169] D Moscone, D D'ottavi, Dario Compagnone, G Palleschi, and A Amine. Construction and analytical characterization of prussian blue-based carbon paste electrodes and their assembly as oxidase enzyme sensors. *Analytical Chemistry*, 73(11):2529–2535, 2001.

[170] Maryann P O'Halloran, Miloslav Pravda, and George G Guilbault. Prussian blue bulk modified screen-printed electrodes for h2o2 detection and for biosensors. *Talanta*, 55(3):605–611, 2001.

[171] Linan Wang, Na Wang, Jianping Wen, Yongjuan Jia, Shangshu Pan, Hailang Xiong, Yang Tang, Jie Wang, Xiaojin Yang, Yanzhi Sun, et al. Ultrasensitive sensing of environmental nitroaromatic contaminants on nanocomposite of prussian blue analogues cubes grown on glucose-derived porous carbon. *Chemical Engineering Journal*, 397:125450, 2020.

[172] Osamu Sato, Shinya Hayami, Yasuaki Einaga, and Zhong-Ze Gu. Control of the magnetic and optical properties in molecular compounds by electrochemical, photochemical and chemical methods. *Bulletin of the Chemical Society of Japan*, 76 (3):443–470, 2003.

[173] Hyungwoo Lee, Minbaek Lee, Seon Namgung, and Seunghun Hong. Wide contact structures for low-noise nanochannel devices based on a carbon nanotube network. *ACS nano*, 4(12):7612–7618, 2010.

[174] Jill Chastain and Roger C King Jr. Handbook of x-ray photoelectron spectroscopy. *Perkin-Elmer, USA*, page 261, 1992.

[175] A Deryło-Marczewska, J Goworek, S Pikus, E Kobylas, and W Zgrajka. Characterization of melamine- formaldehyde resins by xps, saxs, and sorption techniques. *Langmuir*, 18(20):7538–7543, 2002.

[176] Liang-Hong Guo, H Allen, and O Hill. Direct electrochemistry of proteins and enzymes. *Advances in inorganic chemistry*, 36:341–375, 1991.

[177] Muhammad Adeel, Md Mahbubur Rahman, Isabella Caligiuri, Vincenzo Canzonieri, Flavio Rizzolio, and Salvatore Daniele. Recent advances of electrochemical and optical enzyme-free glucose sensors operating at physiological conditions. *Biosensors and Bioelectronics*, 165:112331, 2020.

[178] VJ Razumas, JJ Jasaitis, and JJ Kulys. Electrocatalysis on enzyme-modified carbon materials. *Bioelectrochemistry and Bioenergetics*, 12(3-4):297–322, 1984.

[179] A Amine and J-M Kauffmann. Preparation and characterization of a fragile enzyme immobilized carbon paste electrode. *Bioelectrochemistry and bioenergetics*, 28(1-2): 117–125, 1992.

[180] György Marko-Varga, Jenny Emnéus, Lo Gorton, and Tautgirdas Ruzgas. Development of enzyme-based amperometric sensors for the determination of phenolic compounds. *TrAC Trends in Analytical Chemistry*, 14(7):319–328, 1995.

[181] Juan Li, Swee Ngin Tan, and Hailin Ge. Silica sol-gel immobilized amperometric biosensor for hydrogen peroxide. *Analytica Chimica Acta*, 335(1-2):137–145, 1996.

[182] Bernard S Munge, Richard S Dowd, Colleen E Krause, and Lines N Millord. Ultrasensitive hydrogen peroxide biosensor based on enzyme bound to layered nonoriented multiwall carbon nanotubes/polyelectrolyte electrodes. *Electroanalysis: An International Journal Devoted to Fundamental and Practical Aspects of Electroanalysis*, 21(20):2241–2248, 2009.

[183] Ionel Cãtãlin Popescu, Gunilla Zetterberg, and Lo Gorton. Influence of graphite powder, additives and enzyme immobilization procedures on a mediatorless hrp-modified carbon paste electrode for amperometric flow-injection detection of h2o2. *Biosensors and Bioelectronics*, 10(5):443–461, 1995.

[184] YJ Teng, SH Zuo, and MB Lan. Direct electron transfer of horseradish peroxidase on porous structure of screen-printed electrode. *Biosensors and Bioelectronics*, 24 (5):1353–1357, 2009.

[185] Tanin Tangkuaram, Chatchai Ponchio, Thippayawadee Kangkasomboon, Panadda Katikawong, and Waret Veerasai. Design and development of a highly stable hydrogen peroxide biosensor on screen printed carbon electrode based on horseradish peroxidase bound with gold nanoparticles in the matrix of chitosan. *Biosensors and Bioelectronics*, 22(9-10):2071–2078, 2007.

[186] VG Gavalas, NA Chaniotakis, and TD Gibson. Improved operational stability of biosensors based on enzyme-polyelectrolyte complex adsorbed into a porous carbon electrode. *Biosensors and Bioelectronics*, 13(11):1205–1211, 1998.

[187] Ulla Wollenberger, Joseph Wang, Mehmet Ozsoz, Elisa Gonzalez-Romero, and Frieder Scheller. Bulk modified enzyme electrodes for reagentless detection of peroxides. *Journal of Electroanalytical Chemistry and Interfacial Electrochemistry*, 321 (2):287–296, 1991.

[188] Yidan Liu, Xiuhui Liu, Zhipan Guo, Zhongai Hu, Zhonghua Xue, and Xiaoquan Lu. Horseradish peroxidase supported on porous graphene as a novel sensing platform for detection of hydrogen peroxide in living cells sensitively. *Biosensors and Bioelectronics*, 87:101–107, 2017.

[189] Yue Wang and Yasushi Hasebe. Carbon felt-based bioelectrocatalytic flow-through detectors: Highly sensitive amperometric determination of h2o2 based on a direct electrochemistry of covalently modified horseradish peroxidase using cyanuric chloride as a linking agent. *Sensors and Actuators B: Chemical*, 155(2):722–729, 2011.

[190] Cun-Xi Lei, Shun-Qin Hu, Guo-Li Shen, and Ru-Qin Yu. Immobilization of horseradish peroxidase to a nano-au monolayer modified chitosan-entrapped carbon paste electrode for the detection of hydrogen peroxide. *Talanta*, 59(5):981–988, 2003.

[191] Wenzhi Jia, Stefanie Schwamborn, Chen Jin, Wei Xia, Martin Muhler, Wolfgang Schuhmann, and Leonard Stoica. Towards a high potential biocathode based on direct bioelectrochemistry between horseradish peroxidase and hierarchically structured carbon nanotubes. *Physical Chemistry Chemical Physics*, 12(34):10088–10092, 2010.

[192] Willem Norde. The behaviour of proteins at interfaces in relation to their structural stability. In *Studies in Organic Chemistry*, volume 47, pages 3–11. Elsevier, 1993.

[193] Elisabeth Csoeregi, Lo Gorton, Gyoergy Marko-Varga, Anna Judit Tuedoes, and Wim Theodore Kok. Peroxidase-modified carbon fiber microelectrodes in flow-through detection of hydrogen peroxide and organic peroxides. *Analytical Chemistry*, 66(21):3604–3610, 1994.

[194] Benoît Limoges, Jean-Michel Savéant, and Dounia Yazidi. Quantitative analysis of catalysis and inhibition at horseradish peroxidase monolayers immobilized on an electrode surface. *Journal of the American Chemical Society*, 125(30):9192–9203, 2003.

[195] John H Crowe, Lois M Crowe, John F Carpenter, and C Aurell Wistrom. Stabilization of dry phospholipid bilayers and proteins by sugars. *Biochemical Journal*, 242 (1):1, 1987.

[196] Akshay Jain, Veronica Ong, Sundaramurthy Jayaraman, Rajasekhar Balasubramanian, and MP Srinivasan. Supercritical fluid immobilization of horseradish peroxidase on high surface area mesoporous activated carbon. *The Journal of Supercritical Fluids*, 107:513–518, 2016.

[197] Tanji Yin, Dawei Pan, and Wei Qin. All-solid-state polymeric membrane ion-selective miniaturized electrodes based on a nanoporous gold film as solid contact. *Analytical chemistry*, 86(22):11038–11044, 2014.

[198] Monia Fibbioli, Werner E Morf, Martin Badertscher, Nicolaas F de Rooij, and Ernö Pretsch. Potential drifts of solid-contacted ion-selective electrodes due to zero-current ion fluxes through the sensor membrane. *Electroanalysis: An International Journal Devoted to Fundamental and Practical Aspects of Electroanalysis*, 12(16): 1286–1292, 2000.

[199] Kimberly F Abbett, Amyn S Teja, Janusz Kowalik, and Laren Tolbert. Preparation of conducting composites of polypyrrole using supercritical carbon dioxide. *Journal of applied polymer science*, 90(4):1113–1116, 2003.

[200] Shutaro Kurosawa, Amyn S Teja, Janusz Kowalik, and Laren Tolbert. Preparation and properties of conducting composites of polypyrrole and porous cross-linked polystyrene with and without supercritical carbon dioxide. *Synthetic metals*, 156 (2-4):146–153, 2006.

[201] Andreas Wurm, Dirk Lellinger, Alexander A Minakov, Tetyana Skipa, Petra Pötschke, Radu Nicula, Ingo Alig, and Christoph Schick. Crystallization of poly ($\varepsilon$-caprolactone)/mwcnt composites: A combined saxs/waxs, electrical and thermal conductivity study. *Polymer*, 55(9):2220–2232, 2014.